RUHR
UNIVERSITÄT
BOCHUM

RUB

Discharge Characteristics of a Micro Cavity Plasma Array in Helium-Oxygen Mixtures: Oxygen as a Model System for Plasma Catalytic Applications

DISSERTATION

zur
Erlangung des Grades
„Doktor der Naturwissenschaften"

an der Fakultät für Physik und Astronomie
der Ruhr-Universität Bochum

von
David Frithjof Steuer
aus Herne

Bochum 2024

1. Gutachter: Jun.-Prof. Dr. Judith Golda

2. Gutachter: Prof. Dr. Achim von Keudell

Datum der Disputation: ....

Contents

1 Introduction

1.1 Motivation

Over 99% of all visible matter in the universe is in the plasma state [1]. This includes stars like the sun, the solar wind, and the interstellar medium. On Earth, plasmas appear as lightning and auroras, caused by solar particles interacting with the Earth's magnetic field. While natural plasmas are widely recognized, the artificial plasmas encountered in everyday life, such as those in neon signs, car headlights, plasma TVs, and plasma welding, often go unnoticed. They are also crucial in production, especially for surface modification. Plasma applications include coating materials with functional layers [2], such as mirrors, non-stick coatings, tool hardening, food packaging protection, and heat-resistant layers for aircraft turbines. Additionally, surfaces can be cleaned or activated for painting or bonding [3]. Plasma etching [4], essential in semiconductor manufacturing, allows mass production of integrated circuits. The latest chips are made using EUV lithography, which employs plasma-generated radiation at $13.5\,\mathrm{nm}$ [5]. Plasma medicine [6, 7] is another growing field, utilizing plasmas for disinfecting medical tools and body parts, and treating dental issues, wounds, and skin cancer. Finally, nuclear fusion [8] research relies on the plasma state for thermonuclear reactions, potentially solving future energy supply challenges.

In recent years, there has been considerable interest in using plasmas to dissociate and convert molecular gases, such as volatile organic compounds (VOCs), marking another noteworthy area of research. A new approach, plasma catalysis or plasma-assisted catalysis, combines the properties of a plasma with those of conventional heterogeneous catalysts [9–12]. In classical catalysis [13], materials (catalysts) are usually used in solid form to accelerate chemical reactions, influence their selectivity or activate

them in the first place. The catalyst reduces the activation energy of the reaction, but does not change the chemical equilibrium and is not consumed in the process. Typically, the reactions in classical catalysis are thermally driven. However, this is to be changed by using a non-equilibrium plasma [14]. This type of plasma is characterized by the fact that neutral particles and ions remain close to room temperature, while electrons are heated to temperatures in the range of a few $10000\,\mathrm{K}$. The electrons drive the plasma chemistry mainly through collisions and generate excited and reactive species. Especially molecules that are excited to high vibrational states have a low dissociation energy and thus an increased reactivity at the surface of a catalyst [15]. The aim of plasma catalysis is therefore to reduce the reaction temperatures and thus increase the energy efficiency and simplicity of the reactors and the associated usability in industry. Moreover, the thermal equilibrium required in classical catalysis means that the energy is not selectively distributed to different (possibly unwanted) reactions. By using a plasma, the selectivity for certain reactions can be increased and controlled by the choice of plasma parameters [16] (voltage waveform, reactor geometry, etc.). In addition, a plasma can be switched on and off very easily and is operated exclusively with electrical energy. This makes it very suitable for use in industry and offers opportunities for concepts such as "Power to X", in which surplus renewable energy can be stored or used for other purposes.

Atmospheric pressure discharges are ideal for industrial-scale gas conversion or plasma catalysis [17] . They eliminate the need for complex vacuum systems and allow for very high gas flow rates. However, atmospheric pressure plasmas have a limitation: according to Paschen's law, the ignition criterion is met only within a narrow parameter range. Balancing the electrode distance, which defines the plasma volume, with the applied voltage is crucial. Typically, microplasmas with electrode gaps ranging from a few micrometers to a few millimeters are used to keep the ignition voltage within a practical range of several kilovolts [18]. The transition to an erosive thermal arc discharge, can be suppressed using a dielectric barrier even at high voltages [19]. Consequently, dielectric barrier discharges (DBDs) hold significant potential for plasma catalysis [20].

Despite the dielectric barrier, the distance between the electrodes is small in relation to the desired treatment volume. This can be solved in different ways. For example, many individual microplasma reactors can be used simultaneously (e.g. connected in parallel or in series). Alternatively, DBDs offer the possibility of surface discharges which, in contrast to volume discharges, do not ignite in the gap between two electrodes, but on a surface [21]. As a result, large plasma expansions can be achieved with relatively small reactor sizes. A combination of both concepts is used in this work. An array of thousands of cavities with a diameter and height in the µm range is used as a reactor [22]. All cavities are arranged on one electrode so that only a single reactor is required although there are many individual discharges. For industrial applications, the reactor could be scaled to significantly higher numbers of cavities.

The concept of microplasma arrays originates from the work of G. Eden's group [23–26]. They used micro structure techniques to incorporate cavities into a silicon wafer, which could then be coated with a dielectric layer and an additional electrode layer. This cavity structure is particularly valuable for research, as the enclosed discharge limits the plasma to a specific volume, simplifying characterization despite the inherent complexities of phenomena such as collisions and plasma-wall interactions. The large number of identical cavities also allows for good statistical measurements with relatively moderate effort. Micro plasma arrays have proven to be effective UV light sources and are already employed in various industrial applications, including disinfection of large surfaces, water treatment, ozone generation, and as light sources [27].

Metal grid arrays represent an advance over silicon-based arrays [22]. In this design, cavities are laser-cut into a metal foil, complemented by a dielectric foil and a grounded electrode. This reactor offers several advantages for research. Its modular setup allows for the variation of parameters and easy replacement of defective parts by exchanging components. Notably, the dielectric foil can be coated with a catalyst, facilitating direct plasma-catalyst interactions for detailed study. Post plasma treatment, the modular setup can be disassembled for surface diagnostics. Typically, the reactor is operated using a helium gas flow. Initial measurements indicate that, despite the new design, the discharge dynamics are comparable to those of silicon-based structures [22]. The

reactor's durability and associated reproducibility have enabled the determination of fundamental properties, such as the electric field. These measurements reveal very high electric fields within the cavities, which could enhance plasma catalysis [28]. The reactor's simple design and well-defined discharge dynamics offer advantages over traditional packed bed reactors [29]. In packed bed reactors, discharges occur directly between the catalyst materials, potentially increasing efficiency. However, due to the presence of catalytic material, the discharge dynamics are much less controlled than in micro cavity designs. In addition, packed bed reactors offer limited access for diagnostic tools, making micro cavity plasma arrays a superior option for research purposes.

To comprehensively characterize this type of discharges, and to enable a model description, further fundamental properties must be determined. In addition to the electric field strength, the direction of the electric field is relevant for tracking the transport of charged particles to the surfaces and thus to the catalyst material. Surface charges also play a decisive role, especially in dielectric barrier discharges. These charges can shield the applied electric field and thereby significantly influence the ignition and discharge dynamics. Additionally, models show that surface charges can positively affect the conversion efficiency of plasma catalytic reactors [9, 30]. Therefore, the ability to monitor or even control these charges would be an important tool for plasma catalysis. Lastly, the power dissipated into the plasma should be known to compare the efficiency of the reactor for various applications.

A wide variety of systems are currently being investigated worldwide where plasma catalysis could enhance efficiency. A broad range of plasma reactors, gas mixtures, and catalyst materials are being tested. In addition to ammonia synthesis, the main research focus is the conversion of volatile organic compounds (VOCs) [31, 32]. Given the complexity of these systems, a comprehensive plasma chemistry model is often necessary for fundamental understanding. Therefore, it makes sense to begin with a model system that has comparable properties. One candidate for this is oxygen. This is often admixed to more complex systems, such as CO_2 [33], methane [33], n-butane [34] or NO_x [35]. In plasma, molecular oxygen is dissociated into atomic oxygen, which can either react with the gas to be treated or the catalytic surface (change in oxidation

state, reduction of metal oxide catalysts to their metallic form, reduced coke formation, change in work function) [36]. It is known that even small additions of oxygen can lead to significant changes in the discharge mode [37, 38]. If this influence is understood, discharge parameters and reactor properties can be adjusted and optimized for more complex systems.

To determine the exact performance of the conversion, the densities of the species must be measured with spatial and temporal resolution wherever possible. The most accurate diagnostics typically rely on laser spectroscopic methods or light absorption techniques, such as absorption spectroscopy or Fourier transform infrared spectroscopy. However, these methods require extensive optical access to the discharge, which is often unavailable, especially when a catalyst is used. Optical emission spectroscopy presents an alternative. While it also requires optical access, the extent needed is usually less than that of the previously mentioned methods. The primary challenge of optical emission spectroscopy, however, is that it necessitates numerous assumptions or models about the observed discharge to interpret the results accurately. Therefore, the development of new diagnostics for monitoring plasma catalytic processes is essential.

1.2 Research questions and thesis outline

The following section should clarify which of the previously mentioned aspects are to be addressed in this work. Therefore, the main objective is divided into various research questions that are to be explicitly answered throughout this study.

The overarching goal of this work is to fundamentally characterize the micro cavity plasma array with respect to discharge dynamics and the formation of reactive species. By combining different diagnostics, the various plasma properties such as electric field, surface charges, dissipated power or the formation of reactive species are to be decoupled. This enables systematic investigation of plasma catalytic mechanisms in relation to diverse plasma parameters.

First, a basic helium system is investigated to understand the discharge dynamics. Current, voltage and emission measurements are used for this purpose. By varying parameters such as the applied voltage or frequency, the ignition and discharge behavior are investigated. The aim is to determine properties such as ignition times, dissipated power or plasma expansion. This leads to the first research question:

> **How can the discharge be fundamentally characterized? Is it possible to assign the discharge to a known DBD mode in order to compare the reactor with others?**

Once the question of the discharge mode has been clarified, a pure helium discharge is considered further, focusing on charged particles. As already mentioned, charge carriers can change the plasma catalytic properties [30]. For this reason, the charge transported by the discharge and the surface charges are determined. New methods are developed to answer the following questions:

> **How do charge carriers on the surface affect the discharge? What is the charge carrier density and can the concentration be manipulated externally, for example to influence plasma catalytic effects?**

The charged particles are accelerated by the electric field during discharge, impacting the surfaces. However, the electric field is influenced by charge carriers and their associated shielding effects. Therefore, to comprehend the transport mechanism, it is crucial to also examine the electric field. Beyond the previously determined electric field strength [28], it is essential to investigate the spatial distribution and direction of the electric field.

What is the spatial distribution of the electric field? In which direction does the electric field point, and how is it influenced by charge carriers?

After the discharge has been characterized under pure helium, oxygen is to be added in order to create a model system for plasma catalysis. It is known from the literature that the addition of other gases can cause significant changes in the discharge dynamics and can even lead to a new discharge mode with completely different properties [37, 38]. Therefore, fundamental characteristics such as the emission, the dissipated power or the electric field are investigated again to determine possible changes due to the new gas mixture.

What influence does the addition of oxygen have on the discharge dynamics? Does the discharge mode change?

The dissociation of oxygen is then discussed in the final part of this thesis. To this end, a new diagnostic method based on optical emission spectroscopy is developed. This allows absolute atomic oxygen densities to be determined with spatial and temporal resolution despite the limited optical access within the cavities. By determining the degree of dissociation, initial findings on the conversion efficiency of the reactor can then be obtained.

Which degrees of dissociation can be achieved with the reactor and what does the degree of dissociation depend on? What is the spatial and temporal distribution of the atomic oxygen density? Is the micro cavity plasma array a suitable reactor for gas conversion?

In addition to the generation of atomic oxygen within the discharge, the two-dimensional distribution of these atoms outside the cavities is also of interest. Here, the reactive species could interact with the gas to be treated or with possible surfaces. Since there is no plasma emission in this area, the atoms must be actively excited with a laser for detection.

What is the density distribution of atomic oxygen outside the cavities? How far can the reactive species exit the cavities, and what are the dominant transport and loss mechanisms? How are the densities outside the cavity related to those inside?

If the formulated research questions are answered, it lays the foundation for a systematic investigation of various plasma-catalytic systems. This enables the examination of the influence of individual plasma parameters on conversion or selectivity and the identification of dominant plasma-catalytic mechanisms. In the future, this knowledge can help design large-scale, efficient reactors for industrial applications.

2 Fundamentals

In the following chapter, the physical fundamentals underlying this work are discussed. Specifically, dielectric barrier discharges and micro structured discharges are examined in detail.

2.1 Dielectric barrier discharges

Dielectric barrier discharges (DBDs), also referred to as silent discharges or ozonizers, are known primarily for their numerous industrial applications. The latter term dates back to the first description of a DBD for the generation of ozone by *Werner von Siemens* in 1857 [39]. In addition to the generation of ozone, DBDs are used today for surface functionalization [40], plasma medicine [7], excimer lamps [41], plasma displays [42] or plasma aerodynamics [43] and many other applications [19].

All applications mentioned above have in common that they should be applicable at atmospheric pressure, since the use of low pressure chambers is either not possible or not profitable due to the low particle numbers. However, igniting and maintaining plasmas at atmospheric pressure is a technical challenge because of the risk of thermal arcing. This is due to the common ignition mechanism of atmospheric pressure discharges, the streamer mechanism [44], which is discussed in more detail in section 2.1.2. Here, an avalanche of electrons travels through the gas, generating such a large electric field at the so-called streamer head that the surrounding area can also be ionized, creating a self-sustaining mechanism. A quasi neutral channel remains behind the streamer. When this channel connects the two electrodes, a breakdown occurs at which a very high current flows. Due to the resulting high temperatures, these arc or spark discharges are used, for example, for plasma welding. However, the transition to a thermal spark discharge is to be prevented for the majority of applications,

since on the one hand the electrodes can be severely damaged and on the other hand heat-sensitive surfaces such as plastics or human skin are to be treated. This can be achieved in different ways. One way is to use voltage pulses in the nanosecond range or a radio frequency to stop the plasma before the breakdown could occur (typically about 500 ns [45]). Alternatively, dielectric barriers can be inserted into the gas gap to prevent current flow between the electrodes and to protect the reactor [19, 46, 47]. This type of discharge is discussed in more detail in the following.

In the simplest case, a DBD consists of two planar electrodes. The dielectric is either on one of the two electrodes, on both electrodes or between the electrodes (see Figure 2.1 a)). These discharges are referred to as volume DBDs (v-DBDs). In contrast, surface DBDs (s-DBDs) ignite the plasma only on the dielectric surface. Again, different electrode arrangements are possible (see Figure 2.1 b)). Depending on the application, however, there are also very complex electrode arrangements, such as tilted or cylindrical electrodes. The dielectric typically consists of glass, quartz, ceramics, enamel, mica, plastics, silicon rubber or teflon [47]. Since the direct current (DC) through the dielectric is prevented, DBDs are operated with (pulsed) alternating voltage (AC). At atmospheric pressure, voltages between 1-100 kV at a frequency between a few Hz up to several MHz are commonly used. The electrode gap is between 0.1-10 mm. [19, 46, 47]
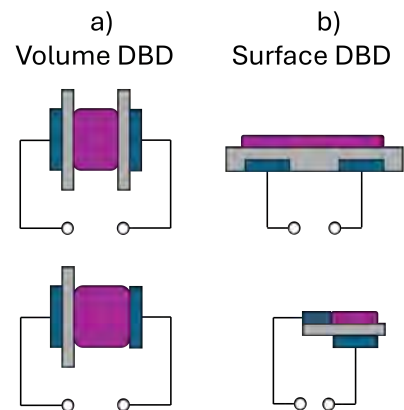
Figure 2.1: Typical barrier-discharge configurations based on [47].

Due to their structure, DBDs can be considered as capacitive elements. If a low AC voltage is applied without igniting a discharge, a displacement current can be measured which depends on the time derivative of the applied voltage and the total capacitance of the reactor. A conduction current can only pass through the reactor when there is a breakdown. However, this conduction current transports charges to the surface of the dielectric. These create an electric field, which counteracts the applied voltage, so that

the discharge extinguishes again. As described above, this prevents the transition to an arc or spark discharge and the plasma remains non-thermal, which is the core idea of a DBD. Despite this general behavior, the discharge characteristics of different DBDs can differ greatly. Depending on reactor geometry, pressure, voltage or gas composition, the number and duration of discharge pulses can vary. Also, the appearance can be filamentary or diffuse depending on the conditions.

2.1.1 Memory effect

One of the main unique features of DBDs is the fact that successive discharge pulses can influence each other, even across half-phases of the AC voltage. This is described as the memory effect [48]. Although this effect is not fully understood, several factors can be identified.

Depending on the gas type and applied frequency, species generated in the previous pulse can survive until the next ignition. If low electric fields prevail, slow ions can remain in the gas gap until the next ignition due to ambipolar diffusion [49]. If there are enough ions in the region in front of the cathode during the next breakdown, they can generate secondary electrons to support ignition. However, since the ion density decreases with time, the effect diminishes at low excitation frequencies. In addition, depending on the discharge, the external field is not very strongly shielded, causing the ions to be accelerated towards the cathode even before the next ignition. Another species that can survive between two discharges are metastable atoms or molecules. If the flux of these species to the cathode is large enough, they can also contribute significantly to the secondary electron production. However, in the case of noble gases such as helium, this effect is small because dimer formation occurs here, resulting in a lifetime that is only in the range of µs [50]. On the other hand, for instance nitrogen forms very long-lived metastables even at atmospheric pressure, which can release their potential energy through various reactions to produce electrons [49].

Surface effects have an even greater, and above all more long-lasting effect than volume effects. As described before, the discharge pulses transport charges onto the dielectric. These can influence the discharge in various ways. First, the external field is shielded.

In the case of filamentary discharges, this leads to new filaments preferentially igniting at other locations, since the electric field is less strongly shielded there. However, if the polarity of the external field is reversed, the surface charges actually strengthen the external field. In certain cases, a back-discharge can occur, where the effective electric field is large enough to ignite a discharge in the opposite direction even before the zero crossing of the external voltage. In most cases, the ignition voltage reduces at least, since the necessary effective field can be reached earlier. The locations on the dielectric where a filament appeared during the previous half-phase become preferred sites for new ignition, as a significant accumulation of charges at these spots enhances the local electric field [51]. In addition to shielding, surface charges also affect secondary electron emission. The electrons on the surface are weakly bound in shallow traps (1-2 eV) and can thus be more easily released than intrinsic ones [52]. This means that as long as the surface is charged, the secondary emission coefficient γ is increased. Therefore, the ignition of the next pulse is significantly supported.

The exact nature of the surface charges has not yet been definitively determined. It is assumed that negative charges consist of weakly bound electrons on the surface. In the case of a dielectric with positive electron affinity, however, the electrons can also enter the material and are located in the conduction band. Positive charges, on the other hand, are assumed to be electron defects resulting from electron-ion recombination on the surface. These defects are found in the valence band of the dielectric. [53, 54]

Besides electron flow, the surface can also be charged by electron desorption, ions, photoelectric effects or electron attachment [47]. Depending on the discharge, the lifetime varies from seconds to several hours. Thus, the memory effect due to surface charges can be observed for a much longer time than the discussed volume effects.

2.1.2 Discharge modes

DBDs can be operated in various discharge modes depending on voltage amplitude, excitation frequency, gas mixture, pressure or reactor geometry. The main difference is caused by the underlying breakdown mechanism. DBDs can be ignited with a streamer breakdown or with a Townsend breakdown [49]. The former case is usually manifested

by a filamentary appearance, while the latter case tends to generate a homogeneous discharge. The different characteristics, as well as the possibility of mode transitions, are explained in the following.

Filamentary mode

The majority of DBDs operating at atmospheric pressure are operated in a filamentary mode generated by the streamer mechanism [19, 47]. When a free electron is accelerated in an external electric field, collisions with the surrounding gas take place. Atoms or molecules can be ionized, creating further electron-ion pairs. These are also accelerated in the electric field, resulting in an avalanche effect. Due to the high pressure, many collisions take place and high charge carrier densities are quickly reached at the avalanche front. The mass difference between electrons and ions and the associated inertia of the ions cause charge separation and an eigenfield is created. This superimposes the external electric field and can become large enough to ionize by itself. Since the breakdown is now no longer dependent on the electron drift, the process can take place on the ns time scale. Behind the negative streamer head, a channel is formed in which surrounded electrons are collected and a quasi-neutral region is created. Under certain conditions, the process can be assisted by the generation of UV photons which are responsible for photoionization. A more detailed description of the streamer mechanism can be found in the literature [44, 45, 55].

If the quasi-neutral channel connects the two electrodes, a micro discharge (distinct from micro plasmas or micro structured discharges) forms. The filament behaves like a transient glow discharge, characterized by a cathode fall and a positive column [19]. As charges accumulate on the dielectric from the incoming current, an opposing field develops, typically extinguishing the discharge within 10-100 ns [47]. Increasing the voltage can raise the number of micro discharges per active phase, but the location changes with each breakdown due to residual charges shielding the field.

Despite the streamer mechanism, it is possible to achieve a more or less diffuse appearance of the discharge. This can be realized if the individual micro discharges develop as simultaneously as possible and the streamers couple with each other. One way to

achieve this is by pre-ionization, e.g. by photon ionization, and the use of very short voltage pulses [49]. Another possibility for superposition is to increase the diameter of the filaments. This can be controlled, for example, by the choice of gas, since the diameter of a filament depends on the ionization coefficient α. For electronegative gases, the value of α is reduced since electron attachment is more likely, so that the streamer diameter becomes comparatively small. In contrast, with noble gases such as helium, wider filaments can be produced [19]. Another advantage of helium is its high thermal conductivity. This can prevent thermal instabilities, which can lead to further contraction of the plasma. Overall, however, these diffuse-appearing discharges are to be distinguished from real homogeneous discharges.

Homogeneous mode

In addition to diffuse DBDs, which are ignited by the streamer mechanism but prevent the formation of individual filaments, there are also homogeneous DBDs which are ignited by the Townsend mechanism [37, 49, 56]. This ignition phenomenon is known from low pressure DC glow discharges. Here, an electron avalanche also plays a central role. However, the propagation speed is lower than in a streamer (µs instead of ns). This slower speed allows ions to reach the cathode, where secondary effects generate further electrons, supporting ignition and maintaining the discharge. The result is a homogeneous discharge that, unlike filamentary discharges, covers the entire electrode surface. In order to achieve ignition by the Townsend mechanism or to suppress a streamer, certain conditions must be met. Overall, the propagation of the electron avalanche should be slowed down to prevent the separation of charges and to avoid a field at the avalanche front that is large enough to ionize by itself. To ensure this, the external electric field should be as small as possible. Another way to keep the ionization rate low is to reduce the pressure, which corresponds to an increase in the free path length and a decrease in the collision rate. Although this is done in low pressure plasmas known for the Townsend mechanism, it is ruled out for most applications of DBDs for which atmospheric pressure is necessary. An alternative is offered by the reactor geometry, or more precisely, the electrode distance. If this is chosen to be small, the proportion of surface reactions or secondary electrons increases in comparison to the volume ionization. All in all, the product of pressure and electrode

gap, which is known from Paschen's law, is decisive for the mechanism with which the discharge ignites. At large values (>200 Torr cm), the discharge ignites preferentially in the streamer mechanism. At low values (<30 Torr cm), the Townsend mechanism is favored [49].

Even if the plasma is ignited by the Townsend mechanism, different discharge modes can result. In the literature, a distinction is made between atmospheric pressure Townsend discharge (APTD) and atmospheric pressure glow discharge (APGD) [49]. Both types have a homogeneous appearance, but differ, for example, in the burning duration or the conducted current.

Atmospheric Pressure Townsend Discharge (APTD)

When the ionization level is so low that no cathode fall can form, it is called a Townsend discharge, which is also known from low-pressure discharges. Here, no quasi-neutral positive column (plasma bulk) is formed, so that the external electric field is barely shielded. At atmospheric pressure, this form of discharge occurs primarily with nitrogen or noble gases.

A simulation of the voltage-current characteristic allows the discharge to be divided into different phases. A nitrogen discharge with a negative voltage of 15 kV at a frequency of 6 kHz was used [57]. Initially, the discharge is not ignited at low voltages. The current is determined by the displacement current. If the voltage is increased further, the discharge current increases. Electron avalanches run through the gas gap. The resulting ions reach the electrode and produce secondary electrons, which causes the discharge current to increase exponentially. As the voltage across the dielectric drops and the electron density on the surface decreases, secondary electron yield is reduced. The discharge current saturates. From this point on, the gap voltage remains constant despite further increasing applied voltage. This is due to the better conductivity of the plasma and the accumulating charges on the surfaces, which shield the external field. At the end, the discharge current slowly drops and the discharge is extinguished when the applied voltage drops again.

A Townsend discharge does not have to consist of only one pulse per half phase as described above, but can also show several pulses [58]. Each pulse can be described by the previously described discharge mode. However, after a discharge has been extinguished, further pulses can be ignited as long as the external voltage continues to rise, i.e. the reversal point has not yet been reached. The type and manner of the pulses is determined by the electrode distance, the dielectric material, the voltage and the frequency. An important influence is the desorption of electrons at the cathode, which were adsorbed there during a pulse before. These act as start electrons for a new avalanche. Thus ions are created in this area, which influence the electric field, so that there is no quasi-neutrality. The time it takes for the ions to travel from the cathode, where they were created, to the anode, where they can produce secondary electrons, is responsible for the pulsing behavior.

Atmospheric Pressure Glow Discharge (APGD)

If the ionization level is higher, a glow discharge can be ignited by the Townsend mechanism, at which the Townsend plateau is exceeded. A cathode fall, a negative glow, a Faraday dark space and a positive column are formed, i.e. a quasi-neutral plasma bulk [59]. The latter shields the external electric field. Since the plasma quickly becomes highly conductive, the gap voltage collapses and the discharge is extinguished. In addition, the deposited surface charges further shield the electric field. Thus, the discharge pulses of an APGD are significantly shorter (factor of 10) than in an APTD. Typically, such a discharge mode takes place in noble gases such as helium or neon. The electrode gap can be larger than for APTD and is in the range of a few millimeters.

Also in APGD it is possible that the discharge consists of more than one pulse per half phase. This is called a pseudo-glow discharge or pulsating glow discharge [56]. Again, each individual pulse can be described as an APGD. As discussed before, the discharge is extinguished after a few µs because surface charges shield the external field. However, if the external voltage is increased further after the discharge is already extinguished, the charges are no longer sufficient and a new breakdown can occur. This can be repeated until the applied voltage does not increase any further. The number of pulses can therefore be adjusted by the frequency, waveform and voltage amplitude.

Since the pulses follow each other in short time intervals, excited species such as metastable atoms or molecules can survive in the gas gap. These support the ignition because they are easy to ionize or generate electrons by Penning ionization. Thus, subsequent discharges can be ignited at lower gap voltages in the same half phase. If the number of discharge pulses is very large, they can overlap each other [37]. A quasi continuous glow discharge with one pulse is formed.

Determination of the discharge mode

In order to decide whether a homogeneous discharge is an APTD or an APGD, a number of parameters have been identified in the literature that can be used to compare the characteristics of a discharge [49].

As previously described, the major difference is in the degree of ionization, which in APGD is sufficient to shield the external electric field and form a quasi-neutral region. The electron density in APGD is in the range between 10^{10}-10^{11} cm^{-3}, while in APTD it is between 10^7-10^8 cm^{-3}. Even though this value is crucial for the discharge, it is very difficult to determine in the case of atmospheric pressure plasmas because, for example, Langmuir probes cannot be used due to the dimensions. Another method could be the measurement of the electric field. In an APTD, this corresponds to the field applied across the gas gap. In the case of an APGD, this is shielded in the positive column and is correspondingly smaller.

An easier access is provided by optical measurements of the emission. As described before, the pulses of an APTD are significantly longer (approximately 10 µs) than those of an APGD (approximately 1 µs). However, attention must be paid to the time resolution. Slow camera or photomultiplier setups might not separate fast pulses properly and make them appear as one longer pulse. In addition, the superposition of short pulses in pseudo glow mode, for example, can result in longer pulses than in APTD.

Another possibility is offered by the measurements of voltage and current characteristics. The current density of APGD is between 10 and 100 mA cm^{-2}, while this is

significantly lower (0.1-$10\,\mathrm{mA\,cm^{-2}}$) for APTD. Furthermore, the course of the gap voltage differs. In the case of APTD, this remains constant even after ignition. In APGD, on the other hand, it collapses very quickly. However, there are also deviations here. In the case of pulsating APTD, the gap voltage collapses in intermediate periods, whereas the voltage can remain constant in the case of pseudo-glow discharge.

Table 2.1: Order of magnitude of different quantities to distinguish between homogeneous discharge modes adopted from [49].

Quantity	APTD	APGD
Electron density / $\mathrm{cm^{-3}}$	$10^7 - 10^8$	$10^{10} - 10^{11}$
Ion density / $\mathrm{cm^{-3}}$	10^{10}	10^{11}
Quasi-neutrality	No	Yes
Metastable of dilution gas	10^{13}	10^{11}
Current density / $\mathrm{mA/cm^2}$	0.1-10	10-100
Gap voltage variation	Constant (Townsend plateau)	Decrease (cathode fall formation)
Dilution gases	N_2, Air, N_2O	He, Ar, Ne
Typical gas gap / mm	< 2	> 2
Typical frequency range / kHz	< 10	> 1
Power / $\mathrm{W/cm^3}$ (at $10\,\mathrm{kHz}$)	≈ 1	≈ 0.1
Diagnostics	Current, Optical	Photomultiplier, ICCD

Overall, due to the exceptions and deviations, different parameters should be used for the determination. An overview of various reference values is shown in table 2.1.

Mode transitions

As described above, the discharge mode depends significantly on the type of gas used. This leads to the fact that discharge mode transitions can be observed when the gas type is changed by small admixtures. For example, if oxygen is added to a nitrogen [60] or neon [61] discharge, the discharge transitions from a homogeneous mode to a filamentary mode. The exact admixtures required for a transition depend not only on the gas mixture but also on the reactor geometry and the applied voltage.

In this work, a helium plasma with small oxygen admixtures is used. For this case, a transition from a diffuse discharge to a filamentary discharge is also known from the literature [37, 38]. Figure 2.2 shows the existence range of the different modes as a function of applied voltage and oxygen admixture. Again a DBD reactor was used, but with a very different geometry to that used later in this work. For this reason, the Figure can only reflect the basic behavior with the admixture of oxygen.

Without oxygen admixture, the discharge is initially diffuse. This is especially known for helium discharges, since the thermal conductivity is particularly high here and instabilities that can lead to filamentation are prevented. If a small amount of oxygen is added, the voltage required to maintain the discharge increases. At admixtures between 0.025% and 0.5%, the discharge is partially filamentary. This means that there is an asymmetry between the two half phases of the AC voltage, which

Figure 2.2: Existence diagram for the filamentary and diffuse barrier discharges depending on the oxygen admixture to helium taken with permission from [38].

is due to the reactor geometry. At higher admixtures, the discharge is then completely filamentary.

This behavior can be attributed to various properties of oxygen. Initially, the energy consumption increases because the vibrational and rotational states of the oxygen molecule are excited [62]. In addition, dissociative processes occur, which require further energy. Moreover, oxygen tends to form negative ions. This means that free electrons that would contribute to the discharge are lost due to attachment [63]. Besides, a different balance of electrons, positive and negative ions is established, which can affect both the plasma density and the electron energy distribution function (EEDF).

In the case of helium, the discharge is supported by metastable species that generate seed electrons by step-wise ionization or chemo-ionization [64]. Oxygen can effectively quench these long-lived metastable species, reducing their role in the process to a minor level [65].

In addition to the formation of filaments and increased required voltage, the behavior of the current changes as well [37, 38]. While only a few discharge pulses were visible without admixture, the number increases more and more with admixture. Thereby each individual pulse becomes shorter. In addition, the current amplitudes change. With low admixtures, the first pulse is the strongest and the subsequent pulses have smaller and smaller amplitudes. With larger admixtures, the amplitude of the first pulse increases significantly. The subsequent pulses, however, are significantly smaller and no longer ordered by their amplitude.

Overall, attention must be paid to the discharge characteristics for admixtures of reactive gases. For most industrial applications, the highest possible admixture is interesting. However, a compromise must be found here, as these admixtures lead to strong current pulses that can damage the reactor and are not necessarily energy-efficient. Furthermore, the filamentation mode is not as suitable for the uniform treatment of surfaces as a homogeneous discharge.

2.2 Micro structured discharges

As previously described, the ignition of a plasma, the associated ignition voltage, and the resulting discharge mode depend on Paschen's law and are thus proportional to the product of pressure and electrode gap. Since atmospheric pressure is required for many applications, the electrode spacing is very decisive. In order to keep the ignition voltage in a practicable range (a few 100 V) and at the same time to achieve a discharge as homogeneous as possible, micro plasmas with electrode distances in the µm or mm range are preferred. To achieve this in the context of DBDs, there are several reactor geometries. In addition to the classical reactors already discussed, there are also more sophisticated electrode arrangements such as arrays of individual micro cavities (micro cavity plasma arrays), which are the focus of this work.

Micro cavity plasma arrays (MCPAs) typically consist of thousands of cavities in the µm range, in which a plasma is ignited and confined. A cavity thereby resembles a hollow cathode and neighbors at least on the bottom side, depending on the reactor also on the sides, a grounded electrode, which is separated from the volume by a dielectric. At the upper end, the cavity is surrounded by a powered electrode, which is either directly exposed to the plasma or is also separated by a dielectric. Thus, the cavities are a hybrid of volume and surface DBD. A widely used possibility to realize MCPAs are silicon-based devices [18, 23, 25, 66]. Here, the structures are incorporated into a silicon wafer by wet etching and the wafer is coated with various materials (dielectric, electrode). The exact procedure can vary, resulting in cylindrical [66] or pyramid-shaped [23] cavities, for example. Figure 2.3 (a) shows a cross-section of a silicon-based cavity. Here, a square pyramid shape was utilized and the individual layers, such as silicon, polyimide, nickel and silicon nitride, which serve as electrodes or dielectrics, are demonstrated. In addition, an SEM image and a 500×500 array in operation are shown (Figure 2.3 (b) and (c)).

Due to their ability to effectively generate UV radiation, MCPAs offer a wide range of technical applications as VUV photolithography and nanopatterning [27]. Another example is the generation of ozone, which is used for example in swimming pools or for the treatment of drinking water. Furthermore, the radiation can be used to disinfect
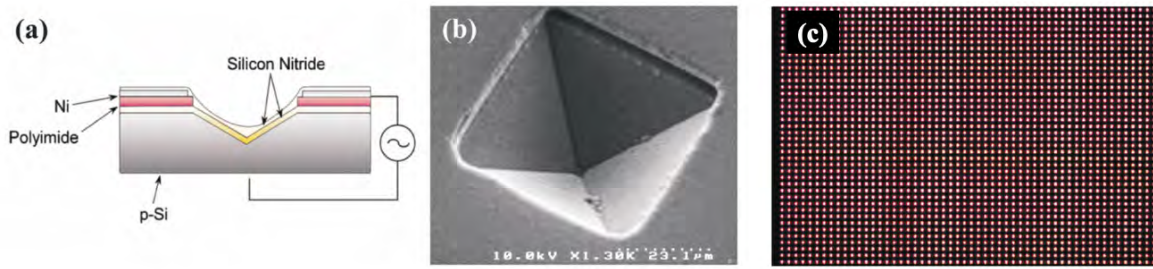
Figure 2.3: (a) Cross-sectional diagram of an Si microplasma device having an inverted square pyramid microcavity and a dielectric structure designed for ac or bipolar operation; (b) An SEM of a single device viewed from above; (c) Optical micrograph of a segment of a 500×500 array, recorded with a telescope and CCD camera. Taken with permission from [18].

surfaces or air [27]. Even in the private sector, lamps are sold that contain a MCPA and can produce particularly white light due to a fluorescent layer [67].

Unlike industrial applications, silicone-based arrays in science tend to have a short lifetime of a few hours or even just minutes [23, 66]. This is because the manufacturing process as a whole consists of many complex steps, each of which must be carried out under very clean conditions. In the case of technical applications, large quantities are produced with the same parameters in each case in an industrial process. In research, on the other hand, the quantities are much smaller and production is often in-house. In addition, there should be optical access and the parameters, such as materials or geometries used, should be explicitly varied. These points lead to deviations or inaccuracies in production, which show up in different ways. For example, if the array was manufactured under impure conditions, the bonding between individual layers is insufficient, which can significantly shorten the lifetime [66]. In addition, the dielectric can be damaged, causing a short circuit. If there are deviations from the geometry (in the µm range) due to the manufacturing process, the electric fields can become particularly high at certain points. This can lead to destruction of the dielectric layer by ion bombardment or excessive temperatures.

Metal grid array

In addition to silicon [23, 25, 68], other materials such as ceramics [69], glass [70] or nanoporous aluminum [71] can be micro structured to form array reactors. A recently introduced type of MCPAs are modular constructed metal grid arrays [22, 28]. Here, the cavities are incorporated into a nickel grid. This is held on a dielectric by a magnet which serves as a grounded electrode. Due to the magnetic mounting, the setup is modular, which offers a number of advantages and is ideal for research. For this reason, the reactor is used in this work and is described in more detail below.
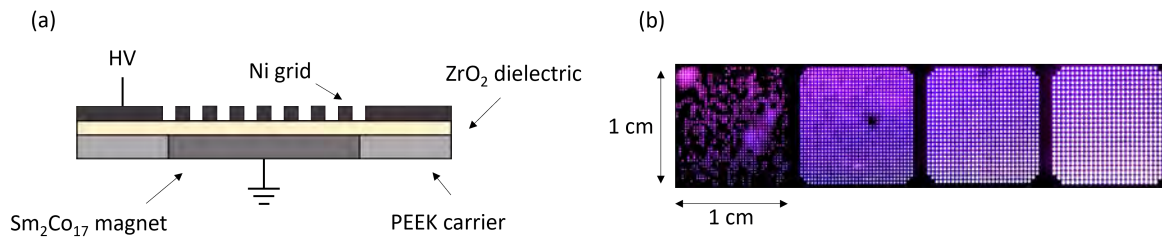

Figure 2.4: Schematic sketch of the metal grid micro cavity plasma array (a) and head on photography in operation (b).

The structure of the modular constructed metal grid array is shown in Figure 2.4 (a). A Sm_2Co_{17} magnet (50 mm x 15 mm x 5 mm) serves as a grounded electrode and is embedded in a mounting made of polyether ether ketone (PEEK). On top of this is a ZrO_2 dielectric with a thickness of 40 µm ($\epsilon_r \approx 27$). The last layer consists of a 50 µm thick nickel foil in which thousands of cavities in the µm range were cut in by a laser. The nickel grid works as a powered electrode. The three layers, magnet, dielectric and nickel grid, are held together only by the magnetic forces (B $\approx$ 260 mT) between magnet and nickel grid. Since the gyration radius (r $\approx$ 3 cm for an electron with an energy of 6 eV) is significantly larger than the mean free path ($\lambda \approx 0.6$ µm), the discharge is not influenced by the magnetic field [22]. The magnet makes the reactor modular and offers numerous possibilities for research. For example, individual parts such as the grid or dielectric can be removed after operation and analyzed. This opens up possibilities for surface diagnostics such as microscopy or XPS. Furthermore, the modularity allows individual parts to be exchanged without having to build a completely new reactor. This means that any anomalies or defects that may arise, e.g. due to inaccurate

construction or operation under particularly critical conditions, can be corrected in a short time. Figure 2.4 (b) shows a metal grid array during operation. In this case, four cavity structures, each with a different cavity diameter (50-200 µm), were used. The distance between two cavities is 200 µm and can be customized like the cavity diameter. This has the advantage that dependencies on the dimension can be determined directly with only one setup, which simplifies the experiments and increases the comparability and reproducibility.

Overall, micro structured arrays, regardless of the material, provide a very exciting area of research. In addition to the large number of possible applications, they also exhibit very special discharge characteristics that deviate from classical dielectric barrier discharges. For example, it has been observed that not all cavities ignite at the same time, but that a wave-like ignition occurs from cavity to cavity [22, 68, 72, 73]. This wave has a velocity in the range of km/s [74] and depends on the applied voltage and frequency [72]. Several of these waves can occur per phase, resulting in a self-pulsing discharge. It follows that the individual cavities can interact with each other in some way, such as photo electron emission. Despite initial attempts at numerical modeling [75, 76], the phenomenon has not yet been conclusively explained. However, the metal grid array offers the possibility for further investigations due to its significantly increased lifetime compared to the silicon based array [22]. Especially high temporal resolution measurements, which are necessary for wave observation and require long measurement times, are possible with the new design.

In addition to established research areas, the metal grid array presents opportunities for exploring new topics. Its simple design facilitates easy modifications of the plasma source. For instance, a concave electrode can be utilized so that the dielectric and metal grid adapt to its shape, allowing side-view observations of the cavities and enabling studies of discharge expansion from the cavity [22]. Alternatively, replacing the grid structure with a channel offers optical access to the entire cavity cross-section, which aids in observing discharge dynamics within the cavity [77]. A particularly promising modification involves using a catalytic material on the dielectric surface [22]. For example, MnO_2 can be spray-coated onto the surface, placing the catalyst in direct

contact with the discharge, allowing for observation of their interactions. This setup can be employed for applications such as the conversion of volatile organic compounds (VOCs). By directing a gas flow across the cavities through a quartz cover, optical access is maintained, and the catalyst can enhance efficiency or influence reaction selectivity. The combination of catalyst and plasma opens up a range of reactions that are not feasible with plasma conversion or catalysis alone [9]. Reactive species and charged particles interact with the catalyst surface, while the plasma can clean the surface, prevent carbon buildup, and produce synergistic effects. The modular metal grid array is ideally suited for investigating plasma-catalytic reactions. Different catalysts can be tested and compared at varying concentrations, and treated surfaces can be examined using various diagnostic techniques.

Asymmetry between increasing and decreasing potential phase

As noted previously, the complex geometry of MCPAs can be thought of as a hybrid between a volume and a surface DBD. However, the asymmetry between grounded and powered electrode leads to an asymmetric discharge characteristic. When using an AC voltage, the increasing potential phase (IPP) is very different from the decreasing potential phase (DPP). This behavior was observed in both silicon-based [68, 72, 79] and metal grid arrays [22, 77]. The distinction is most striking in head on ICCD images of the emission. In the IPP, increased emission can be seen at the edges of the cavity. A ring structure is formed. In the DPP, on the other hand, the emission is more concentrated in the center of the cavity. This result could be confirmed by a channel device, where the cavity can be observed from the side [77]. Here it can be seen that the discharge in the IPP glows particularly at the edges and also in the volume above the cavity. In the DPP, on the other hand, the discharge is very concentrated within the cavity.
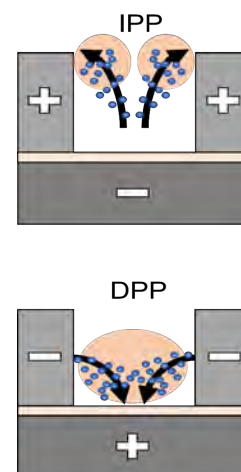

Figure 2.5: Schematic sketch of electron motion and plasma propagation in IPP and DPP taken from [78].

The described behavior can be explained by electron movement and is schematically sketched in Figure 2.5. In the case of IPP, the electric field accelerates the electrons out of the cavity or in the direction of the powered electrode at the edges. In DPP, on the other hand, the electrons are accelerated into the cavity in the direction of the grounded electrode. Due to the geometry, the dynamics differ substantially. In the DPP, the attracting electrode is significantly smaller than the repelling one, resulting in a focusing effect. In the IPP it is the other way around, which leads on the one hand to the ring structure, but on the other hand also to a rather diffuse discharge, because the volume into which the electrons are accelerated is much larger.

Electric fields

One of the most fundamental parameters for understanding a plasma is the electric field. This determines the generation of all plasma species, the flow of charged particles, their energy and interaction with surfaces. This means that by knowing the electric field, many other plasma parameters can be derived. Due to the design of the metal grid array, which is optimized for diagnostics, and its increased lifetime, more complex measurement campaigns could be carried out on this reactor. This made it possible to determine the electric field by optical emission spectroscopy (OES) using the Stark effect [28]. Here, the emission of the discharge is analyzed so that an electric field could be determined depending on different parameters such as voltage, frequency, pressure, cavity diameter or time within the phase. A more detailed description of the diagnostics follows in section 3.2.1.

Figure 2.6 shows the electric field as a function of time. In addition, the applied voltage, as well as the emission (PMT signal) is shown. The electric field is in the order of $25\,\mathrm{kV\,cm^{-1}}$ and hardly changes in time within one half phase. However, a difference between IPP and DPP of about $8\,\mathrm{kV\,cm^{-1}}$ can be seen, with a stronger field in DPP. First of all the absolute values fit very well to model calculations in similar devices [75, 80]. Furthermore, they fit to the known DBD behavior that the electric field remains constant during a half phase. As soon as a critical field for ignition is reached, charge carriers are transported to the dielectric. These act against the external field and shield it. The effective field which is present during a discharge is therefore always constant.
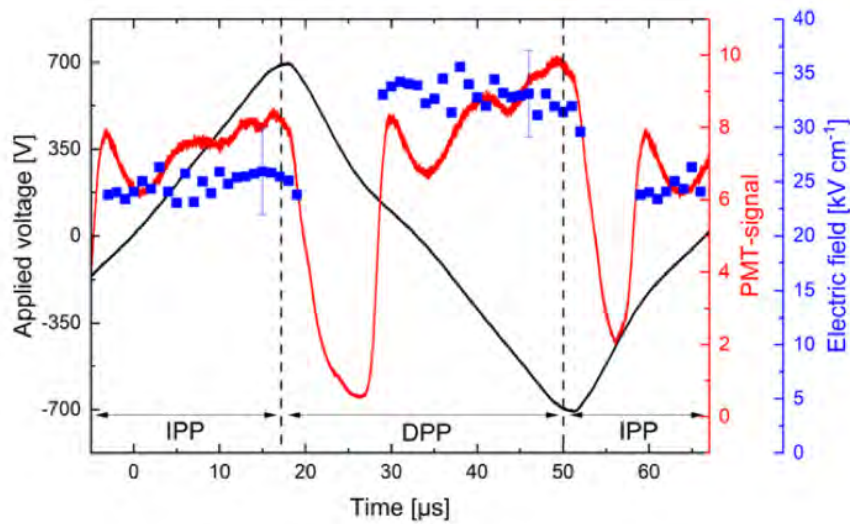
Figure 2.6: Time-resolved electric fields, emission an applied voltage. Conditions: V = 700 V, f = 15 kHz, d = 200 µm, helium flow = 2 slm at ambient pressure, time-resolution = 1 µs. Adopted with permission from [28].

Nevertheless, there can be differences between the half phases, which is related, among other things, to the diagnostic itself. The electric field is determined at the location where the emission is highest. In the DPP, the discharge ignites enclosed in the cavity, where the electric field is also strongest. In the IPP, on the other hand, the diffuse discharge is widespread, even in places with a lower electric field, which explains the difference. [28]

Other variations also show that higher fields are measured in the DPP than in the IPP. Besides the time, the cavity diameter significantly affects the field strength, with the electric field decreasing as the diameter increases. This is because the strongest field is concentrated at the interface between the nickel foil and the dielectric. In smaller cavities, this interface constitutes a larger portion of the total volume, resulting in higher observed electric fields. The relationship between the applied voltage and the electric field is particularly counter intuitive: the field remains constant or even decreases with increasing voltage. This behavior can be attributed to the DBD characteristic, where the external field is partially shielded by surface charges. Moreover, as the plasma density increases with higher voltage, the shielding effect within the volume of small cavities is enhanced, which can lead to reduced measured electric fields. [28]

3 Diagnostics

The following chapter is dedicated to the diagnostics employed in this work to answer the research questions. To fundamentally characterize the discharge, electrical measurements, more precisely the equivalent circuit approach, are suitable for determining quantities such as current, voltage, power, and surface charges. The second part of this chapter focuses on optical emission spectroscopy. First, it describes how the method of electric field measurement via Stark shifting and splitting can be extended to determine not only absolute field strengths but also the direction of the field. Next, it is explained how optical emission spectroscopy can be used to measure atomic oxygen density distributions and mean electron energies. Therefore, a new method called *Helium State Enhanced Actinometry* (SEA) is developed and tested on a reference plasma source in the course of this work. The final part of the chapter is dedicated to laser spectroscopy, which enables spatially and temporally resolved measurements of density distributions of reactive species even outside the discharge.

3.1 Electrical characterization of a DBD

Electrical measurements of current and voltage are the most popular method to characterize a discharge due to their non-invasive nature and experimental simplicity. One of the most important parameters to compare different plasmas is the coupled power. Especially in typical fields of atmospheric pressure plasmas, such as the conversion of gases, the energy efficiency is crucial for the application in industry. In addition to efficiency, current and voltage characteristics are of particular interest, as these describe the fundamental discharge behavior. In the case of dielectric barrier discharges, the determination of surface or volume charges is also of importance, since these can strongly influence the discharge characteristics through shielding or the memory effect.

3.1.1 Voltage, current and power measurements

The voltage $V(t)$ and current $I(t)$ can be measured using commercially available probes. $V(t)$ is the voltage between the live and grounded electrodes. The total current $I(t)$ consists of the discharge current $j_R(t)$ and the displacement current $i_d(t)$. The discharge current $j_R(t)$ describes the charge transfer within the gas channel. If the plasma has not ignited at low voltages, the reactor cell behaves as an ideal capacitor C_{cell} and the displacement current is given by:

$$i_d(t) = C_{cell} \frac{\mathrm{d}V(t)}{\mathrm{d}t} \tag{3.1}$$

The average power within the voltage period T can be calculated from $V(t)$ and $I(t)$ as follows:

$$P = \frac{1}{T} \int_{t_0}^{t_0+T} V(t)I(t)\mathrm{d}t \tag{3.2}$$

However, with this method it is only possible to determine the power averaged over a voltage period. If the power is to be measured in a time-resolved manner, knowledge of the gap voltage $U_g(t)$ and the discharge current $j_R(t)$ is required.

$$P(t) = U_g(t)j_R(t) \tag{3.3}$$

In most cases, however, $U_g(t)$ and $j_R(t)$ are not known. One way to determine the quantities is the equivalent circuit approach, which is explained below. [81–83]

3.1.2 Equivalent circuit approach

Although electrical measurements are experimentally simple, the evaluation is not. For an understanding of the measurements, models based on a number of assumptions are necessary. Especially in the case of complex reactor geometries, simplifications are required to interpret the measurements. A frequently used model to investigate dielectric barrier discharges is the equivalent circuit approach. This was introduced by *Manley* in 1943 [84].

Here, charges are measured in addition to voltage and current. This is possible either by means of measuring a voltage drop over a monitor capacitor in the circuit or by integrating the measured current:

$$\int_0^t I(\tau)\mathrm{d}\tau = Q(t) + const \tag{3.4}$$

However, integrating the current signal has two decisive disadvantages. Firstly, the unknown integration constant must be determined. This can be realized, for example, by assuming that the average charge should cancel out over a voltage period. Secondly, numerical integration can lead to deviations in the case of possibly noisy data. For this reason, the use of a monitor capacitor is preferable. However, the size of the capacitor must be chosen carefully. If the capacitance is too large, very low voltages have to be measured, which can lead to uncertainties. If the capacitance is too small, the discharge can be influenced and the voltage to be measured can be too high (for example for the oscilloscope used). Accordingly, the monitor capacity should be significantly larger than that of the reactor cell ($C_m \gg C_{cell}$). As a rule of thumb, ratios of approximately 100:1 are favorable [83].

A key aspect of the theory is the evaluation of Lissajous figures or QV-diagrams in which the charge $Q(t)$ is plotted against the voltage $V(t)$. Typically, a parallelogram is formed here for ideal DBDs. For real DBDs, there may be deviations in the shape, which is discussed later.

(a) Parallelogram-shaped QV-diagram
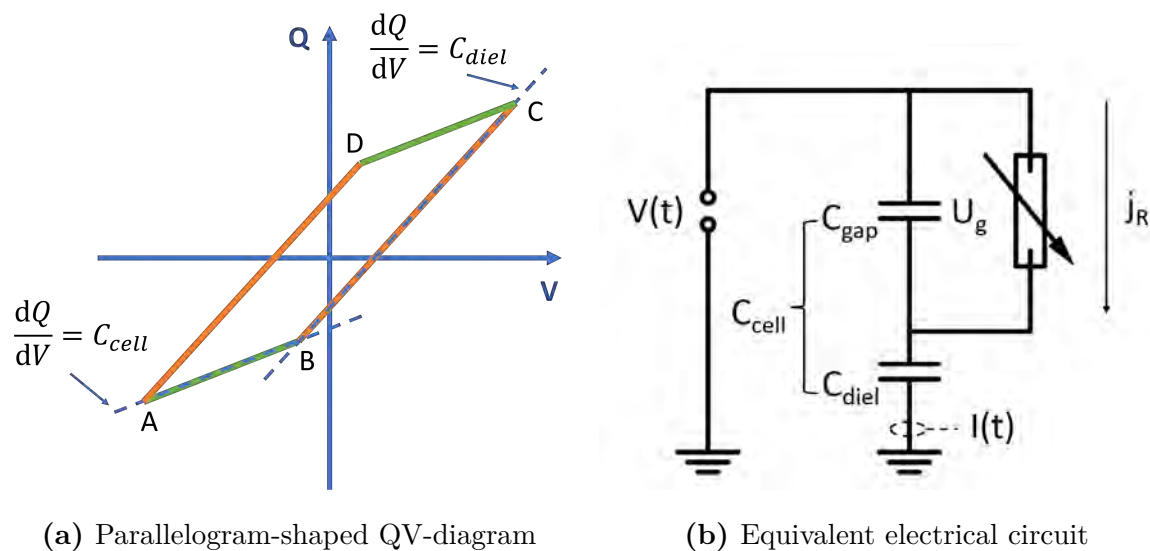
(b) Equivalent electrical circuit

Figure 3.1: QV- diagram (a) and equivalent electrical circuit (b) for an ideal dielectrical barrier discharge.

Figure 3.1 (a) shows a typical parallelogram-shaped QV-diagram of an ideal DBD. The diagram can be divided into two different phases. The passive phase (between points

A and B or C and D, marked green) in which the plasma is not ignited and the active phase (between points B and C or D and A, marked orange) in which there is a plasma in the discharge gap. It is noticeable that the effective capacitance, which corresponds to the slope of the diagram, differs between the phases. This can be explained with the simplest equivalent circuit diagram of a DBD (Figure 3.1 (b)). Here, a DBD is understood as a series of two capacitances, which correspond to the discharge gap and the dielectric. In the passive case, this means that the total capacitance of the reactor cell can be calculated using Kirchhoff's laws:

$$\frac{1}{C_{cell}} = \frac{1}{C_{gap}} + \frac{1}{C_{diel}} \tag{3.5}$$

In the active case, however, the discharge gap is filled with a conductive plasma and is therefore short-circuited. It follows that the effective capacitance corresponds to that of the dielectric C_{diel}. With simple reactor geometries (electrode area A, distance d) and known material properties (ϵ_r), C_{gap} and C_{diel} can also be calculated directly:

$$C = \epsilon_r \epsilon_0 A/d \tag{3.6}$$

However, most real reactors are so complex that an estimation without a QV-diagram is not possible. As already mentioned, the discharge current j_R and the gap voltage $U_g(t)$ are more relevant for characterizing the discharge than the total current $I(t)$ or voltage $V(t)$. These can be derived from the equivalent circuit diagram (Figure 3.1 (b)) and Kirchhoff's laws. The gap voltage $U_g(t)$ is the total voltage minus the voltage that drops across the dielectric $U_d(t)$. $U_d(t)$ can be calculated from the charge $Q(t)$ and C_{diel}:

$$U_g(t) = V(t) - U_d(t) = V(t) - \frac{Q(t)}{C_{diel}} \tag{3.7}$$

The discharge current $j_R(t)$ is the total current $I(t)$ minus the displacement current i_d:

$$j_R(t) = I(t) - i_d(t) \tag{3.8}$$

In the active case, $i_d(t)$ cannot be calculated with equation 3.1, but the gap voltage $U_g(t)$ must be included:

$$i_d(t) = C_{gap} \frac{\mathrm{d}U_g(t)}{\mathrm{d}t} \tag{3.9}$$

If the equations are combined, an expression for the discharge current follows:

$$j_R(t) = \left[1 + \frac{C_{gap}}{C_{diel}}\right] I(t) - C_{gap} \frac{\mathrm{d}V(t)}{\mathrm{d}t} \tag{3.10}$$

Since C_{gap} does not follow directly from the QV-diagram, equation 3.5 can be substituted, so that $j_R(t)$ depends only on C_{cell} and C_{diel}:

$$j_R(t) = \frac{1}{1 - \frac{C_{cell}}{C_{diel}}} \left[I(t) - C_{cell} \frac{dV(t)}{dt} \right] \tag{3.11}$$

The charge transported through the gas gap $q_R(t)$ can also be determined directly from the discharge current by integration:

$$q_R(t) = \frac{1}{1 - \frac{C_{cell}}{C_{diel}}} \left[Q(t) - C_{cell} V(t) \right] + q_0 \tag{3.12}$$

The integration constant can be determined if q(t) is known at zero time. If zero point is chosen so that $V(0) = Q(0) = q_R(0) = q_0 = 0$, the constant cancels [81].

Knowing the discharge current and the gap voltage, the power can now be determined time-resolved using equation3.3. In addition to the time-resolved power, the averaged power can be determined from the QV-diagram by transforming equation 3.2.

$$P = \frac{1}{T} \int_{t_0}^{t_0 + T} V(t) \frac{dQ(t)}{dt} dt = \frac{1}{T} \oint V(t) dQ(t) = \frac{1}{T} \oint Q(t) dV(t) \tag{3.13}$$

Thus, the power corresponds to the area within the QV-diagram. [81–83, 85–87]

Partial discharging in real DBDs

Many real DBDs differ from an ideal DBD. Due to the numerous different applications of DBDs, a large number of diverse, sometimes very complex geometries exists. These can result in part of the electrode never being covered with plasma, or only under certain conditions. This means that the assumption that C_{gap} would be short-circuited when the plasma is ignited is invalid and C_{diel} can no longer be easily determined from the QV-diagram. This phenomenon was studied by *Peeters and van de Sanden* [85]. They used a discharge with tilted electrodes and found that C_{diel} changed with the applied voltage, which cannot be explained by the theory of ideal DBDs. It was concluded that the discharge volume expands with increasing voltage and thus the capacitance changes. In order to be able to use the formulas derived above also in this type of discharges, the equivalent circuit must be modified.

Figure 3.2 shows an equivalent circuit
adapted for partially discharging DBDs.
Here, the equivalent circuit of an ideal
DBD has been extended by two addi-
tional capacitors. The idea behind this is
to split the reactor into a non-discharging
(α) and a discharging (β) part. The sum
of both parts must be $\alpha + \beta = 1$ under all
conditions. Thus, the respective capaci-

Figure 3.2: Equivalent electrical circuit for
a partially discharging DBD.

tances are dependent on the expansion of the discharge volume. As already mentioned,
the slope of the active phase in the QV-diagram no longer corresponds to C_{diel}, but to
an effective capacitance ζ_{diel}. ζ_{diel} can become at most as large as C_{diel} with complete
expansion of the plasma ($\alpha = 0$, $\beta = 1$). Accordingly, the following applies:

$$\zeta_{diel} = \alpha C_{cell} + \beta C_{diel} \tag{3.14}$$

and

$$\zeta_{diel} \leq C_{diel} \tag{3.15}$$

From this, the plasma expansion β or the non-discharged part α can be derived as
follows:

$$\alpha = \frac{C_{diel} - \zeta_{diel}}{C_{diel} - C_{cell}} \tag{3.16}$$

$$\beta = \frac{\zeta_{diel} - C_{cell}}{C_{diel} - C_{cell}} \tag{3.17}$$

In order to investigate the effects on the gap voltage, discharge current and charge,
the two new capacitors can be combined into a single parasitic capacitance C_p for
simplicity:

$$\frac{1}{C_p} = \frac{1}{\alpha C_{gap}} + \frac{1}{\alpha C_{diel}} \tag{3.18}$$

The resulting current must be corrected for the fraction that flows off via the parasitic
capacitance:

$$j_{corr} = I(t) - C_p \frac{\mathrm{d}V(t)}{\mathrm{d}t} \tag{3.19}$$

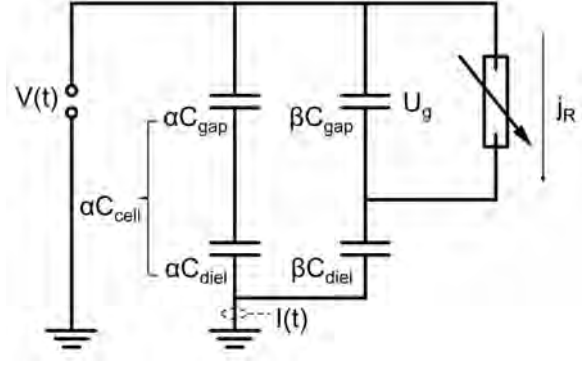The same applies to the charge:

$$Q_{corr} = Q(t) - C_p V(t) \tag{3.20}$$

ζ can thus be rewritten as ζ_{cell} and ζ_{diel}:

$$\zeta_{cell} = C_{cell} + C_p \tag{3.21}$$

$$\zeta_{diel} = C_{diel} + C_p \tag{3.22}$$

Using these relationships, gap voltage and discharge current can be determined equivalently to the ideal DBD:

$$U_g(t) = \frac{1}{1 - \frac{C_p}{\zeta_{diel}}} \left[V(t) - \frac{Q(t)}{\zeta_{diel}} \right] \tag{3.23}$$

$$j_R(t) = \frac{1 - \frac{C_p}{\zeta_{diel}}}{1 - \frac{\zeta_{cell}}{\zeta_{diel}}} \left[I(t) - \zeta_{cell} \frac{dV(t)}{dt} \right] \tag{3.24}$$

C_p is usually not known. However, if C_{diel} can be estimated, the expressions can also be represented using the coefficients α and β.

$$U_g(t) = \left[1 + \frac{\alpha C_{cell}}{\beta C_{diel}} \right] V(t) - \frac{1}{\beta C_{diel}} Q(t) \tag{3.25}$$

$$j_R(t) = \left[1 + \frac{C_{gap}}{C_{diel}} \right] \left[I(t) - \alpha C_{cell} \frac{dV(t)}{dt} \right] - \beta C_{gap} \frac{dV(t)}{dt} \tag{3.26}$$

From $\alpha + \beta = 1$ and a substitution of C_{gap} it follows that the discharge current is independent of α and β and thus corresponds to that of the ideal DBD. Accordingly, also the charge does not change in comparison to the ideal DBD.

$$j_R(t) = \frac{1}{1 - \frac{C_{cell}}{C_{diel}}} \left[I(t) - C_{cell} \frac{dV(t)}{dt} \right] \tag{3.27}$$

$$q_R(t) = \frac{1}{1 - \frac{C_{cell}}{C_{diel}}} \left[Q(t) - C_{cell} V(t) \right] \tag{3.28}$$

More detailed explanations and precise derivations of the formulas can be found in the literature. [81–83, 85, 88]

Surface dielectic barrier discharges (sDBDs)

Previously, it was assumed that the expansion of the discharge remains constant within a voltage period, even though it may change with the applied voltage amplitude (partial discharging). But, this is only correct in the case of a plane parallel configuration. Since the gap width is constant here, the plasma ignites at a certain ignition voltage. However, this changes with more complex geometries. Especially the behavior of s-DBDs differs drastically from this approach. Here, the plasma initially ignites close

to the powered electrode, but can then spread over a large surface area as the voltage increases. This expansion occurs within a voltage period, causing the capacitance ζ_{diel} to change with time. As a result, the QV-diagram changes its shape from a parallelogram to an almond. This behavior is indicated in Figure 3.3. On the right side, a schematic sketch of an sDBD is shown. Here, the plasma propagates further and further on the surface between the time points t=1 and t=3. This characteristic is also reflected in the almond-shaped QV-diagram (left), where the slope becomes steeper with each time point. This makes the evaluation of the QV-diagram more complex. On the one hand, clear edges within the diagram that separate the active from the passive phase may disappear. Then other methods, for example the use of a photomultiplier, must be used to find the ignition times. On the other hand, the evaluation of ζ_{diel} is more complicated due to the time dependence. For example, an average could be taken or the maximum at the end of the period could be used. The latter is necessary, for example, if C_{diel} is to be determined from the QV-diagram and the entire gas gap should therefore be short-circuited. [82, 83]

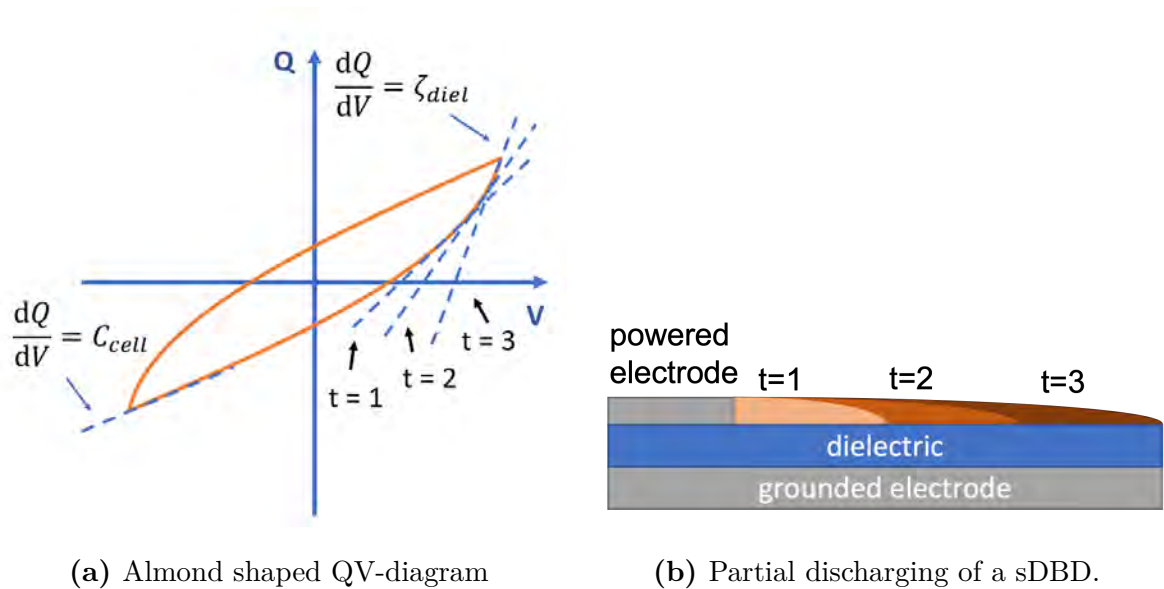(a) Almond shaped QV-diagram   (b) Partial discharging of a sDBD.

Figure 3.3: Equivalent circuit approach for sDBDs with almond shaped QV-diagrams, where ζ_{diel} is (a) time- or (b) discharge expansion-dependent, respectively.

3.1.3 Determination of surface charges

As shown before, surface charges are essential for the understanding of DBDs. They significantly influence the ignition and discharge behavior and are responsible for the memory effect. Furthermore, they play a role in plasma conversion if they interact with catalytic surfaces. For this reason, an analysis of these charges is crucial for the applications of DBDs in the context of plasma catalysis.

Various diagnostics are available to measure surface charges in dielectric barrier discharges. However, not every diagnostic is suitable for every type of DBD. For instance, when the discharge operates with a steep rising voltage ramp, surface charges can be estimated from the delay between the voltage and the current pulse [89]. Another approach is to scan the dielectric after the plasma operation with a voltage probe [90]. This method requires the dielectric to be accessible and involves a time lag between discharge and measurement.

A method that enables real-time measurement utilizes the Pockels effect [51, 91]. In this technique, a BSO (bismuth silicon oxide) crystal serves as the dielectric, becoming birefringent when subjected to an electric field. The polarization of reflected light then depends on the applied electric field created by surface charges. In a reactor setup, the crystal dielectric is illuminated with polarized light, for example through a transparent counter-electrode. The reflected light is recorded by an analyzer and an ICCD camera, allowing for time- and spatially-resolved charge measurements.

While the method offers valuable insights into the fundamental properties of DBDs and surface charges, it is not without limitations. Its applicability is constrained by the inability to utilize it with complex electrode geometries and the notable divergence in the properties of the crystals from those of the materials commonly employed, including a higher relative permittivity and a lower secondary electron emission coefficient. Moreover, the impact of the crystal thickness on the outcome is a crucial factor. To ensure a robust signal-to-noise ratio, a minimum crystal thickness must be selected, which introduces additional complexities in integrating the component into existing reactor designs.

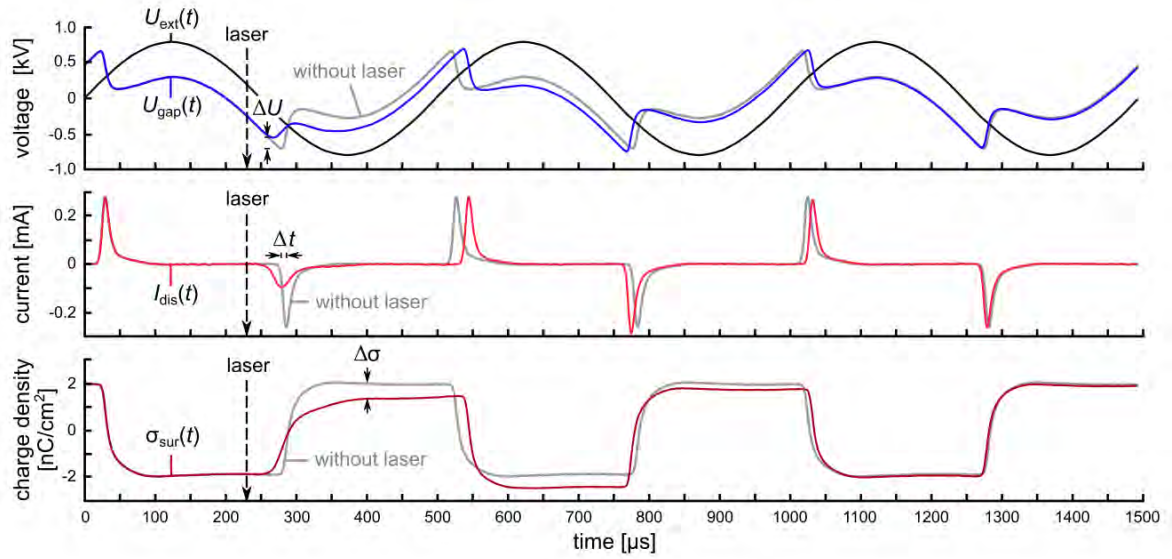**Laser photodesorption for active surface charge manipulation**

Figure 3.4: Laser photodesorption effect for one discharge breakdown per half-cycle: temporal behavior of applied voltage and gap voltage (top), discharge current (center), and surface charge density (bottom) for the discharge without laser pulse (gray lines) and with laser pulse (colored) marked by an arrow at the time 230 μs. The laser beam hits the cathodic dielectric that is charged with residual surface electrons at this time. Applied voltage amplitude U = 0.8 kV. Laser: $\lambda = 532$ nm, E = 70 mJ. Taken with permission from [92].

An even more advanced diagnostics for determining surface charges, also during operation, is laser photodesorption. Here, a laser is directed at the dielectric to remove weakly bound charges from the surface. The detached charges can then be collected with an additional measuring electrode, for example. However, the reactor geometry must be adapted for this. A simpler possibility is the equivalent circuit approach described above. Here, gap voltage, discharge current and transported charge can be determined in real time. This allows both, the charge itself and the influence on the discharge, to be monitored. For example, the detached charges have a different effect on the memory effect and thus also influence the gap voltage and the discharge current in the following pulses. However, in order not to influence the general discharge behavior (apart from the surface charges) with these diagnostics, the correct choice of laser is important. Firstly, the photon energy must be high enough to dissolve surface charges (around 1 eV [93, 94], and secondly, the laser should not induce any

processes in the volume (e.g. photo detachment of negative oxygen ions at 1.46 eV [95]).

An example of this method is shown in Figure 3.4. Here, it can be seen that there is no change in the charge signal when the laser is incident. This is due to the fact that only a few charge carriers are released and the change in the total density is below the detection limit. However, the detachment of the charges becomes clear in the following pulses. Here, the discharge initially ignites earlier than without the laser, since the detached charges in the volume support the ignition. In the following pulse, however, the picture is different. Since the ignition after the laser was supported by free charge carriers, the discharge pulse is weaker overall, so that fewer charges are applied to the dielectric. This reduces the memory effect and higher voltages are required for ignition. Nevertheless, after a few periods, equilibrium is restored. It becomes clear that with this method, the surface charges and their influence on the discharge can not only be investigated, but the discharge can even be actively manipulated. [92]

Surface charge determination using the equivalent circuit approach

As shown before, charges can in principle be determined using the equivalent circuit approach. This is generally possible for most DBD reactors without changing the reactor (Pockels effect, subsequent scanning of the dielectric). However, this measurement is always integrated over the entire electrode surface, so that no spatial resolution is possible. Furthermore, the measured charge is the charge transported by the discharge (integrated discharge current). Under certain conditions, this can differ from the surface charge, since, for example, not all charge carriers reach the surface and some remain in the volume.

There are various ways of separating the volume charges from the surface charges during the evaluation. If, for example, only one of the charge types (volume or surface) is influenced from the outside, the change can be used to infer the other. An example of this is the laser detachment discussed above, in which only surface charges are to be manipulated with the laser. In contrast, an exclusive manipulation of the volume charges can be achieved by a quick disconnection of the voltage supply. This extinguishes the discharge and volume charges are no longer moved by external electric

fields and recombine or diffuse from the volume within a short time. Nevertheless, the surface charges are bonded and can remain on the surface for a number of seconds or even longer.

3.2 Optical emission spectroscopy

In addition to the previously described non-invasive electrical measurements of voltage, current, and charge, the light emitted by the discharge can be analyzed through optical emission spectroscopy (OES) [96, 97]. In OES, light is separated into its spectral components using a spectrometer, and the wavelength-dependent intensity distribution is investigated. The spectral characteristics can vary significantly depending on the plasma type. For example, thermal plasmas, like the sun, exhibit a continuous blackbody spectrum dependent on temperature, while non-equilibrium plasmas typically show a non-continuous line spectrum caused by atomic or molecular transitions. Here, an excited species transitions to a lower energy state, emitting a photon with energy corresponding to the difference between the energy levels. In molecules, numerous vibrational and rotational transitions result in band structures in the spectrum due to overlapping transitions. In contrast, atoms or ions display fewer transitions, leading to spectra with distinct lines, which, however, can also include multiple transitions in some cases.

Each optical transition appears in a spectrum with a certain intensity at a central wavelength and specific width. These characteristics are influenced by parameters such as the Einstein coefficient for spontaneous emission, as well as fundamental plasma properties. For instance, the position of the peaks can indicate the species present in the discharge. The width of the peaks can provide information about the gas temperature [98] or electron density [99]. The intensity ratio of different lines can be used to infer the densities of individual species [100] or even the electric field [101].

Although OES offers diverse diagnostic possibilities, its applicability depends on the specific discharge being examined. Certain diagnostics are only possible with specific transitions, meaning the relevant species must be present in the plasma and detectable

in the spectrum. Additionally, interfering factors such as overlapping lines can complicate the analysis. One advantage of OES is that most discharges are naturally bright enough, providing sufficient signal strength for the method. This makes it applicable to very small discharges with limited optical access, such as microplasmas. However, strong emission does not guarantee homogeneously distributed intensity, leading to results weighted by location-dependent intensity distribution. Consequently, regions with stronger emission may disproportionately influence the results, despite a large area being integrated.

In contrast to laser spectroscopic methods or absorption spectroscopy, OES does not require an additional light source. Excitation of species is typically achieved through electron collisions within the discharge, and emission occurs via spontaneous emission when the state de-excites. This has two main advantages: the experimental setup is simplified as only the plasma light needs to be detected, and the method is non-invasive, so the discharge remains unaffected by the diagnostics. Despite its experimental simplicity, OES evaluation can be complex. For example, to infer electron energy, information is typically derived from the excitation process. However, since only the emission is directly measurable, a collisional-radiative model must be employed. This model links the excitation to the subsequent de-excitation by spontaneous emission or other processes such as collisions, allowing for an indirect determination of excitation properties.

In conclusion, OES is a non-invasive, easy-to-use diagnostic tool for determining fundamental plasma parameters. However, its limitations are mainly dependent on the specific discharge under investigation and the implemented model. The following sections describe three OES diagnostic schemes used in this work in more detail: Stark splitting to study the electric field, actinometry to determine atomic oxygen densities, and the measurement of gas temperatures by molecular band analysis.

3.2.1 Stark effect for electric field component detection

The electric field is a crucial parameter in a plasma, influencing both ignition and the transport of charged particles during discharge. Therefore, accurate diagnostics are essential. One commonly used technique is electric field induced second harmonic

generation (E-FISH) [102], but it involves a complex laser setup. This method is particularly challenging for microplasmas due to the difficulty of adjusting the laser in the µm range without unwanted scattering. Moreover, it is not suitable for single cavities as it requires optical access from two sides. An alternative is optical emission spectroscopy, which often uses nitrogen line ratios [101]. However, this approach relies on complex models with assumptions about electron density and energy, and it requires the presence of nitrogen in the discharge. Another option is to use the Stark effect, which causes the shifting and splitting of spectral lines based on the electric field [28, 103–105]. This method, grounded in quantum mechanical calculations [106], requires fewer assumptions about the plasma. The Stark effect method is described in detail and utilized in this work.

The splitting of energy levels under the influence of an electric field follows from a perturbation-theoretical calculation of the stationary Schrödinger equation and can thus be theoretically determined as a function of the electric field [106]. The displacement of the energy levels leads to the fact that at a transition from a higher to a lower level light is emitted with a wavelength which depends on the displacement and thus on the electric field. Energy levels are usually described with three quantum numbers, the principal quantum number n, the azimuthal quantum number l and the magnetic quantum number m. For an optical dipole transition the selection rules apply:

$$\Delta l = \pm 1 \tag{3.29}$$

$$\Delta m = 0, \pm 1 \tag{3.30}$$

In addition to dipole transitions, quadrupole transitions also occur in the helium atom in the presence of strong electric fields. These are characterized by the fact that they violate the selection rules described above and are therefore also called forbidden transitions. The wavelengths of the forbidden and allowed transitions are shifted in dependence of the electric field. While the allowed lines move to longer wavelengths, forbidden lines move to shorter wavelengths. Thus, the electric field can be determined not only from the displacement of a state (or the corresponding wavelengths) but also from the difference between a forbidden and an allowed line. This has two advantages. First, an absolute wavelength calibration is not mandatory, since only relative

wavelengths are needed. Second, the experimental uncertainty is reduced, since the resulting larger shifts are farther from the detection limit of typical spectrographs.
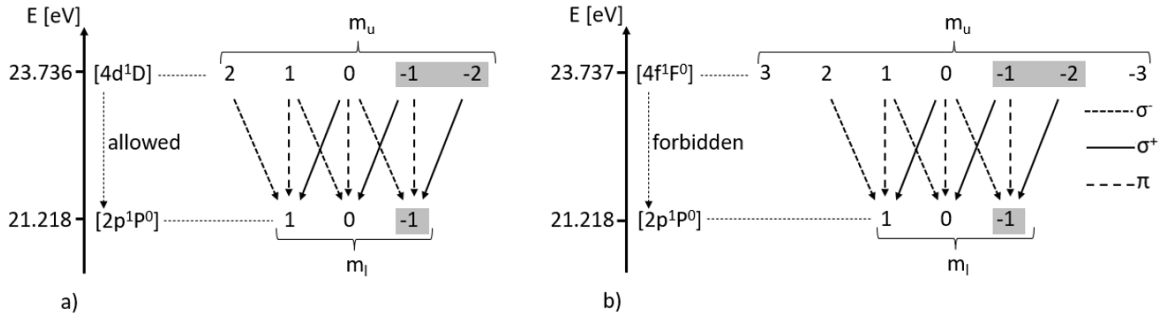

Figure 3.5: Schematic sketch of possible (a) allowed and (b) forbidden transitions depending on magnetic quantum number. Taken with permission from [28].

The exact splitting depends on the transition chosen. For diagnostic purposes, a compromise between strong splitting and high intensities (especially of the forbidden subtransitions) must be made. Furthermore, the line pair should not be disturbed by other lines so that an interpretation of the spectra is easily possible. Such a compromise is given by the allowed transition at 492.19 nm (^{1}D $\rightarrow$ ^{1}P^0, $\Delta l = -1$) and the forbidden transition at 492.06 nm (^{1}F^0 $\rightarrow$ ^{1}P^0, $\Delta l = -2$). Furthermore, these transitions have also been applied in previous work on the plasma source used [28]. A more detailed discussion on the selection of the transitions is given elsewhere [28, 104, 107].

The number of subtransitions of the selected transitions results from the selection rules and is shown in Figure 3.5. In total, there are nine allowed and nine forbidden transitions. Since in the electric field the degeneracy is not resolved with respect to m, the sign can be neglected (marked in grey). This leaves five transitions, which are listed in table 3.1. The transitions are marked with σ and π, respectively, which describes the type of polarization, which is discussed in more detail below.

Table 3.1: Summary of transitions and corresponding polarisation states depending on upper magnetic quantum number [28].

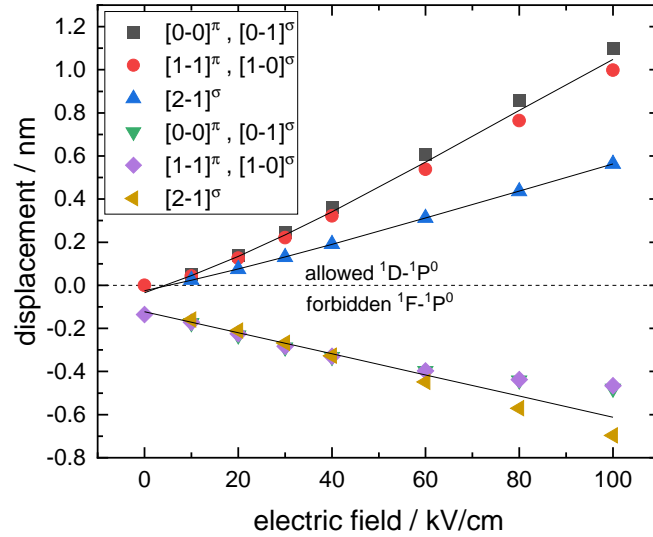| m (upper state)	Transition
2	[2-1]$^\sigma$
1	[1-1]$^\pi$,[1-0]$^\sigma$
0	[0-0]$^\pi$,[0-1]$^\sigma$

Figure 3.6: Displacements for allowed and forbidden transitions depending on the electric field, based on the calculation of *Foster* [106]. The reference value (dotted line) is the position of the field free allowed line. Adapted from [28, 107].

The theoretical shift of the wavelength as a function of the electric field was calculated as early as 1927 [103, 106]. It follows from the calculation that the lower states into which de-excitation takes place are only weakly influenced by the electric field. Thus the splitting is mainly dependent on the magnetic quantum number of the upper state. This becomes particularly clear when the displacement of the individual subtransitions is plotted as a function of the electric field (see Figure 3.6). It can be seen that as the field increases, the individual subtransitions move further and further away from the field-free line at 492.19 nm. Nevertheless, at large fields, no distinction is observed between different magnetic quantum numbers in the lower state. Consequently, the points in Figure 3.6 have been grouped together for all potential magnetic quantum numbers in the lower state ($m = 0$ or $m = 1$). Moreover, the distinction between the various forbidden transitions is in general very small, so that these transitions can also be combined (lower black line). The same is true for the allowed transitions where the upper state involves $m = 0$ or $m = 1$ (upper black line). This means that the original ten sub-transitions can be approximated by three spectral lines (black lines) and the field free line (dottet line). The dependence on the electric field can be fitted in each case with a 2nd order polynomial, where the dependence is almost linear. A more detailed description of the diagnostics and their application to the microplasma array can be found in the literature [28, 103–105].

Polarization and its role in determining electric field components

As noted above, the emitted light is polarized. The type of polarization depends on the change of the magnetic quantum number. In the case of a transition with $\Delta m = 0$, the light is linearly polarized parallel (π) to the electric field. In the case of $\Delta m = \pm 1$, the light is vertically circularly polarized (σ). Some works [103–105] exploit this property by using linear polarization filters that can filter out the σ component. This makes the spectrum easier to analyze.

However, whether components can be filtered out also depends on the reactor geometry and the field distribution within the reactor. In the case of micro cavities, for example, this is not possible, as shown in Figure 3.7. At the edges of the cavity, the field points towards the center of the cavity, while inside the cavity it points from the dielectric (bottom) towards the opening (see Figure 3.7 (a), row 1). The second line shows the polarization of the emitted light. The component pointing to the opening generates only σ-polarized light when viewed from above. If a polarizing filter is used, it becomes clear that no matter in which direction the filter is turned, both π- and σ-polarized light is observed. This is due to the complex field structure and the geometry of the reactor and means that the spectrum cannot be simplified by a filter. [107]

However, if a reactor is designed in which the emission can also be observed from the side, for example through a channel instead of a cavity, polarization can also be exploited here. This is sketched in Figure 3.7 (b). Here, still not all σ- or π-transitions can be suppressed, but the direction of the field component can be inferred. If the polarization filter is not rotated ($\varphi_{pol} = 0°$), the shift of the π-transition can be assigned to the field component in x-direction and that of the σ-transition in y-direction. If the polarizer is set to $\varphi_{pol} = 90°$, the assignment is the other way around. This allows to determine not only the absolute field strength but also the dominating direction of the field. For diagnostics a transition should be chosen which is exclusively composed of one polarization type. For the state considered here, the allowed $[2,1]^{\sigma}$ transition is therefore the only possibility. [107]
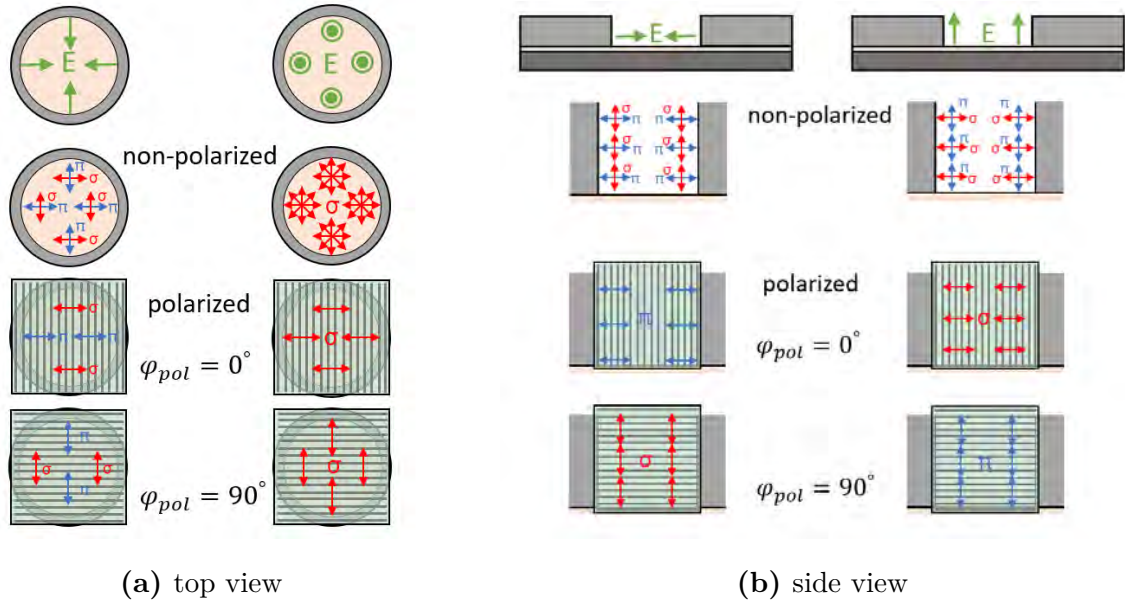
(a) top view

(b) side view

Figure 3.7: Schematic sketch of the directions of the electric field, associated emitted polarization and influence of a polarization filter as seen from above (a) and from the side (b) in a MCPA taken from [107].

Fitting routine to calculate the electric field strength and direction

In order to be able to determine an absolute field strength or even a direction using polarization from the measured spectrum, a fitting is required. For this purpose, a superposition of four Lorentz profiles is chosen (one each for the transition clusters described above and one for the field-free component). The field-free component is necessary because in a plasma, regions can occur in which the field can be completely shielded by free charges.
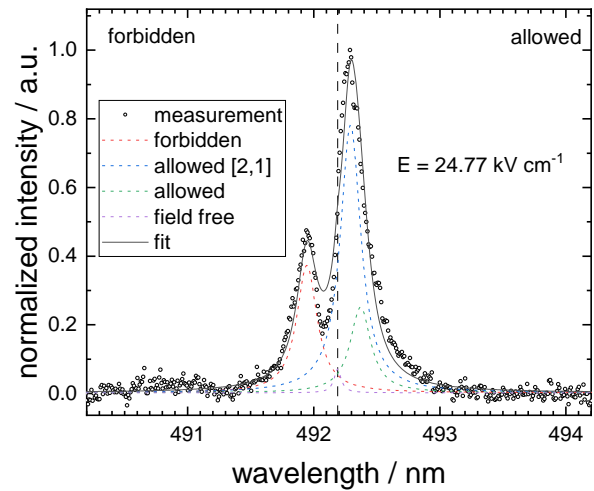

Figure 3.8: Measurement and fit of the 492.19 nm line. Adapted from [107].

Free parameters are the electric field, the half-width (FWHM) of the profile, and the amplitudes. The electric field in this case is directly dependent on the displacement of the lines, i.e. the central wavelength (see Figure 3.8). If the measurement is carried out from the side with a polarization filter, the assumption of a constant electric field for all sub-components is no longer given. In this case, different field components are measured for the different types of polarization. One way to take this into account is to determine the distance of the $[2,1]^{\sigma}$-transition to the unshifted line. Since this unshifted line is not visible in the spectrum in most cases, a precise calibration of the spectrometer must be performed. Figure 3.8 shows an example measurement of the 492.19 nm line, as well as the fit used. The two allowed, the forbidden and the field-free transitions become clear. The fit of the combination can reproduce the measured values properly. In this case, an electric field of $24.77 \pm 2.20\,\mathrm{kV\,cm^{-1}}$ results.

The shape of spectral lines is typically influenced by various broadening mechanisms, especially under atmospheric pressure. These include Doppler broadening, resonance broadening, Van der Waals broadening, Stark broadening, and natural broadening. In addition, each spectrometer has an instrument profile. An estimation shows that for the parameters used in this work, only the resonance broadening and the instrument profile make a contribution to be taken into account [28, 107]. Since the lines are shifted only minimally, it can be assumed that all transitions considered have the same half-width.

3.2.2 Helium state enhanced actinometry (SEA)

The helium state enhanced actinometry diagnostics was developed in the course of this thesis. Parts of this chapter have already been published [108–110].

The generation of reactive species is key to many applications of non-equilibrium plasmas. In plasma catalysis, for example, atomic oxygen can interact with both the gas to be treated and the catalytic surfaces used. To understand and optimize the processes, the absolute densities need to be monitored. Typically, this can be done by using laser spectroscopic measurements, such as Two-Photon Absorption Laser Induced Fluorescence (TALIF). However, this method is very complicated and costly. A laborious

laser setup is required, as well as a complex calibration procedure, which makes the diagnostic unsuitable for industrial applications. Furthermore, especially in the case of microplasmas, it is challenging to guide the laser beam into and the fluorescence signal out of the discharge due to the small dimensions and limited optical access. An alternative method for diagnostics is optical emission spectroscopy, which can be used to quantify atomic oxygen densities through a technique called actinometry.

Originally designed for silicon etching processes, the actinometry approach is known for its simplicity [100, 111–113]. In this method, the density of atomic oxygen is calculated by analyzing the intensity ratio between two specific spectral lines. These spectral transitions are associated with the target species (atomic oxygen in this case) and an actinometer gas with a known density, often argon. The selection of excited states for analysis is based on their similar energy dependencies and thresholds of the electron impact excitation cross-sections. Two commonly utilized states are the atomic oxygen state $O(3p^3P)$ (λ=844.6 nm) and the argon state $Ar(2p_1)$ (λ=750.4 nm). The basic actinometry approach assumes that the excited levels of both O and Ar states are solely populated by direct electron impact excitation from their respective ground states. This approach disregards processes like dissociative electron impact excitation during electron collisions with molecules or excitation from metastable states. It's important to note that there are additional assumptions and prerequisites outlined in the literature that need validation before applying this diagnostic method [100]. These assumptions generally hold true only under specific conditions and for particular types of plasma sources.

However, especially dissociative excitation can make a large contribution to the population of excited atomic oxygen. To account for this, the shape of the electron energy distribution function (EEDF) and the mean electron energy would have to be known either from measurements or model calculations. But in most cases these are not available. [100]

Energy resolved actinometry (ERA)

A more sophisticated approach, the energy resolved actinometry (ERA), was presented by *Greb et al.* [114, 115]. Here, actinometry is complemented by a third state $O(3p^5P)$ (λ=777.4 nm). Furthermore, a two-term approximation Boltzmann equation solver BOLSIG+ [116] is used to determine the shape of the EEDF, as well as the resulting effective rates for electron impact and dissociative excitation. By comparing experimentally determined excitation rates with the calculated values, the atomic oxygen density and the mean electron energy can be determined. A benchmark against TALIF measurements as well as numerical simulations shows a good agreement of the results [114]. Nevertheless, it is discussed in the literature that the additional oxygen state, $O(3p^5P)$, included in ERA can be populated via step-wise processes involving metastable oxygen atoms $O(3s^5S° \rightarrow 3p^5P)$ or molecules $O_2(a^1\Delta_g)$ in addition to electron impact excitation and dissociative excitation from ground state atoms and molecules [100, 117].

To check the influence of secondary processes mechanisms besides electron collision excitation and de-excitation by spontaneous emission, phase-resolved (PROES) measurements of the excitation were performed in the course of this thesis. The COST reference microplasma jet is used as plasma source [118]. This reactor is a micro atmospheric pressure plasma jet (µAPPJ), which consists of two 30 mm long and 1 mm wide stainless steel electrodes to which an rf-voltage is applied. The discharge gap is 1 mm wide and enclosed by quartz panes. It was developed as a reference source to ensure the comparability of results from research groups all over the world. Due to its reproducibility, the COST reference microplasma jet is widely used and well characterized [118, 119]. The PROES measurements were acquired by an ICCD (Andor iStar DH334T-18U-73) equipped with a tunable filter (VariSpec NIR-RM-HC-20). The setup is described in more detail in chapter 4.

The excitation $E_i(t,x)$ can now be calculated from the time and spatially resolved intensity $I_i(t,x)$:

$$E_i(t,x) = \frac{1}{n_0}\left(\frac{\mathrm{d}n_i(t,x)}{\mathrm{d}t} + \frac{1}{\tau_{eff}}n_i(t,x)\right) \tag{3.31}$$

$$n_i \propto \frac{I_i(t,x)}{A_{ik}h\nu_i} \tag{3.32}$$

Here, n_0 is the ground state density, n_i is the excited state density, τ_{eff} is the effective lifetime of excited state i, A_{ik} is the corresponding Einstein coefficient, and $h\nu_i$ is the energy of the emitted light.
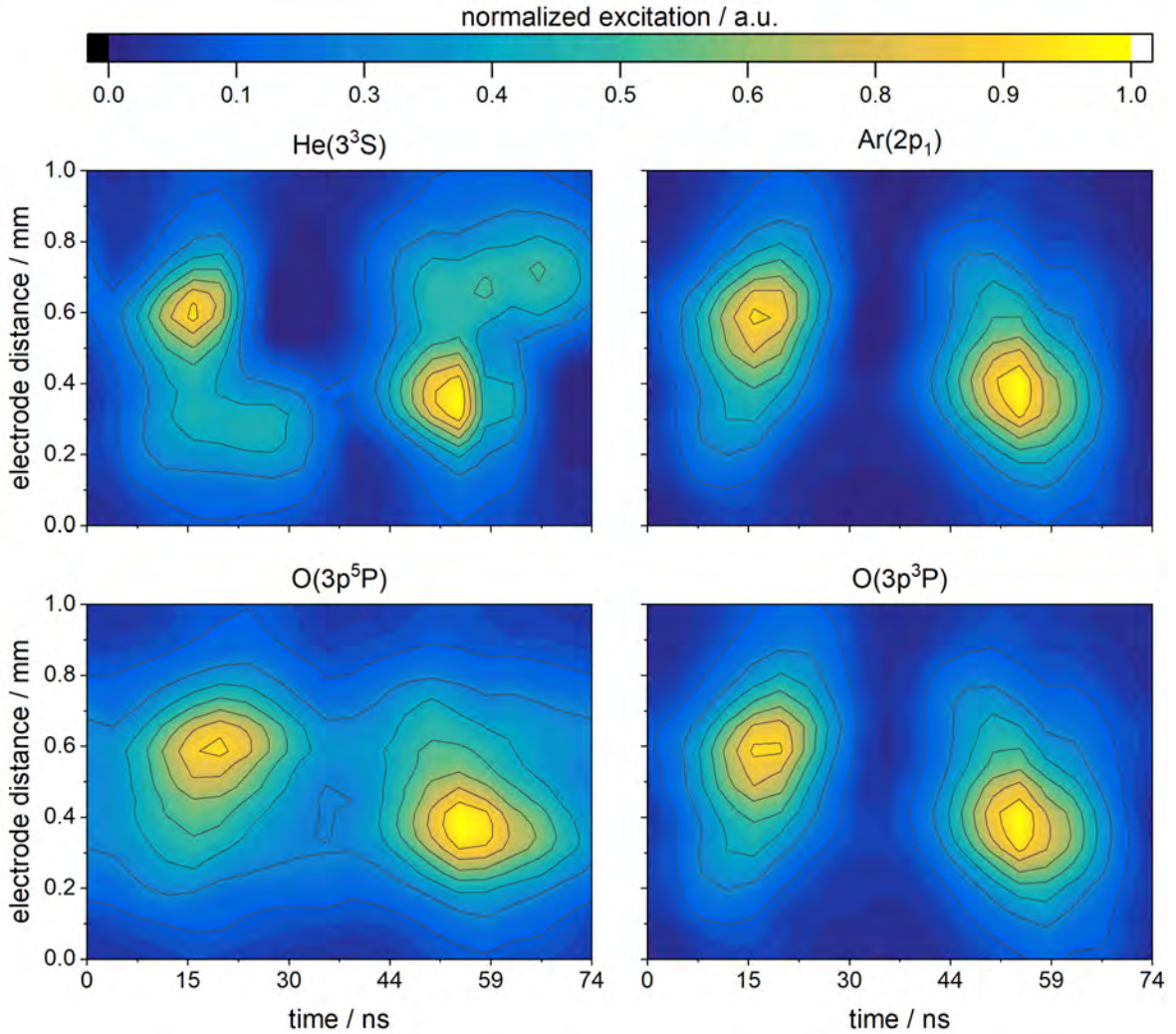

Figure 3.9: Phase resolved excitation into the states He(3^3S), Ar($2p_1$), O($3p^5$P) and O($3p^3$P) in the COST reference microplasma jet. Conditions: $1\,$slm He + 0.5% O_2 + 0.05% Ar, 270 V, f = 13.56 MHz.

The results for different states are shown in Figure 3.9. During one rf-period two excitation maxima are observed. Both occur at the time of high current, when the sheath expands at the grounded electrode and collapses at the powered electrode. At this time within the rf-period, the observed excitation pattern is similar to the electron dynamics observed in low pressure electronegative CCPs [120, 121], where electrons are accelerated by the combination of a strong drift electric field in the plasma bulk and

ambipolar electric fields on the bulk side of the sheath edges. In the case of helium, a strong excitation can also be seen on the opposite side of the respective maxima. This is caused by electrons generated inside the sheath via Penning ionization as a consequence of helium metastable excitation.

To compare the different excitations, it was integrated over the spatially resolved dimension. Figure 3.10 shows the excitations as a function of time. Here, another difference becomes apparent. The states $He(3^3S)$, $Ar(2p_1)$ and $O(3p^3P)$ are highly modulated and almost not excited between the maxima. This indicates that single step electron impact processes dominate their formation and that their effective decay rates are of the same order. The state $O(3p^5P)$, on the other hand, is less modulated and is still populated between the maxima. The lower modulation could, in principle, be explained either by stepwise excitation of the $O(3p^5P)$ state by metastable atoms or molecules or by lower collisional quenching. The latter can be excluded by comparing the collisional quenching rates constants with molecular oxygen as quenching partner ($k_{O_2,777} = 10.8 \times 10^{-16}$ m^{3}s^{-1} [122], $k_{O_2,844} = 9.4 \times 10^{-16}$ m^{3}s^{-1} [123]).

It follows that the lower modulation may be explained by an additional dissociative excitation channel for the formation of the $O(3p^5P)$ state via metastable molecules as suggested by *Katsch et al.* [100], or stepwise excitation via metastable atoms as suggested by *Caplinger et al.* [117]. The case for metastable atoms is supported by the much larger cross section for electron impact excitation of the metastable $O(3s^5S°) \rightarrow O(3p^5P)$ (emission at 777 nm), when compared with electron impact excitation from $O(3s^5S°) \rightarrow O(3p^3P)$ (emission at 844 nm), as reported by *Barklem* [124]. In addition, the

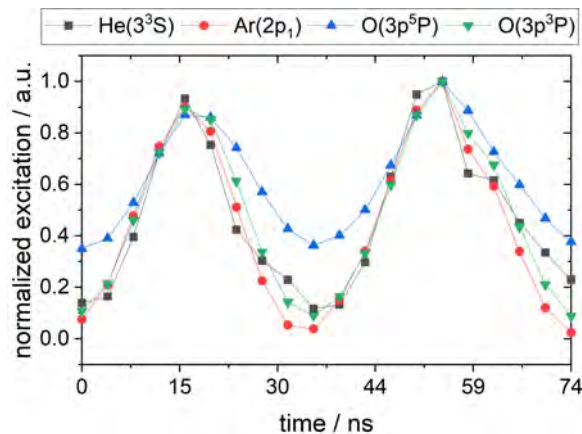**Figure 3.10:** Spatially integrated time resolved excitation into the states $He(3^3S)$, $Ar(2p_1)$, $O(3p^5P)$ and $O(3p^3P)$ in the COST reference microplasma jet. Conditions: 1 slm He + 0.5% O$_2$ + 0.05% Ar, 270 V, f = 13.56 MHz. Adapted from [108].

lifetime of $O(3s^5S°)$ can be estimated under the conditions employed using the rate constants for collisional quenching given in reference [125] for He ($1.8 \times 10^{-21} \mathrm{m}^3\mathrm{s}^{-1}$) and O_2 ($2.2 \times 10^{-16} \mathrm{m}^3\mathrm{s}^{-1}$). This is approximately $37 \, \mathrm{ns}$. Therefore, it can be concluded that $O(3s^5S°)$ can survive for a significant fraction of the radio frequency period, during which it could contribute to step wise excitation. From these simple arguments, it is plausible that step-wise excitation $O(3s^5S°)$ contributes to the emission at $777 \, \mathrm{nm}$ under our conditions. However, to properly quantify the role of this process would require a more detailed model that also considers the density of this state.

Development of new diagnostics: helium state enhanced actinometry (SEA)

Incorporating metastable excitation into the actinometry approach is not straightforward. To reduce the uncertainty due to neglect, helium state enhanced actinometry (SEA) is introduced in the course of this work. Here, the previously used oxygen state $O(3p^5P)$ ($\lambda = 777.4 \, \mathrm{nm}$) is replaced by a helium state $He(3^3S)$ ($\lambda = 706.5 \, \mathrm{nm}$). This has several advantages. First, as discussed earlier, the uncertainties due to metastable excitation can be reduced by the choice of the state. Furthermore, the excitation energy changes from $10.7 \, \mathrm{eV}$ to $22.7 \, \mathrm{eV}$ which extends the range of the EEDF that is probed and improves the energy measurement. By measuring the three optical transitions, two emission intensity ratios can be formed.

$$\frac{I_{844}}{I_{750}} = c_1 \frac{f_{O_2}}{f_{Ar}} \frac{\nu_{844}}{\nu_{750}} \frac{a_{844}}{a_{750}} \frac{2r_O k_{844,d}(\epsilon) + k_{844,de}(\epsilon)}{k_{750,d}(\epsilon)} \tag{3.33}$$

$$\frac{I_{706}}{I_{750}} = c_2 \frac{f_{He}}{f_{Ar}} \frac{\nu_{706}}{\nu_{750}} \frac{a_{706}}{a_{750}} \frac{k_{706,d}(\epsilon)}{k_{750,d}(\epsilon)} \tag{3.34}$$

The emission of a transition depends on the fraction of the species in the total gas mixture f, the respective dissociation degree $r_O = [O]/(2[O_2])$, the photon energy $h\nu_\lambda$ and the energy-dependent effective excitation rates $k_\lambda(\epsilon)$ calculated by BOLSIG+ [116]. Factors c_1 and c_2 indicate calibration factors that compensate for the wavelength-dependent sensitivity of the setup. The indices d and de indicate direct electron impact excitation and dissociative excitation, respectively. Collisional quenching was considered for the optical branching ratio of the observed fluorescence transition (i $\rightarrow$ k):

$$a_\lambda = \frac{A_{ik}}{A_i + \sum_q k_q n_q} \tag{3.35}$$

where A_{ik} is the Einstein coefficient for spontaneous emission, A_i the total spontaneous emission decay rate, k_q the quenching rate coefficient and n_q the absolute density of

a quencher. Quenching rates for oxygen and argon can be found in the literature [122, 123, 126]. For the helium state, quenching rates by helium, argon and oxygen are unknown. However, it can be expected that the quenching by a molecular gas such as oxygen is significantly stronger than by atomic gases. Here, we assume that the quenching by molecular oxygen is of the order of molecular hydrogen, for which quenching rates are available [127]. In any case, for oxygen admixtures below 1% as considered in this work, collisional quenching does not modify the optical branching ratio significantly, although deviations should be considered for larger admixtures.
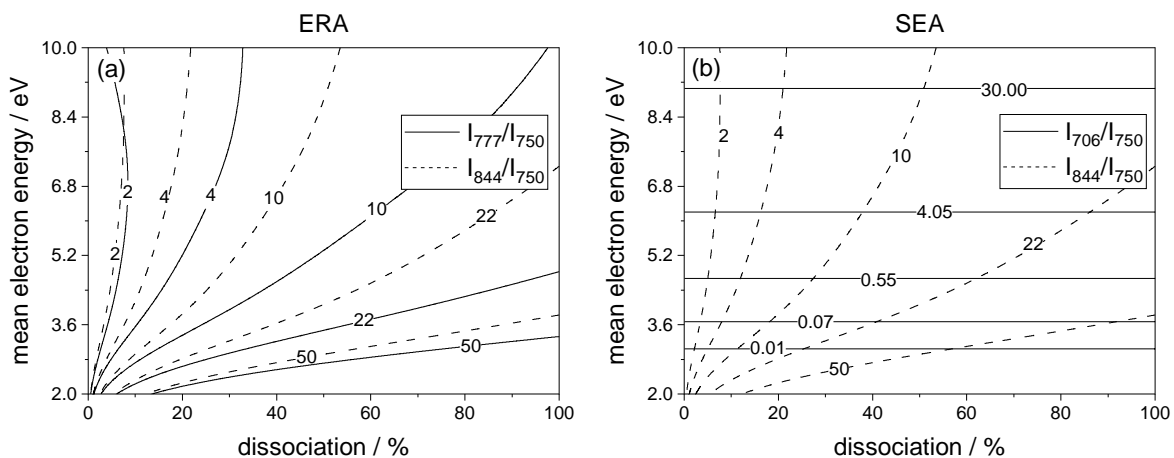

Figure 3.11: Exemplary calculated intensity ratios for (a) ERA: I_{777}/I_{750} and I_{844}/I_{750}, (b) SEA: I_{706}/I_{750} and I_{844}/I_{750} depending on the degree of dissociation r_O and the mean electron energy ϵ. Numbers on the curves indicate the fixed intensity ratio. Conditions: $1\,\text{slm He} + 0.5\%\ O_2 + 0.05\%\ Ar$; $T_{gas} = 350\,\text{K}$. Adapted from [108].

For these calculations, the cross section sets for He and O_2 from the S.F. Biagi's Fortran code version 8.97, Magboltz database (LXCAT) [128] were used as input to BOLSIG+ [116]. In addition, the cross section for direct electron impact excitation of the $Ar(2p_1)$ state was taken from [129], while the cross sections for direct and dissociative excitation of the $O(3p^3P)$ and $O(3p^5P)$ states were taken from [130] and [131], respectively. This combination of cross sections is chosen here for consistency with previous works on ERA [114, 115], and are also comparable with those used in other actinometry studies [117]. However, it should be noted that other cross sections are available in the literature and that a different combination of cross sections is likely to change the absolute densities and mean electron energies inferred from the actinometry calculations.

Figure 3.11 shows example solutions of equations 3.33 and 3.34 as a function of the degree of dissociation and the mean electron energy for the conditions in the COST reference microplasma jet. Each contour represents a fixed intensity ratio which can be measured. A solution of the equation system represents an intersection between two intensity ratios in Figure 3.11. While Figure 3.11 (a) shows the ratios using the oxygen 777 nm line, Figure 3.11 (b) shows the ratios using the helium 706 nm line. In this context, the additional benefit of SEA utilising the helium line becomes evident. The intensity ratio of helium and argon depends only on the mean electron energy but not on the dissociation degree. This leads to the fact that the contour lines in Figure 3.11 (b) intersect nearly perpendicularly. Using the oxygen line, however, the intensity ratios are nearly parallel under commonly used conditions for atmospheric pressure plasma jets (He + 0.5% O_2), which makes it more complex to find unique solutions of the equation system [132].

Typically, excitation ratios are used for ERA instead of simple time and space integrated intensities. The necessity for this is obviated when using SEA, as can be seen again in Figure 3.10. Locations and times with maximum electron heating can be identified, since the fraction of single step electron impact processes in the excitation is highest here. This reduces the uncertainty due to other excitation mechanisms such as metastables, which is particularly important for the state $O(3p^5P)$. However, if the other three states $He(3^3S)$, $Ar(2p_1)$ and $O(3p^3P)$ are used, where the phase-resolved measurements imply that single step electron impact processes dominate at all times, time and space-averaged measurements become possible. This is a major advantage of SEA over ERA. On the one hand, no complex ICCD setup is needed, but a spectrometer is sufficient. On the other hand, the diagnostics become accessible for a wide range of plasma sources, including those operated at kHz frequencies, where the usually required costly ns-resolved measurements are simplified.

Benchmarking the new method against TALIF measurements

To qualify the SEA method, a benchmark against TALIF measurements is performed in the following. The setup used for TALIF, the performed calibration procedure

and an estimate of the accuracy are described in detail in reference [133, 134]. For actinometry measurements, a spectrometer (Avantes AvaSpecULS2048x64TEC-EVO 2011261U1) with an optical fiber (OceanOptics QP600-2-UV-BX) is used. The spectrometer has been relatively calibrated with a known light source (OceanOptics DH-3PLUS-BAL-CAL) and can resolve the spectral lines used to separate unused lines (0.3 nm resolution). To minimize uncertainties due to the low argon flows, a mass flow controller (Analyt) with a maximum flow rate of 1 sccm was used to precisely control small admixtures. All measurements are carried out in the center of the jet (z = -15 mm).

A comparative analysis between the classical actinometry approach, energy resolved actinometry, state enhanced actinometry and TALIF is shown in Figure 3.12 (a). The atomic oxygen density was determined in dependence of the applied driving voltage using the different methods. The confidence intervals of the actinometry approaches result from the size of the parameter range of dissociation degree and mean energy that are consistent with the solution of the system of equations. The accuracy of the TALIF measurements is based on the reproducibility of the data, as well as the noble gas calibration with xenon, which is described in more detail elsewhere [133]. Systematic errors that could affect the absolute densities, such as the choice of the two-photon excitation cross section ratio are not included in the confidence intervals [135].

The TALIF measurements show an approximately linear increase of the atomic oxygen density from 1 to $3 \times 10^{21} \mathrm{m}^{-3}$ between 170 and 270 V. Both, the trend and the absolute value of the density are comparable to previous works [133, 134]. In contrast, the classical actinometry approach shows significantly higher densities (up to $13 \times 10^{21} \mathrm{m}^{-3}$). This was expected, since the dissociative part of the excitation is not taken into account and therefore the density is overestimated.

As described above, both time-resolved and time-integrated measurements can be used for actinometry. To underline the difference between time-resolved and time-averaged measurements, the intensity ratios were modified. Here, a time-resolved measurement
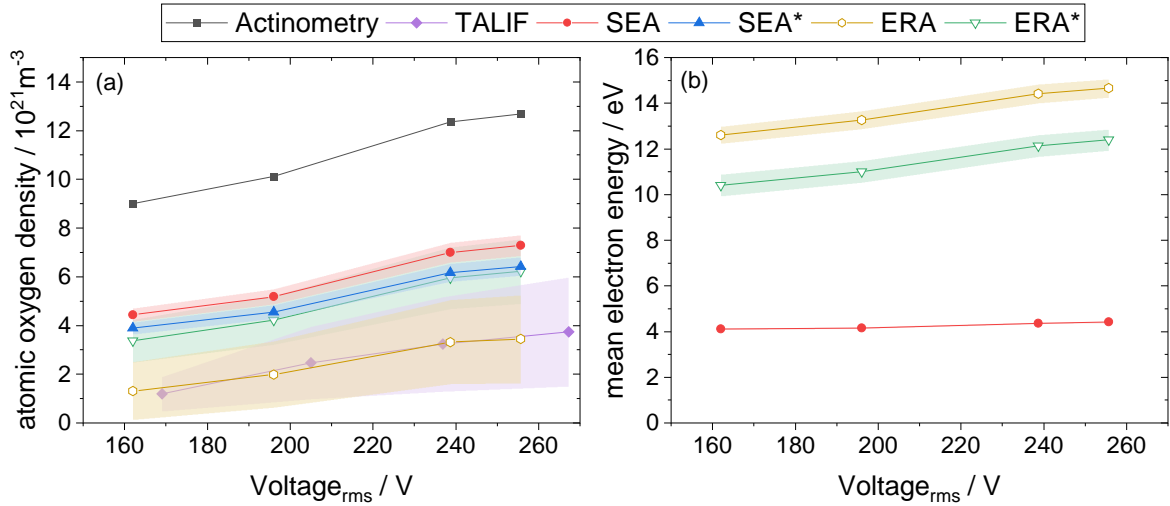
Figure 3.12: Atomic oxygen density (a) and mean electron energy (b) determined by various methods as a function of applied voltage. Colored areas: confidence intervals. Conditions: $1\,\mathrm{slm}$ He + 0.5% O_2 + 0.05% Ar. Adapted from [108].

is evaluated and the ratio between the intensity ratios at the maximum and the time-averaged intensity ratios is determined. This results in a correction factor that compensates for the difference between time-resolved and time-averaged measurements. The corrected values are marked with a star. It is noticeable that the difference between corrected and uncorrected values is significantly greater in the case of ERA than in the case of SEA. This is mainly due to the modulation of the excitation described above. In the case of the intensity ratio I_{777}/I_{750}, for the data shown in Fig 3.10, the difference between time-resolved ratio (defined as the ratio between the absolute intensities at the time of maximum emission) and the time-integrated ratio (defined as the ratio between the absolute intensities averaged over one cycle) is 45%. Accordingly, when using the $O(3p^5P)$ state, a time-resolved measurement is required in order to use emission / excitation ratios at the time of maximum emission when an actinometry scheme that does not include step-wise excitation via metastable atoms and / or molecules is used. The remaining states, on the other hand, are modulated in such a way that the deviation of excitation ratios due to time averaging is only 10%.

The absolute densities with the uncorrected ERA method are between 1 and $3\times10^{21}\mathrm{m}^{-3}$ and are in close agreement with the TALIF measurement. However, the corrected measurements show significantly higher densities. This is due to the fact that metastables

likely play a role in the measured excitation, which cannot be taken into account in the ERA model. If, the physical model underlying the ERA approach is incorrect when applied to temporally and spatially integrated spectra, it can be assumed that the close agreement between ERA and TALIF measurements of atomic oxygen density is coincidental.

By using the SEA method, issues related to the population of the $O(3p^5P)$ via metastable levels can be avoided. Again, the intensity ratios were also corrected (SEA*). However, since the deviations between maximum excitation and integrated excitation are very small for the states used with SEA, the atomic oxygen density determined with and without a correction are very similar. The difference in the results from the corrected SEA* and SEA is only 10% and the densities are in a range between 4 and $7 \times 10^{21} \text{m}^{-3}$.

In addition to atomic oxygen densities, the method can also be used to determine mean electron energies (see Figure 3.12 (b)). For ERA these are in the range between 13 and 15 eV, which is significantly higher than expected. This, in turn, can be explained by the fact that excitation by metastables is not taken into account. Since the fraction of the excitation has to be compensated, it can be assumed that the mean energy is over-estimated. Even the corrected values are between 0 and 12 eV and are still significantly higher than expected. For SEA the mean electron energies are lower (4.0 to 4.5 eV) than for ERA. No difference can be observed between SEA and SEA*. In literature, electron temperatures in the range between 2 and 3 eV are given for the COST reference microplasma jet [136–138] which are related to mean electron energies between 3 and 5 eV under the assumption of a Maxwell-Boltzmann distribution, thus there is a reasonable agreement with the SEA method. However, the energies differ significantly when ERA is used, although *Greb et al.* [114] reported a good agreement (3-6 eV) with this method in a comparable jet. The difference shows clearly that ERA is most reliable when performed with phase-resolved measurements, otherwise the influence of excitation via metastables and other processes is too large.

In addition to a difference in the absolute atomic oxygen density and mean electron energy, also a difference in the confidence intervals of ERA and SEA is noticeable. While

the uncertainties for ERA are up to 90% (25% for ERA*), for SEA uncertainties of around 5% are obtained. This difference results from the more clearly defined crossing points of the excitation ratios in the SEA scheme. This means that the ranges of dissociation degree and mean electron energy for which the experimentally measured ratios are consistent with the calculated ratios, are smaller. In addition, it becomes clear that the SEA method can access a larger energy range of the EEDF, which should allow it to provide a more robust estimate of the mean energy. Nevertheless, the confidence intervals indicate only the uncertainties of the calculation and not the systematic uncertainty caused by the numerous assumptions of actinometry.

In summary, helium state-enhanced actinometry developed in this work offers the possibility to determine atomic oxygen densities and mean electron energies simultaneously. SEA and TALIF measurements show good agreement for the atomic oxygen density in the COST reference microplasma jet and mean electron energies known from the literature could be reproduced. The use of time-averaged emission makes only one spectrometer necessary. This significantly reduces the experimental complexity compared to laser diagnostics or phase-resolved spectroscopy measurements. Nevertheless, if a different plasma source is used, the systematic error due to time-integrated measurements should be experimentally verified. Furthermore, the helium line used can be observed in a large number of plasmas without the need to change the gas mixture. However, SEA can also be used in plasma sources operated without helium by using a low helium and argon admixture. This makes the diagnostics feasible for a larger number of applications in research and industry.

3.2.3 Rotational temperatures

In addition to densities of species and electric fields, gas temperature can also be determined using optical emission spectroscopy. This is particularly important for the use of actinometry. On the one hand, the total density is influenced by the temperature over the ideal gas law. This influences both the value of the oxygen density and the quenching. On the other hand, the temperature is needed as input parameter for Boltzmann solver calculations.

One commonly used technique for measuring gas temperature involves assessing rotational temperatures from the emission of nitrogen molecules. This approach offers several benefits. Firstly, it allows for the preservation of the gas mixture, as even small impurities of nitrogen found in gas bottles are adequate for generating an emission spectrum. Secondly, this method is non-intrusive and has no impact on the discharge process. Additionally, it does not interfere with actinometry measurements, enabling simultaneous performance of these diagnostics.
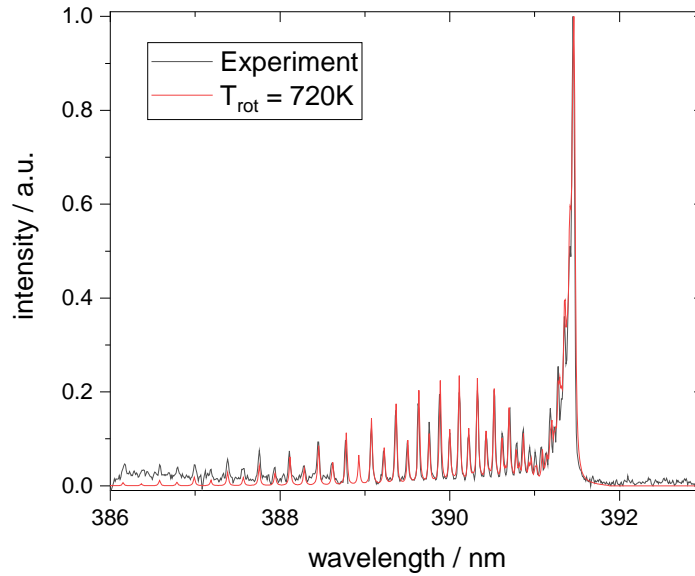

Figure 3.13: Emission of the first negative band of nitrogen ions and fitted rotational temperature in a micro cavity plasma array. Conditions: $2\,\mathrm{slm}$ He, $2\,\mathrm{sccm}$ O_2, $1\,\mathrm{sccm}$ Ar, $V_{pp} = 1600\,\mathrm{V}$.

Here, the emission of the first negative band of nitrogen ions $(N_2^+ B^2 \sum_u^+ (v' = 0) \rightarrow X^2 \sum_g^+ (v'' = 0))$, located at $391\,\mathrm{nm}$, is observed. To determine the rotational temperatures, a theoretical spectrum is calculated assuming a Boltzmann distribution. The temperature of the Boltzmann distribution is used as a parameter and the theoretical spectrum is fitted to the measured spectrum using custom made software (N2 Temp). In thermal equilibrium, the temperature of the rotational motion of the molecules is equal to the temperature of their translational motion. This correspondence allows the gas temperature to be directly inferred from the distribution of rotational states. A more detailed explanation of the diagnostics, as well as the parameters used (Hönl-London coefficients, spectroscopic constants etc.) can be found in reference [139].

Figure 3.13 shows an exemplary measurement of a spectrum. The characteristic band structure between 386 and 392 nm is clearly visible. For the determination of the temperature, the spectrum can be calculated as a function of the rotational temperature. The best agreement is in this case at a temperature of 720 K. Here the band head as well as the following peaks are very well fitted. At the edges the measured spectrum deviates slightly due to a background caused by the experimental setup. The uncertainty is about 50 K.

3.3 Two Photon Absorption Laser Induced Fluorescence Spectroscopy

In addition to optical emission spectroscopy, laser diagnostics such as Two Photon Absorption Laser Induced Fluorescence Spectroscopy (TALIF) [123, 140, 141] offer the possibility of determining atomic oxygen densities. While the excitation observed in OES is typically achieved by electron impact, a laser is used for TALIF allowing densities also to be determined outside the active plasma volume. This means that fewer assumptions are necessary overall, as the electron collisions are fundamentally linked to the EEDF and discharge dynamics, which reduces the uncertainty of the method compared to actinometry. However, laser diagnostics have a decisive disadvantage, especially in combination with microplasmas: optical access is required both for the laser beam and for a fluorescence signal. For cavities in the µm range, alignment is very difficult or even impossible due to scattering or even fluorescence at surfaces. For this reason, in this work the method is used exclusively in the effluent of the reactor, while the densities inside the cavities are determined by optical emission spectroscopy. A basic diffusion model should then connect the two diagnostics.

The basic principle of laser-induced fluorescence is as follows: an atom or molecule is excited out of its ground state using a laser. When the atom or molecule de-excites to a lower energy level, a photon is emitted. The ground state density can then be determined by measuring the emission. When exciting light atoms such as oxygen, high energies (approximately 11 eV) are needed. This would require lasers with wavelengths

in the VUV range, which in practice could only be used at great effort. One solution to this problem is the use of two photons. Here, the upper and lower energy levels are not resonantly coupled via intermediate states. The first photon excites the atom into a virtual intermediate state. In a short time interval (due to a short lifetime) after this excitation, a second photon can lift the atom into the desired state. [142]

The excitation rate R can be described by the generalized cross section for two-photon excitation ($\hat{\sigma}^{(2)}$) and the fluxes of the two photons.

$$R = \hat{\sigma}^{(2)} \left(\frac{I_L}{h\nu_L} \right)^2 \tag{3.36}$$

The cross section $\sigma^{(2)}$ is calculated from a time-dependent perturbation calculation. In addition, the photon statistical factor $G^{(2)}$ and the line profile of the two-photon excitation $g(\Delta\nu)$, which is composed of the profile of the transition, the velocity distribution of the atoms and the laser profile, must be taken into account. [142]

$$\hat{\sigma}^{(2)} = G^{(2)} g(\Delta\nu) \sigma^{(2)} \tag{3.37}$$

The ground state density can be calculated using a rate model in which the excitation from the ground state is linked to the emission and all population and depopulation mechanisms are taken into account. The ground state $|1\rangle$ can be excited to state $|3\rangle$ with rate R_{13}. This is then de-excited to level $|2\rangle$ by spontaneous emission, which can be described by the Einstein coefficient A. In addition, level $|3\rangle$ can also be depopulated by radiationless quenching Q. Processes such as photoionization or induced two-photon emission can be neglected in the unsaturated case, where the excitation rate is proportional to the laser intensity. Accordingly, the change of the excited state follows:

$$\frac{\mathrm{d}}{\mathrm{d}t} n_3 = R_{13}(t) n_0 - (A_3 + Q_3) n_3 \tag{3.38}$$

The solution for a laser pulse of length T is as follows:

$$n_3(t) = \begin{cases} n_0 \int_0^\infty R_{13}(t) e^{-(A_3+Q_3)(t-t')} dt' & \text{für } 0 < t < T \\ n_3(T) e^{-(A_3+Q_3)(t-T)} & \text{für } t > T \end{cases} \tag{3.39}$$

Integration over time and volume yields the number of photons N, where $a_{ik} = \frac{A_{32}}{A_3+Q_3}$ describes the optical branching ratio. Accordingly, the fluorescence signal is linearly

dependent on the atomic oxygen density and quadratically dependent on the laser intensity. [142]

$$N_F^{tot} = A_{32} \int_V \int_0^\infty n_3(t) \mathrm{d}t\mathrm{d}V = a_{32}\hat{\sigma}^{(2)} n_0 \int_V \int_0^\infty \left(\frac{I_L}{h\nu_L}\right)^2 \mathrm{d}t\mathrm{d}V \qquad (3.40)$$

Xenon calibration

The exact number of fluorescence photons is difficult to determine. Typically, photomultipliers or ICCD cameras are used for detection. In order to be able to determine the exact number of photons, the properties of all optical elements in the beam path must be known in addition to the characteristics of the detector. It is more straightforward to calibrate the measured signals by making a comparative measurement with a noble gas of known density [143]. For oxygen, xenon is typically used for calibration. The O(3p ^{3}P$_{1,2,0}$) and xenon Xe(6p'[3/2]$_2$) state pair is very suitable. Here, the excitation wavelength only differs by approximately 1.3 nm. The fluorescence signal changes by approximately 10 nm. The small changes offer the advantage that the setup used barely needs to be changed and so the experimental conditions remain almost the same. Typically, only the optical filters have to be replaced and the wavelength-dependent sensitivity of the detector has to be taken into account.

The TALIF signal, which is proportional to the oxygen density, can be represented as a measured variable M (voltage at photomultiplier or counts of ICCD) normalized to the laser intensity:

$$S = \frac{M}{\int_V \int_0^\infty \left(\frac{I_L}{h\nu_L}\right)^2 \mathrm{d}t\mathrm{d}V} \qquad (3.41)$$

The aim of the calibration is to find a factor χ that links the signal to the atomic oxygen density.

$$n_O = \chi S_O \qquad (3.42)$$

This can be calculated by measuring the xenon signal S_{Xe} for a certain density n_{Xe} and forming the ratio to an oxygen signal. In addition, various properties of the setup, such as transmission of the filters T, photon yield of the detector η and branching ratio a must be taken into account.

$$\frac{S_{Xe}}{S_O} = \frac{T_{Xe}\eta_{Xe}}{T_O\eta_O} \frac{a_{Xe}\sigma_{Xe}^{(2)}}{a_O\sigma_O^{(2)}} \frac{n_{Xe}}{n_O} \qquad (3.43)$$

Since the two-photon excitation cross-section $\sigma^{(2)}$ is only defined for spectrally integrated signals, but the measurements are typically carried out at only one wavelength, the deviation must be corrected. For this purpose, a wavelength scan is performed for both excitation wavelengths (O and Xe). The correction factor I results from the area under the signal divided by the maximum signal (at the wavelength used for the measurements).

Since the oxygen ground state is a triple degenerate, but the measurements are only carried out at (J=2), it is not possible to draw direct conclusions about the ground state density from the signal. The proportion of the total ground state in the J=2 state can be determined using a Boltzmann distribution:

$$\frac{n_{0,J=2}}{n_0} = \beta = \frac{(2J+1)\exp\left(\frac{E_J}{k_B T}\right)}{\sum_{J=0}^{J=2}(2J+1)\exp\left(\frac{E_J}{k_B T}\right)} \tag{3.44}$$

At room temperature, the proportion is $\beta = 74.17\%$.

To reduce the uncertainty, it is advisable to carry out the comparative measurement for several xenon densities. The TALIF signals are then plotted against the density. The linear relationship can be fitted and the slope m used to calculate the calibration factor.

$$\chi = \frac{a_{Xe}\eta_{Xe}T_{Xe}\sigma_{Xe}^{(2)}I_{Xe}}{a_O\eta_O T_O\sigma_O^{(2)}I_O}\frac{1}{m}\frac{1}{\beta} \tag{3.45}$$

4 Experimental setup

The experimental setup is described in the following section. A sketch with the most important parts of the setup is shown in Figure 4.1. The micro cavity plasma array reactor is at the center of the setup. In addition, there are components for the various diagnostics, which are discussed step by step. Moreover, the setups for more specialized diagnostics, such as the laser manipulation of surface charges, the triple photomultiplier setup or the laser induced fluorescence setup, are described separately.
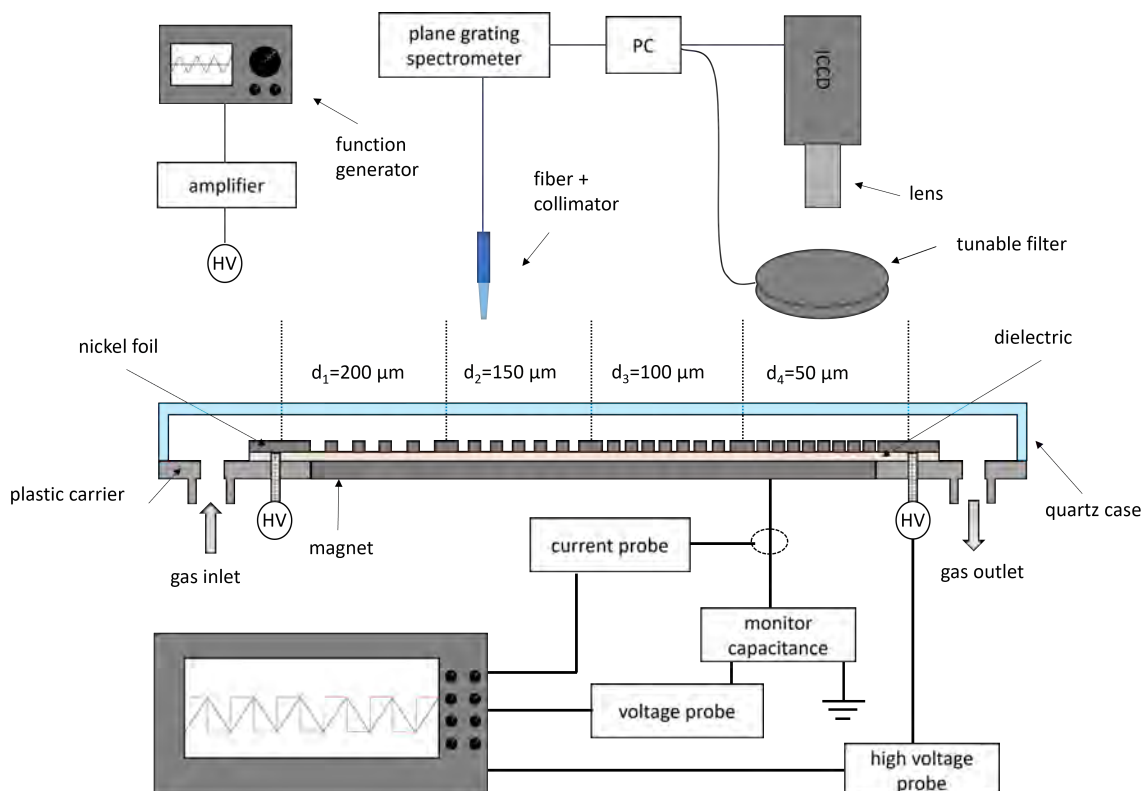

Figure 4.1: Schematic sketch of the experimental setup adopted and expanded from [110].

4.1 Design of the used plasma reactors

The plasma reactor used in this work is a micro cavity plasma array (MCPA). Depending on the diagnostics, the exact design of the reactor can be slightly modified. The differences are discussed in the following section.

Quadruple metal grid array

A quadruple metal grid array (MGA), already described in section 2.2, is used for the majority of the measurements. A neodymium magnet ($50x15x5\,mm^3$) is placed flush in a carrier made of polyetherether ketone (PEEK) and acts as a grounded electrode. A $40\,\mu m$ thin zirconium dioxide layer ($63x20\,mm^2$, relative permittivity $\epsilon_r \approx 27$) separates the grounded magnet from a high-voltage supplied nickel grid and thus works as a dielectric barrier. The nickel grid is laser-cut into a $50\,\mu m$ thin nickel foil and consists of thousands of cavities arranged in four sub-structures ($10x10\,mm^2$), which differ in the diameter of the cavities (50-$200\,\mu m$). The distance between individual cavities is $200\,\mu m$, while the distance between adjacent sub-structures is $1\,mm$. The triple layer (magnet, dielectric and nickel grid) is held together by the magnet and is placed on an aluminum mounting. The entire construction is tightened with a quartz cover. This allows a defined gas flow across the cavities. The distance between grid and cover is $4\,mm$, which enables optical diagnostics from above and from the side. The average flow velocity at a gas flow of $1\,slm$ is then $0.21\,m/s$. The MGA is mounted on an x-y-z-stage (custom made, not shown). As feed gas helium (purity 5.0) with a constant gas flow of $2\,slm$ is used. In addition, a variable molecular oxygen admixture (purity 4.8, 0-$50\,sccm$) and $1\,sccm$ argon (purity 5.0) as actinometer gas are added. The gas flows can be set and controlled by three mass flow controllers (Analyt 358 Series, $2\,slm$, $50\,sccm$ and $1\,sccm$.). A function generator (Tektronix AFG 3021B) is connected to the MGA via an amplifier (Trek MODEL PZD700A M/S). The power supply provides voltages up to an amplitude of $800\,V$ and is used with a bipolar triangular frequency of $15\,kHz$. A relay (V23100-V4305C000) is connected between the amplifier and the function generator (not shown in the Figure) in order to switch the reactor on and off quickly (in the range of µs), for example to observe the decay of surface charges. This can be controlled using another function generator that is synchronized with the voltage waveform. [22, 28, 110]

Single metal grid array

As described above, the MGA is usually used with four sub-array structures to vary the cavity diameter or cavity spacing. However, depending on the diagnostics, it is not possible to separate the effects of the different structures from each other. For this reason, a single array structure is used for certain measurements in this work. One structure of the single array has the same dimensions as a substructure of the quadruple array. Apart from the omission of the other sub-structures and the resulting smaller geometry, the design is the same as before except for two differences. Firstly, there is no sealed quartz cover for the single array, thus it is typically operated in a vacuum chamber with helium atmosphere, close to atmospheric pressure. Secondly, a cylindrical (h = 5 mm, d = 16 mm) samarium cobalt magnet is used instead of a block-shaped neodymium magnet. The edges around the cavity structure are pressed onto the surface with a magnetic metal frame to ensure stability despite the smaller magnet.

Design of micro scaled plasma trenches

With the cavity structure typically used, it is not possible to observe the discharge from the side. However, this is necessary if the components of the electric field are to be determined. For this reason, a micro scaled plasma trench device (MSPT) was developed in the course of this work. This consists of a metal grid with the same dimensions as the cavity grid and can therefore be used with the same setup (carrier, magnet, dielectric, etc.). A sketch comparing the two grids is shown in Figure 4.2.
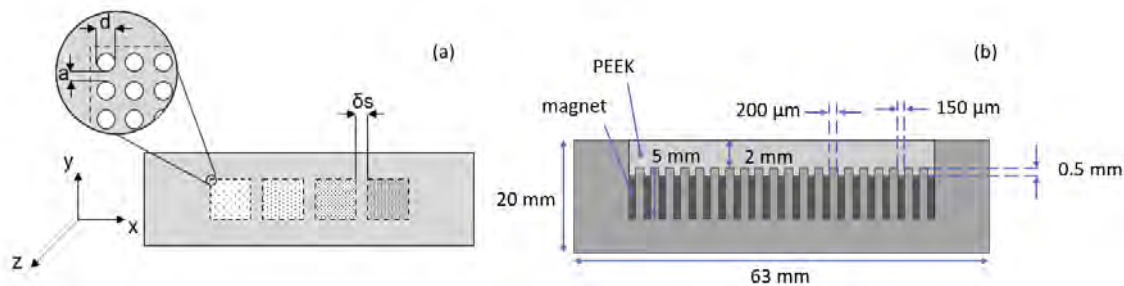

Figure 4.2: Schematic sketches of the various metal grids. (a) cavity structure taken from [28] and (b) trench structure.

The grid consists of metal strips (200 µm). Trenches (150 µm) are formed between them in which the discharge can be ignited. As with the cavities, optical diagnostics can be performed from above through the cover. In addition, the trenches now offer the possibility of observing the discharge from the side. The geometry of the grid was chosen in such a way that the tips of the strips are no longer above the magnet (grounded electrode). This means that the discharge remains very homogeneous and the field increase at the tips has no influence. Overall, a compromise had to be found for the length of the trenches. The longer the trenches, the greater the discharge, which results in stronger emissions for diagnostics, for example. However, the thin metal strips are very delicate and challanging to handle. During assembly, this can lead to interactions with the magnet, for example, where not all of the trenches are aligned parallel to each other or individual strips may even bend. Here, stability can be increased by using shorter trenches.

4.2 Setup for optical diagnostics

The setup for optical diagnostics is shown above the array in Figure 4.1. For temporally and spatially resolved measurements, one sub-array structure is imaged on an intensified charge-coupled device (ICCD) camera (Andor iStar DH334T-18U-73) using a long distance microscope (Questar QM 1). Alternatively, another modular lens system (KX InfiniMax) can be used. Here, the focal length can be adjusted by exchanging lenses to allow either entire sub-array structures (lens MX-1) or individual cavities (lens MX-6) to be imaged. A relative calibration was performed using a broadband lamp (Ocean Optics DH-3 plus). The wavelength can be set with a tunable fil-
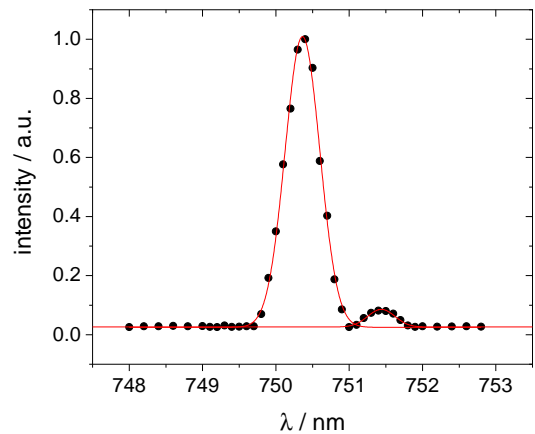

Figure 4.3: Spectrum of argon lines at 750.4 nm and 751.5 nm recorded through tunable filter. Both lines were fitted with a Gaussian profile. Adopted from [110].

ter (VariSpec NIR-RM-HC-20) in a range of 550-1000 nm in 0.1 nm steps. The filter

can switch very quickly between the different wavelengths (response time of 100 ms). This makes it possible to acquire 2D measurements of all wavelengths required for actinometry within seconds, thus ensuring comparability. The FWHM is approximately 0.55 nm, providing sufficient resolution to separate adjacent spectral lines, such as the Ar 750.4 nm and Ar 751.5 nm (Figure 4.3), which is essential for actinometry. If the main objective is the wavelength-independent emission, the filter can be removed from the optical path allowing shorter exposure times to be achieved. [110]

In addition to the ICCD camera, the emission can be collected using an optical fiber (with collimator if required). The fiber can either be connected to a photomultiplier (Hamamatsu R3896, not shown) for time-resolved emission measurements or to a two-meter focal length plane grating spectrometer (PGS-2, Zeiss Jena) for wavelength-resolved measurements. Additionally, depending on the diagnostics, a filter such as a bandpass or rotatable polarization filter (Thorlabs LPVISE100-A) can be inserted into the optical path. According to the wavelength region, the spectra can be used to measure the electric field through the Stark splitting of a helium line or to determine the rotational temperature from a nitrogen spectrum.

The spectrometer is equipped with an ICCD camera (Andor iStar DH320T-25U-A3). This makes it possible to achieve a high signal-to-noise ratio even with low emissions. The effective resolution with a slit width of 25 μm and the camera used is 8 pm. Furthermore, the camera can be synchronized with the discharge so that phase-resolved measurements are possible. Typically, the emission is collected via an optical fiber bundle and guided into the spectrometer. In this case, a special split fiber is used. This has the advantage that a calibration lamp can be connected in addition to the discharge. The fiber bundles are sorted in such a way that different areas on the ICCD chip are illuminated and the light sources can be separated accordingly. This is particularly important when determining the electric field using Stark splitting. Precise wavelength calibration is essential here, so that a hollow cathode lamp filled with helium and argon can be used simultaneously with the discharge. This makes changes in the wavelength calibration, for example due to temperature fluctuations, visible in real time. However, as an alternative to the fiber, the discharge can also be positioned directly in front of

the slit. This has various advantages and disadvantages. Firstly, the reactor must be mobile enough to be positioned in front of the slit. This is not possible, for example, if the measurements are to be carried out in a vacuum chamber. Furthermore, it is very time-consuming to align the discharge precisely in front of the slit. The advantages on the other hand are, firstly, the increased light yield, as the optical path is shorter. Secondly, there is a spatial resolution, as the discharge is imaged directly onto the lines of the ICCD camera.

Triple photomultiplier setup

In addition to the ICCD setup already described, the actinometry measurements can also be carried out with a triple photomultiplier setup. This has the advantage that all three required transitions can be observed simultaneously with high time resolution. This is not possible with the ICCD setup, as the filter has to be switched between the measurements. In addition, optical filters with enhanced transmission properties can be employed instead of the tunable filter. This substitution could significantly increase the light yield, reducing the need for averaging and potentially enabling single-shot measurements. Moreover, the measurement, including the evaluation, is greatly simplified. The ICCD produces large amounts of data which, if the spatial resolution is not required, are unnecessary and make evaluation time-consuming. Furthermore, the photomultiplier setup is cheaper than an ICCD setup, making it usable for more laboratories.
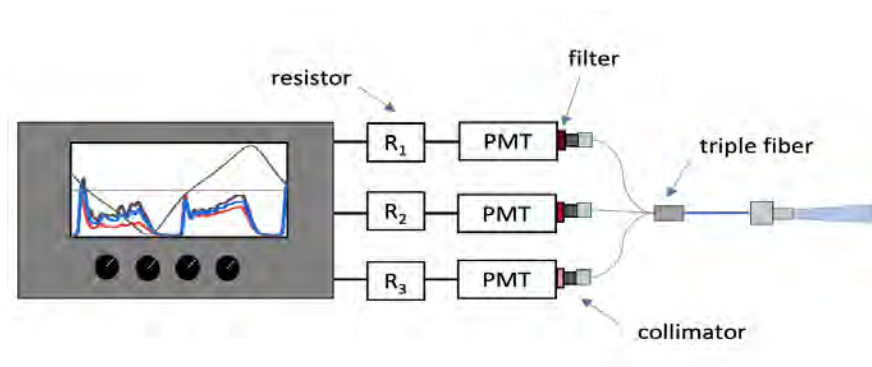

Figure 4.4: Schematic sketch of the triple photomultiplier setup.

Figure 4.4 shows the triple photomultiplier setup. Three identical photomultipliers

(Hamamatsu R13456) are used. Optical filters for the different transitions (Thorlabs, 710 nm, 750 nm and 840 nm) with a FWHM of 10 nm are mounted in front of the photomultipliers. Despite the increased transmission compared to the tunable filter, there is a disadvantage. Due to the width of 10 nm, the argon 750 nm line can no longer be separated from the argon 751 nm line. This can lead to deviations in the measurements and must be taken into account when interpreting the results. The heart of the setup is an optical triple fiber (Avantes FC3-UVIR400-2-ME). This consists of three individual 400 μm fiber cores that converge to form one fiber. The three fiber ends are connected to the photomultipliers via collimators. The single end can be used to detect the light. The integration times of the photomultipliers can be regulated via adjustable resistors. The signals can then be evaluated simultaneously on an oscilloscope.

A compromise between intensity and time resolution must be found for the integration time. The low argon admixture results in the lowest intensity for the argon transition, which is therefore the limiting signal. In order to still achieve a sufficient signal to noise ratio, the integration time was set to 1 μs for all photomultipliers. Before the setup can be used for actinometry, a relative intensity calibration must first be performed, for which a calibration lamp (Ocean Optics DH-3PLUS-BAL-CAL) is used as with the ICCD setup.

4.3 Setup for electrical diagnostics

The setup for electrical measurements is shown below the reactor in Figure 4.1. The applied voltage can be measured using a high voltage probe (Tektronix P6015A). The current is monitored using a current clamp (Tektronix P6021) mounted on the connecting cable from magnet (grounded electrode) to ground. In order to measure the transported charge, a monitoring capacitance (67 nF) is integrated in the circuit to measure the voltage drop with the help of another voltage probe (Teledyne LeCroy PP006A). All signals converge in a digital oscilloscope (Teledyne Lecroy WavePro 404HD). This means that all measured variables required for the equivalent circuit approach are available. The results can be observed in real time via the oscilloscope and partially evaluated directly with the help of Labview, e.g. to display the power.

Setup for laser manipulation of surface charges

As previously discussed, it is not trivial to determine the surface charges using the equivalent circuit approach, as surface effects must be separated from volume effects. For this reason, a laser is used that only manipulates the surface charges allowing the surface charge density to be inferred. The setup is shown in Figure 4.5.
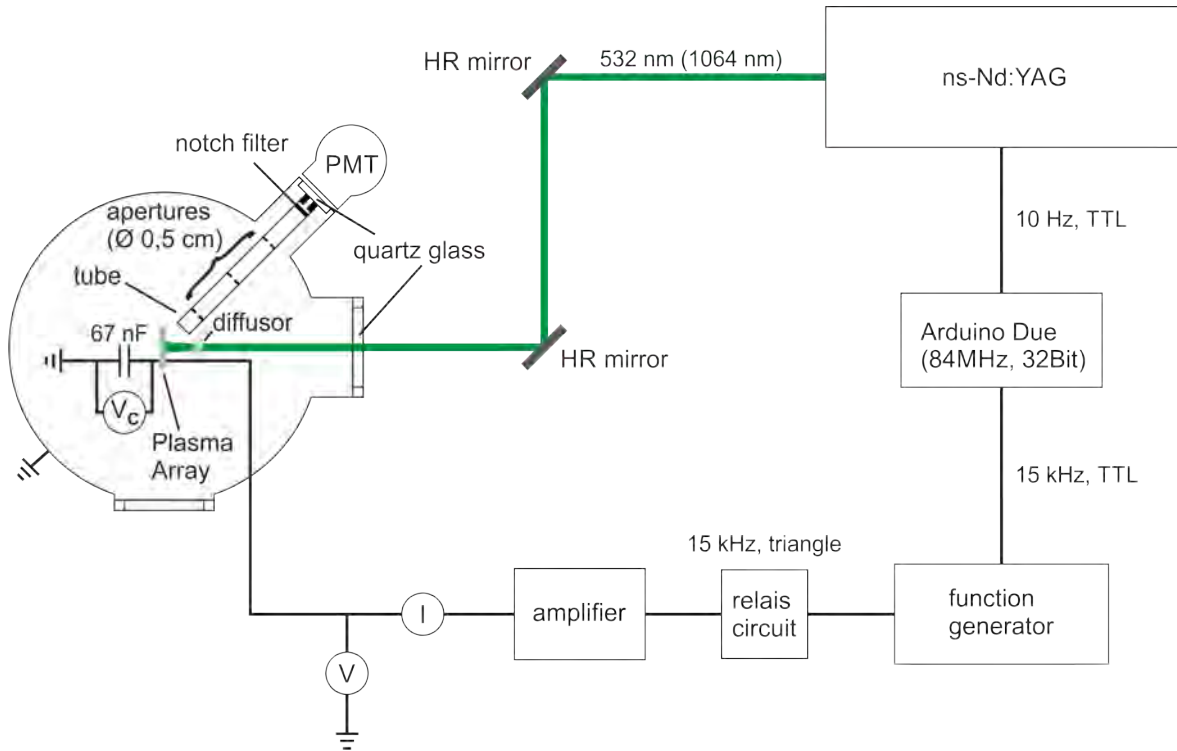

Figure 4.5: Schematic sketch of the setup for laser manipulation of surface charges. Adopted from [144].

As the electrical measurements are integrated over the entire discharge, the single array described above is used for the charge measurement. This device is mounted in a vacuum chamber under helium atmosphere close to atmospheric pressure. As before, the reactor is operated using a function generator in combination with an amplifier. The measurement of current, voltage and charge also remains the same. An ns-pulsed Nd:YAG laser (Continuum Powerlite 8010) is used to manipulate the charges. The laser is operated with a pulse frequency of 10 Hz and a pulse duration of 10 ns. Either the fundamental wavelength of 1064 nm or the second harmonic (532 nm) can be used. The timing of the laser is controlled by a delay generator (Stanford Research Systems DG645). To synchronize the laser with the voltage applied to the reactor (15 kHz),

an Arduino Due (84 Mhz, 32 Bit) is used as a frequency divider. This allows phase-resolved measurements to be carried out.

The laser beam (from 0.9 cm to 1.2 cm diameter) is guided into the chamber via mirrors and through a quartz window. Inside the chamber, the beam passes a diffuser plate, which expands the beam to illuminate all cavities on the one hand and homogenizes the beam on the other hand. After the diffuser, the beam hits the center of the array. Typically, the angle between the surface and the beam is perpendicular, but can be varied using a rotation stage (Zaber X-RSW-SV1).

The emission of the discharge can be measured simultaneously using a photomultiplier. To do this, however, the reflections caused by the laser must be attenuated. For this purpose, a 30 cm long black tube is used in front of the photomultiplier. At the end of the tube a notch filter (Edmund Optics 87-021) with an optical thickness of OD 6 for 532 and 1064 nm (50 nm FWHM) is installed. For other wavelengths between 400 and 1200 nm there is a transmission of >90%. As the filter only works with perpendicular beam incidence, three apertures with a diameter of 0.5 cm are positioned in the tube to parallelize the beam. Overall, the scattered light can be significantly reduced. In combination with background measurements, the plasma emission can be observed without the influence of scattered light.

Relay setup for measuring surface charges

An alternative method of separating surface charge from volume charges is to rapidly switch off the discharge. Here, volume charges should vanish in a short time, for example through recombination or diffusion. Surface charges, on the other hand, are retained for longer and can therefore be measured separately.

In this work, a relay circuit (V23100-V4305C000) is employed for this purpose, capable of precisely ($\Delta t < \pm 1$ µs) turning off the external voltage. It is powered by a function generator (Tektronix AFG3251) and synchronized with the plasma array's excitation cycle. Digital solutions, such as a digital switch or predefined waveforms, were also tested but resulted in uncontrollable overshoots in the amplifier.

4.4 Setup for TALIF measurements

A separate setup is used for the TALIF measurements (see Figure 4.6). A ps-laser system (EKSPLA, PL2231A) generates a laser beam with a repetition frequency of 50 Hz and a pulse width of 30 ps. The energy at a wavelength of 225 nm measured directly at the laser output is 130 µJ. This is focused via UV mirrors and a lens (f = 500 mm) through the quartz cover of the micro cavity plasma array. Here, the beam has a round shape with a diameter of approximately 200 µm. The reactor is mounted on a computer-controlled translation stage (Newport, VP-25XA) and can be moved in the x, y and z directions to vary the relative position between the laser and the reactor. The resulting fluorescence signal with a wavelength of 844.9 nm is focused with a lens (Sigma, 105 mm, set to 1:1 magnification) through a band pass filter (Andover, 840FS10-50) onto the chip of an ICCD camera (Andor, iSTAR DH334T-18U-73). To prevent the laser light from reaching the detector, the camera is aligned perpendicular to the beam. In principle, a top view would make sense, as the discharge could then be observed at the same time. However, if measurements are taken close to the surface, the laser is scattered by the grid of the reactor. In addition, fluorescence occurs on the dielectric and the actual TALIF signal can be reflected. To eliminate both effects, the camera is positioned at the side. The position is selected in such a way that the first cavity structure (200 µm) is fully captured. In addition, part of the subsequent structure (150 µm) can be observed. The two-dimensional image of the camera therefore shows the y component along the beam and the z component of the density perpendicular to the beam.

To measure TALIF signals, it is crucial to synchronize the fluorescence measurement with the laser. This is achieved by using a pre-trigger signal from the laser, generated 1 ms before the laser beam, to trigger a digital delay generator (Stanford Research Systems, DG645). The digital delay generator then controls the timing of all devices. The ICCD camera is timed to fire exactly during the fluorescence, with its gate width set to 30 ns to account for a jitter of 1-2 ns and ensure reliable recording of the entire TALIF signal. In this setup, the reactor uses a different amplifier (Matsuda Precision AMT-1B60), controlled by a function generator (Stanford Research Systems, DS345). A sinusoidal voltage waveform of 15 kHz is
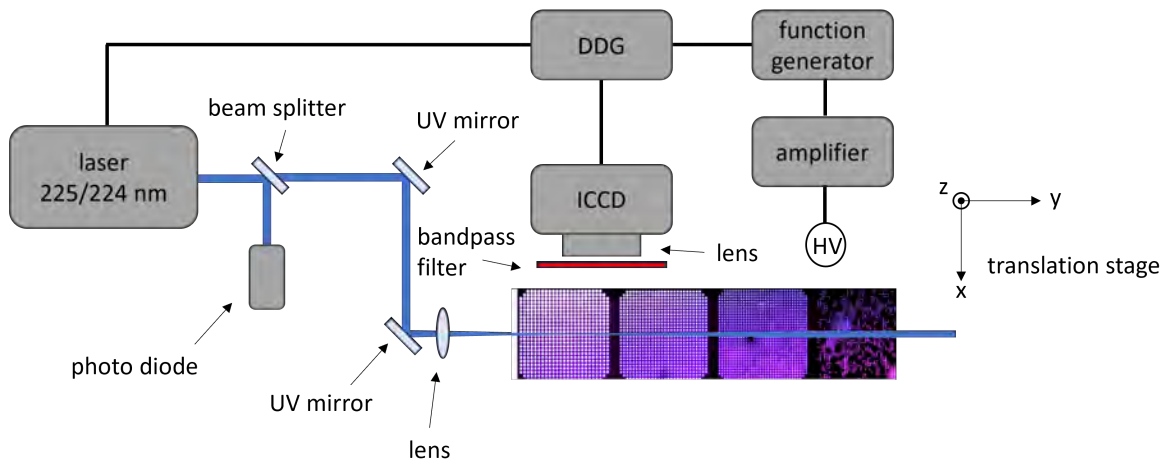
Figure 4.6: Schematic sketch of the setup for TALIF measurements. Adapted from [145].

applied in burst mode, generating 60 pulses per trigger signal, with the voltage remaining off until the next trigger. The digital delay generator also controls the burst mode start, allowing the voltage waveform to shift relative to the laser for temporal scans. The gas system is modified for TALIF measurements, utilizing a helium-oxygen mixture (95% helium / 5% oxygen) instead of individual gas bottles. Pure helium can be added to adjust the mixture. Gas flows are controlled with MFCs (MKS, GE50A). Xenon, which can be mixed with helium, is available for calibration.

As described in the fundamentals (section 3.3), the measured counts are normalized to the square of the laser intensity. A beam splitter is used for this purpose, which directs part of the beam onto a photodiode (ThorLabs, DET10A). The signal can be read out via an oscilloscope (Teledyne Lecroy, HDO6104). In addition, the oscilloscope can be used to monitor the voltage applied to the reactor and to monitor the synchronization of laser, camera and voltage. Furthermore, the energy of the laser is of particular importance for the measurement. On the one
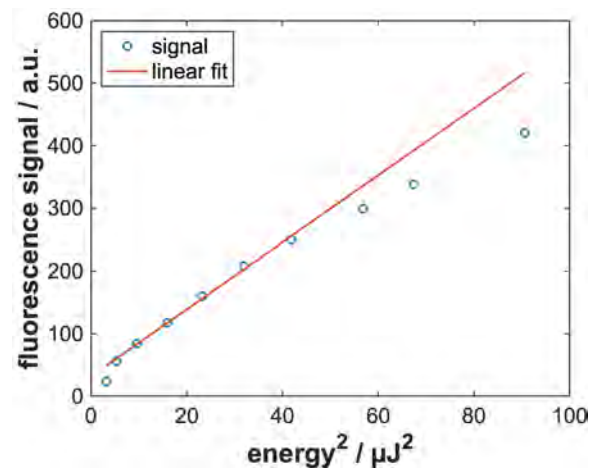

Figure 4.7: Fluorescence signal depending on the laser energy. Conditions: 1 slm total gas flow (He + 0.1% O_2); 700 V; gate time = 30 ns; exposure time = 60 s.

hand, this is incorporated quadratically into the measured signal and must therefore be permanently checked with the diode. On the other hand, too high energy can lead to effects such as photo-dissociation, resulting in atomic oxygen being produced only by the laser. To rule out these effects, the energy of the laser can be varied via the amplification of the laser and monitored with an energy meter (Newport 1919-R). If the resulting fluorescence signal is plotted against the square of the energy, a linear relationship should become visible. If the measurement deviates from this, for example due to saturation, undesired effects occur and the rate model used can no longer be applied. An example measurement is shown in Figure 4.7. Here, it is clear that there is a linear relationship at energies up to approximately $7\,\mu J$. At higher energies, the signal saturates.

Xenon calibration for the determination of absolute densities

In order to be able to measure absolute atomic oxygen densities with the TALIF setup described above, a noble gas calibration with xenon (see section 3.3) must first be carried out. The setup only needs to be changed minimally for this. The laser wavelength must be moved from $225.64\,\mathrm{nm}$ to $224.29\,\mathrm{nm}$. In addition, a different bandpass filter (Andover, 834.7/1.5-68381) is used to change the observed wavelength from 844.9 to $834.9\,\mathrm{nm}$. Traditionally, the calibration measurement is carried out in a vacuum chamber filled with xenon. In this work, however, xenon is added directly to the gas mixture, i.e. a helium/xenon mixture at atmospheric pressure is used. The mixing ratio is chosen in a way that the xenon density corresponds approximately to the expected oxygen density.

First, the constants required for calibration must be determined. The transmission T of the filters can be measured by means of the laser used here. The laser is set to the respective wavelength and the intensity is measured in front of and behind the filter. The wavelength-dependent sensitivity η of the ICCD camera can be found in the manufacturer's data sheet. The ratio of the excitation cross-sections can be found in the literature. A list of the constants used is given in table 4.1.

Since a ps laser is used, the temporal resolution is basically sufficient to measure the

Table 4.1: Parameters used for calibration.

Parameter	Value	Reference
optical branching ratio Xe a_{Xe}	0.003	[141]
optical branching ratio O a_O	admixture dependend	see section 6.1
sensitivity at 834.91 nm η_{Xe}	0.195	manufacturer
sensitivity at 844.87 nm η_O	0.180	manufacturer
transmission at 834.91 nm T_{Xe}	0.480	this work
transmission at 844.87 nm T_O	0.567	this work
spectral correction for xenon I_{Xe}	0.0277	this work
spectral correction for oxygen I_O	0.0219	this work
cross-section ratio $\sigma_{Xe}^{(2)}/\sigma_O^{(2)}$	1.9	[123, 146]
Xe density calibration m	2.34×10^{-10} cm^3	this work
Boltzmann correction β for 300 K	0.7417	this work

lifetime of the excited state directly and thus determine the branching ratio. For oxygen, the value is discussed as a function of the gas composition in chapter 6.4.1. In the case of xenon, however, the lifetime at atmospheric pressure is so short that it cannot be measured exactly with the setup used here (limited by 3 ns gate of the ICCD). For this reason, a literature value for a helium/xenon mixture at atmospheric pressure was used.

As already mentioned, the two-photon excitation cross-section is only defined for spectrally integrated signals. If only one single wavelength is used, it must therefore be corrected. For this purpose, the wavelength of the laser is varied in 2 pm steps and scanned over the respective central wavelength of the state. The TALIF signal is measured for each point. A measurement for the excitation of oxygen and xenon is shown in Figure 4.8. The measured maxima are only shifted by a few pm from the theoretical central wavelengths (O 225.64 nm, Xe 224.29 nm). This means that the wavelength calibration of the laser is very accurate. Due to fluctuations from day to day (e.g. due to temperature or humidity), the measurement is repeated daily and the wavelength is set to the maximum signal. The measurement shows an almost Gaussian line profile, indicating minimal collisional broadening (Lorentz profile). This Gaussian shape is likely due to the laser profile or Doppler broadening. Given the laser profile's
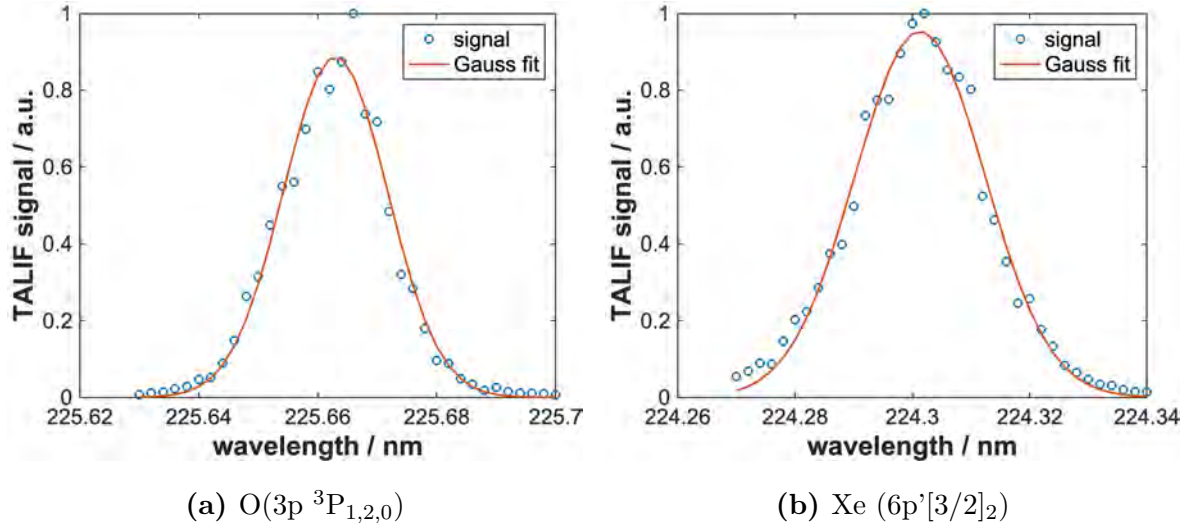
(a) O(3p ^{3}P$_{1,2,0}$)   **(b)** Xe (6p'[3/2]$_2$)

Figure 4.8: TALIF signal of oxygen (left) and xenon (right) depending on the laser wavelength. Conditions: 1 slm total gas flow (He + 0.1% O$_2$ / He + 0.1% Xe); 700 V; gate time = 30 ns; exposure time = 60 s.

FWHM of up to 38 pm (according to manufacturer), the resolution is insufficient to resolve individual oxygen sub-transitions. Consequently, the line appears as a single transition, limiting further analysis like temperature determination. However, due to the measuring position outside the cavity and within the gas flow, a temperature close to room temperature can be assumed. Thus, the Gaussian fit is used only to find the central wavelength and calculate the spectral correction factor.

The core of the calibration is the comparative measurement with a known xenon density. For this purpose, a helium/xenon gas mixture is used at atmospheric pressure and the mixing ratio is varied. For each admixture, 10 signals are recorded. Figure 4.9 shows the mean values and the standard deviation of the measurements as a function of the xenon density. At densities below 3x10^{17} cm^{-3} a clear linear relationship can be seen. This can be fitted and the slope used to calculate the calibration factor. At higher densities, however, saturation occurs. It can be assumed that the density is so high here that the laser intensity decreases due to the excitation of many atoms.

As described earlier, a two-dimensional signal is captured using an ICCD camera. This signal is influenced by the laser beam and the density of atomic oxygen. When the density is spatially uniform, the resulting signal fully illuminates the chip along the
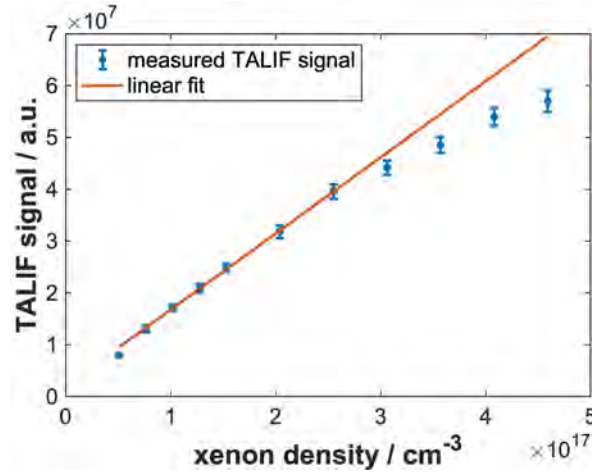
Figure 4.9: TALIF signal depending on the xenon density. Conditions: 1 slm total gas flow (He + Xe); discharge off; gate time = 30 ns; exposure time = 60 s.

y-axis (aligned with the laser's propagation path) and is shaped by the beam's profile width along the z-axis. Depending on the specific measurement, different sections of this imaged signal can be selected for analysis. To optimize the signal-to-noise ratio, it is beneficial to utilize as much of the fluorescence image as possible. However, spatial resolution can be enhanced by focusing on specific areas of the image, which may reduce the overall signal amplitude. Consequently, the xenon calibration process is tailored to the selected signal regions, ensuring consistent use of the sensor areas.

5 Fundamental discharge behavior

In the following chapter, the micro cavity plasma array is to be fundamentally characterized. Initially, electrical methods are used to determine parameters such as voltage, current, and power. These measurements, in turn, allow the derivation of parameters like discharge current, gap voltage, and transported charge. Optical measurements, on the other hand, provide insights into ignition times and the duration of discharges. The first objective of this work, to classify the discharge within a DBD mode, is to be achieved through these measurements. Subsequently, surface charges are observed to understand their influence on the discharge and to determine the achievable charge carrier densities. Additionally, it is examined whether surface charges can be externally influenced, for instance, by a laser, which addresses the second research question. The final section of this chapter focuses on the measurement of the electric field using the Stark broadening and shift of a helium line pair. This should answer the third research question concerning the spatial distribution of the electric field and how it is affected by charge carriers. The combination of these research questions should provide information on the extent to which the reactor is generally suitable for plasma catalytic applications and whether fundamental mechanisms of plasma catalysis can be investigated on the basis of the discharge with the diagnostics used here.

5.1 Determination of the discharge mode

This section should assign the discharge to a discharge mode known from the literature (see section 2.1.2 and table 2.1). This should enhance the understanding of the discharge dynamics and mechanisms within the micro cavity plasma array, and enable comparisons with other types of reactors. It is important to note that parameters such as current, voltage, charge, and emission detected by a photomultiplier can only be measured as an integration over the entire reactor. In the case of the micro cavity

plasma array, this means that thousands of individual cavities are considered as a single discharge entity. This complicates the evaluation of the measurements, as micro discharges within the different cavities overlap and cannot be individually distinguished. The complexity increases if a micro cavity plasma array with varying cavity diameters is used, since discharges with fundamentally different properties can occur simultaneously and overlap [28]. Therefore, a single array with a uniform cavity structure is utilized for the subsequent measurements to minimize these issues.

5.1.1 Voltage, current and emission

First, typical current, voltage and emission profiles are studied. In Figure 5.1 (a) this is shown for a ramp voltage excitation with an amplitude of 440 V. First, the period can be separated into two parts (dotted line): the increasing potential phase (IPP) and the decreasing potential phase (DPP). As can be seen from the emission, the discharge ignites once per phase, shortly after the zero crossing of the voltage. As soon as a reversal point of the voltage is reached, the discharge is extinguished. This fits very well with the classical DBD theory. As the voltage increases, the dielectric becomes more and more charged and thus compensates for the externally applied electric field. If the voltage is not further increased (or decreased), the resulting electric field in the discharge gap is not sufficient to maintain or re-ignite a plasma. Only when the external field points in the other direction (zero crossing) is it no longer compensated by the surface charges and re-ignition is possible. Again, it should be noted that the emission of the entire array is considered and individual cavities could ignite more frequently than once per phase, which is discussed in more detail later.

The current shows an almost rectangular shape. This can be explained by the displacement current which is determined by the derivative of the applied voltage. The deviations from the rectangular shape result mainly from deviations of the voltage signal, which is due to the used amplifier. Another deviation is caused by the discharge current. This becomes visible as an offset to the rectangular signal as soon as the plasma is ignited (see emission signal). When the plasma is extinguished, the current drops quickly. The difference in the decay time between current and emission can be explained by the integration time of the photomultiplier (a few µs). Differences be-
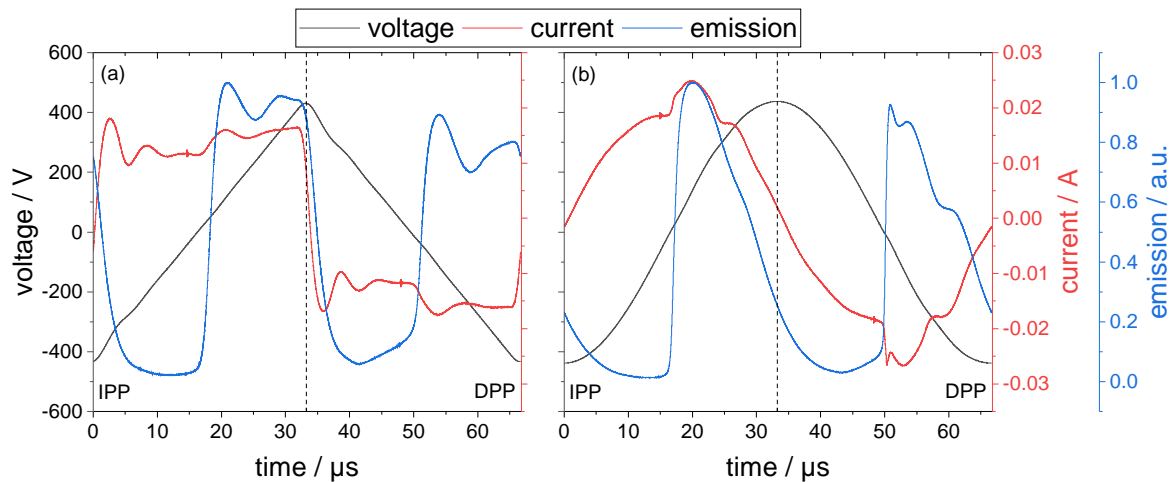
Figure 5.1: Voltage, current and emission characteristics for ramp (a) and sinusoidal (b) excitation. $V_{pp} = 880\,V$, $f = 15\,kHz$, $d = 200\,\mu m$, $950\,mbar$ helium atmosphere.

tween IPP and DPP can be identified in both current and emission, which is discussed later.

An additional measurement with a sinusoidal excitation is shown in Figure 5.1 (b). The basic discharge behavior does not change. However, there are fewer deviations of the applied voltage by the amplifier, so that the displacement current can be described by a cosine. Thus, the deviations due to the discharge current are clearly visible and match the measured emission very well. Especially in the DPP, it is even possible to reproduce individual peaks. Despite the lower interference from the amplifier, only a ramp excitation is to be used in the following. This has the advantage that the change in voltage (dV/dt) remains constant within a half-phase, which simplifies the understanding of the fundamental behavior. Moreover, the measurements can be compared with previous studies [22, 28, 147].

5.1.2 Power measurements

In addition to a qualitative discussion of the temporal characteristics, the measurement of current and voltage also offers the possibility of calculating quantitative parameters such as the dissipated power. As described in section 3.1.2, there are several ways to determine the power. On the one hand, the product of measured current and voltage can be integrated over a period. On the other hand, the charge can be measured over

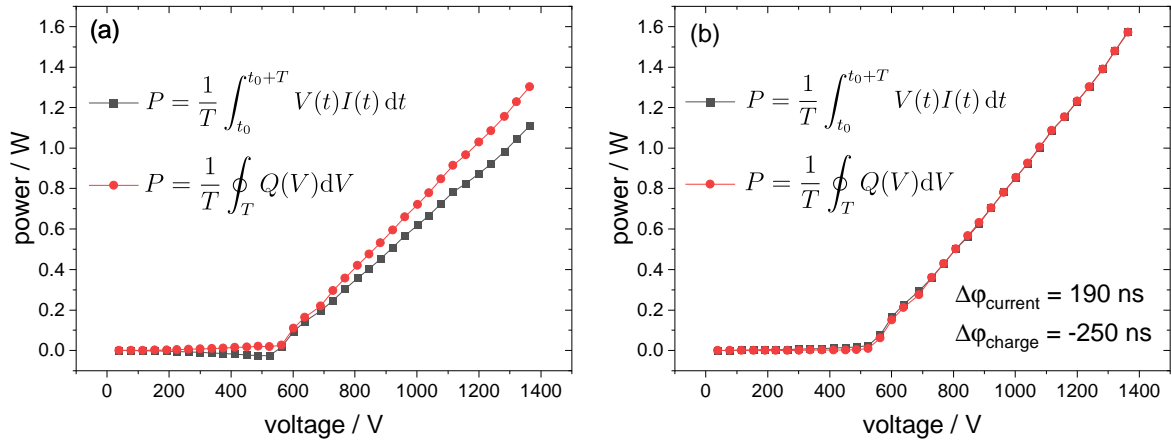a monitor capacitance to determine the power from the area of a QV-diagram.

Figure 5.2: Power depending on the applied voltage without (a) and with (b) corrected phase shift. Conditions: f = 15 kHz, d = 200 µm, 950 mbar helium atmosphere.

Figure 5.2 (a) shows a comparison of the two methods as a function of the applied voltage. It is striking that both curves differ from each other. The product of current and voltage initially becomes negative in the unignited case and then shows a lower slope than the evaluation of the QV-diagram. The difference can be explained by a phase shift $(\Delta\varphi)$ between the three measurements (voltage, current and charge) in the range of 200 ns. This can be caused, for example, by capacitances or inductances within the probes and must be corrected. In the unignited case, the reactor can be described as a capacitance, where the current corresponds to the displacement current and is 90° phase shifted to the voltage. Since the displacement current can be determined by the derivative of the voltage, the additional phase shift by the experimental setup can be determined by a comparison. This works similarly for the charge measurement, with the difference that it should be in phase with the voltage.

The corrected power measurements are shown in Figure 5.2 (b). Here, it appears that both measurements are aligned accurately. The phase shifts of current and charge with respect to voltage are 190 ns and -250 ns, respectively. If the plasma is not yet ignited at low voltages, no power is dissipated. From about 550 V the discharge ignites and the power increases linearly with the applied voltage.
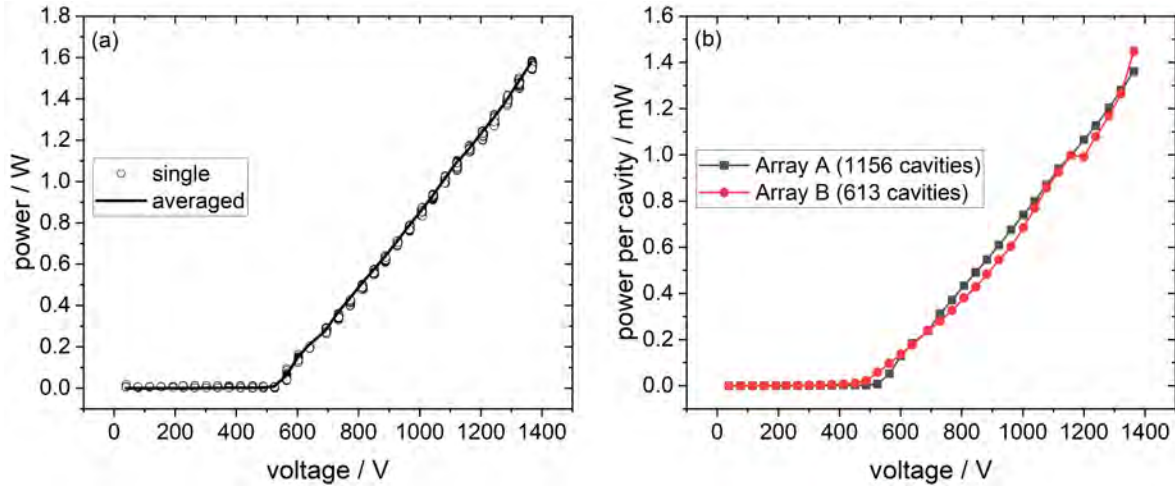
Figure 5.3: Power depending on the applied voltage with 40 single measurements per voltage (a) and power per cavity for different reactors (b). Conditions: f = 15 kHz, d = 200 μm, 950 mbar helium atmosphere.

Typically, the measured current, voltage and charge signals can be averaged directly on the oscilloscope. This has the advantage that even noisy signals can be evaluated, for example to determine the phase shift. The disadvantage is that individual features such as current pulses are also averaged out. However, these cannot be resolved in the reactor used anyway, since each measurement represents an integration over 1156 cavities. Nevertheless, it must be checked whether the averaging influences the power measurement. Figure 5.3 (a) shows a comparison between an averaged power measurement (400 periods) and 40 individual measurements as a function of voltage. Both measurements show exactly the same profile that is already known from Figure 5.2. The individual measurements scatter only slightly around the averaged measurement. The standard deviation is independent of the applied voltage and is approximately 0.01 W. It follows that the average percentage deviation can be up to 25% at low power levels, but drops to less than 1% at higher power levels. This means that the individual measurements vary only negligibly, so that averaging does not influence the result, but can provide smoother outcomes.

Power measurement is a particularly useful tool when comparing different reactors. As described above, there are single and quadruple structure cavity arrays. In addition, the number of cavities, size and spacing can vary. In order to check comparability,

two single array structures with the same cavity diameter but different numbers (1156 and 613 cavities) are therefore compared. The results are shown in Figure 5.3 (b). The measurement indicates that the absolute dissipated power is higher in the array with more cavities, as expected. However, the power per cavity is almost exactly the same in both reactors. This means that, on the one hand, the method of power measurement is reproducible even with different reactors. On the other hand, it also shows that the individual cavities and even different reactors deliver very comparable and reproducible results and that the power is very strongly related to the number of ignited cavities. This means that the number of ignited cavities should be known for power measurements and generally for measurements that integrate over the entire reactor. Otherwise, the dissipated power is related to a too large volume and could therefore appear smaller per cavity than it actually is.

5.1.3 QV-diagram evaluation

By measuring the charge via a monitor capacitance, in addition to determining the power, a QV-diagram can be created. An example is presented in Figure 5.4. The diagram shows a measurement at a voltage amplitude of 700 V. It is noticeable that no classical parallelogram is formed, but the Lissajous figure is rather almond-shaped. This can be attributed to the s-DBD character of the micro cavity plasma array. Here, the capacitance and thus the slope of the diagram changes within one period (see section 3.1.2). Furthermore, it is noticeable that the ratio of surface area to circumference is small compared to Lissajous figures known from

Figure 5.4: Example of a QV-diagram including determination of power and fitting of capacitances. Conditions: $V_{pp} = 1400\,V$, $f = 15\,kHz$, $d = 200\,\mu m$, 950 mbar helium atmosphere.

the literature [85, 88]. This has several causes. Firstly, the micro cavity plasma array is only operated with low voltage amplitudes up to 800 V, while other DBDs use volt-
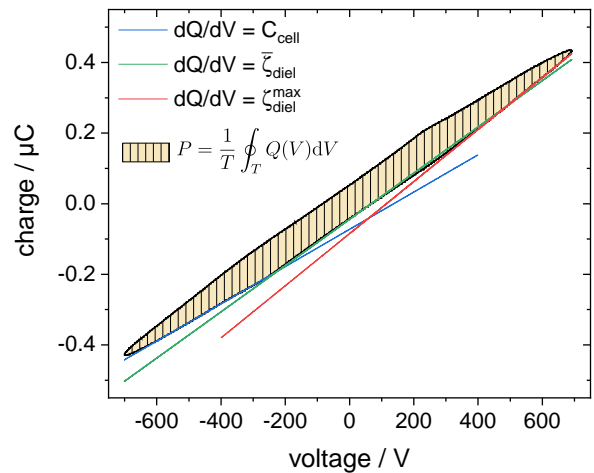
ages up to $100\,\text{kV}$. This leads to larger discharge currents or charge transport and thus to a larger area and power. On the other hand, the capacitances in the ignited and unignited case do not differ very much from each other. The difference is determined by a short circuit of C_{gap} (see equation 3.5). In the case of the micro cavity plasma array, however, C_{gap} plays only a minor role, since the cavities that represent the gas gap only account for a part of the total electrode. Increasing the ratio of cavity area to electrode area would change the QV-diagram.

Despite the small area, the QV-diagram can be evaluated to determine the capacitances C_{cell} and ζ_{diel} by linear fits. Due to the almond shape, no clear edge can be seen when the discharge is ignited. However, since C_{cell} must be determined during the passive phase, several methods can be employed to establish the fitting limits. One approach is to initially fit only a few data points and then examine the voltage at which the plot deviates from a straight line. Alternatively, the ignition point can be identified using emission or discharge current measurements. If the active phase can be separated from the passive phase, the capacitances C_{cell} and ζ_{diel} can be determined for the respective voltages (see Figure 5.4). Due to the fact that the capacitance ζ_{diel} changes with the voltage, unlike in an ideal DBD, it makes sense to specify a value of $\bar{\zeta}_{diel}$ averaged over the active phase. In addition, the value ζ_{diel}^{max} can be considered, which only includes the range of the maximum slope. For the sake of clarity, the fits (colored lines) are only shown for the IPP, but can also be carried out the same way for the DPP.

Capacitances

The capacitances C_{cell} and ζ_{diel} can be determined using the QV-diagram (see Figures 3.1 (a) and 5.4). The result is shown in Figure 5.5 as a function of the applied voltage. For voltages between 0 and $524\,\text{V}$, the discharge is not yet ignited. Since no power is dissipated, it follows that the QV-diagram represents a straight line and not a parallelogram. In reality, however, there are small losses so that the power is not exactly zero and a parallelogram with a very small area is created. The capacitance of the reactor C_{cell} can be determined by a linear fit of the passive phase. This can be done for both IPP and DPP. Both curves match each other very well. In the unignited case, the capacitance is constant at $0.44\,\text{nF}$. When the discharge is ignited, the capacitance

jumps to $0.48\,\mathrm{nF}$ and then continues to grow linearly with the voltage to $0.56\,\mathrm{nF}$. Since C_{cell} only depends on C_{gap} and C_{diel}, i.e. the materials and the geometry of the reactor, the value should be voltage-independent according to theory. However, an increase in C_{cell} is known from the literature [85, 88], but could not yet be conclusively explained, whereby temperature effects were excluded [85]. Since C_{cell} depends only on C_{diel} and C_{gap}, but C_{diel} is only material and geometry dependent, the effect can be attributed to C_{gap}. It is assumed that charges from the previous discharge remain in the gap. This space charge zone forms a plasma sheath to the surrounding surfaces, which can act as a parallel capacitance to C_{gap} [83]. The theory is supported by the fact that the emission and plasma current decay only slowly after the reversal point of the voltage (see section 5.1.3). The higher the voltage, the greater the effect on C_{cell}, since the temporal share of the previous discharge in the passive phase is increased. For this reason, the plasma unaffected capacitance $C_0 = 0.44\,\mathrm{nF}$ is introduced here (see Figure 5.5).
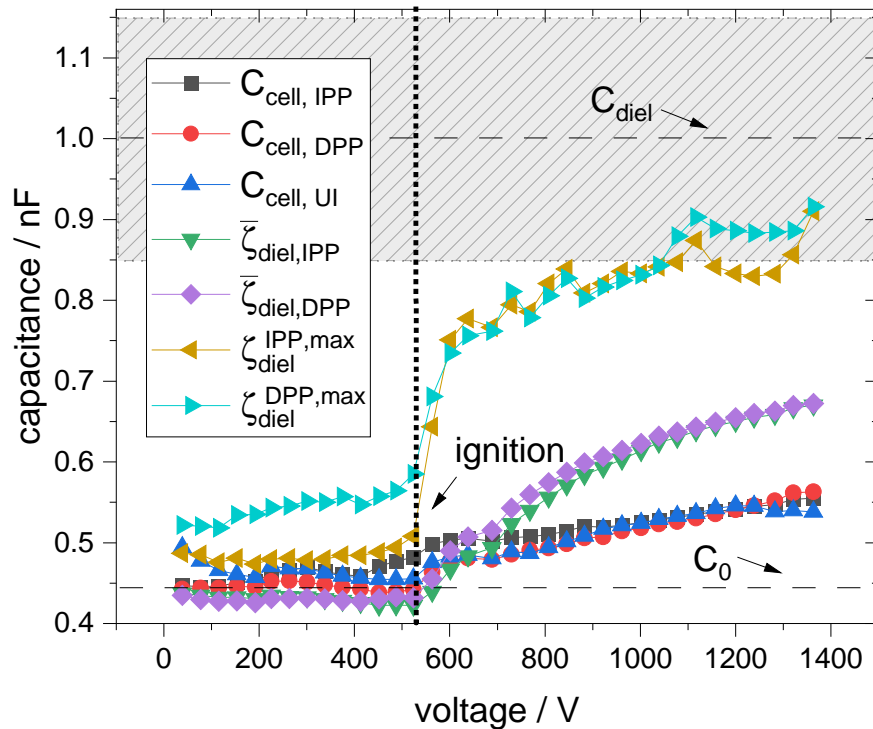
Figure 5.5: Capacitances as a function of the applied voltage. Conditions: $\mathrm{f} = 15\,\mathrm{kHz}$, $\mathrm{d} = 200\,\mathrm{\mu m}$, $950\,\mathrm{mbar}$ helium atmosphere.

An alternative way to determine C_{cell} is to compare the measured current with the time

derivative of the applied voltage. In the unignited case, there is no discharge current, but only displacement current, which depends directly on C_{cell}. The calculated values are also shown in Figure 5.5 (marked with $C_{cell,UI}$) and show good agreement with the results from the linear fits.

As described in section 5.1.3, two different values for ζ_{diel} can be determined from the QV-diagrams. On the one hand, the value $\bar{\zeta}_{diel}$ averaged over the entire active phase and, on the other hand, the maximum value ζ_{diel}^{max} at the end of the active phases. Both values can be determined for the IPP and DPP respectively and are again plotted in Figure 5.5. In the unignited case, all values are close to the C_0 value. This was to be expected, as there is no active phase in this case and the QV-diagram is a straight line. However, there are slight deviations because, as previously discussed, there are minor losses even without discharge. With ignition, there is a clear difference between $\bar{\zeta}_{diel}$ and ζ_{diel}^{max}. $\bar{\zeta}_{diel}$ rises very smoothly and approaches a value of $0.68\,\mathrm{nF}$. ζ_{diel}^{max}, on the other hand, rises much more steeply and approaches a value of $0.92\,\mathrm{nF}$. It is noticeable that the values for ζ_{diel}^{max} are noisier than those of $\bar{\zeta}_{diel}$, since the linear fit was formed over a smaller range. It seems that the capacities at $1360\,\mathrm{V}$ are not yet fully saturated. However, higher voltages could not be applied for experimental reasons. Overall, it can be seen that ζ_{diel} is slightly larger in the DPP than in the IPP. This means that the gas gap is more conductive. This fits very well with the known behavior of micro cavity plasma arrays. In the IPP, the electrons move from the cavities to the edges and into the area above the cavity, creating a relatively diffuse plasma. In DPP, on the other hand, the electrons move into the cavity, causing the discharge to fill the gas gap in a very concentrated way, which leads to higher conductivity.

According to theory, ζ_{diel} should approach the capacity C_{diel}. However, the determination of C_{diel} is not trivial in the case of a complex reactor geometry such as that of the micro cavity plasma array. In the simplest case, C_{diel} can be estimated as for a plate capacitor with known electrode area A, dielectric thickness d and relative permittivity ϵ_r:

$$C_{diel} = \epsilon_r \epsilon_0 A/d = 0.96\,\mathrm{nF} \tag{5.1}$$

Here, however, it is neglected that the powered and grounded electrodes have different

sizes and only the smaller grounded electrode is included. If the complex geometry is to be included, an approximation from the literature can be used [148]. In this case, the larger electrode is considered to be infinitely large. However, it is assumed that the finite electrode has an area of $A = \omega \cdot l$, where ω and l are the edge lengths. In the case of the micro cavity plasma array, however, the electrode is round (diameter = 1.6 cm), so the edge lengths are transformed to $\omega = l = 1.42$ cm. The constant c is the speed of light under vacuum.

$$C_{diel} = \frac{\epsilon_r l \left[\frac{\omega}{d} + 1.393 + 0.667 \cdot \ln\left(\frac{\omega}{d} + 1.444\right)\right]}{120\pi c} = 0.98 \, \text{nF} \qquad (5.2)$$

It is clear that the capacitance with both approaches barely differs and is around 1 nF. However, the cavities located in the electrode were neglected in both calculations. Furthermore, the dimensions used are subject to uncertainties. On the one hand, the manufacturer of the ceramic foils states an uncertainty of the thickness of 5-10%. On the other hand, the reactor is assembled by hand, so deviations in the distances can occur due to inaccuracies or dust particles. Therefore, a total uncertainty of 15% is assumed. Both, the value for C_{diel} and the confidence interval (grey marked area), are shown in Figure 5.5. It can be seen that ζ_{diel} is very close to C_{diel} at high voltages, taking into account the error interval, which means that almost all gas gaps are short-circuited.

Discharge surface covering

By determining the capacities C_{diel}, C_{cell} and ζ_{diel}, the parameters α and β can now be determined (see equation 3.16 and 3.17). The value of β indicates which part of the electrode is covered with plasma, i.e. to what extent the gas gap is conductive. The advantage of the micro cavity plasma array is its accessibility for optical diagnostics. With the help of an ICCD camera, the propagation of the plasma can be verified. Typically, only a few cavities ignite at low voltages. As the voltage is increased, more and more cavities are added until the array is fully ignited. This can be explained by irregularities in the structure of the array. If the metal grid is not perfectly parallel to the dielectric, for example due to dust particles or inaccurate positioning, the electrode gap varies slightly from cavity to cavity and thus also the ignition voltage. Such a measurement is shown in Figure 5.6 (a). At low voltage of 540 V, individual cavities
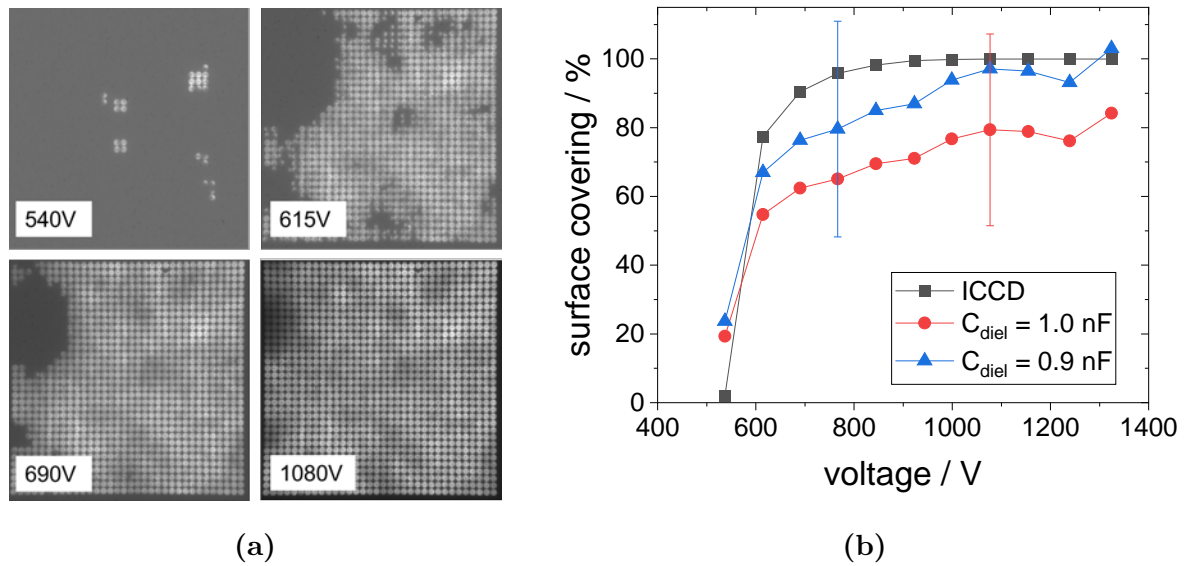
(a)

(b)

Figure 5.6: Surface covering depending on the applied voltage determined by ICCD images (a) and QV-plot evaluation (b). Conditions: f = 15 kHz, d = 200 μm, 950 mbar helium atmosphere.

ignite. If the voltage is increased, the plasma spreads out. However, it is noticeable that there are areas in which many neighboring cavities do not ignite, such as in the upper left corner. This can be attributed to a slight bump in the metal grid. Only at voltages above 1000 V all cavities are ignited.

By evaluating the camera images, a measure of surface covering can be found. Using a script that separates the cavities from the background and detects the ignition, the number of ignited cavities can be determined. This evaluation is plotted against the applied voltage in Figure 5.6 (b). It shows that the surface covering increases with the voltage until all cavities are ignited and the curve saturates at 100%. This result can now be compared with the evaluation of the QV-diagrams. For this purpose, the capacitances C_{cell} and ζ_{diel}^{max} are determined for each voltage and the parameter β is calculated. As discussed before, the value C_{diel} used for this is difficult to determine and has an uncertainty of 15%. Furthermore, the linear fits performed also have uncertainties. For C_{cell}, the uncertainty is 5%. For ζ_{diel}^{max}, on the other hand, a smaller voltage range is used for the fit, which increases the uncertainty to 10%. The confidence interval can be calculated from the uncertainty propagation and lies between 30-40%.

The results are also plotted in Figure 5.6 (b). The red curve shows the values for $C_{diel} = 1\,\text{nF}$ and the blue curve for $C_{diel} = 0.9\,\text{nF}$. Both curves reproduce the profile measured with the ICCD camera very well, whereby the absolute values with $C_{diel} = 0.9\,\text{nF}$ show better agreement. As previously discussed, the error bars are very large and are only drawn at two points for the sake of readability. Even though both curves reproduce the measurement of the ICCD camera taking into account the errors, the result suggests that C_{diel} is $0.9\,\text{nF}$ rather than the previously calculated $1\,\text{nF}$. Nevertheless, finally it is not possible to determine an exact value for C_{diel}. On the one hand, the calculation gives only an upper limit due to the neglect of the cavities, thus a value of $C_{diel} = 0.9\,\text{nF}$ seems realistic. On the other hand, it seems that the curves are not yet completely saturated. This would imply that β continues to grow at higher voltages and in the case of $C_{diel} = 0.9\,\text{nF}$ would take on values above 100%. This would again suggest a value of $C_{diel} = 1\,\text{nF}$. In addition, the camera measurement must also be discussed. Here, a distinction can only be made between ignited and non-ignited cavities. In reality, however, the plasma density and thus also the conductivity changes with the applied voltage. This cannot be resolved with this measurement and could also explain the deviations of the profiles.

In conclusion, the good agreement between optical and electrical measurements is a great success and offers many possibilities for future applications. In plasma catalysis, diagnostics can help determine the plasma coverage of a catalytic surface. As upscaling can result in more complex geometries and thus limited optical access, camera measurements are no longer possible. QV-plot evaluations can provide a valuable alternative here. Moreover, the measurements show that the estimation of $C_{diel} = 1\,\text{nF}$ is justified, allowing the parameters α and β to be used for further evaluations, such as gap voltage or discharge current.

Gap voltage, discharge current and transported charge

In addition to the surface covering, the gap voltage, the discharge current and the transported charge can also be calculated with the help of the determined capacitances. The results are exemplary shown in Figure 5.7. All curves shown are from a simultaneous measurement of voltage, current, charge and emission, including an evaluation of the
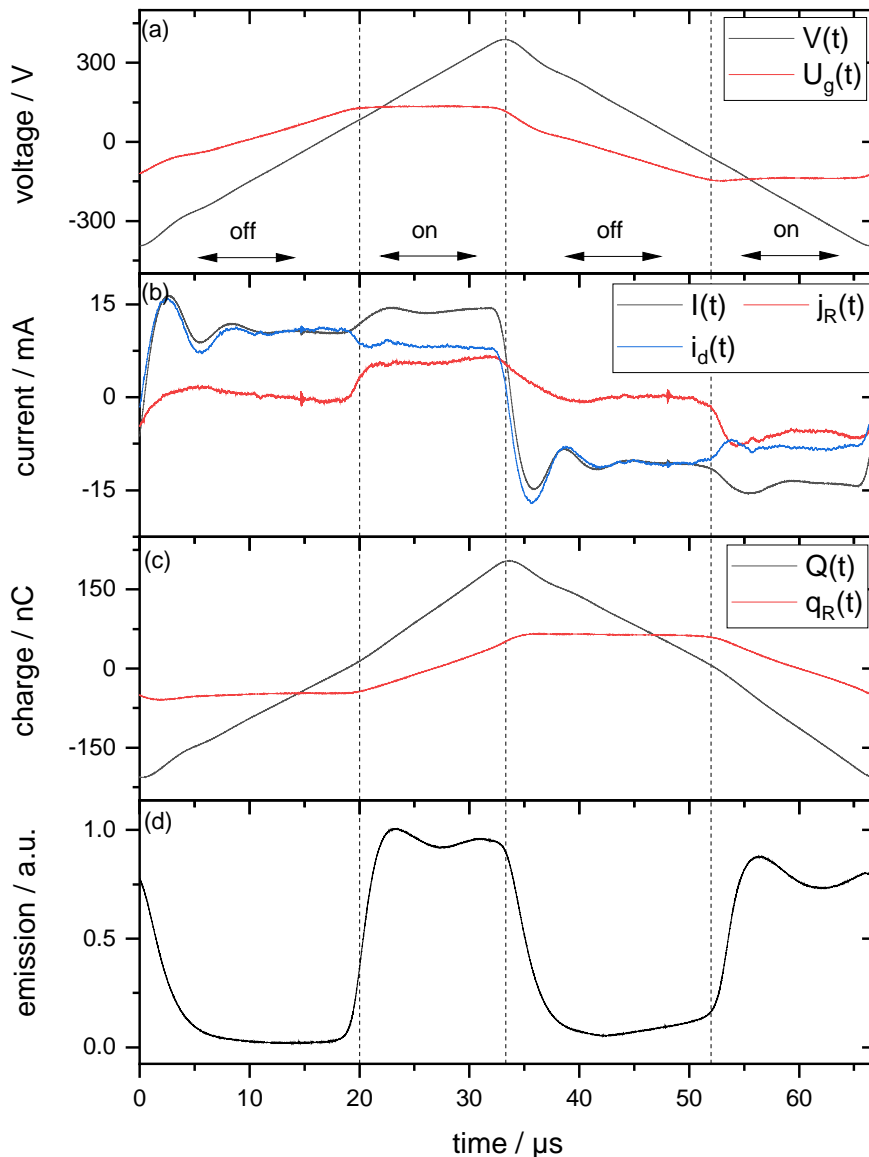
QV-plot.

Figure 5.7: Voltage, current, charge and emission characteristics. $V_{pp} = 780\,\text{V}$, $f = 15\,\text{kHz}$, $d = 200\,\mu\text{m}$, $950\,\text{mbar}$ helium atmosphere.

The first plot (Figure 5.7 (a)) compares the applied voltage $V(t)$ with the calculated gap voltage $U_g(t)$, which takes into account the shielding by surface charges. The areas where the discharge is on or off can be determined using the emission. It is noticeable that the gap voltage follows the applied voltage in the phases without discharge. However, as soon as the plasma ignites, the voltage remains constant. This fits perfectly with the classical DBD theory. The plasma current deposits charges on the dielectric which counteract the external field. Only by increasing the external voltage the result-

ing electric field can be kept constant. When the external voltage is reversed, the gap voltage drops as well. The slope is lower than that of the external voltage, since there is still an influence of the surface charges.

The next plot (Figure 5.7 (b)) compares the measured current $I(t)$ with the discharge $j_R(t)$ or displacement current $i_d(t)$ calculated from the QV-diagram. Although the displacement and discharge current were determined independently, the sum of the two is fairly close to the measured current. In the unignited case, the displacement current (determined by the change in external voltage) is equal to the measured current because there is no discharge current. With a ramp voltage, this current would result in a square wave signal. Small deviations in the voltage caused by the amplifier result in differences from this shape, such as a peak at the beginning. The ignition of the plasma is indicated by an increase in the discharge current, which also shows up as an offset in the measured current. Here, the displacement current deviates from the square wave form as well, since it is influenced by the shielding charges. The discharge current remains quite constant with a slight dip in the middle of the active phase. When the polarity of the voltage is reversed, the current does not disappear immediately, contrary to expectation. A slow exponential decay is visible over a few µs. This means that charges continue to be transported in the same direction as before. It could imply that the surface charges do not fully compensate for the external field. This also fits to the measurement of the gap voltage, which does not show a different polarity directly after the reversal point. Furthermore, the emission (Figure 5.7 (d)) shows a slow decay (approximately 6 µs), which is not exclusively due to the decay time of the photomultiplier (approximately 1 µs). Since the decay of the discharge extends into the actually passive phase, the measurement of C_{cell} is influenced, which can lead to an increase at high voltages.

The third plot (Figure 5.7 (c)) compares the directly measured charge $Q(t)$ with the calculated charge moved through the volume onto the surface $q_R(t)$. Again, the expectations from the classical DBD theory are fulfilled. As soon as a plasma current is present, charges are transported towards the surface, where they build up. Since the discharge current is constant, the charge buildup is linear. Once the discharge is

extinguished, the charge remains constant. Only when the discharge is ignited again, the charges are reduced again, or the surface is charged with the other polarity.

In the measurements shown, a relatively low voltage of 780 V was used. The discharge behavior changes significantly at higher voltages. Figure 5.8 shows a comparison of the measurements with voltages between 600 and 1400 V.
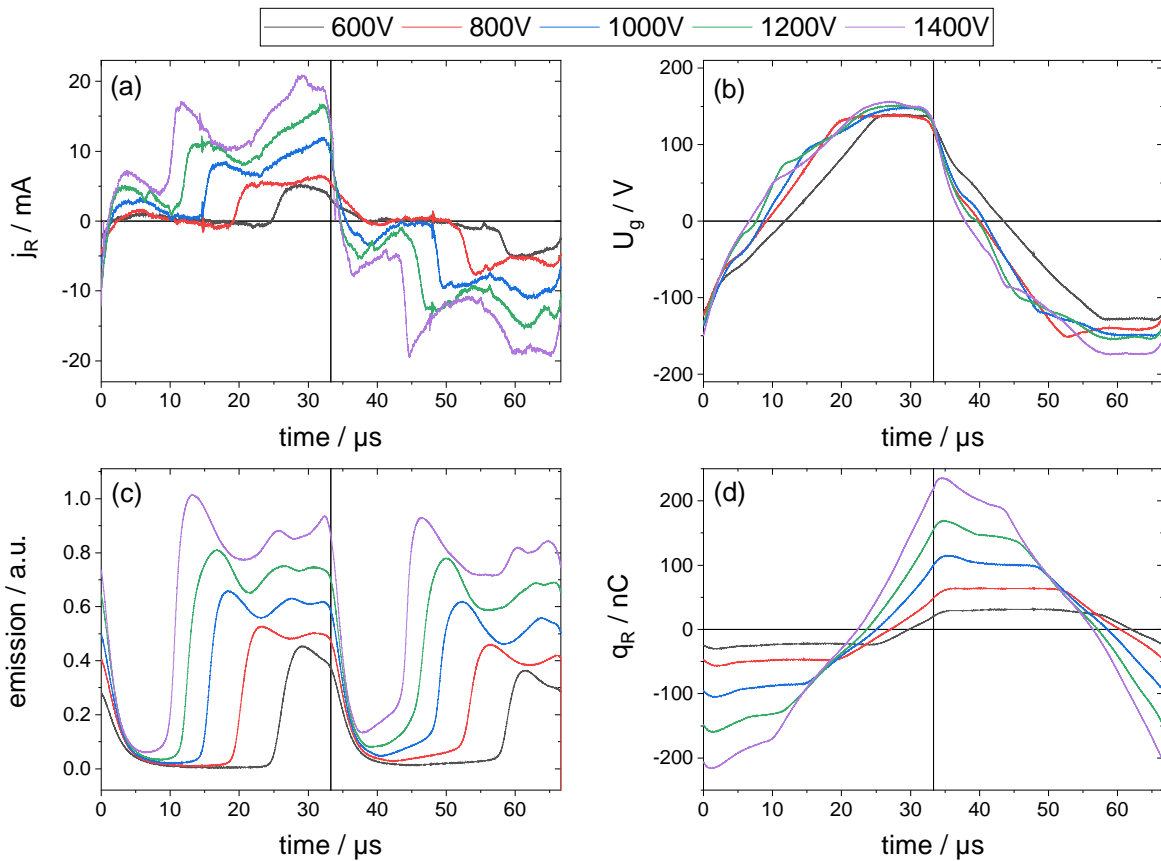

Figure 5.8: Discharge current (a), gap voltage (b), emission (c) and charge (d) depending on the applied voltage. Conditions: $f = 15\,\text{kHz}$, $d = 200\,\mu\text{m}$, 950 mbar helium atmosphere.

The most significant difference is visible in the discharge current (Figure 5.8 (a)). With higher voltage, the discharge ignites earlier within the period, since the ignition voltage is reached more quickly. In addition, the amplitude of the discharge current increases from 5 mA to up to 20 mA. The previously described dip in the middle of the active phase becomes more pronounced with increasing voltage, so that two maxima per half phase become clearly visible. The higher the applied voltage, the faster the discharge

current decays after the reversal point. From 1000 V, the discharge current does not only decay but even changes its direction. This phenomenon is known as back discharge. Here, the field induced by the surface charges from the previous discharge becomes so large that charges are accelerated in the opposite direction or even a new discharge can ignite. This effect can also be seen in the photomultiplier signal (Figure 5.8 (c)), where the emission increases already before the actual ignition, or does not drop to zero.

The effect of longer discharge is also visible in the gap voltage (Figure 5.8 (b)). However, the gap voltage does not saturate immediately upon ignition as is the case with small voltages. Initially, the slope of the gap voltage flattens out. Only later in the active phase does the voltage become constant. This indicates that at higher voltages the surface charges are initially not sufficient to completely compensate for the external voltage and that equilibrium can only be achieved during the course of the discharge. For all voltages used, the maximum is about 150 V. This agrees with measurements of the electric field. Here, the field is also independent of the applied voltage [28].

Another difference for higher voltage becomes apparent in the charge (Figure 5.8 (d)). This is no longer constant at higher voltages in the passive phase, but forms a peak. After that, the charge decays slowly until a constant value is reached again or, at very high voltages, the next discharge is ignited directly. Interestingly, the maximum charge is reached after the reversal point of the voltage. This can be explained again by the continuing gap voltage, which is sufficient to transport volume charges further through the gas gap. If no back discharge takes place, the charge slowly decays as charge carriers diffuse in the volume or recombine and the external field becomes smaller and smaller and at some point is no longer sufficient for transport. Then, only the surface charges remain until the next ignition.

A sketch describing the various contributions of the charges is shown in Figure 5.9. The part of the surface charge is shown in light grey and the part of the volume charge in dark grey. For comparison, the measured total moved charge and the calculated gap voltage are also shown. Here it is particularly clear that the surface charge remains
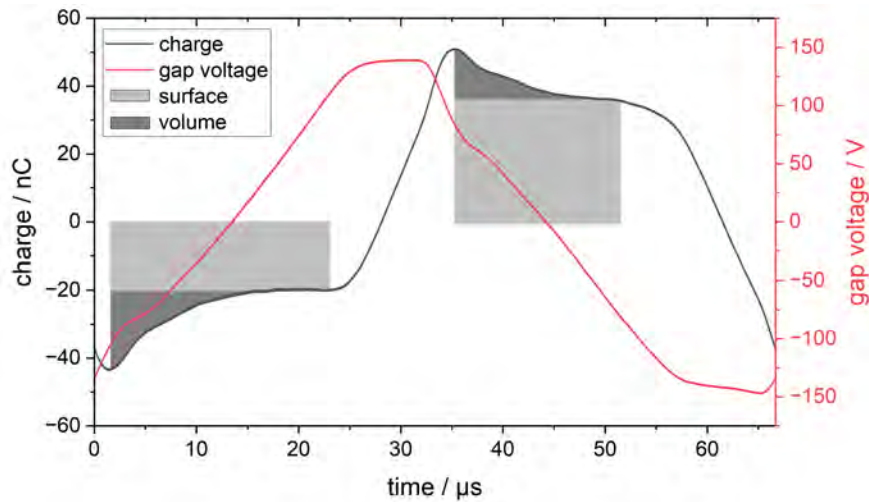
Figure 5.9: Sketch of the assumed contributions of surface and volume charge to the measured charged. Conditions: $V_{pp} = 690\,\text{V}$, $f = 15\,\text{kHz}$, $d = 200\,\mu\text{m}$, 950 mbar helium atmosphere.

constant after the discharge has expired, while the volume charges drop exponentially with a decay time of approximately 6 µs. This behavior is almost identical for both half-phases, although a shift of the absolute charge amplitude to positive charges can be seen. This could be attributed to the geometry of the reactor, but is not fully understood.

The emission also changes with the voltage (see Figure 5.8 (c)). As already described, the ignition times shift further and further forward. In addition, there is the effect of the back discharge, so that the discharge hardly extinguishes and is almost permanently ignited. During the active phase, several peaks can be detected in the emission. As with the discharge current, it must be noted here that the signal is integrated over thousands of cavities. This means that individual discharge pulses cannot be resolved. However, the result shows that the discharge exhibits a global pulsing behavior.

5.1.4 Modeling of power profiles

As described above, the power in the case of the single array is almost perfectly linearly dependent on the applied voltage. This is consistent with the theory of ideal volume DBD (v-DBD), where the dependence of the power on the applied voltage follows from a geometric view of the QV-plot [84]. Here, C_{cell} and C_{diel} are constant for each voltage

and the discharge always ignites with the same ignition voltage V_0. This means that all sides of the parallelogram can be described and the area or the dissipated power is only dependent on the applied voltage V and frequency f, resulting in a linear curve [149]:

$$P = 4f(C_{diel} - C_{cell})V_0(V - V_0) \tag{5.3}$$

However, the reactor consists of many individual cavities, so the linear behavior must be questioned. Even if a combination of many different linear processes would result in an overall linear process, it is known from the previous measurements that the ignition times of the individual cavities are different. This means that the number of ignited cavities initially changes significantly with the applied voltage. As it was previously shown that the power is directly proportional to the number of cavities (see section 5.1.2), a non-constant slope would have been expected. For this reason, the dependence of the power should be examined in more detail.

An exemplary power measurement as a function of the voltage is shown in Figure 5.10. Here again the linear dependence is dominant. However, there is a slight deviation from this behavior at low voltages. This deviation can be explained by the already discussed surface covering (see section 5.1.3). At low voltages, scattered cavities initially ignite. As the voltage increases, more and more cavities are added until at some point all cavities are ignited. If the measured power is multiplied by the fraction of ignited cavities, it becomes clear that the deviation from
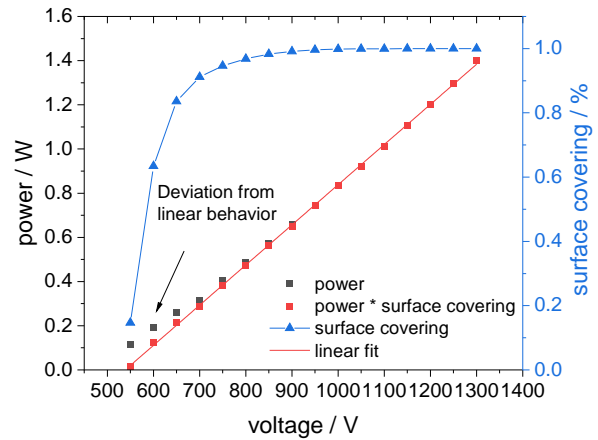

Figure 5.10: Power and surface covering depending on the applied voltage. Conditions: f = 15 kHz, d = 200 µm, 950 mbar helium atmosphere.

linear behavior disappears. It can be concluded that the individual cavities and thus also the combination of many cavities exhibit linear behavior, like a classic volume DBD. However, if the number of cavities or the discharge expansion changes with the voltage, deviations arise that are reminiscent of the behavior of a surface DBD.

The behavior of surface DBDs (s-DBD) is very different. In this case, profiles are often observed that deviate significantly from a linear behavior and are frequently described in the following form [150]:

$$P = A(V - V_0)^n \tag{5.4}$$

Here, A and n are interdependent parameters, with n typically lying between 2 and 3. This behavior can be explained by the fact that the geometric considerations of the ideal DBD no longer apply to an s-DBD. It is true that C_{cell} is also constant in this case. However, C_{diel} is time and voltage dependent, as the discharge can spread across the surface.

An approach that attempts to solve the problem of time depended capacitances in order to describe the power dependence of s-DBDs on the applied voltage was presented by *Pipa et al.* [151]. Here, the equivalent circuit approach is extended. The used circuit consists of the elements typical of DBDs (see section 3.1.2), but with the difference that these are represented as multiple identical and sequential elements in order to take the expansion of the discharge into account. It is concluded that the active phase of the discharge can be described as follows:

$$Q = \alpha(V^2 - V_0^2) + C_{cell}V \tag{5.5}$$

In addition to the parameters already described, the parameter α is used to consider the properties of the dielectric. The idea of the approach is to approximate the curved shape of the active phase of the QV-plot (e.g. almond shape) in order to be able to determine the power geometrically again:

$$P = \frac{\alpha}{3}V^2(V - V_0) \tag{5.6}$$

Figure 5.11 shows the different models in comparison to the measurement data in the micro cavity plasma array. In addition, micro scaled plasma trenches (MSPT) were investigated. These differ from the normal cavity structure, as a larger plasma volume is possible here, which leads to higher overall power. Due to the larger electrode area, a more pronounced s-DBD characteristic can be assumed.
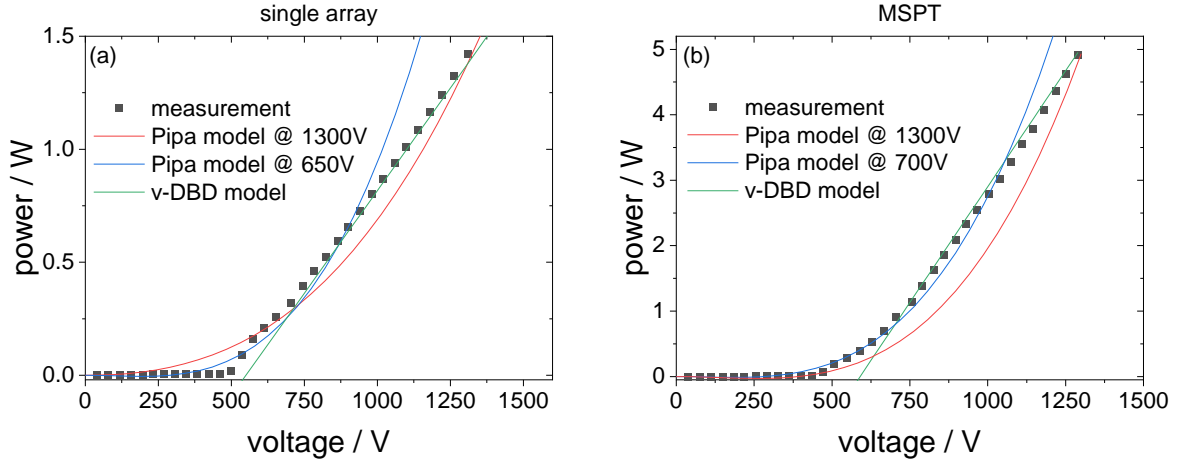
Figure 5.11: Power as a function of the applied voltage for a single cavity structure array (a) and a MSPT structure array (b) in comparison with a v-DBD and s-DBD model. f = 15 kHz, d = 200 µm, 950 mbar helium atmosphere.

The linear model of the ideal v-DBD and the non-linear model that approximates the almond-shaped QV-plot of an s-DBD were used. The parameters required for the models were determined in each case from the QV-plot. However, the voltage at which the QV-plot is evaluated must be discussed. For the v-DBD model, it is assumed that the capacitances C_{cell} and C_{diel} are constant for all voltages. As shown in Figure 5.5, this is not the case for the micro cavity plasma array. In addition, the slope of the active phase changes over time, as it is usual for an s-DBD, thus it is not clear which slope has to be chosen exactly. The best agreement with the measured data is achieved for both, the cavities and the trenches, for the voltage above which almost no cavities are added (single array: 750V, MSPT: 700V). The average capacitance $\bar{\zeta}_{diel}$ was used in each case.

In the literature, the s-DBD model is typically applied to the highest applied voltage. At this point, the model can reproduce the power very well. However, this approach tends to underestimate power at lower voltages. Conversely, when the QV-plot is evaluated at a lower voltage, where not all cavities have ignited, the model can better capture the curve's shape at these lower voltages. Nonetheless, this adjustment leads to an overestimation of power at higher voltages.

Overall, single array and MSPT show comparable results. For both reactors, it can be concluded that they initially behave at low voltages like an s-DBD. Here, a higher volt-

age leads to an expansion of the plasma along the surface (see Figure 5.12). This can be the ignition of new cavities (macroscopic) as well as expansion within the cavities or trenches (microscopic). However, the potential discharge expansion is limited due to the small geometric dimensions. Once the entire surface is covered, both reactors behave like a v-DBD. In this case, the discharge can only spread in the direction of the cavity volume.

The main difference between the two reactors is the area that can theoretically be covered by the discharge. In the case of the MSPT, the larger surface area means that the s-DBD characteristic persists for higher voltages than with the cavities and thus becomes more pronounced. The same effects are also observed for the typically used quadruple array structure with different cavity diameters in one reactor (not shown here). Accordingly, the models can provide a simple picture that reflects a combination of v-DBD and s-DBD characteristics. However, both approaches only work for very specific parameters, thus direct measurements are recommended over the model for application.
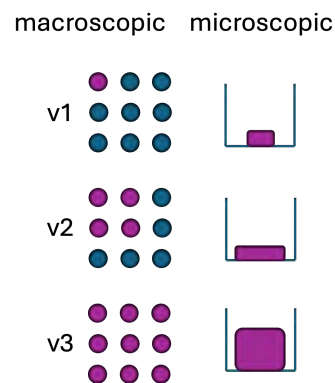

Figure 5.12: Sketch of macroscopic and microscopic discharge propagation depending on voltage (v1<v2<v3).

The main reason for the deviation of the models lies in the QV-plots used. A perfect parallelogram with voltage-independent slopes is assumed for the v-DBD model. In the s-DBD model, on the other hand, an almond-shaped QV-plot is fitted. In reality, however, the measurements available here are more likely to be described as a hexagon. The passive phase is again described by C_{cell}. The active phase initially starts with a capacitance ζ. Towards the end of the active phase, the capacitance is increased again to ζ_{max}, creating a third side. Due to the symmetry of IPP and DPP, a hexagon is formed in which the opposite sides are parallel. The observation of two different slopes in the active phase matches the observations of emission and current, in which, in addition to an ignition peak, a further peak was also visible at the end of the

discharge (see Figure 5.8). One possible explanation could be that the volume or surface DBD mode is not only dependent on the voltage amplitude, but that both modes can be observed simultaneously within a half-phase. When a single cavity is ignited, the discharge initially spreads along the dielectric. Once the surface is covered, the discharge can only spread in the direction of the volume. Depending on the voltage amplitude applied, the critical voltage at which the surface is completely covered is reached faster in time. With large voltage amplitudes, this means that the s-DBD characteristic only accounts for a small fraction of the total period and therefore the v-DBD characteristic dominates. At low voltage amplitudes, it is the other way round.

5.1.5 Discharge duration and ignition voltage

The differences between IPP and DPP can be particularly observed in their ignition behavior. For this purpose, the ignition timings, corresponding voltages, and discharge durations can be analyzed based on the previously discussed photomultiplier measurements. The results are shown in Figure 5.13.
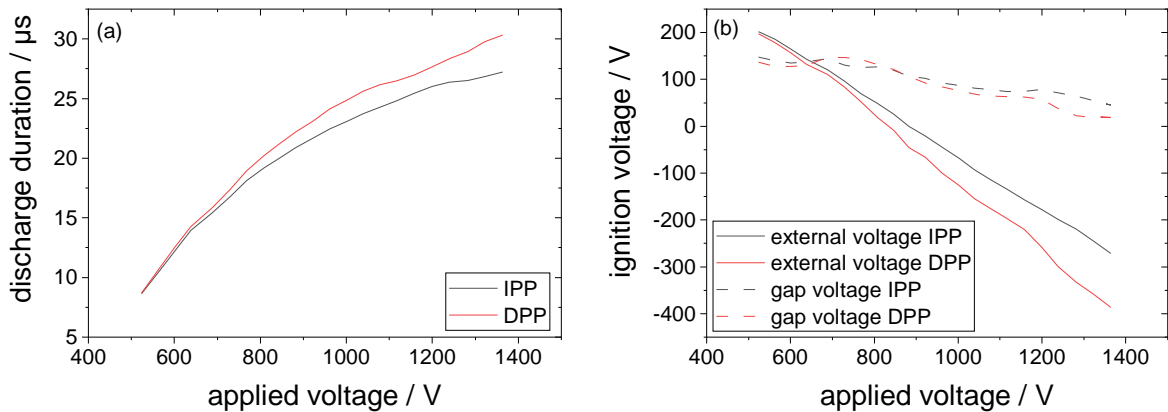
Figure 5.13: Discharge duration (a) and ignition voltage (b) depending on the applied voltage. Conditions: f = 15 kHz, d = 200 µm, 950 mbar helium atmosphere.

The discharge durations of the respective half-phases, depending on the applied voltage, are displayed in Figure 5.13 (a). It becomes evident that with increasing voltage, the discharge can be sustained for longer durations. At an applied voltage of 1300 V, the discharge can be maintained for nearly 30 µs, which is almost the duration of a half-period. Since the end of the discharge is determined by the voltage reversal point,

a longer discharge duration implies an earlier ignition time. This behavior is expected, as a higher voltage amplitude at a constant frequency allows the necessary ignition voltage to be reached earlier.

However, when examining the ignition voltage (see Figure 5.13 (b)), it is not constant but decreases with the applied voltage. This effect is so pronounced that at an applied voltage of approximately 800 V, it is already possible to ignite before the zero crossing, i.e., with reversed polarity. This effect is caused by the so called memory effect e.g. by residual charges from the previous period. The charges are applied to the dielectric in the previous half-phase and shield the field. If the external voltage is reversed, the charges no longer shield the field, but increase it additionally. As a result, the field required for ignition is reached earlier. This effect is considered in the discussed gap voltage (also shown in Figure 5.13 (b)). It becomes apparent here that the effective electric field, which is influenced by surface charges, points in the same direction regardless of the applied voltage, meaning its polarity does not change. However, the ignition gap voltage is also not constant, but decreases with increasing voltage. This can have various causes. On the one hand, the memory effect goes beyond the surface charges. For example, metastable atoms, which are easy to ionize and thus simplify ignition, can survive between the discharge phases in the volume. As the time between two discharges becomes shorter and shorter, the memory effect becomes more significant. On the other hand, as the voltage increases, the gas temperature also increases, causing the gas density and, according to Paschen's law, the ignition voltage to decrease. Furthermore, the temperature and surface charges can also change the coefficients for secondary electron emission, which could further support the ignition.

Another information that can be taken from the measurements is the difference between IPP and DPP. Figure 5.13 (a) shows that the discharge in the DPP generally lasts longer than the IPP, which means earlier ignition. This effect becomes even stronger with increasing voltage. The same effect can be seen in the ignition voltage (see Figure 5.13 (b)). Here, for comparability, the sign of the ignition voltage of the DPP has been reversed. The results show that the memory effect works differently in the two half-phases. In the IPP, positive charges or electron vacancies are deposited

on the dielectric. These are assumed to be in the valence band and are therefore more strongly bound than negative charges that are assumed to be on the surface or in the conducting band. This means that the lifetime of the surface charges after the IPP, i.e. before the DPP, is longer than in the contrary case. The higher number of surface charges before the DPP supports the field with the result that a sufficient ignition voltage is reached earlier in the period.

The gap voltage shows only minor differences between IPP and DPP, which are in the order of magnitude of the uncertainty of the diagnostics. However, it cannot be ruled out that there are also differences here due to the volume memory effect. This includes, for example, ionization by metastable helium atoms, which cannot be taken into account by the methods used here.

5.1.6 Influence of the applied frequency on the discharge

In addition to the applied voltage, the frequency is also a parameter that can be used to control the discharge performance and that can influence the discharge mode. Figure 5.14 (a) shows a power measurement as a function of frequency for different voltages. A clear linear dependence can be seen. This was to be expected, since more discharges per time are ignited linearly with increasing frequency. Nevertheless, it is striking that the discharge behavior per discharge apparently barely changes with frequency.

The similarity of the individual discharges becomes particularly apparent when individual QV-plots are compared (see Figure 5.14 (b)). The area indicating the dissipated energy per period changes only slightly for different frequencies. Nevertheless, small changes can be observed. For example, the shape of the QV-plot at low frequencies more closely resembles a parallelogram than at higher frequencies. This difference is most visible in the passive phases. This can be explained by the memory effect. As discussed before, the slope of the QV-plot or the capacitance can be influenced by surface or volume charges. The lower the frequency, the lower the influence of these charges, since the time between two pulses increases significantly. Therefore, C_{cell}, i.e. the slope of the passive phase, is influenced by charges from the last pulse, especially at high frequencies. At low frequencies, the memory effect plays a more subordinate role due
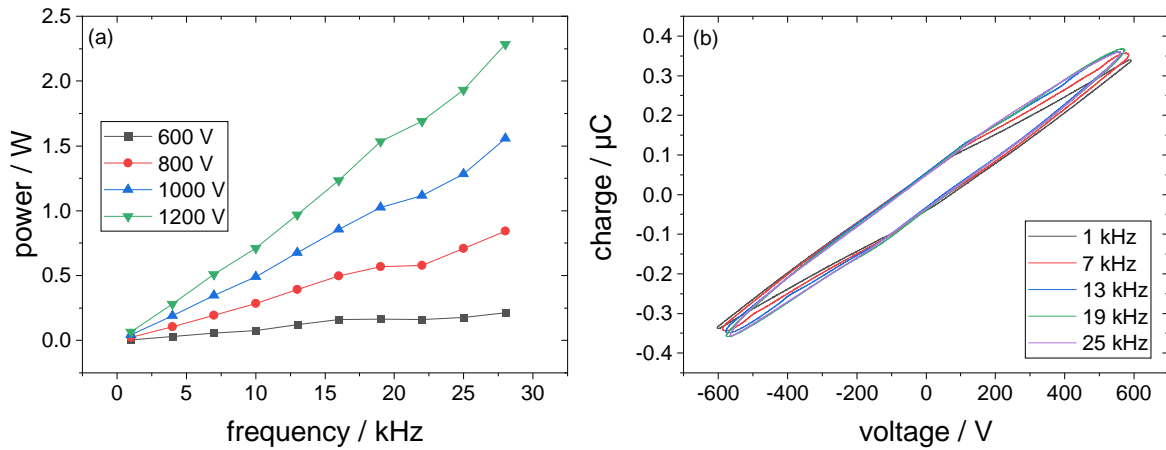
Figure 5.14: (a) Power as a function of frequency for different voltages. (b) QV-plot for different frequencies at 1200 V applied voltage. d = 200 µm, 950 mbar helium atmosphere.

to the larger time interval, leaving the slope unaffected and the QV-plot parallelogram-shaped.
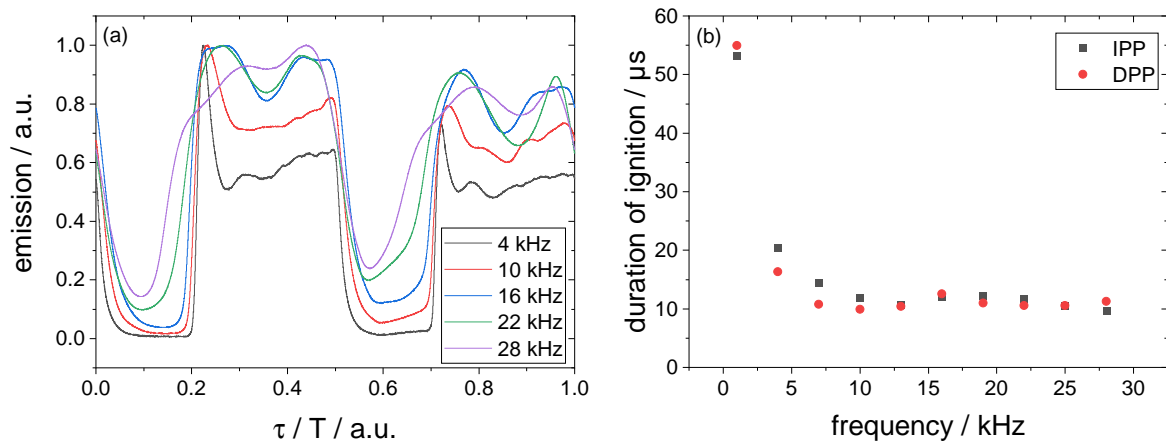
Figure 5.15: (a) Emission for different frequencies at 1200 V applied voltage. (b) Duration of ignition depending on the frequency. d = 200 µm, 950 mbar helium atmosphere.

The influence of the memory effect is particularly noticeable when observing the emission. Figure 5.15 (a) shows the optical emission for different frequencies. For better comparability, one period is shown for each measurement, which means that the time axis is based on different period durations. As assumed before, the emission shows similar characteristics for all frequencies. Ignition occurs in the IPP and DPP in the

form of a strong pulse. This pulse then changes into a constant emission, whereby the emission increases again towards the end of the half-phase before the plasma is extinguished. The higher the frequency, the earlier in the period the plasma can be ignited, since the time to the last pulse is short and thus charges or excited species can support the ignition. At high frequencies, the effect is so strong that the plasma can ignite again immediately after extinguishing, allowing emission to be measured almost continuously.

The support of the ignition by the memory effect has the consequence that the discharge characteristic adapts slightly. While at low frequencies a distinct narrow ignition pulse can be seen, this pulse becomes increasingly wider in the case of high frequencies. At very high frequencies, this pulse can no longer be separated from the rest of the emission. This effect is also caused by the representation of the time axis. A wider pulse does not necessarily mean a temporally longer ignition phase. For this reason, the widths of the ignition pulses in Figure 5.15 (a) have been converted into a time (see Figure 5.15 (b)). It is noticeable that in reality this duration is not longer but even shorter for higher frequencies. While the ignition phase at $1\,\mathrm{kHz}$ lasts approximately $55\,\mathrm{\mu s}$, the duration for higher frequencies becomes constant at approximately $10\,\mathrm{\mu s}$. This can again be explained by the fact that ignition is supported by the memory effect. At low frequencies, the time between pulses is so long that fewer charged or excited species are present to support ignition. This makes ignition more difficult in general. Since the measurement is integrated over many cavities and ignition takes place at different times (not supported by memory effect), the peak is broadened.

5.1.7 Conclusion: Classification of the discharge mode

After the fundamental properties of the discharge have been characterized with the help of electrical and optical measurements, it can now be classified to a discharge mode. In pure helium, a homogeneous and not a filamentized discharge was observed here. For this reason, a distinction must be made in the following between APTD and APGD (see section 2.1.2). Table 2.1 can be used as a reference point for differentiation. However, two important points should be noted here. Firstly, the table refers to a single DBD. In the case of the MCPA, the properties of 1156 cavities are superimposed, which makes the interpretation of the results very complex. Secondly, not all

parameters for determining the discharge mode could be measured in this work. For example, there is no knowledge about the electron, ion or metastable densities.

One of the easiest parameters to measure is the current density. This is between 10 and $55\,\mathrm{mA/cm^2}$ when considering only the discharge current for the parameters used here and the cavity area. The order of magnitude is comparable to previous measurements [22, 147] and can be assigned to the APGD mode. The situation is different with the power density. In this work, this is between 55 and $400\,\mathrm{W/cm^3}$ at $10\,\mathrm{kHz}$. These values are significantly higher than the reference values in Table 2.1 and cannot be included in the evaluation as a result. One reason could be the difference between the plasma volumes. In the literature, reactors with an electrode spacing of a few mm were commonly considered. In this case, the cavities are only $50\,\mathrm{\mu m}$ high. In addition, the discharge is not limited to the cavity of which the volume was used for the calculation, but can also exist in the area above, so that the volume cannot be clearly defined.

The gap voltage provides further insight into the discharge mode. Here, a Townsend plateau forms in the APTD and the voltage is constant, whereas in the APGD a cathode drop is observed and the voltage decreases [49]. In the measurements shown here, a clear influence of the ignition on the gap voltage can be seen. At low applied voltages, this is constant or even decreases slightly after ignition. At higher applied voltages, the gap voltage initially increases and saturates at a later point in time. Here too, it is difficult to assign the discharge to a specific mode, as characteristics of both modes are observed. In addition, the gap voltage can again only be determined for all cavities simultaneously, which means that it is smoothed to a certain extent.

However, the most significant difference between APTD and APGD is the length of the discharge pulses. In the APTD, these differences are in the range of $10\,\mathrm{\mu s}$ while in the APGD they are in the range of $1\,\mathrm{\mu s}$ [152]. The previously drawn discharge current or emission pulses have a width of 5-10 µs and can therefore be associated with APTD at first glance. However, these measurements are strongly broadened due to the averaging over all cavities. In addition, as mentioned way above the temporal resolution of the photomultiplier used is limited. In Figure 6.3, the emission of a single cavity is mea-

sured using an ICCD camera, which is discussed in more detail later. Nevertheless with the ICCD, it can be seen that at least the first ignition peak is significantly narrower than previously observed and can be assigned to the APGD.

In summary, it can be stated that the discharge pulses can most likely be classified as an APGD, even if the distinction is not clear due to a lack of information for example on electron densities and the superposition of many cavities. This finding fits very well with the literature, in which most helium discharges are assigned to an APGD [47, 49, 59, 153, 154]. Besides, APGDs occur mainly at larger electrode distances in the mm range. This is where the regions typical for a glow discharge form, such as a positive column. In the case of cavities in the µm range, it can be assumed that not all regions can form completely and, for example, the positive column, i.e. the quasi-neutral plasma region, only accounts for a small part of the discharge. All in all this makes the discharge comparable to a glow discharge, although there are still slight differences.

Even if the discharge can be categorized as an APGD, this classification does not yet fit completely, as it is only defined for a single discharge pulse. However, when looking at the emission or the discharge current, it is noticeable that the discharge does not extinguish after the ignition pulse, but is maintained. Depending on the parameters, further pulses follow. This can be assigned to a pseudo-glow or quasi-continuous glow discharge mode. This occurs when the applied voltage continues to rise after the ignition of an APGD. The charges on the dielectric are then no longer sufficient to shield the field and the discharge can ignite again. If the gap voltage is equal to the ignition voltage again after ignition of the first pulse, a further discharge pulse follows. This can be the case either after a few µs (pseudo glow) or instantaneously (continuous/quasi-pulseless glow) [37, 155], so that the discharge does not extinguish until the voltage reverses.

In the case of pure helium, the discharge could additionally be supported by metastables. These are formed during the first ignition and can assist ignition by Penning ionization of trace impurities such as nitrogen or by stepwise ionization. As a result, the ignition voltage is reduced and is already reached again during the first discharge

pulse. The influence of the metastables between the two half-phases is particularly noticeable. Especially at higher voltages and thus earlier ignition times, the discharge no longer extinguishes at all (see Figure 5.8). Despite a short lifetime of 5 µs, the density is apparently sufficient to maintain the discharge, albeit weakly. One reason for this is that the largest loss channel of the metastables is the formation of dimers, which still have an energy of 19.2 eV and are therefore likewise sufficient for Penning ionization of the impurities. Only when the time between half-phases becomes too long the losses, e.g. due to diffusion and collisions, are sufficiently high that a completely new ignition is required.

In addition to the discharge mode of the individual pulses, the results indicate that the reactor cannot be distinctly classified as either volume DBD or surface DBD. Instead, it exhibits characteristics of a mixed form, where one type may dominate depending on external parameters. Additionally, it is evident that the discharges are significantly influenced by the memory effect.

5.2 Influence of surface charges on the discharge

The following results on surface charges, were developed in collaboration with Robin Labenski, whose master thesis was supervised in the course of this dissertation. For this reason, some parts of the following section have already been published in the master's thesis entitled "Laser-induced manipulation of charges in a dielectric barrier surface discharge at atmospheric pressure" (2023) [156]. Moreover, a joint paper has emerged from the results, which has already been published [144].

In the following section, surface charges deposited during the discharge phases are discussed in more detail. Initial insights into the charges have already been gained using the equivalent circuit approach. In addition, a simplified model has been developed that distinguishes between surface charges and volume charges (see Figure 5.9). However, only the combination of surface charges and volume charges can be measured directly with the equivalent circuit approach. A number of assumptions are necessary to separate the two types of charge. To change this, a relay circuit was added to the

experimental setup as described in chapter 4. Furthermore, a laser setup is used to not only detect the charges, but also to actively manipulate them in order to study their influence on the discharge.

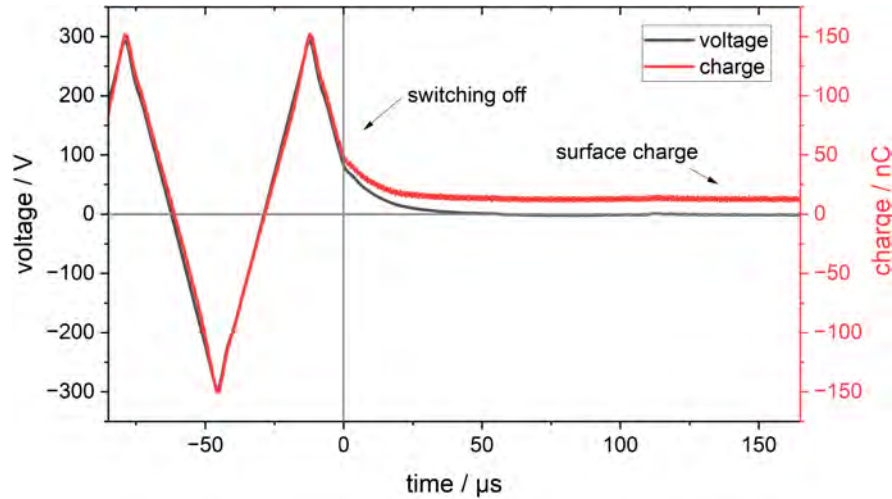## 5.2.1 Determination of the surface charge by a relay circuit

Figure 5.16: Switching off the external voltage by means of a relay circuit to determine the surface charge. Measured voltage and charge (volume + surface) depending on time. Conditions: V = 600 V, f = 15 kHz, d = 200 μm, 950 mbar helium atmosphere. Adapted from [144].

A relay circuit enables the reactor to be disconnected from the applied voltage within a short time. Without an applied voltage, the volume charges diffuse out of the volume under consideration within a short period of time. However, the surface charges have a significantly longer lifetime, allowing them to be measured at a later point in time. Figure 5.16 shows the switching-off behavior of the circuit with additional relay. For this purpose, the measured voltage and the charge are shown as a function of time. The voltage drops quickly to zero when switching off. The charge on the other hand also drops rapidly at first, but saturates at a certain value. The relationship between volume and surface charge becomes clear here. The volume charges have a short lifetime due to recombination or diffusion and decay within a few μs. The surface charges, however, can persist for minutes or even longer. This means that a near-equilibrium charge is created as soon as the volume charge has decayed. This equilibrium then corresponds purely to the surface charge. In the following, the surface charge is always

determined 100 µs after switching off the voltage. Due to the surface charges long decay time, their quantity at the instant the relay is switched must be practically identical to that evaluated 100 µs later. Using this, the moved charge q_R at t=0 can be determined using equation 5.7, which is simplified compared to equation 3.28, as no voltage is applied. Since the volume charges are no longer included in the measurement, the transported charge now corresponds to the surface charge.

$$q_r(t=0) = \frac{1}{1 - \frac{C_{\text{cell}}}{C_{\text{diel}}}} Q(t = 100\,\text{µs}) \tag{5.7}$$

The advantage of the relay circuit is that it can be controlled using a function generator. This in turn can be triggered with the desired frequency and delay, allowing the measurement of the surface charge to be carried out at different phases of the discharge. This allows the results to be displayed as a Lissajous figure. However, it is not the measured total charge that is plotted here, but only the surface charge against the applied voltage (see Figure 5.17). The result is an almost perfect parallelogram. During the active phases, the surface charge increases linearly with the voltage. This was to be expected, as the growing external electric field repeatedly overcomes the opposing field through the surface charges and further charge carriers can be transported to the surface through the discharge. Once the voltage has reached its maximum (or minimum), the discharge expires as the surface charges compensate for the external field. No further charge carriers are added and the surface charge remains constant. As the polarity of the applied voltage changes, the surface charges support the next ignition and the process runs in the opposite direction.

Figure 5.17) (b) shows a disadvantage of the method of switching off. At higher voltages, the surface charge saturates at the end of the active phases before the discharge extinguishes. This effect can be attributed to the phenomenon of back discharging. If the surface charge is very high and the discharge is switched off quickly, the electric field resulting from the surface charge can be sufficient to ignite the discharge directly in the reverse direction. This reduces the surface charge, as charge carriers of the opposite polarity reach the surface, which means that it is no longer possible to determine the actual surface charge. However, this effect only occurs at higher voltages and is initially so small that the actual charge can still be estimated. Furthermore, the di-
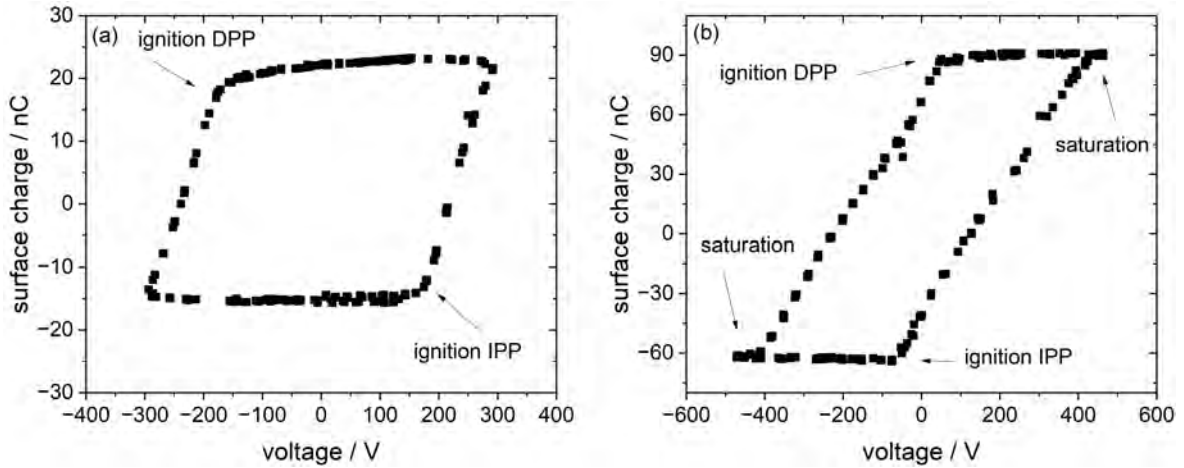
Figure 5.17: Surfaces QV-plot for 600 V (a) and 1000 V (b). Conditions f = 15 kHz, d = 200 µm, 950 mbar helium atmosphere. Adapted from [156].

agnostics of surface charges are particularly interesting for plasma catalysis. As more complex gas mixtures are used here, which generally require higher ignition voltages than pure helium, back discharges are reduced.
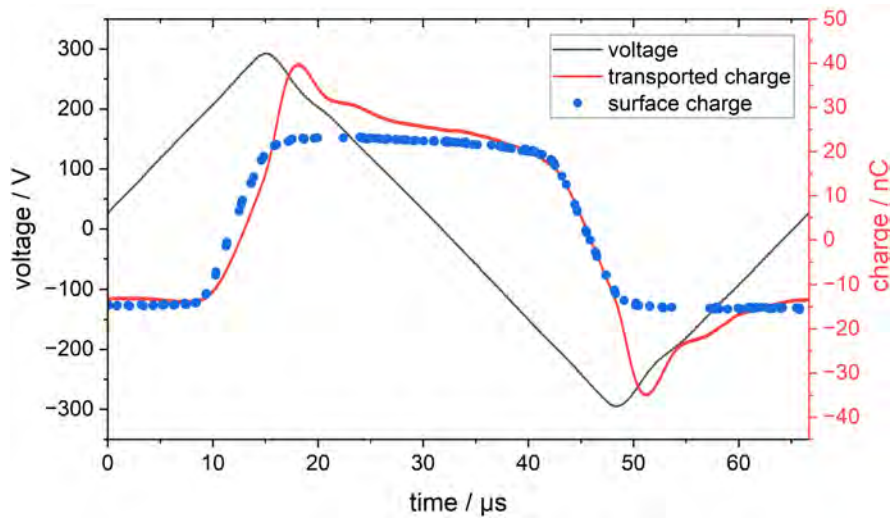
Figure 5.18: Comparison of the calculated transported charge with the measured surface charge. Conditions: V = 600 V, f = 15 kHz, d = 200 µm, 950 mbar helium atmosphere. Adapted from [144].

Instead of drawing a plot of the surface charge against the applied voltage, it can also be plotted against time (see Figure 5.18). Here, a comparison can be made between the calculated transported charge and the surface charge. During the discharge (active phase), the transported charge and surface charge are almost identical. Both ampli-

tude and profile match each other very well. The difference becomes clear again when the discharge ends. Here, the surface charge remains constant, while the transported charge continues to increase. This can be explained by the persistent gap voltage (see section 5.1.3). If the gap voltage also decreases, no more charges can be transported and the volume charge carrier density slowly decreases until only the surface charges are present.

The method described can therefore be used to determine absolute charge carrier densities in addition to the qualitative behaviour of the surface charge. In the case shown above, for example, the charge reaches a maximum of $24\,\mathrm{nC}$. With 1156 cavities integrated using this method, this corresponds to a mean charge density of approximately $16\,\mathrm{nC/cm^2}$. However, it should be noted that not all cavities may be ignited at the same time. Furthermore, it is not known whether the charges are evenly distributed over the cavity surface or occur in clusters. For this reason, the value of $16\,\mathrm{nC/cm^2}$ is only of limited significance. Nevertheless, the measured order of magnitude of the charge carrier density on the surface is quite comparable with other dielectric barrier discharges in the literature [51, 85, 91, 157, 158].

In addition to the possibility of using the method as a diagnostic, it can also be used to control the surface charge. The discharge can be used to charge the surface and switched off as soon as the desired charge is reached. This has various applications. On the one hand, as shown below, the subsequent discharges can be modified, as the memory effect can be manipulated and adjusted. On the other hand, the method offers promising possibilities for further investigations of the surface charges. For example, a catalyst could be charged using the method and then the catalytic properties could be investigated in dependence of the surface charge.

The influence of pre-charging the surface on the discharge is shown in Figure 5.19. The ignition of the increasing potential phase (IPP) is observed here. This means that a negative precharge of the surface supports ignition. The more negative the charge, the lower the ignition voltage. If the surface is charged more positive, the ignition voltage increases, as the electric field is partially shielded and the surface charges must

be compensated. The scattering of the measured values can be explained by the generally statistical nature of the ignition process. Nevertheless, a clear linear trend can be identified. Without precharging, the ignition voltage is 347 V. A linear fit demonstrates that, for each nC of precharge, an additional voltage of 5.75 V is required for ignition. For charges greater than 22 nC, the discharge can not be ignited in every case but only coincidentally in the IPP. Only a change of polarity (start of DPP), in which the surface charges no longer have a shielding but a supporting effect, leads to a new ignition.

In this way, the discharge or the first ignition can be strongly manipulated. Due to the shielding effect of the charge, it can be expected that the effective electric field remains almost unchanged during ignition despite the increasing voltage. However, since the local charge distribution is not known, it can be assumed that an increased ignition voltage in combination with inhomogeneously distributed surface charges can lead to a significantly different electric field distribution in the volume. This would have an influence on the acceleration and resulting energy of electrons and thus on the overall discharge dynamics. Although this investigation goes beyond the scope of this work, it could offer the possibility of tailoring the discharge for applications such as plasma catalysis in the future.
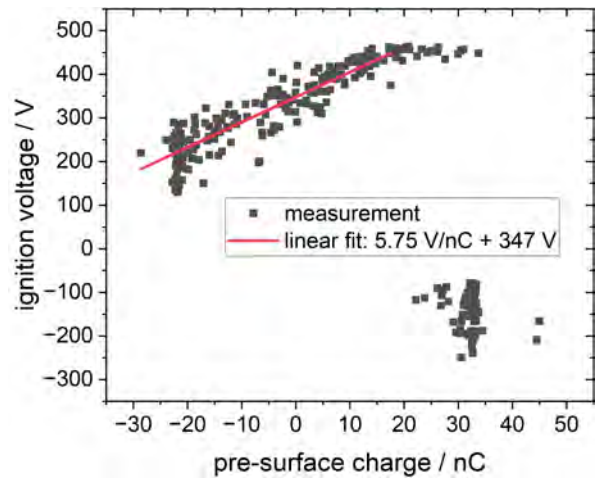
Figure 5.19: Ignition voltage as a function of the pre-surface charge within the IPP. Conditions: V = 960 V, f = 15 kHz, d = 200 μm, 950 mbar helium atmosphere. Adapted from [144].

5.2.2 Laser charge manipulation

In the following section, the surface charge is to be influenced with a laser instead of switching off the discharge. This has various advantages. Firstly, a laser offers the possibility of influencing the discharge in a spatially and temporally resolved manner.

In addition, modification is possible during plasma operation. This reduces a drawback of the switching-off method, as the discharge is repeatedly interrupted and requires a few seconds to return to the previous equilibrium when switched on again. By using a laser, the discharge can be operated continuously.

The method has already been applied by *Tschiersch et al* [92]. The results were summarised in section 3.1.3. The setup used in the following is described in section 4.3. A laser (532 or 1064 nm) irradiates the dielectric of the reactor to influence the surface charges. At the same time, the plasma emission is observed using a photomultiplier and the charge or surface charge is monitored as before. Due to the structure of the array, the metal grid is inevitably irradiated by the laser in addition to the dielectric, which can cause further effects.

Volume effects, in contrast, can be excluded to a certain extent. The laser wavelengths used are not sufficient to ionize helium or helium metastables. Although the experiments are carried out in a vacuum chamber, the possibility of small amounts of oxygen or nitrogen impurities entering the discharge cannot be ruled out. Negative oxygen ions would be generated in the discharge and laser photo ablation would play a role. However, it is known from the literature that these effects are significantly stronger at 532 nm than at 1064 nm due to the photon energy required [95]. As no differences could be observed in this work between measurements at different wavelengths, it is concluded that laser photo ablation plays a subordinate role here, if any. For this reason, a distinction can only be made between surface and electrode effects.

Figure 5.20 shows the results of the laser charge manipulation analogue to the measurements of *Tschiersch et al* [95]. The upper Figure shows the voltage, as well as an emission measurement from the period before the laser (pre) and an emission measurement from the period directly after (post) the laser. The lower Figure shows the difference in the measured charge. A point in time was selected for the laser at which the dielectric is negatively charged and the discharge has not yet ignited. For this reason, no emission is initially visible. However, it can be seen that the ignition occurs earlier, but slightly weaker, than in the case without the laser. This is known from
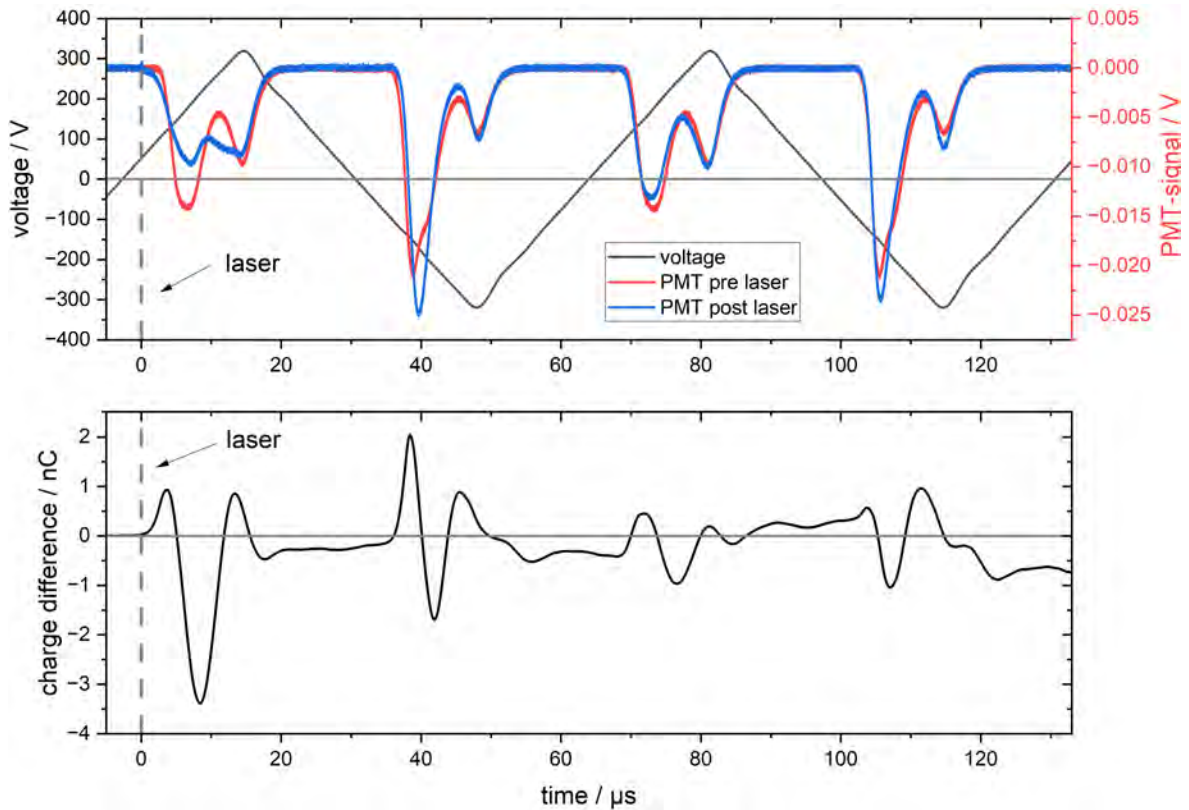
Figure 5.20: Laser charge ablation shortly before ignition with a wavelength of $\lambda = 532\,\mathrm{nm}$ before ignition of the IPP. Conditions: $V = 600\,\mathrm{V}$, $f = 15\,\mathrm{kHz}$, $d = 200\,\mathrm{\mu m}$, $950\,\mathrm{mbar}$ helium atmosphere. Adapted from [144].

the literature and can be attributed to detached surface charges that support the next ignition. The lower ignition voltage results in a lower electric field, so that the charge carriers are accelerated less and the ionization, excitation and thus emission is less strong. This also means that, due to the lower memory effect, the next pulse is ignited later but more strongly.

Instead of showing a comparison of the charge, the difference between the charge before and after the laser is shown, as the differences here are in the low percentage range. As known from the literature [95], no difference in the charge is visible when the laser hits, as the number of charges released is below the detection limit. However, the effect of the laser is clearly visible in the discharge, as the detached charges are sufficient to change the memory effect and thus the entire discharge.

Due to the exact reproduction of the results known from the literature, it can be

assumed that laser charge ablation also works in the micro cavity plasma array. Overall, however, there are two differences to the literature. Firstly, the effect can only be recognized at low applied voltages. This can be attributed to the volume charges at high voltages. These increase with the voltage and can compensate for the low number of charges released from the surface, so that the effect is no longer visible. But if the laser is fired at low voltages shortly before ignition, as in this example, there are hardly any or no volume charges, and the ignition is supported exclusively by the detached charges. A second difference is that the effects can be observed in both half-phases. This means that, unlike in the literature, positive charge carriers can also be released. This can have two explanations. Firstly, a different dielectric material (zirconium oxide instead of float glass) is used. This material may bind positive charges less strongly due to the different electron affinity. On the other hand, the powered electrode is also hit by the laser in addition to the dielectric. No surface charges are expected here due to the conductive properties. However, the laser could potentially also release charges from the material here, which would have the same influence on the discharge as in the other half phase.

In the measurements discussed so far, the main aim was to reproduce the results known from the literature, in which the surface was charged but no discharge had yet been ignited. In the following, the behaviour of the discharge when the laser hits the surface during the active phase is investigated. First, the behaviour shortly after ignition of the DPP ($T_L = 26 \, \mu s$) is considered (see Figure 5.21).

Unlike before, the measured charge changes immediately when the laser hits the surface. Accordingly, more charges are transported here than in an uninfluenced discharge. The difference then stabilises around zero again, albeit with a slight negative offset. This means that the next pulse can be ignited more easily. This behaviour can also be seen in the emission. Unfortunately, the laser intensity could not be completely eliminated from the PMT data in this measurement, so that the emission within the first $4 \, \mu s$ overlaps that of the discharge. Nevertheless, it can be assumed that the emission increases at this point due to the increased charges. Gradually, the discharge returns to the charge equilibrium that prevailed before the laser and the effect of the laser
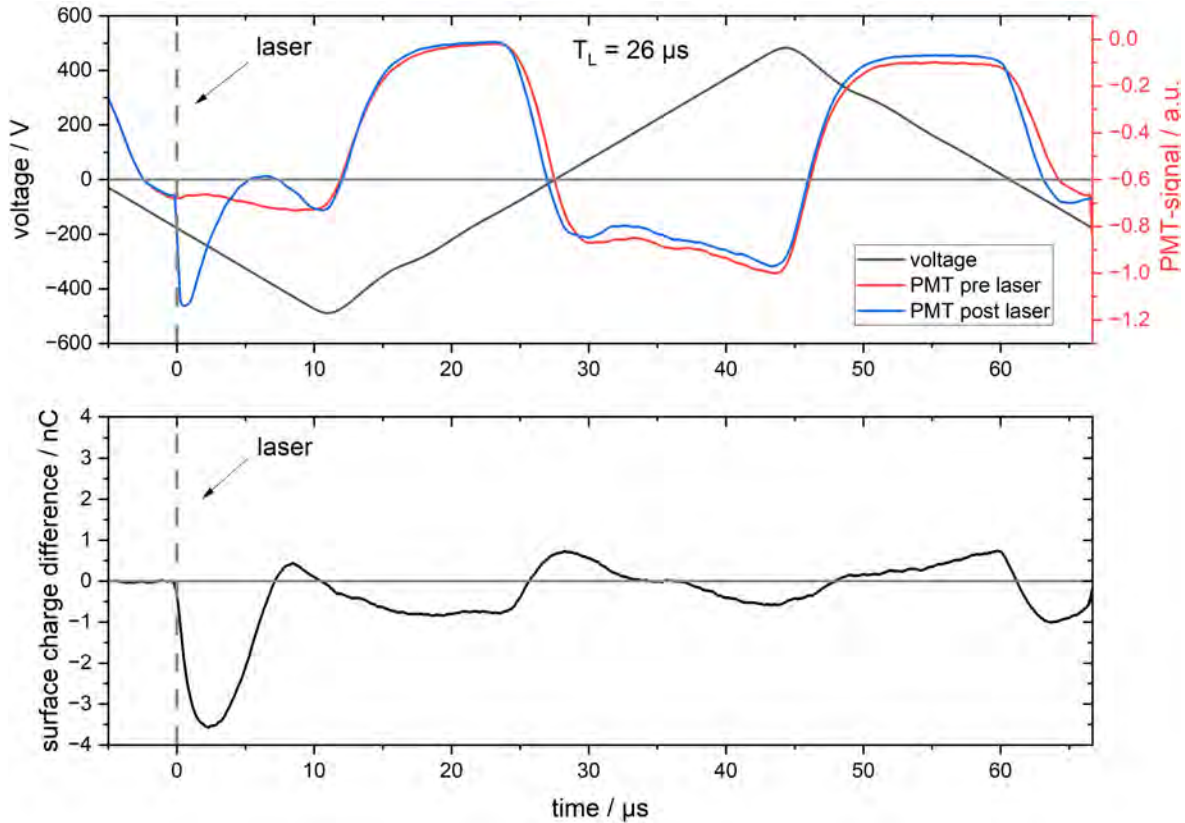
Figure 5.21: Laser charge ablation shortly after ignition with a wavelength of $\lambda = 532\,\text{nm}$ within the DPP. Conditions: $V = 962\,\text{V}$, $f = 15\,\text{kHz}$, $d = 200\,\mu\text{m}$, $950\,\text{mbar}$ helium atmosphere. Adapted from [144].

becomes smaller. In the case shown here, although, the next half-phase also ignites earlier. However, this effect is not reproducible in all measurements and could not be clarified conclusively. It should be noted that the results discussed here are independent of the voltage amplitude applied, unlike in the case discussed above.

If the laser is now used towards the end of the DPP ($T_L = 26\,\mu\text{s}$), the result changes (see Figure 5.22). The influence of the laser is also immediately visible here, resulting in a large difference in the surface charge. The difference, however, is that the discharge extinguishes shortly after the laser emission. This means that the discharge no longer has time to reduce the charge imbalance and the disturbance remains until the next ignition. The additional charges enable the next discharge to be ignited significantly earlier.

The difference in the ignition times depending on the time at which the laser hits the
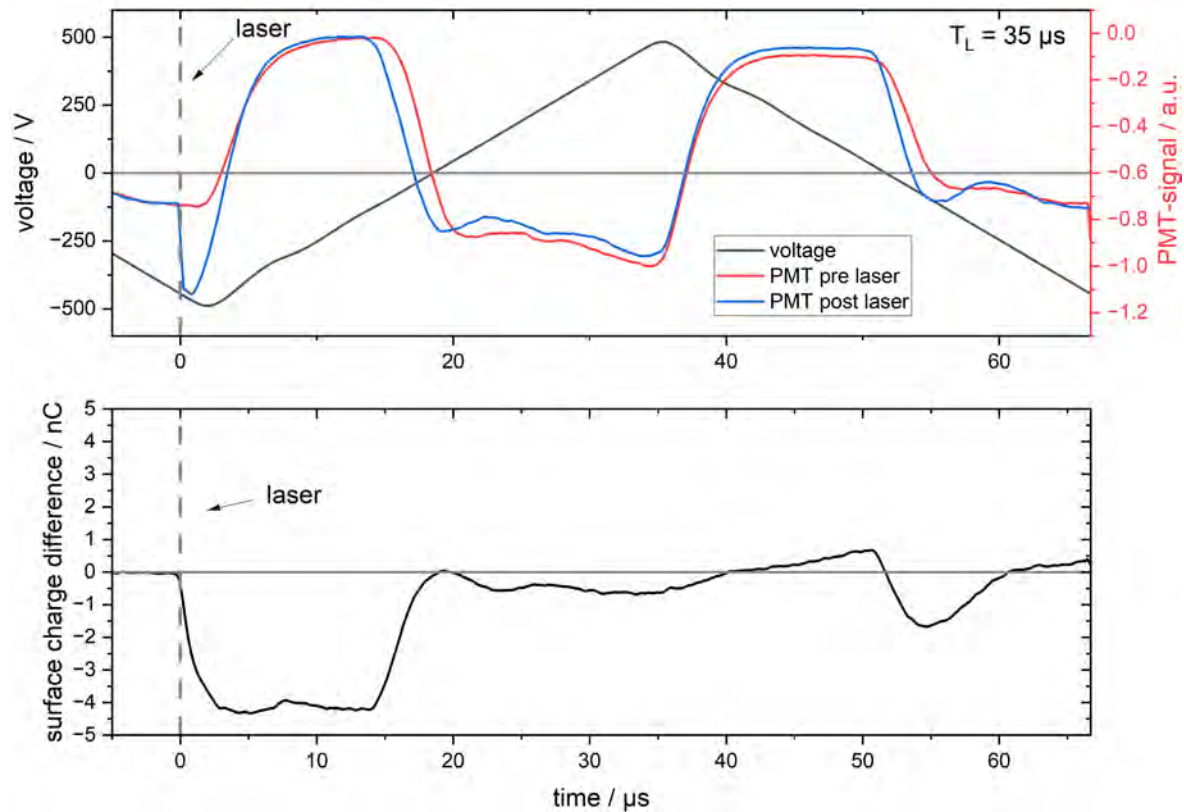
Figure 5.22: Laser charge ablation shortly before extinction with a wavelength of $\lambda = 532\,\text{nm}$ within the DPP. Conditions: $V = 962\,\text{V}$, $f = 15\,\text{kHz}$, $d = 200\,\mu\text{m}$, $950\,\text{mbar}$ helium atmosphere. Adapted from [144].

surface is shown in Figure 5.23. If the laser hits the surface at the beginning or shortly before discharge, charges are released and the ongoing pulse is amplified. However, the discharge continues for so long that the discharge returns to its old equilibrium. For this reason, the influence of the additional charges on the next pulse is visible but relatively small. The situation is different at the end of the half-phase. Here, the additional charges cannot be dissipated until the next half-phase and significantly increase the memory effect, whereby the next discharge can ignite up to $1.4\,\mu\text{s}$ faster.

Laser metal grid interaction

Overall, the behaviour of IPP and DPP is very comparable, so that the results of IPP are not presented here. However, this comparability of the two half-phases is very surprising, especially given the results shown so far and the asymmetry of the reactor. One reason could be the influence of the metal grid, which is hit by the laser in addition to the dielectric. If a large influence comes from this grid, the effect is the
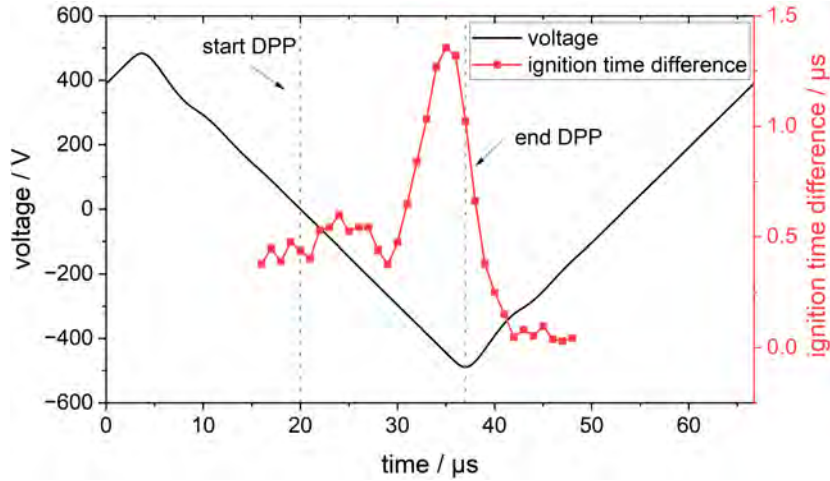
Figure 5.23: Ignition time differences depending on the time of laser emission. V $=$ 962 V, f $=$ 15 kHz, d $=$ 200 µm, 950 mbar helium atmosphere. Adapted from [144].

same in both half-phases and the presumably asymmetrical effects within the cavity would be superimposed. However, this would change if the laser no longer hits the array exclusively vertically, but at an inclined angle. In this case, the grid part within the cavities (edges of the cavities) would additionally be irradiated and an influence could become visible. For this reason, the angle between the reactor and the laser is to be increased in the following. As a result, the dielectric is gradually shaded, but the area of the irradiated grid increases due to the addition of the cavity edges.

The results are shown in Figure 5.24. The normalised maximal surface charge difference was determined as a function of the angle between the laser and the surface. For comparison, the theoretical area irradiated by the laser was calculated in combination with the laser cross section on the surface. The IPP is initially not sensitive to the angle. Only when the angle is too large the shadowing is so strong that the laser no longer has any influence on the charge.

Basic geometric model

The behaviour in the IPP can be understood by basic geometric considerations. Most of the shading comes from the metal frame with a height of 0.7 mm that holds the grid on the reactor (see Figure 5.25 (a)). In addition, it must be noted that the rotation increases the effective area of the laser beam. As the beam previously irradiated the entire array structure, by rotating it, areas outside the array are now also exposed.
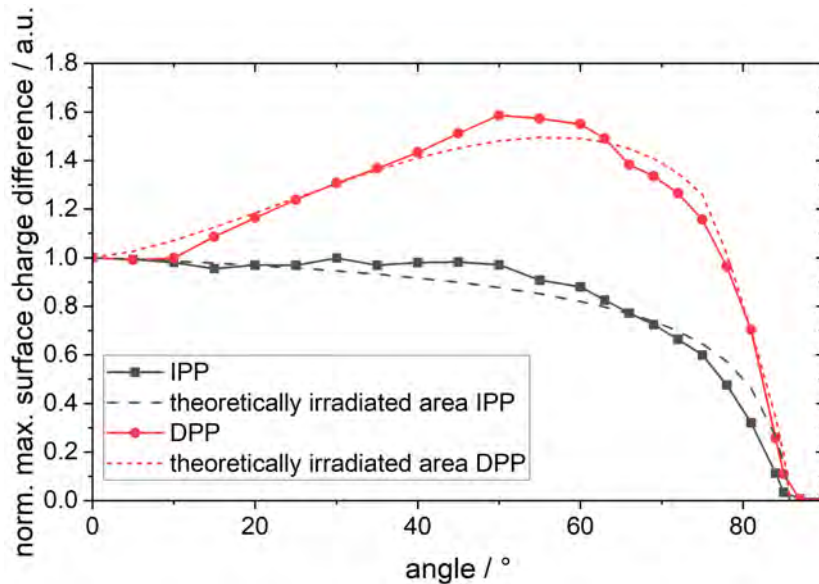
Figure 5.24: Normalised maximum surface charge difference depending on the angle between laser beam and surface. In addition, the normalised theoretical surface area hit by the laser was calculated in combination with the incoming laser intensity. Conditions: V = 1173 V, f = 15 kHz, d = 200 μm, 950 mbar helium atmosphere. Adapted from [144].

This reduces the intensity reaching the array, which can be described using a cosine term. The unshaded area combined with the incoming laser intensity can be expressed as follows:

$$A_{\text{top}}(\phi) = \left[1 - \frac{0.07}{\tan(90° - \phi)}\right] \cos^a(\phi) \tag{5.8}$$

However, the laser intensity depends not only on the geometry, but also on the beam profile itself. In the simplest case of a flat-top profile, the cosine term would be sufficient. Typically, Gaussian beam profiles are used, as in this work. In this case, the influence at the edges would only be significant at larger angles. This can be taken into account with the help of the parameter a. In this case, $a = 0.1$ was chosen, which leads to a very good agreement with the measurements.

In the calculations discussed so far, the shading of the dielectric by the grid has been neglected and nevertheless an almost perfect agreement between theory and experiment has been achieved. In a calculation analogous to the shading by the metal frame, it is noticeable that the dielectric is already completely shaded at $\phi = 75°$. However, as

the charge effects are still visible up to $\phi > 80°$, it can be concluded that the dielectric surface hit by the laser has no or a negligible influence on the charge dynamics and that the greatest effects are caused by the metal grid.

However, the situation is completely different in the DPP. Here, the influence of the angle on the charges initially rises significantly and then decreases at larger angles as in the IPP due to the shadowing. The increase can be explained by an additional term for the walls of the cavities:

$$A_{\text{top+wall}}(\phi) = A_{\text{top}}(\phi)[1 + x^b] \qquad (5.9)$$

Here, x expresses the fraction of the cavity wall that is exposed to the laser beam (see Figure 5.25 (b)). For $\phi \leq 75°$ the wall's entire length of $50\,\mu\text{m}$ is irradiated. A simple sinusoidal relationship follows from the projection of the wave front. For larger angles, the wall is in turn shaded from the opposite side, which must be taken into account:

Figure 5.25: a) Schematic representation of the laser irradiated reactor of for an incidence angle ϕ enclosed by the laser's propagation direction $\vec{k}$ and surface normal $\vec{n}$ of the plasma array. b) Microscopic view of one plasma cavity during laser irradiation in the DPP discharge. Taken from [144].

$$x = \begin{cases} \sin(\phi), & \text{for } \phi \leq 75° & (5.10\text{a}) \\ \sin(\phi) \cdot \dfrac{4}{\tan(\phi)} = 4\cos(\phi), & \text{for } 75° < \phi < 90° & (5.10\text{b}) \end{cases}$$

The parameter b can be used to describe the influence of the additional area on the discharge. A value of $b = 1$ indicates a linear response of the discharge to the additional surface area. However, the discharge is not distributed homogeneously along the cavity wall. In the DPP in particular, it can be assumed that the lower area of the wall has
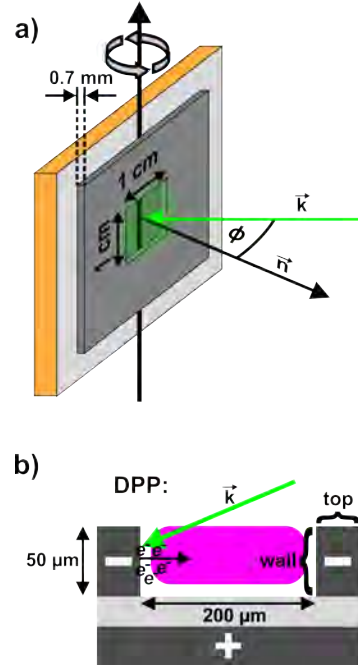
a greater influence on the discharge than the upper part, because that is where the electrons are accelerated to. A value of $b = 1.4$ best reproduces the measured data.

Differences between IPP and DPP

Even if both the angle-dependent behaviour of the IPP and the DPP can be described geometrically, the question arises as to why there is a difference between the half-phases in contrast to the previous measurements. Why is the influence of the angle so different in the DPP than in the IPP and why does the irradiated area of the dielectric play only a negligible role?

The main difference between IPP and DPP is the direction of discharge and the associated expansion of the discharge. In IPP, the electrons are accelerated out of the cavity, where a diffuse, widespread discharge is created, which ignites more strongly at the edges and also in the area above the cavity. In the DPP, on the other hand, the electrons are accelerated into the cavity, whereby the discharge volume is limited to the cavity and the discharge ignites in a very centered manner. This means that the discharge in the IPP can be strongly influenced by the laser even at small angles, as the top of the grid is also part of the discharge. In the DPP, on the other hand, the discharge is only in contact with the inner sides of the grid, which are only irradiated by the laser at larger angles. Another argument in favor of the difference is the different discharge volume. As the DPP has a significantly smaller discharge volume, the influence of an additional surface is greater than in the IPP.

Obviously, a large proportion of the observed effects are caused by the metal surface. It is conceivable that the surface is heated by the laser. This could, for example, lead to thermal emission of electrons which are then amplified in the plasma volume in an avalanche-like manner. On the other hand, the secondary electron emission coefficient could be increased by the laser. As a result, the discharge itself generates new charge carriers on the surface. Both effects fit very well with the differences between IPP and DPP, as the secondary electrons are mainly caused by ions that hit the surface and the thermal emission is caused by electrons that leave the surface. Both effects would therefore be amplified in the DPP, as electrons are accelerated away from the grid and

ions are accelerated towards the grid. In the IPP, on the other hand, the effect is weakened because the electric field points in the opposite direction.

The minor influence of the dielectric also matches the results already shown. Only when the laser is fired at the charged surface before discharge at low voltages it is possible to assume surface charges on the dielectric and to reproduce the results from the literature. In the other cases (higher voltage, laser during discharge), the measured effects can also be explained by surface effects on the metal grid. It can therefore be assumed that there are always effects on both the dielectric and the metal grid, but that the grid effects are so dominant that the effects on the dielectric can be neglected. At low voltages, for example, the discharge volume in the IPP could be so small that the discharge does not have contact with the grid surface that is hit by the laser. In addition, the secondary electron emission at the surface is also dependent on the ion density or energy, which could be lower at lower voltages. In this case, the effects on the dielectric could dominate and become visible in the measurements. However, it is very complex to experimentally verify this theory. The angle-dependent measurement for low voltage has the disadvantage that not all cavities necessarily have to be ignited. This means that it is not possible to determine the effective area irradiated by the laser.

Overall, the method can be used to adjust the discharge similarly to the switch-off method, with several distinct advantages. Firstly, the laser offers spatial resolution, allowing for precise manipulation of the discharge, which may be beneficial for future applications. Additionally, the laser provides time resolution, enabling continuous operation without needing to switch the discharge off and on as before. This continuous operation reduces the risk of back discharges and makes the process voltage-independent. However, a downside is that the charge can be set only indirectly via additional charge carriers from the metal grid, making the setup more complex and requiring modeling of the discharge for specific applications.

5.3 Determination of electric field components

The following results on the electric field were developed in collaboration with Henrik van Impel, whose thesis was supervised in the course of this dissertation. For this reason, some parts of the following section have already been published in the master's thesis entitled "Analysis of the electric field in a micro-scaled dielectric barrier discharge" (2023) [78]. Moreover, a joint paper has emerged from the results, which has already been published [107].

In addition to an electrical characterization and a discussion of the surface charges, a consideration of the electric field is an useful approach for a fundamental description of the discharge. This was already determined in a previous work by *Dzikowski et al.* [28] as a function of various parameters using the Stark splitting of a helium line pair (see section 3.2.1). In the following, these results are extended by further aspects. On the one hand, the measurements are carried out with spatial resolution in order to be able to determine the distribution of the electric field within the cavities. On the other hand, the polarization of the emission observed is used to measure not only the strength of the electric field but also its direction.

5.3.1 Spatial distribution of the electric field

For previous measurements of the electric field using the Stark effect, a setup typical for optical emission spectroscopy was used, in which the light from the discharge is guided through an optical fiber to a spectrograph. This has the advantage that the light can be transported over long distances with low losses, making the experiment very flexible. However, depending on the numerical aperture of the fiber used, the spatial resolution of this measurement is very limited, meaning that averages are sometimes taken over large volumes. Even if the resolution can be improved with optics, it is challenging to resolve the cavities in the µm range to be examined here. An alternative to the fiber is to image the discharge directly onto the slit of the spectrograph. This has the advantage that the spatial information is not lost through the fiber, but is retained. The light is imaged onto an ICCD chip at the end of the spectrograph. The resulting 2D images show the wavelength dependence in one dimension and a 1D spatial dependence in the

other dimension. In the case of the micro cavity plasma array, this method can be used to measure along the diameter of several cavities simultaneously. To improve the signal to noise ratio, the signals of the individual cavities can be accumulated to obtain the average spatial dependence. Unfortunately, it is not directly possible to achieve 2D resolution with this method. Nevertheless, it is conceivable to move the discharge in front of the slit of the spectrograph to scan along the second spatial dimension. However, this is beyond the scope of this work.
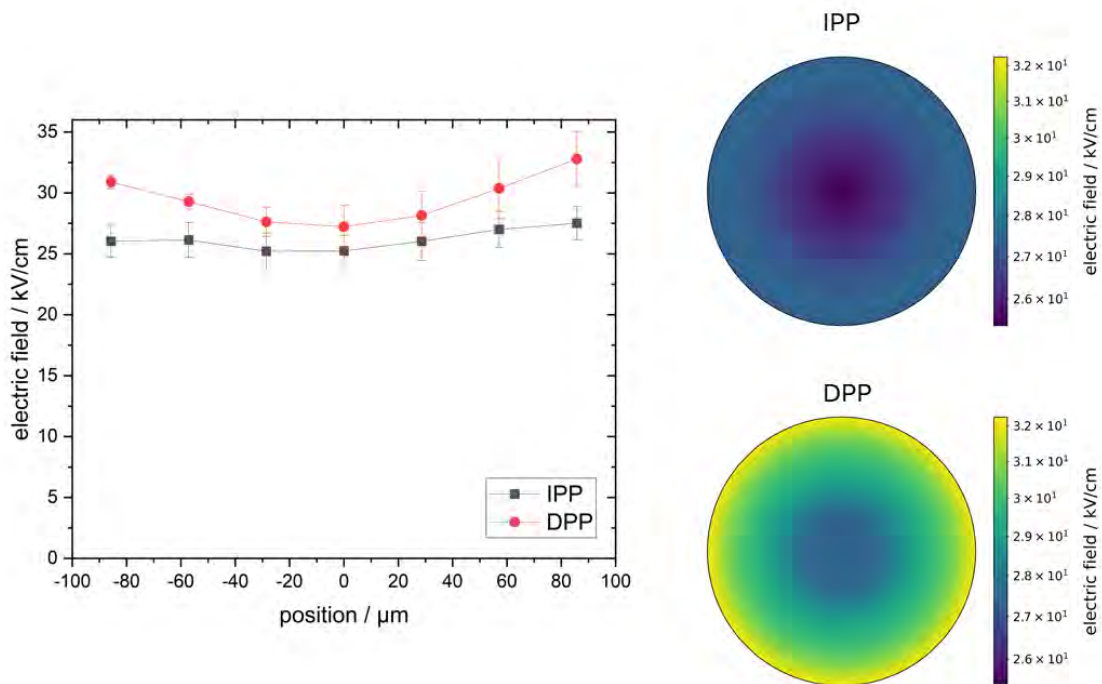
Figure 5.26: 1D (left) and 2D (right) electric field distribution of the IPP and DPP. Conditions: V = 1600 V, f = 15 kHz, d = 200 µm, exposure time = 3.5 min. Adapted from [78].

Figure 5.26 shows the spatially resolved field strength for IPP and DPP. The actual measurement is shown on the left, where each point corresponds to a pixel line of the ICCD. As the data points at the edge of the cavities are strongly influenced by scattered light, they could not be evaluated at this point. For a better illustration of the results, the measured 1D profile was extrapolated for the entire 2D cavity on the right-hand side, assuming a symmetrical distribution. It is noticeable that the fields in the center of the cavity are smaller and increase towards the edges. This effect is much

more significant in the DPP compared to the IPP, where the distribution of the field remains almost constant when the error bars are taken into account. In addition, it is clear that the overall field strength in the IPP is lower than in the DPP, as previously observed by *Dzikowski et al.* [28]. Both effects can be discussed on the basis of a field distribution calculated using COMSOL.

Figure 5.27 shows a 2D-COMSOL simulation for the geometry of a cavity. An electrostatic analysis was carried out, whereby no plasma effects were included. However, the applied voltage was adjusted to the previously determined gap voltage, thus taking into account the shielding by surface charges, even if not spatially resolved.

The simulation can firstly reproduce the measured field strengths very well. This means that the influence of the discharge on the electric field is already largely taken into account by the use of the measured gap voltage and, beyond that, is negligible. Moreover, the simulation also reproduces the measured field distribution. Here, it becomes clear that the maximum field is present at the corners, i.e. at the interfaces between the powered electrode and the dielectric. The field strength decreases towards the center of the cavity and upwards towards the opening.
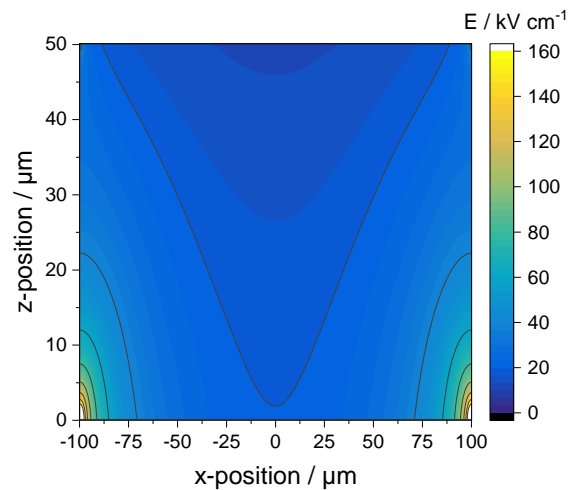
Figure 5.27: Static COMSOL simulation of the electric field strength distribution in a cavity at 200 V applied voltage. The dielectric surface is at y=0 µm and the cavity edges at x=0 µm and x=200 µm. Adapted from [78].

The fact that a more significant location dependence of the field distribution prevails in the DPP than in the IPP can presumably be explained by further shielding effects. It is known that the discharge in the DPP ignites very concentrated in the cavity, so it can be assumed that the surface charges also tend to concentrate in the center of the

cavity. The IPP, on the other hand, tends to ignite at the edges. In the simulation, only the total surface charge was taken into account, but not its spatial dependence. As a result, the geometry-related field increase tends to be amplified at the edges in the DPP, as less can be shielded here, but more in the center. In the IPP, on the other hand, the field profile is more balanced, as the surface charges tend to be at the edges and thus shield the strong field.

The difference in field strength between IPP and DPP can be explained by optical emission spectroscopy. In the case of the micro cavity plasma array, the emission is integrated in the y direction (line of sight). However, the measured field strength does not correspond to the mean field in the volume under consideration, but is weighted with the intensity distribution. In the DPP, the discharge ignites exclusively within the cavities. As the electric field is also particularly high here, high fields are measured in this case. In the IPP, however, the discharge ignites also in the area above the cavities. As smaller fields tend to prevail here, the measured value is lower, even if the real field inside the cavity could be the same as in the DPP.

A closer look at the measurement reveals a slight asymmetry between the left and right edges. This can be explained by the alignment of the array relative to the slit of the spectrometer. If the two components are not perfectly parallel to each other, this leads to shadowing effects in the corners of the cavity. As this is precisely where the largest fields prevail, the integration of the lines of sight means that even the smallest deviations in the alignment are enough to influence the result. Despite these effects, however, it was possible to keep the deviations due to shadowing to a minimum.

All in all, these diagnostics allow the already known electrical field measurements to be extended by a spatial resolution. The results correspond closely to the discharge dynamics already discussed.

5.3.2 Direction of the electric field components

In addition to the spatial distribution of the electric field, the dominant field directions are interesting, as these influence the transport of charge carriers to the (catalytic)

surface. The Stark splitting method can again be used for this. Here, the diagnostics makes use of the fact that the emission of the observed helium transition is polarized depending on the electric field direction (see section 3.2.1). As already mentioned, it is not possible to determine the electric field direction with the conventional micro cavity plasma array. Here, the field components under consideration are superimposed in such a way that a polarization filter has no influence on the measurement (see section 3.2.1). For this reason, the following measurements are carried out with the use of micro scaled plasma trenches. These have the same dimensions as the micro cavities, but with the possibility of observing the discharge from the side and thus being able to distinguish between the different electric field directions.
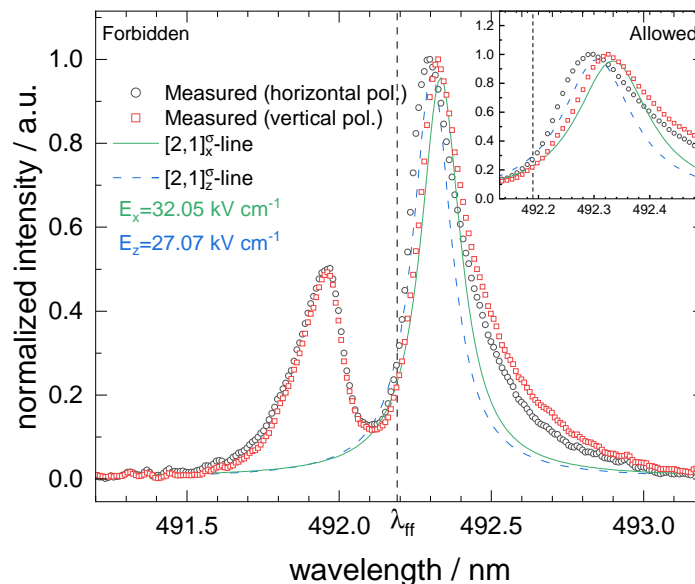
Figure 5.28: Fit of the $[2,1]^{\sigma}$ transition of the $492\,\mathrm{nm}$ helium line for two perpendicular positions of the polarizer in the DPP. Conditions: $V = 1200\,\mathrm{V}$, $f = 15\,\mathrm{kHz}$, $d = 150\,\mathrm{\mu m}$. Adapted from [107].

Figure 5.28 shows a spectrum of the helium line pair under consideration at $492\,\mathrm{nm}$ within the DPP. Here, the polarization filter was set horizontally and vertically to the dielectric or to the bottom of the trench. It becomes clear that the forbidden component is not changed. However, a clear shift in the allowed component can be seen. This is due to the $[2,1]^{\sigma}$ component. This is the only component of the fit that contains only one type of polarization (π/σ) and is therefore sensitive to the direction of polarization. The observed emission of the $[2,1]^{\sigma}$ component is generated by the

electric field component that is perpendicular to the polarizer's transmission direction. From this relationship, the dominant electric field direction can be determined below. For better illustration, only the fit of the $[2,1]^\sigma$ component is plotted in Figure 5.28 and not the entire fit over all components. To determine the electric field strength, the distance between the field-free component and the $[2,1]^\sigma$ component was considered in this case.

The polarizer can be rotated incrementally to check the dominant electric field direction. The alignment of the filter at 0° corresponds to a measurement of the x-component. The z-component, on the other hand, can be measured at ±90°. The results are shown in Figure 5.29 for IPP and DPP. It is evident that, as previously observed, the field strength in the DPP is higher than in the IPP. In addition, an angular dependence can be seen in the DPP. The component in x-direction is significantly larger than the component in z-direction. The field strength of the IPP, however, does not show a dominant component. The error bars shown for the

Figure 5.29: Phase-resolved field strength components as a function of the rotation of the polarization filter. Conditions: V = 1200 V, f = 15 kHz, d = 150 µm. Adapted from [78].

first and last result are from the wavelength calibration of the spectrometer.

When looking at a static analysis of the direction-dependent field strengths by COMSOL (see Figure 5.30), the measurement results discussed above seem surprising. Here, in the middle of the trench or near the dielectric, the field in the z-direction exceeds the field in the x-direction. However, this contradiction to the measurements can be resolved again with the spatial distribution of charges neglected in the simulation. In the DPP, the discharge ignites centrally in the trench or in front of the dielectric surface. This means that charges are deposited on the surface that shield the field, particularly in the z-direction, thus resulting in the measured x-component being stronger than

Figure 5.30: Static COMSOL simulation of the field strength of the x-component (a) and z-component (b) in a trench at 200 V applied voltage. Adapted from [107].

the z-component. In the IPP, the discharge ignites in the upper area of the trench or even in the area above it, so that the effect of the shielding surface is significantly lower. Furthermore, the simulation shows that the calculat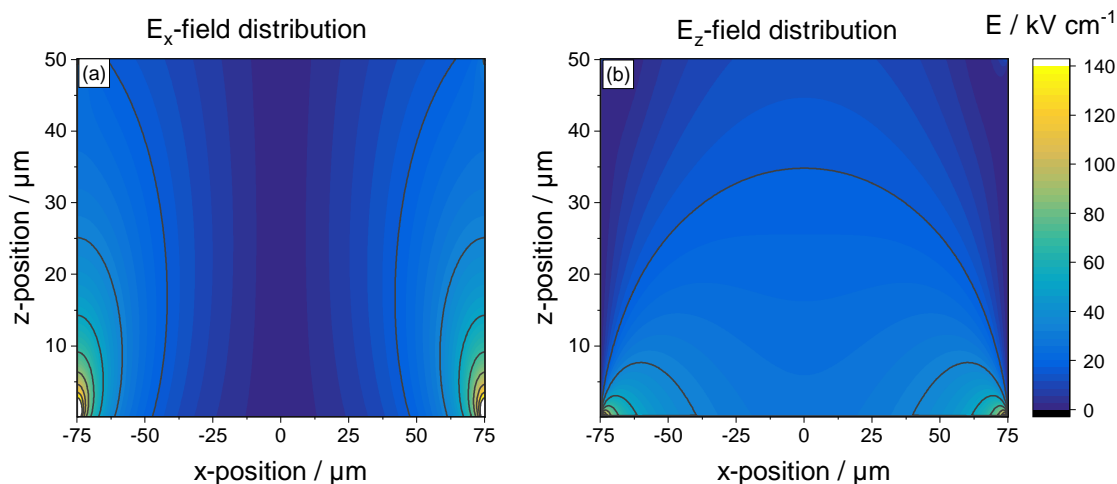ed field strengths for x- and z-components are of the same order of magnitude in the upper area where the discharge mainly ignites, which explains the non-angle-dependent behavior.

5.4 Outcome: Usability for plasma catalytic systems

In summary, the results presented in this chapter highlight the interaction between (surface) charges and the electric field and their impact on discharge dynamics, which could answer the first three research questions. By combining various diagnostic techniques, a comprehensive picture of the discharge characteristics emerges, particularly distinguished by its quasi-pulseless glow character, which sets it apart from typical streamer-dominated discharges. Thereby, the reactor exhibits properties of both volume and surface DBDs due to its cavity structure. Notably, the influence of surface charges and the resulting memory effect are significant.

Furthermore, the results demonstrate that the micro cavity plasma array is an exciting reactor for investigating plasma-catalytic mechanisms. Within the cavities, high electric fields prevail, accelerating charge carriers which can drive plasma chemical reactions. The measurements also indicate that charge carrier transport is directed

primarily towards the dielectric surface, which can be spray-coated with a catalyst. Here, the transport of plasma species (charge carriers, excited atoms or molecules, reactive species) to the surface can trigger new catalytic processes or lower the temperature required for the reaction. Furthermore, the asymmetry of the two half-phases can help to address different aspects of plasma catalysis. While in the DPP the interaction with the surface is in the foreground, in the IPP a larger gas volume can be treated, as the discharge also ignites outside the cavity.

From the results shown here, it follows that the micro cavity plasma array is suitable for the application of plasma catalysis. But above all that, the reactor is exceptionally suitable for systematically investigating the fundamental mechanisms of plasma catalysis. The diagnostics shown here can, for instance, be used to study how surface charges influence plasma-catalytic reactions. Additionally, these methods can be employed to control the memory effect, thereby setting the electric field distribution and tailoring the transport of charge carriers, which could be beneficial for plasma-catalytic systems. By measuring conversion rates as a function of the surface charges or the tuned field distribution, the various processes can be decoupled and the dominant mechanisms identified.

6 Characterization of the reactive model system oxygen

In order to approach the overall goal of plasma catalysis in a micro cavity plasma array, a model system consisting of helium and molecular oxygen is investigated in the following. This system is used to observe the effect of molecular gases and reactive species on the discharge. In addition, diagnostics, e.g. for the determination of species densities, can be tested. The choice of oxygen is particularly suitable for plasma catalysis, as it is required for the oxidation of molecules such as n-butane. In addition, oxygen can interact with the catalytic surface and, for example, activate it or prevent it from coking. For this reason, the gas is needed for the subsequent application in any case, but is easier to analyze than more complex molecules such as n-butane, methane or carbon dioxide due to the less complex plasma chemistry. By understanding the model system oxygen, optimal operating parameters or reactor designs, e.g. for the conversion of gases, can then be determined in a next step in order to prepare studies with more complex molecules and catalytic surfaces.

To characterize the oxygen system, the discharge dynamics are first compared to the previously discussed pure helium system. This addresses the question of how oxygen influences the discharge and whether the discharge mode changes. In the final part, the effectiveness of molecular oxygen dissociation and the resulting density distribution is examined. The densities of atomic oxygen is determined both within the cavities and in the area above them. By linking these measurements, insights into the transport of reactive species can be gained.

6.1 Discharge mode transition: from helium to oxygen

It is known from the literature that adding oxygen to helium can drastically change the discharge mode (see section 2.1.2). To verify this in the micro cavity plasma array, the previously discussed helium mode is used as a starting point, and oxygen is incrementally added. The changes in the discharge are observed using various diagnostics, such as power measurements, optical ICCD imaging, and electric field measurements.

6.1.1 Dissipated power depending on the oxygen admixture

A very simple method to observe the influence of the admixture on the discharge is to measure the dissipated power. For this purpose, a voltage variation was carried out for different oxygen admixtures (see Figure 6.1 (a)). It can be seen that the already known linear dependency after ignition is maintained. However, both the ignition voltage and the slope of the curve change with the admixture. As a result, in the measurements shown here, the dissipated power decreases with the added oxygen for a given applied voltage. Nevertheless, since the slope of the voltage increases with the admixture, it can be assumed that this behavior is reversed at higher voltages resulting in the dissipated power with admixture being higher than without admixture. Unfortunately, this could not be investigated with the discharge used.
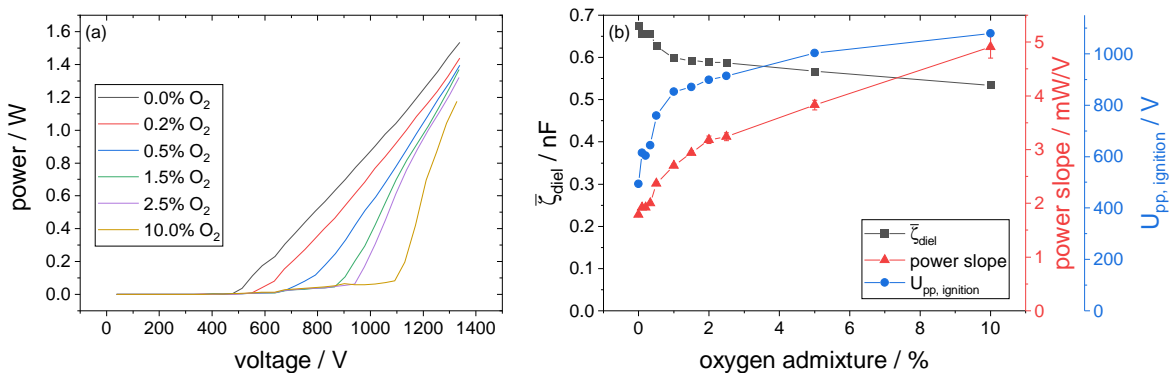

Figure 6.1: Power depending on the applied voltage for different oxygen admixtures(a) and power slope, ignition voltage and ζ_{diel} (b) depending on the oxygen admixture. Conditions: $V_{pp} = 1200\,V$, f $= 15\,kHz$, d $= 200\,\mu m$, 950 mbar helium atmosphere. Adapted from [159].

For better comparability, the slope of the power and the ignition voltage are shown

as a function of the oxygen admixture (see Figure 6.1 (b)). In addition, the QV-plots of the measurements were evaluated and ζ_{diel} was determined, which represents the capacitance in the case of a short-circuited discharge (active phase) (see section 3.1.2). As previously observed, the slope and the ignition voltage increase with the addition of oxygen. The ignition voltage starts at approximately $500\,\mathrm{V}$ and initially rises steeply up to an admixture of 1% and $900\,\mathrm{V}$, leveling off and saturating in a range of $1100\,\mathrm{V}$. The power slope behaves similarly and also rises steeply at first and levels off at approximately 1%, although it does not saturate but continues to rise monotonically. ζ_{diel} shows the opposite trend and initially decreases steeply before continuing to decrease monotonically flatter from 1% admixture. Once the various variables have been determined, the power curves can again be described using equation 5.3, which specifies the power in volume DBDs.

Although the power curves can still be explained with the same model and are quite similar, certain parameters such as ignition voltage and capacity are highly dependent on the admixture. For the ignition voltage, this is already known from the literature and can be attributed to various reasons [38]. On the one hand, part of the energy of the discharge is used for the excitation of vibrational and rotational states of the oxygen molecule and is therefore no longer available for ionization. On the other hand, the EEDF is influenced because additional loss processes such as electron attachment can take place. In addition, metastable helium atoms, which can support ignition, are very effectively quenched by oxygen. A higher voltage is therefore necessary to compensate for these losses. The course of ζ_{diel} can also be explained physically. This value indicates the degree to which the discharge channel is filled with a discharge and is therefore short-circuited. In the case of the MCPA, the drop depending on the admixture can have two causes. Firstly, the number of ignited cavities may decrease. This would be reasonable as the ignition voltage increases. If there are now differences in the electrode distances between the different cavities, for example due to inaccuracies in the construction, the ignition criterion (dependence on distance and voltage) could no longer be fulfilled. On the other hand, the discharge may no longer completely fill the individual cavity, but instead form filaments, for example, which is discussed in more detail later.

Even if the trends of the quantities discussed above are comprehensible, the exact curves still indicate a mode transition. The change is very strong for small admixtures and becomes smaller for higher admixtures. It is also noticeable that all curves show a dip or bump at approximately 0.3% admixture, which is reproducible. This cannot yet be explained on the basis of this measurement, but is taken up again later.

6.1.2 Spatially and temporally resolved imaging of the discharge

The transition of the discharge mode can be observed even more precisely using ICCD images. In Figure 6.2 (a), the discharge was imaged on the ICCD in such a way that only nine individual cavities can be seen, which enables a very high spatial resolution (1.4 µm per pixel) within a single cavity. The Figure shows an image from the IPP and DPP for a pure helium discharge as well as for an oxygen admixture.

(a) 2D resolved emission   **(b)** Mean cavity filling
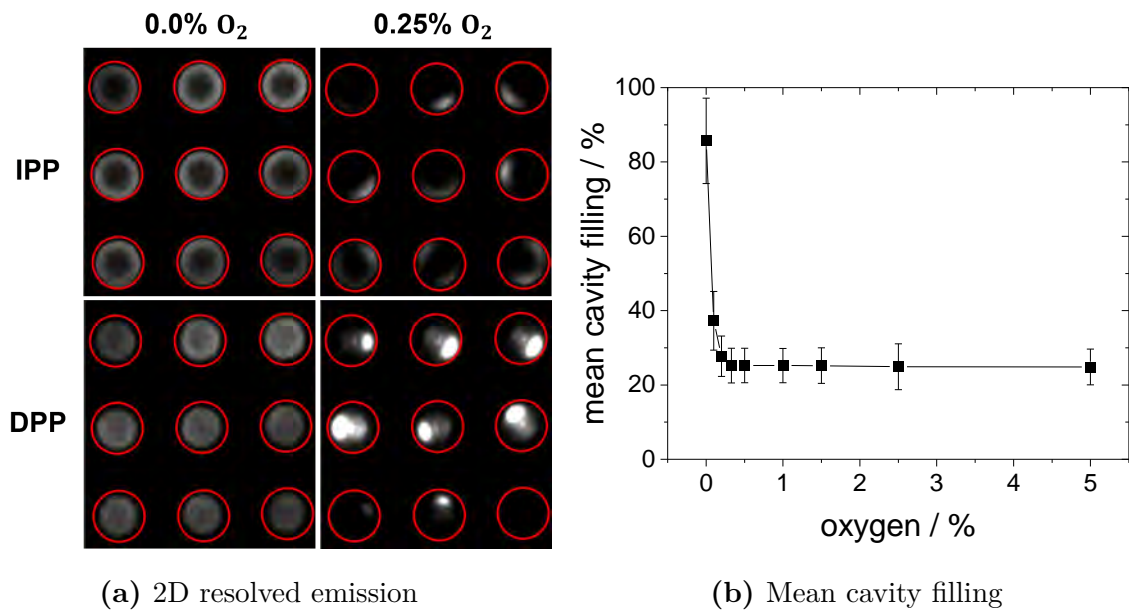
Figure 6.2: 2D resolved emission and mean cavity filling depending on the oxygen admixture. Conditions: $V_{pp} = 1200\,V$, $f = 15\,kHz$, $d = 200\,µm$, gate time = $200\,ns$ (for IPP and DPP each in the center of the half phase), exposure time = $25\,ms$. Adapted from [159].

Without admixture, the already known asymmetrical temporal characteristic between IPP and DPP is visible [22, 28, 77]. In the IPP, the discharge ignites mainly at the

edges, creating a ring structure in the emission, whereas in the DPP, ignition tends to occur more in the center of the cavity. This can again be attributed to the different directions of electron movement. However, a different picture emerges with the addition of oxygen. In the IPP, although a ring structure also forms, it is much less pronounced and in some cases does not extend over the entire circumference of the cavity. The difference is even more striking in the DPP. Here, the emission is particularly strong at a certain edge region and decreases towards the opposite side. The location of this edge region differs from cavity to cavity and appears to be randomly distributed. On closer examination, an emission structure reminiscent of striations is noticeable in the DPP. These can be caused, for example, by an attachment instability, which is known to occur in electro-negative gases such as oxygen [160]. Here, an increase in electron density leads to a reduction in the electric field through shielding. As a result, the electrons are accelerated less, so that the electron temperature drops. At lower temperatures, however, the attachment rate decreases and the loss of electrons is reduced, which effectively leads to a further increase in electron density and the cycle starts all over again. Typically, a longitudinal electric field is required for this instability. This fits very well with the previous results in which a dominant electric field was determined within the DPP in x-direction parallel to the dielectric (see section 5.3.2). While a homogeneous discharge forms in the entire cavity in pure helium, individual filaments form at one location with the addition of oxygen, which can then propagate along the dominant field. Even if propagation in the x-direction dominates, a z-component (e.g., from the upper grid edge to the dielectric) may also be present. However, this cannot be observed, as integration takes place in this direction. It must also be noted that the electric field distribution with admixture can be significantly more complex. On the one hand, the filamentary discharge strongly influences the field in a location-dependent manner. On the other hand, the filaments cause surface charges to be concentrated rather than evenly distributed on the dielectric, leading to a complex field distribution within the cavity.

Overall, it is noticeable that the emission range becomes smaller with admixture, which may indicate a transition to a filamentized discharge. For this reason, Figure 6.2 (b) shows the mean cavity filling as a function of the admixture. The proportion of the

total cavity size accounted for by the discharge or emission was evaluated here. There is a clear drop that starts for pure helium at approximately 86% filling and falls to 25% filling with an admixture of 0.5% oxygen and saturates there. This curve is in good agreement with the previously discussed ζ value, which likewise indicates the surface occupancy to a certain degree. Similar arguments can be introduced here as well. For example, the increased quenching means that in some regions of the cavity, the ignition criterion is no longer fulfilled due to the lack of metastables. Furthermore, a reduction in the size of the discharge is known from the theory of streamers. Here, the radius of a streamer is related to the change in the ionization coefficient with the electric field. In the case of electronegative gases, however, the ionization coefficient must be corrected by the attachment rate resulting in a reduction of the radius [19].

Time resolved imaging of a single cavity

The discharge mode transition becomes particularly clear when the emission of a single cavity is displayed time-resolved (see Figure 6.3). The ICCD images shown above (Figure 6.2) were used here and one cavity was cut out in each case. For each image, the measurement point within the voltage period is shifted by 200 ns in order to achieve a time resolution. One cavity is then cut out of each image and the average intensity is plotted against time. The period begins with the IPP, followed by the DPP. In pure helium, the emission structure is comparable to the structure already known from photomultiplier measurements. However, the different cavities are not superimposed here, making the individual pulses appear much narrower. The APGD mode already discussed, or a quasi-pulseless glow discharge, becomes clear. This changes drastically when oxygen is added. Initially, the emission decreases (not shown here due to normalization). This was to be expected due to the quenching. However, the emission structure also changes fundamentally. Individual, clearly separable discharge pulses can be seen. Here, IPP and DPP differ significantly from each other. In the DPP, the pulses are clearly separated from each other and the discharge extinguishes in the meantime (pseudo-glow), whereas in the IPP, emission can still be seen between the pulses. The DPP shows the emission structure known from the literature with the strongest emission at the beginning and a decreasing intensity with each subsequent pulse. This behavior is known for pseudo glow discharges [37]. The volume memory

effect offers an explanation. With each pulse, volume charges and metastable species are created which can partially survive until the next pulse. These can support the ignition so that lower fields are required. However, this means that the charge carriers are less accelerated and multiplied, resulting in a weaker pulse. As the effect accumulates with each pulse, the subsequent pulses become weaker and weaker.

No clear structure can be seen in the IPP. In many cases, however, the strongest emission can be seen in the middle of the half-phase. The greatest change in the discharge characteristic is noticeable as soon as a very small amount of oxygen is added. If the concentration is increased further, the emission changes only slightly, for example in the number of pulses. One reason for this could be the temporal averaging of the results. Although there is a time resolution of 200 ns, to achieve this it is necessary to accumulate over several periods. In the DPP, it appears that the timing of the pulses per cavity is very reproducible, whereas in the IPP, pulses from different periods are likely to overlap. This observation fits in with the characteristics of IPP and DPP discussed so far. During an ignition in the DPP, the electrons are accelerated into the cavity. The region in which ignition occurs is determined by the geometry (point with the smallest electrode distance) and is therefore very reproducible. In the IPP, the electrons are accelerated out of the cavity. This means that the volume in which ignition takes place is much larger, which generally leads to a more diffuse appearance. Here, the ignition criterion can be fulfilled at different locations at different times. In addition, external effects such as volume charges from previous discharges or cosmic radiation can play a statistically greater role than in the DPP. On the one hand, this increases the absolute number of peaks, as the ignition criterion is more likely to be fulfilled, but on the other hand it can also lead to a superposition of peaks due to the higher randomness when averaging over time. The intensity distribution can thus likewise be discussed. It appears that the emission is significantly higher in the DPP than in the IPP. However, if integrated over the entire half-phase, these are comparable. This is due to the fact that in the DPP the emission is always accumulated at the same times, but in the IPP it is distributed over the entire half-phase.
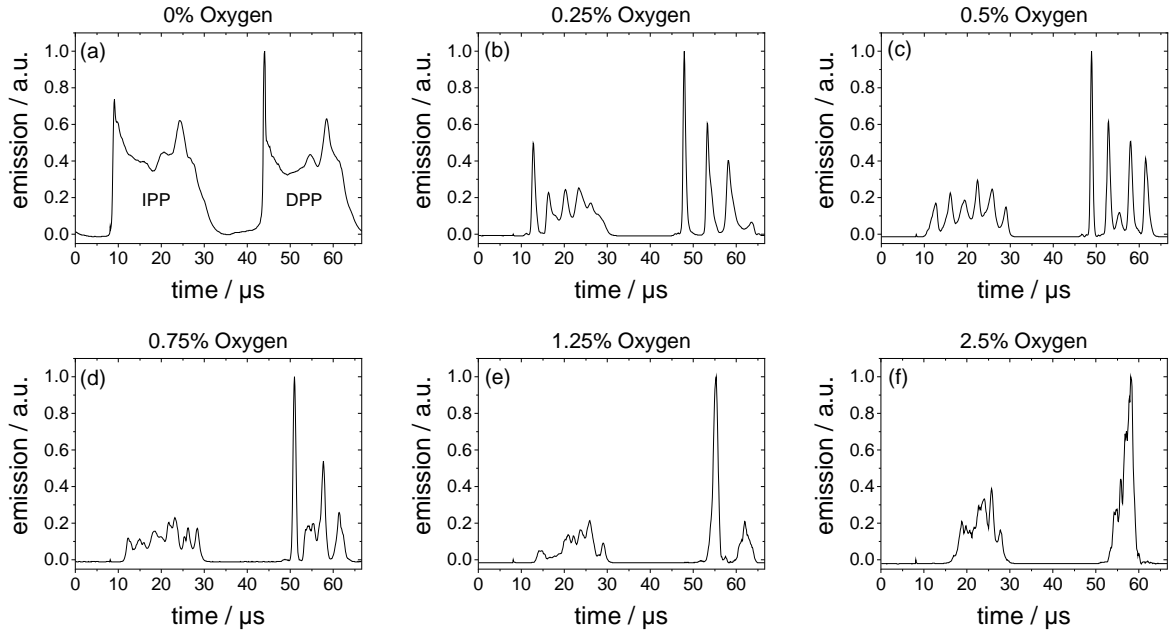
Figure 6.3: Emission of a single cavity depending on the oxygen admixture. Conditions: $V_{pp} = 1200\,\text{V}$, $f = 15\,\text{kHz}$, $d = 200\,\mu\text{m}$, gate time $= 200\,\text{ns}$, $950\,\text{mbar}$ helium atmosphere. Adapted from [159].

Imaging of single cavities depending on the oxygen admixture

The measurement was repeated with a lower resolution (changing the lens) in order to be able to investigate the change with the admixture in more detail. Although the spatial resolution is lower here, meaning that effects such as striations can no longer be observed, it is possible to record the entire cavity structure simultaneously. Features such as the number of discharge pulses, the duration of the discharge, the ignition time or the ratio of maximum to average emission can now be extracted from the measurements. Due to the high number of cavities, meaningful statistics are generated. The results are shown in Figure 6.4 for both IPP and DPP.

First of all, the number of discharge pulses (Figure 6.4 (a)) can be observed. In the case of pure helium, the initial ignition peaks of the half phases dominate here. This is followed by the quasi-pulseless glow. In some cases, further pulses occur at the end of the respective half-phases, resulting in a value of the number of pulses between 2-4. As soon as oxygen is added, individual pulses are visible. The number increases to approximately 6 pulses per half-phase up to an admixture of 0.33% and then decreases again. One explanation is a transition from a quasi-pulseless glow discharge to a pseudo-glow
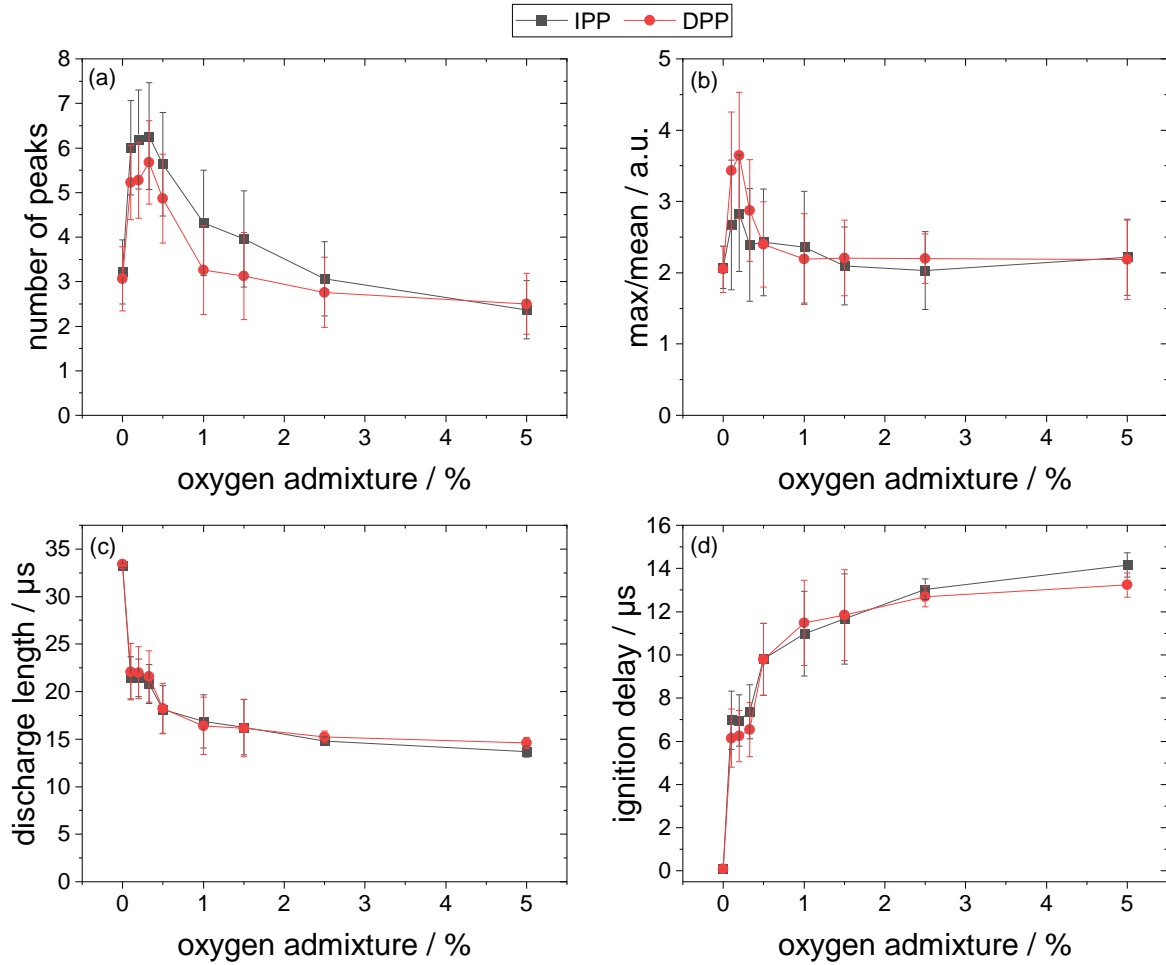
Figure 6.4: Number of peaks (a), ratio of maximum to mean intensity (b), discharge length (c) and ignition delay (d) depending on the oxygen admixture. $V_{pp} = 1200\,V$, f $= 15\,kHz$, d $= 200\,\mu m$, $950\,mbar$ helium atmosphere. Adapted from [159].

discharge, which can be carried less by metastable atoms due to quenching, but is subject to the same mechanisms within its pulses (see section 2.1.2). Thus, pulses become visible at times when the discharge was already igniting before, although without a pulse but only a glow. However, the more oxygen is added, the later the first pulse can ignite. As the pulses have a comparable width and period regardless of the admixture, it can be assumed that the number must decrease with high admixtures, as simply no more pulses can be added into the half-phase. In principle, more pulses can be observed in the IPP than in the DPP, which is related to the easier to achieve ignition criterion already discussed.

To confirm the previous results, another parameter, the ratio of maximum to mean

emission, can be considered (see Figure 6.4 (b)). This provides a measure of whether the discharge is dominated by pulses or by a continuous glow. As expected, the curve is similar to that previously observed for the number of pulses. In addition, it becomes clear once again that the DPP is dominated more by pulses than the IPP, which has already been described previously.

There are hardly any differences between IPP and DPP in the discharge duration or ignition time (see Figures 6.4 (c) and (d)). As the ignition voltage increases with the addition of oxygen, ignition is also increasingly delayed. This results in the discharge becoming shorter and shorter, as the end of the discharge is defined by the reversal point of the voltage and is therefore constant. Even if monotonically increasing or decreasing curves can be seen here and therefore no maximum or minimum occurs, a small dip between 0.2 and 0.33% admixture can still be seen. This is therefore exactly at the point where a maximum was seen in the number of pulses.

Overall, the measurement demonstrates the influence of oxygen on the discharge very well. In pure helium, a quasi-pulseless glow discharge prevails. If some oxygen is added, the discharge changes to a pseudo glow discharge. Here, individual glow discharges are still ignited, but the ignition criterion is no longer fulfilled instantaneously (quenching of the metastables), resulting in individual pulses. If the oxygen concentration is increased further, the metastables have less and less influence on the discharge, meaning that the individual pulses extinguish more quickly. Nevertheless, the discharge can re-ignite more frequently per half-phase. However, as the time of the first ignition occurs later and later, the time window in which ignitions can take place becomes shorter, causing the number of pulses to decrease again from a certain point. As previously seen in the ICCD images, the discharge continues to contract. Accordingly, with an admixture of approximately 1 % a further mode transition takes place here from homogeneous glow discharge (APGD) to a filament discharge, which is dominated by streamers.

6.1.3 Effect of oxygen on the electric field

The following results on the electric field were developed in collaboration with Henrik van Impel, whose thesis was supervised in the course of this dissertation. For this reason, some parts of the following section have already been published in the master's thesis entitled "Analysis of the electric field in a micro-scaled dielectric barrier discharge" (2023) [78].

Another parameter that clearly shows the mode transition of oxygen addition is the electric field. As described above, the electric field in the MCPA can be determined via the Stark splitting of a helium line pair. Figure 6.5 shows two spectra of the helium 492 nm line, which is used for diagnostics, for different oxygen admixtures. At a low addition of 0.25%, the spectra are comparable to the previously discussed spectra in pure helium. The splitting into allowed and forbidden components is evident. The field-free component plays a subordinate role. In comparison, the spectrum with a higher oxygen admixture of 2% differs significantly. Here, the allowed and forbidden components are closer together. In addition, the field-free component makes up a dominant part of the spectrum. This means that the measured electric field is lower and there are even areas in the discharge where the field is completely shielded. Furthermore, it is noticeable that the fit no longer fits the data perfectly, especially on the outer edges. One reason for this could be that the emission is integrated over the entire cavity. In the case of a non-homogeneous discharge, areas with higher and lower electric fields occur here. The more different the fields are, the more components would have to be taken into account in the fit.

Overall, the measurements fit very well with the already discussed mode transition to a filamentary discharge. Filamentary discharges can be described with the streamer mechanism. There are two regions here. The streamer head and the streamer channel. Very high electric fields prevail in the streamer head, which are sufficient to ionize further. If the emission from this region is measured, very high fields and thus a large displacement of the allowed and forbidden lines can be expected. However, the magnitude of these fields can vary, since not only one cavity, but an entire cavity structure is spatially integrated and additionally temporally integrated over several periods. As
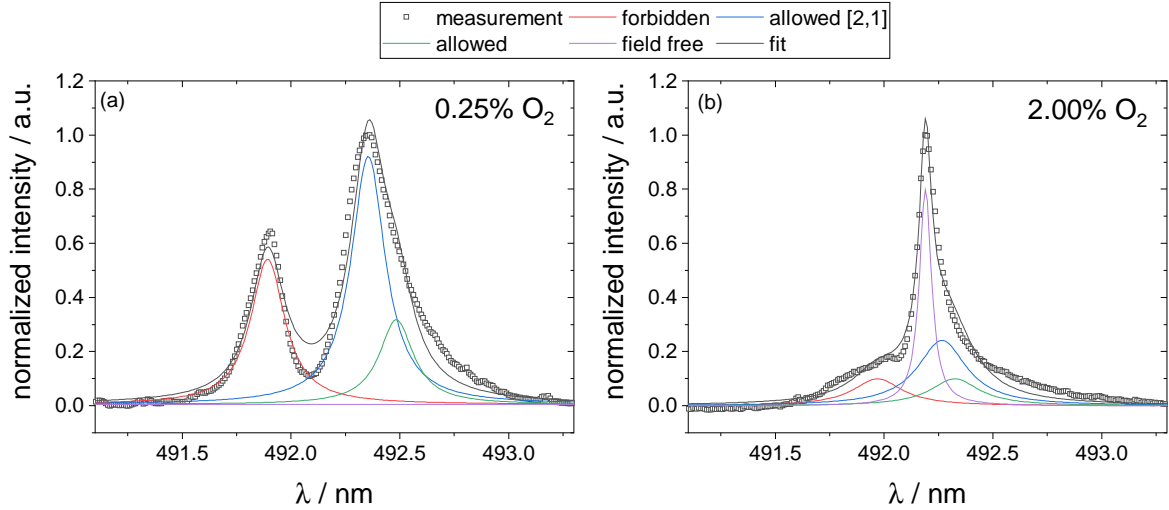
Figure 6.5: Fit of the 492 nm helium line within the DPP to determine the electric field for 0.25% (a) and 2.00% (b) oxygen admixture. Conditions: 2 slm He; 600 V; d = 150 µm. Adapted from [159].

a result, the measured spectrum actually consists of many different displaced lines, which lead to smearing out and uncertainty in the fit, particularly at the outer edges, as only the mean value can be taken into account here. Due to the high charge carrier densities, a shielded quasi-neutral area is created in the streamer channel. Emission from this part of the discharge should therefore not be influenced by an electric field and thus leads to a dominant field-free component in the spectrum.

To further analyze the transition, the electric field is plotted as a function of oxygen admixture (see Figure 6.6). The electric field values range from 20 to 35 kV/cm, aligning with previous studies on pure helium [28, 107]. The fitting uncertainty, estimated to 5 kV/cm, is not displayed in the plot for clarity. Notably, the electric field initially increases with rising oxygen admixture, consistent with earlier findings that show the ignition voltage shifts with increasing admixture, requiring higher electric fields for ignition. However, between 0.25 % and 0.5 % admixture, the measured electric field begins to decrease, which can be attributed to the transition to a streamer-based discharge. In this regime, the high density of charge carriers forms a shielded, quasi-neutral channel. This transition is also evident from the increase in the fraction of the field-free line (also shown in Figure 6.6).

In addition to this mode transition, a distinction is observed between the IPP and DPP. In the IPP, a field-free component appears even at lower admixtures, while in the DPP, no such field-free fraction is initially present. However, from 0.25 % admixture onward, there is a sharp increase in the field-free fraction in the DPP. This difference can be attributed to the larger discharge volume in the IPP, where the discharge extends beyond the cavity. Since the measurements are integrated over a larger volume, particularly

Figure 6.6: Electric field and fraction of the field-free line depending on the oxygen admixture. Conditions: 1 slm He; 600 V; d = 150 µm. Adapted from [159].

in regions farther from the electrode, the overall measured electric fields appear weaker. Moreover, the larger volume increases the likelihood of forming a positive column, which is characteristic of a quasi-neutral region in glow discharges. As the admixture increases, the field-free component in the IPP also rises, though more gradually, suggesting the onset of a filamentary discharge. However, as indicated by emission measurements, this transition is less pronounced compared to the DPP, indicating that the IPP maintains a relatively diffuse, homogeneous discharge.

In contrast, the DPP behaves differently. No field-free component is observed in pure helium, as the discharge remains confined to the cavity where the electric fields are strongest. As the admixture increases, a clear transition in discharge mode occurs between 0.25 % and 0.75 %, with the field-free fraction rising sharply to 0.8. This indicates the formation of a filamentary discharge with a quasi-neutral channel, as shown in Figure 6.2.
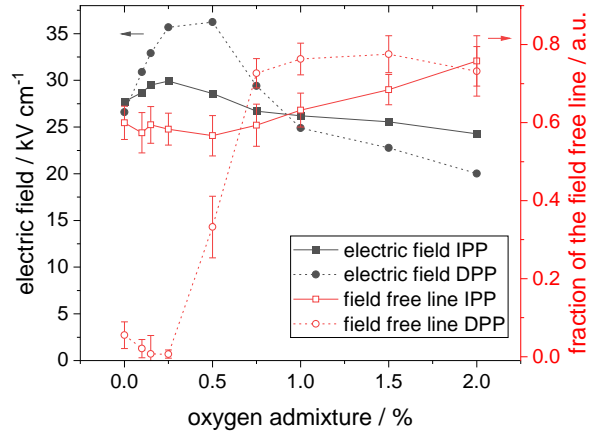
6.2 Spatially resolved densities within micro cavities

Parts of this chapter about SEA measurements within the micro cavity plasma array have already been published [110].

After discussing the transition from a pure helium discharge to a discharge with reactive admixture, atomic oxygen densities in a helium-oxygen discharge are determined in the following. For this purpose, 2D spatially resolved measurements are carried out and parameters such as cavity diameter, applied voltage or oxygen admixture are varied. Helium state enhanced actinometry is used as the diagnostic method, with the advantage that also mean electron energies can be determined simultaneously.

6.2.1 Determination of the gas temperature

If particle densities are to be determined, knowledge of the gas temperature is essential, since this directly influences the density through the ideal gas law. For using energy resolved actinometry, the gas temperature is even more crucial. On the one hand, the temperature is a key parameter for Boltzmann solver calculations. On the other hand, the ideal gas law is used to estimate the quenching of the used excited states, making the knowledge of the gas temperature indispensable. In the following, the gas temperature is determined using the rotational temperature derived from the first negative band of the nitrogen ion (see subsection 3.2.3).
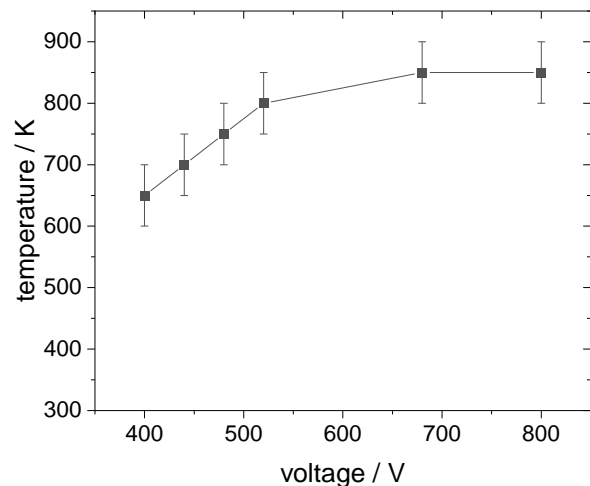

Figure 6.7: Rotational temperatures as a function of voltage derived from the first negative band of the nitrogen ion. Conditions: $2\,\mathrm{slm}$ He, $2\,\mathrm{sccm}$ O_2, $1\,\mathrm{sccm}$ Ar. Adopted from [110].

Figure 6.7 shows the calculated rotational temperatures as a function of the applied voltage. Between 400 and 520 V, the temperature increases linearly from 650 to 800 K. At higher voltages up to 800 V, the temperature saturates and reaches a maximum of 850 K. The temperature range as well as the course of the temperature is known from other micro discharges [18, 161] or DBDs [162]. At low voltages, the plasma is confined in the cavities, where the temperatures are highest due to the strong electric fields. When the voltage is increased, the plasma volume expands out of the cavities, where the electric fields are lower and the plasma species come into direct contact with the gas flow (room temperature) [77]. The losses lead to a saturation of the average temperature. However, no spatial resolution in z-direction can be achieved using this method, so that a temperature gradient, for example with hot temperatures at the bottom of the cavity, cannot be ruled out.

6.2.2 2D spatially resolved density and energy distributions

With the previously introduced state enhanced actinometry (see subsection 3.2.2), atomic oxygen densities and mean electron energies can now be determined within the micro cavity plasma array. The actinometry setup described in section 4.2 is used for this purpose. The ICCD makes it possible to measure the emission of the discharge with 2D spatial and temporal resolution. The tunable filter can reach all wavelengths required for actinometry and switch between the different wavelengths within approximately 200 ms. The combination of ICCD and tunable filter provides a fast setup that is ideally suited for SEA. It allows to calculate the atomic oxygen density and mean electron energy for each pixel of the ICCD with the SEA model with only one measurement. An example measurement is shown in Figure 6.8 and is discussed in the following.

Prior to each measurement, the temperature of the gas was allowed to stabilize to ensure a state of equilibrium. This means that measurements are averaged over at least 75,000 periods. Figure 6.8 (a) shows the atomic oxygen density for a sub-array structure of a quadruple structure array with a cavity diameter of 200 µm. The voltage is 800 V with an oxygen admixture of 0.1%. All except five cavities are ignited. The deviations can be attributed to manufacturing inaccuracies.
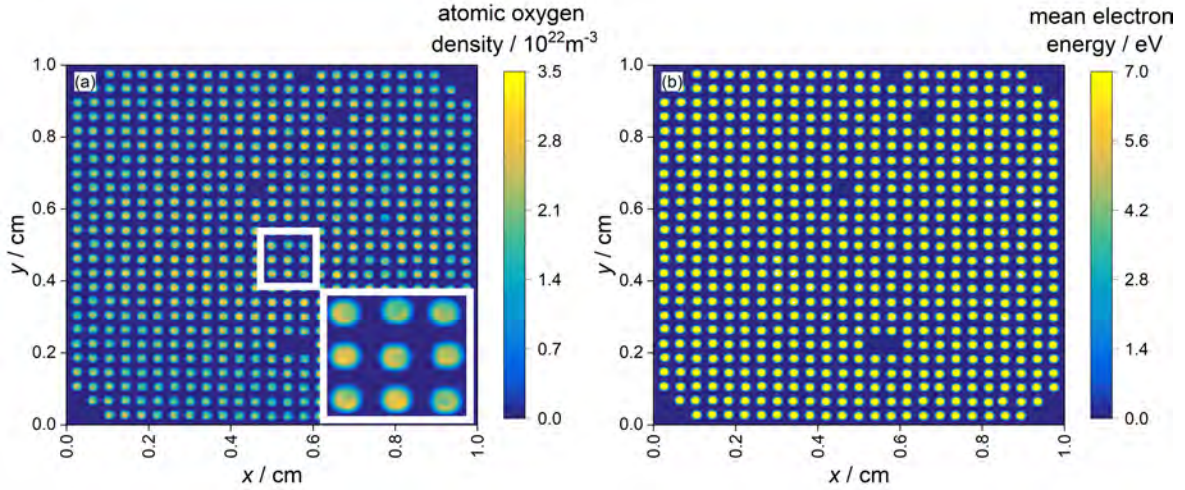
Figure 6.8: 2D resolved oxygen densities (a) and mean electron energy (b). Conditions: $2\,\text{slm}$ He, $2\,\text{sccm}$ O_2, $1\,\text{sccm}$ Ar; $800\,\text{V}$; $d = 200\,\mu\text{m}$; exposure time $= 5\,\text{s}$, adopted from [110].

Overall, atomic oxygen densities in the range of $10^{22}\,\text{m}^{-3}$ were measured. This is associated with a degree of dissociation of almost 100%, which implies that the molecular oxygen is completely converted in the cavities. Very high dissociation degrees were previously expected due to the high electric fields [28]. Moreover, additional oxygen sources, which are not considered in the set gas flow, can affect the degree of dissociation. For example, if oxygen is deposited on the nickel grid or the dielectric between two discharge pulses and is released again within a discharge pulse, the fraction of oxygen in the gas composition increases. Although the high densities in this case appear reasonable, the absolute values should not be overemphasized because of the uncertainties associated with the method used.

Considering the 2D distribution of atomic oxygen, it is noticeable that in the center of the sub-array structure the density is higher than at the edges. One possible explanation for this is a temperature distribution across the cavity structure, in which higher temperatures are present in the center than at the edges due to the higher cavity density. However, only spatially integrated temperatures can be determined by the OES measurements. If the temperature at the edge is lower than assumed, the density at this position is underestimated.

The associated mean electron energies (shown in Figure 6.8 (b)) are in the range of 6-9 eV, which is comparable to the literature [75, 163]. Furthermore, the electron energy is also consistent with the known electric fields within the plasma bulk in the range of 30 kV/cm [28, 77]. With a mean free path length of about 2 µm, electrons can gain about 6 eV between two collisions from the electric field. Overall, the mean electron energy varies much less than the oxygen density and remains almost constant across the sub-array.

Density distributions in single cavities depending on the diameter

In addition to a density or energy distribution over the entire sub-array structure, distributions within individual cavities can also be investigated. Figure 6.8 shows that the atomic oxygen density is higher at the edges than in the center of the cavity. This fits well with the fact that the electric field is higher at the edges than in the center [28]. Even if the local resolution is sufficient to observe the distribution of individual cavities, the evaluation can be improved even further by averaging several cavities. For this purpose, all individual cavities from Figure 6.8 are accumulated to an average cavity. The results for three different cavity diameters (100, 150 and 200 µm) are shown in Figure 6.9 for atomic oxygen density and mean electron energy.

The previously observed ring structure becomes even more clearly visible here. However, the overall variation of density and energy within a cavity is small (10%). Even if the ring-shaped distribution of density and energy matches the measurements of the electric field, these must be critically reviewed. The cavities shown in Figure 6.8 all have in common that the density at the edges is higher than in the center. However, not all of them show a ring structure, but in some cases a non-symmetrical concentration of density on one side of the cavity. By averaging over many cavities, where the distribution is increased on a coincidental side at the edge, a ring structure is created as well. This argument is supported by ICCD measurements at high oxygen admixture and higher spatial resolution (see Figure 6.2 (a)). Here, a strong contraction of the discharge at the edges is also observed. Overall, it can therefore be concluded that although the ring structure is real for most cavities, it is amplified by averaging over many cavities. However, since the general behavior is discussed in the following and
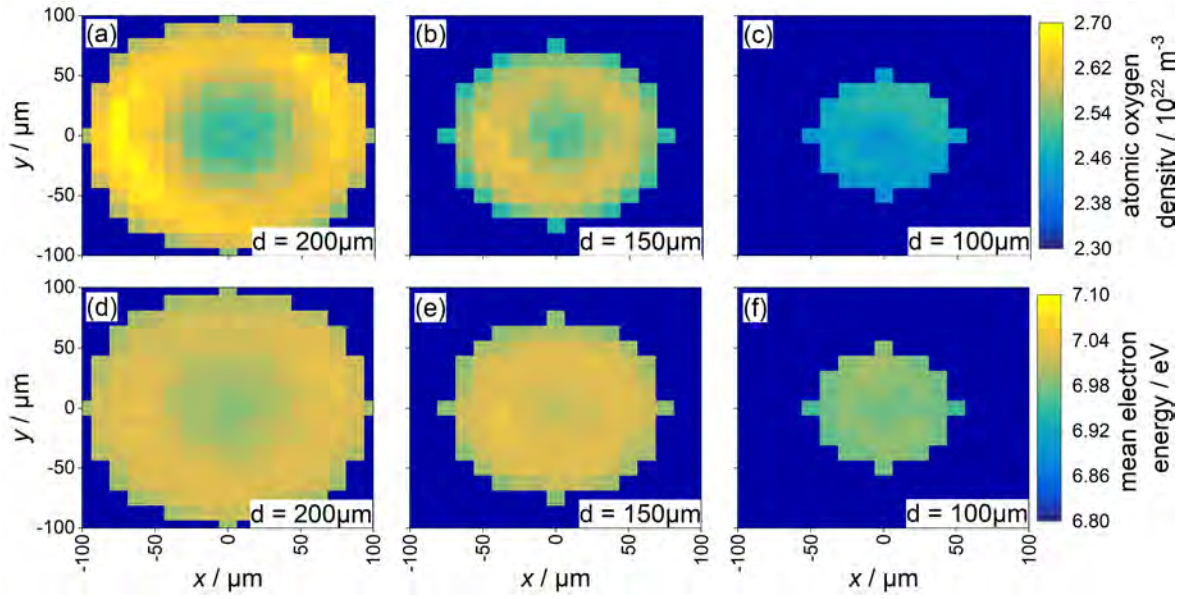
Figure 6.9: 2D resolved oxygen densities (a-c) and mean electron energies (d-f) for different cavity diameters (100-200 µm). Conditions: 2 slm He, 2 sccm O_2, 1 sccm Ar; 800 V; exposure time = 5 s, adopted from [110].

only low oxygen additions are used, in which the discharge is very homogeneous and not contracted, the averaging approach is retained.

The variation of the cavity diameter is mirrored in the ring structure. Nevertheless, this is no longer as pronounced at smaller diameters, since the electric fields from the edges are superimposed. Also oxygen density and electron energy stay of the same order of magnitude. However, the resolution of the setup is limited, resulting in a decrease in the number of ICCD pixels per cavity for small diameters. For this reason, cavities with a diameter of 50 µm could not be evaluated and only the cavities with a diameter of 200 µm is discussed below.

6.2.3 Dependencies on external parameters

In addition to spatial and time-resolved measurements, integrated measurements can be performed to determine the dependence on external parameters.

Voltage variation

The atomic oxygen density and mean electron energy is shown as a function of the applied voltage in Figure 6.10. The mean electron energy was found to be 6.9 eV, independent of the applied voltage. The atomic oxygen density decreases from 2.9 to $2.3 \cdot 10^{22}$ m^{-3}, reaching a plateau at 520 V. This decrease can be explained by the increase in temperature (see Figure 6.7). While the gas temperature increases with the voltage by a total of about 20%, the density decreases by about 20%, making the change in density determined by the ideal gas law. However, this implies that the degree of dissociation remains constant and is independent of the voltage.
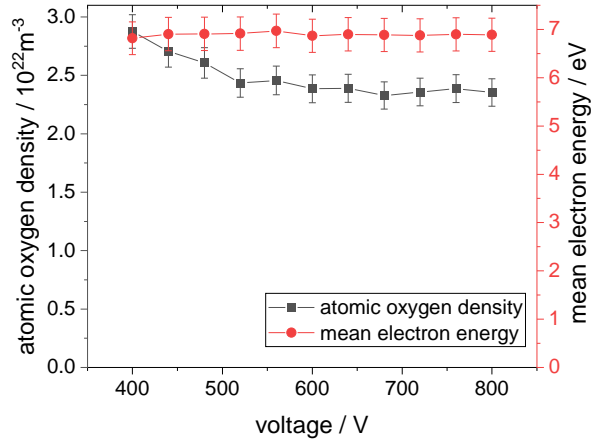
Figure 6.10: Atomic oxygen density and mean electron energy as a function of voltage. Conditions: 2 slm He, 2 sccm O$_2$, 1 sccm Ar; d $= 200\,\mu$m, adopted from [110].

The fact that the degree of dissociation remains constant regardless of the applied voltage is consistent with the measured oxygen densities, which are very high. Even low voltages of 400 V are sufficient to completely dissociate the admixed oxygen, and thus higher voltages can no longer increase the density.

The constant mean electron energy, on the other hand, is a consequence of the characteristics of a dielectric barrier discharge. This ignites independently of the applied voltage amplitude at a certain ignition field strength. By varying the voltage amplitude, the ignition time and the number of ignitions per period can be increased, but the ignition voltage remains constant. As a consequence, the electric field in which the

electrons are accelerated remains almost constant [28], and so does the mean electron energy. In addition, the EEDF is mainly dependent on the gas composition, which remains the same. Furthermore, even at low voltage, the electron energy is sufficient to drive all processes such as ionization and dissociation, thus when the voltage is increased, no further processes are induced and the shape of the EEDF remains the same. However, since the intensity of the emission increases with increasing voltage, it can be assumed that the electron density increases.

Oxygen admixture variation

A different picture emerges when the oxygen admixture is varied (Figure 6.11). Here, the atomic oxygen density and the mean electron energy show a significant dependence on the oxygen concentration. Between 0.01 and 0.15% admixture, the oxygen density increases linearly. Within this regime, the oxygen is completely dissociated, thus an increase of the admixture leads to an increase of the density. At higher admixtures, the degree of dissociation slowly decreases, causing the atomic oxygen density to further increase, although the slope decreases. The mean

Figure 6.11: Atomic oxygen density and mean electron energy as a function of O_2-admixture. Conditions: $2\,\mathrm{slm}$ He, $1\,\mathrm{sccm}$ Ar; $700\,\mathrm{V}$; $d = 200\,\mu\mathrm{m}$, adopted from [110].

electron energy behaves similarly. Initially, it increases steeply in the 0.01-0.15% admixture range from 6 to $7\,\mathrm{eV}$. Afterwards, the slope decreases and reaches $9\,\mathrm{eV}$ at 2.5% admixture. This behavior can be explained by the additional oxygen molecules. These can strongly influence the EEDF. On the one hand, additional vibrations and rotational states are excited. On the other hand, quenching is significantly increased, which leads to a lower ionization and electron density, requiring higher energies to maintain the plasma. In addition, low-energy electrons can be consumed by processes such as electron attachment, which further increases the mean electron energy.
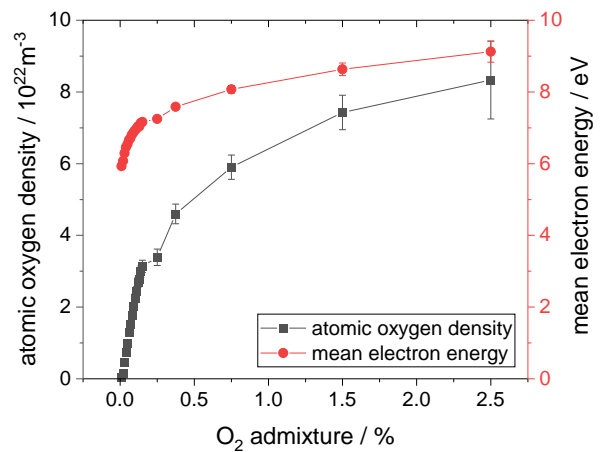
Both the atomic oxygen density and the mean electron energy show a dip between 0.25% and 0.5% oxygen admixture. Here, again the mode transition from a homogeneous helium glow discharge to a pulsed and contracted oxygen discharge is observed. The point of transition is very comparable to the results from section 6.1. Interestingly, the point of transition is exactly the point at which the degree of dissociation decreases (not shown here). This means that the discharge is only slightly disturbed by small admixtures. The molecular oxygen is completely dissociated so that only atomic oxygen is present in the discharge alongside helium. If enough oxygen is added to the discharge that it can no longer be fully converted, i.e. the degree of dissociation decreases, the transition begins. From this point onwards, molecular oxygen now also exists in the discharge alongside helium and atomic oxygen. This makes the composition of the discharge much more complex. In addition to the various atomic states, molecular states such as vibrational and rotational states can now also be excited. Furthermore, negative oxygen ions can be formed by electron attachment and quenching plays a significantly increased role. Through the interplay of these effects, the transition of the discharge mode can be explained very well by the change in gas composition.

6.3 Time-resolved characterization with oxygen admixture

As previously established, the addition of oxygen drastically changes the discharge dynamics. Since the two half-phases differ significantly and the discharge within each half-phase is pulsed, a time-resolved investigation is essential. For this purpose, the ICCD setup previously used for SEA can be utilized to examine not only the temporal properties but also further explore spatial properties. However, since this approach generates large amounts of data and thus makes the analysis complex, this method is only used for a fundamental understanding. A detailed analysis of the time-dependent atomic oxygen density and mean electron energy is therefore conducted using a photomultiplier setup. To evaluate and contextualize these measurements, they are compared to the time-dependent electric field in the following analysis.

6.3.1 Time-resolved ICCD SEA measurements

In addition to a high spatial resolution, the ICCD setup offers the possibility to perform time-resolved measurements. The micro cavity plasma array reactor is again operated with a bipolar triangular voltage, so that IPP and DPP can be compared with each other. The results shown here were each acquired with a gate time of 1 µs at half of the ignited IPP or DPP (10 µs prior to the reversal point at which the discharge extinguishes). Thus there is half a period (approximately 33 µs) between the measurements.
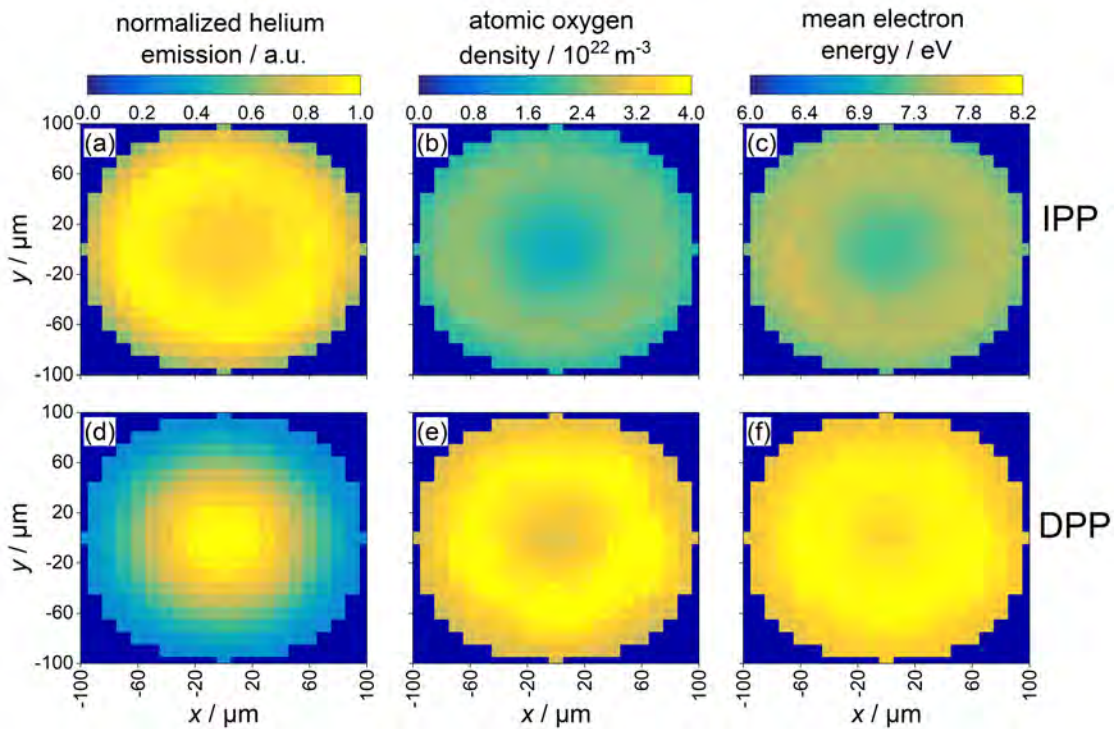
Figure 6.12: 2D resolved helium emissions ($\lambda = 706.5$ nm), oxygen densities and mean electron energies during the increasing potential phase (IPP) and decreasing potential phase (DPP). Conditions: 2 slm He, 2 sccm O_2, 1 sccm Ar; 700 V; d = 200 µm; exposure time = 10 s; gate time = 1 µs, adopted from [110].

Figure 6.12 (a) and (d) show the difference in helium emission ($\lambda = 706.5$ nm, each normalized to itself) between IPP and DPP. While the ring structure is again present in the IPP, the emission within the DPP is centered inside the cavity. Moreover, differences in the measured intensity can be identified. During the DPP, the maximum intensity is higher, however, averaged over the entire area of the cavity, it is lower than in the IPP.

The differences in emission are known from previous measurements and can be explained by different directions of the electric field and the associated electron motion [22, 28, 77]. Within the IPP, electrons are accelerated away from the dielectric cavity bottom towards the edge of the metal grid. Within the DPP, on the other hand, the electrons are accelerated into the center of the cavity in the direction of the grounded electrode. In addition to the different emission distribution, the change in the electric field also leads to a change in the local expansion of the discharge. While the plasma ignites concentrated in the center of the cavity in the DPP, it expands into the area above the cavity as well in the IPP, resulting in a larger plasma volume [22, 77].

Besides the emission, also the atomic oxygen density, and the mean electron energies differ between the IPP and DPP. Within the IPP, the atomic oxygen density reaches a maximum value of $2.5 \cdot 10^{22}\,\mathrm{m}^{-3}$ at the edge of the cavity. In the center, a minimum of $1.5 \cdot 10^{22}\,\mathrm{m}^{-3}$ is formed resulting in a ring structure (Figure 6.12 (b) and (e)). Significantly higher densities can be measured in the DPP. Here, a ring structure can also be seen, although there is a smaller relative difference between the center and the edge ($3.1 \cdot 10^{22}\,\mathrm{m}^{-3}$ and $4.0 \cdot 10^{22}\,\mathrm{m}^{-3}$, respectively). A similar picture appears when looking at the mean electron energy (Figure 6.12 (c) and (f)). This is also higher in the DPP compared to the IPP. However, the difference between the edge and the center is again significantly smaller in the IPP (7.9-8.2 eV and 7.1-7.6 eV, respectively).

The results fit very well into the previously described model of the different directions of electron motion. In the DPP, the electrons are accelerated into the cavity. The plasma ignites in a concentrated way inside the cavity. There, especially at the edges of the cavity, the highest electric fields and electron densities exist [28, 76], which can lead to a strong dissociation as well as heating of the electrons. In the IPP, on the other hand, the plasma expands further out of the cavity. The electric fields decrease with increasing distance from the cavity. In addition, the electrons are accelerated in different directions following the electric field, which results in a lower electron density. This leads to less dissociation, as well as lower mean electron energies. The difference in the ring structure can also be explained by this model. Due to the outward electron movement, the electrons are heated the strongest at the edges and the oxygen

dissociates. Within the DPP, the electrons are accelerated into the center, allowing high oxygen densities and mean electron energies to develop here as well. However, since the electric fields are at a maximum at the edges of the cavities, a ring structure manifests also here [28].

The asymmetry between IPP and DPP offers great potential for plasma catalytic applications. In the IPP, the plasma also ignites outside the cavities, allowing a large gas volume to be treated and, for example, VOCs to be converted. In the DPP, on the other hand, the plasma is in direct contact with the dielectric or a catalytic layer. This can be cleaned and activated. By adjusting the applied voltage waveform or electrode design, one of the two phases could be emphasized more strongly in order to enhance the respective desired effect and thus create optimum conditions for plasma catalysis.

6.3.2 Time-resolved photomultiplier SEA measurements

The following SEA results, which were measured using the triple photomultiplier setup were developed in collaboration with Henrik van Impel, whose thesis was supervised in the course of this dissertation. For this reason, some parts of the following section have already been published in the master's thesis entitled "Analysis of the electric field in a micro-scaled dielectric barrier discharge" (2023) [78].

The photomultiplier setup described in section 4.2 can be used to obtain even more detailed information on the time course. This is characterized by the fact that the three spectral lines used for SEA diagnostics can be measured simultaneously with one photomultiplier each. This allows the mean electron energy and atomic oxygen density to be calculated for each time step in the discharge. Figure 6.13 shows an example measurement with an oxygen admixture of 0.1% and a voltage of 600 V. It shows the applied voltage (without scale for the sake of clarity), the emission at 706 nm, the mean electron energy and the atomic oxygen density. In order to verify whether successive discharge cycles differ or whether the atomic oxygen density accumulates from different periods, a burst mode is used instead of the usual continuous waveform. This consists of 20 periods at 15 kHz followed by a break of approximately 20 ms. For the sake of clarity, only the first and last cycles are shown in Figure 6.13, which is why the time

axis is interrupted. The photomultiplier measurements clearly show that the emission lasts longer than a discharge current would be expected (beyond the voltage reversal point). It follows that in this region (marked by yellow areas) the excitation is not dominated by electron impacts, but is probably caused by impacts with metastable atoms or molecules, or cascade de-excitation. Since these processes are not taken into account in the actinometry model, an evaluation of the density or energy at these points in time is not meaningful.

Before the measurement can be evaluated, the gas temperature must be determined again. As a reactor with a flatter quartz cover was used in this measurement, which increases the effective gas velocity via the discharge, the measured temperatures are lower than in the previous case ($510\,\mathrm{K}$ instead of $825\,\mathrm{K}$).

The absolute values of density and energy of the photomultiplier measurement can reproduce those of the ICCD measurement almost perfectly. With an oxygen admixture of 0.1%, a density of approximately $2\cdot10^{22}\mathrm{m}^{-3}$ is measured in the IPP and a density of $3\cdot10^{22}\mathrm{m}^{-3}$ in the DPP. In time-integrated measurements using ICCD setup, the density was determined to be $2.4\cdot10^{22}\mathrm{m}^{-3}$, which almost corresponds to the mean value between IPP and DPP. The mean energy was determined to be $6\,\mathrm{eV}$ in the IPP and $6.3\,\mathrm{eV}$ in the DPP. This is slightly lower than previously determined with the ICCD setup ($6.9\,\mathrm{eV}$) but is still within the error interval. Small deviations can be attributed to a systematic error of the photomultiplier setup. For the argon line at $750\,\mathrm{nm}$, a filter is used whose spectral width cannot completely block out the adjacent argon line at $751\,\mathrm{nm}$. Even if high-resolution spectra show that the contribution of this line only makes a small contribution to the intensity (less than 10%), the argon component is generally overestimated. In the SEA model, this means that the densities and energies tend to be underestimated. Despite the small deviation, the measurements show very good agreement, so that the triple photomultiplier setup can be used in the following for the discussion of the time profiles.

The photomultiplier measurements (Figure 6.13) can now be used to discuss the temporal developments in more detail. Firstly, it is noticeable that there is a significant
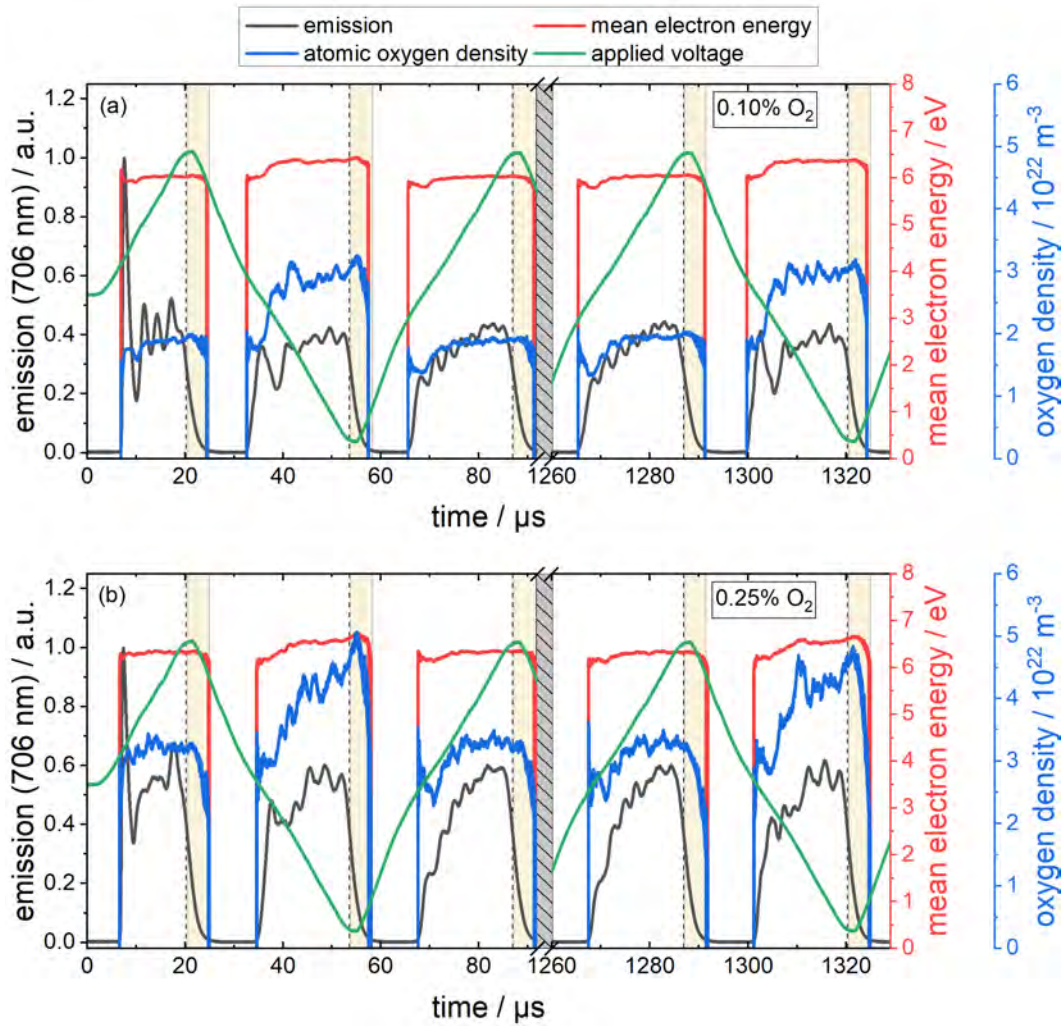
Figure 6.13: Applied voltage, emission, atomic oxygen density and mean electron energy as a function of time measured with a triple photomultiplier setup. Conditions: $2\,\mathrm{slm}$ He, $2\,\mathrm{sccm}$ O_2 (a), $5\,\mathrm{sccm}$ O_2 (b), $1\,\mathrm{sccm}$ Ar; $600\,\mathrm{V}$; $d = 200\,\mathrm{\mu m}$. Adapted from [78].

difference between IPP and DPP. As previously mentioned, the densities and energies in the DPP are higher than in the IPP. However, the measurement reveals another difference. Density and energy remain constant throughout the entire phase in the IPP, while the density builds up within the DPP. This can be associated with the different discharge characteristics with oxygen admixture (see Figure 6.3). Here it becomes clear that the DPP consists of individual strong pulses, while in the IPP, weaker pulses that merge into one another predominate, and the discharge does not extinguish during the half-phase. It can be assumed that each ignition pulse is primarily responsible for dissociation. Since many pulses occur consecutively in the DPP, the density can build

up gradually until the maximum density is reached and the course saturates. In the IPP, the first ignition pulse also causes dissociation, but the subsequent pulses are too weak to further increase the density, being just strong enough to maintain equilibrium.

The difference can further be explained by the discharge behavior. Since the DPP ignites exclusively within the cavity, the gas exchange is not very effective here, so that accumulation effects within a half-phase can play a role. In addition, the discharge is in direct contact with the surfaces. This can release oxygen from possibly oxidized surfaces and thus further increase the density. In the IPP, on the other hand, the discharge also ignites above the cavity, where the gas flow has a greater influence. Although the same density as in DPP can be generated here on ignition, this cannot accumulate as the species are carried away by the gas flow. In addition, surfaces only play a subordinate role in this half-phase.

Furthermore, the electron energy behaves differently in the very first cycle than in the subsequent ones. Here, a maximum in the energy appears first and only then in the emission. This is because the charge carrier density is particularly low in the very first pulse (no memory effect). Ignition occurs later, i.e. at a higher voltage and therefore with higher electron energies. During ignition, many charge carriers are then generated and the energy is distributed among them. These provide excitation in the next step, so that the emission peak is delayed. In the following periods, ignition is then supported by the memory effect again.

In addition to the dynamics within the half-phases, it is also evident from the measurements that no atomic oxygen density builds up from period to period. By using the burst mode, it becomes clear that the maximum density (for both IPP and DPP) is already reached in the very first period. The following periods show the same densities. This means that the time between two discharge phases is long enough for the atomic oxygen to diffuse out of the cavity, recombine or react with the surface.

Figure 6.13 also shows a comparison of two different admixtures. Here, the already known behavior can be reproduced that the density and energy increase with the

admixture. Even if the density increases with a higher admixture, it becomes clear that the degree of dissociation decreases. This matches the density profile of the DPP, which does not saturate as before with small oxygen admixtures, but increases to the end. The discharge cannot generate enough energy to completely dissociate directly, but requires several discharge pulses. It can be assumed that if a lower frequency, i.e. a longer period duration, were used, higher degrees of dissociation could be achieved even with these higher admixtures, due to the accumulation effect in the DPP.

6.4 Atomic oxygen density profiles outside the cavities

The atomic oxygen density measurements described before are all based on optical emission spectroscopy. However, this can only be used for measurements within the active plasma volume. Outside the discharge, active methods such as two photon absorption laser induced fluorescence (TALIF) spectroscopy must be used, as there are no electrons to excite the atoms. In the following section, the TALIF diagnostics are applied to the volume above the micro cavity array to complete the picture of the reactor and to verify the previously shown results. Moreover, the transport of the reactive species from the cavities into the reactor volume is discussed, as this is crucial for plasma catalytic applications.

6.4.1 Influence of quenching on the measurement

The optical branching ratio is one of the key parameters needed for the TALIF calibration factor described in section 4.4. In addition to constant factors such as the natural lifetime, non-radiative collisional de-excitation (quenching) is included in the calculation. Since the quenching rates of different species differ greatly (see table 6.1), the optical branching ratio is strongly dependent on the gas composition and should therefore be customized for each measurement. When using a ps laser, the lifetime of

Table 6.1: Quenching coefficients k_q for $O(3p^3P)$ [123].

Reagent	k_q / $10^{-10}\,\mathrm{cm^3s^{-1}}$
He	0.017
O_2	9.4

the excited state can be measured directly. A minimum gate time of the ICCD camera is used for this purpose. By varying a delay in steps of ns, the TALIF signal can be scanned in time. The decay of the signal can be exponentially fitted to determine the time constant. In this work, however, the gate time cannot be reduced below 3 ns. This means that the measured signal is convoluted with an instrumental profile with a width of 3 ns. This effect can be corrected by deconvolution (not shown here). In the attempt it is noticeable that the excitation can be significantly shortened. However, the decay time barely changes. In addition, the noise is significantly increased by deconvolving the signal, which leads to a higher uncertainty. For this reason, deconvolution is not used in this work to determine the optical branching ratio.

Figure 6.14 shows the measured lifetime of the excited oxygen state $O(3p^3P)$ as a function of the oxygen admixture used. Here, each data point shows the result of an exponential fit to the respective measurement. The error bars indicate the uncertainty of the fit. Overall, the lifetime of the oxygen state is between 2-10 ns and decreases with an inverse density dependence $(1/n)$ known from Stern-Volmer plots. This can be explained by quenching, as the quench rate with molecular oxygen is significantly higher than with helium (see table 6.1). For comparison, the theoretical effective lifetime can be calculated taking into account the gas composition:

Figure 6.14: Measured and calculated effective lifetime of $O(3p^3P)$ depending on O_2 admixture. Conditions: 1 slm total gas flow $(He + O_2)$; 700 V; d = 200 µm; z = 350 µm; gate time = 3 ns; exposure time = 60 s.

$$\tau_{eff} = \frac{1}{\frac{1}{\tau_{nat}(A_{ik}/A_i)} + \sum_q k_q n_q} \tag{6.1}$$

The theoretical values are also shown in Figure 6.14. It is striking that the theory reproduces the measured values almost perfectly. This was not to be expected, as in reality at least ozone is produced from the reaction of atomic with molecular oxygen, for
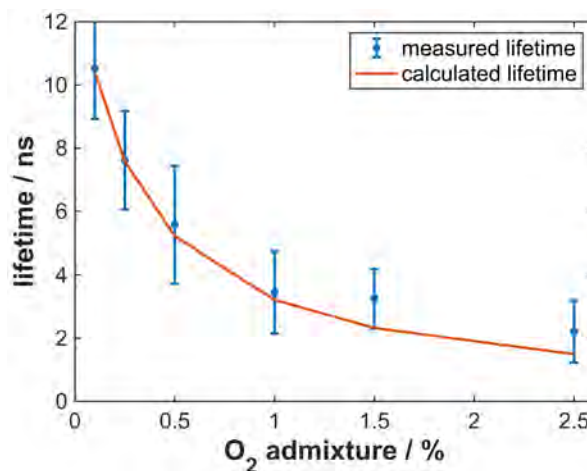
which the exact quenching rate is not known. However, it can be assumed that collisions with ozone can further significantly reduce the lifetime. One possible explanation for longer lifetimes is the limited time resolution of the setup (3 ns gate time). For this reason, the optical branching ratio is calculated below using the theoretical values and the influence of ozone is neglected. When evaluating densities, however, this effect should be kept in mind, as densities may be determined to be too low.

6.4.2 Basic diffusion model to describe atomic oxygen transport

Unlike in other reactors designed for conversion, the gas flow does not pass through the active discharge volume in the micro cavity plasma array. A laminar gas flow between the metal grid and the quartz cover can be assumed, although it is unclear how good the exchange with the gas within the cavity volume is. However, since the reactive species are produced within the cavity, mechanisms such as diffusion are necessary to transport the species into the gas flow volume. In order to describe the density distribution in the region above the cavities and to relate the results to the results within the cavities, a basic diffusion model is developed in the following.

In general, diffusion can be described using Fick's second law. The change in density is described by a diffusion coefficient D. For atomic oxygen, the value is $1.29 \times 10^{-4} \mathrm{m}^2\mathrm{s}^{-1}$ [136].

$$\frac{\partial n}{\partial t} = D\Delta n \tag{6.2}$$

In the case of a helium-oxygen mixture, the dominant loss reaction is the formation of ozone [136]:

$$\mathrm{O} + \mathrm{O}_2 + \mathrm{He} \rightarrow \mathrm{O}_3 + \mathrm{He} \tag{6.3}$$

This can be described with a loss term λ, where $k_L = 3.0 \times 10^{-46}(300/T_\mathrm{g}^{2.6})\,\mathrm{m}^6\mathrm{s}^{-1}$ [164, 165] is the reaction rate of the reaction described above. The densities of helium n_{He} and molecular oxygen n_{O_2} are assumed to be constant:

$$\lambda = k_L n_{\mathrm{O}_2} n_{\mathrm{He}} \tag{6.4}$$

In addition, the external gas flow parallel to the reactor grid (y-direction) can be described by a constant velocity v_y (for 1 slm gas flow and 80 mm^2 cross section $v_y =$

0.21 m/s). Since the TALIF measurements shown later were recorded in two dimensions, it makes sense to calculate the diffusion model also in two dimensions (y and z-direction). This results in the following differential equation:

$$\frac{\partial n}{\partial t} = D_y \frac{\partial^2 n}{\partial y^2} + D_z \frac{\partial^2 n}{\partial z^2} - \lambda n - v_y \frac{\partial n}{\partial y} \qquad (6.5)$$

A numerical method such as the explicit finite difference method can be used to solve the partial differential equation. A starting density, for example a measured value, can be used as a boundary condition at the position z = 0 (transition between cavities and the region above). In order to take the periodic nature of the cavities into account, the boundary condition can even be changed as a function of time. At the remaining edges, the density is set to $n = 0$. To ensure that the result is not distorted by the boundary condition, the model range can be extended in y and z-direction. Only the part of the result that has a certain distance to the edges is then used for the evaluation. Periodic boundary conditions cannot be used in this case, as on the one hand there is a gas flow in y-direction and on the other hand further cavity structures are present in y-direction. For the grid, 540 points are used in y-direction for a range of 13.3 mm. Thus 500 points are in the area that is evaluated later and 20 points on each side are ignored due to the boundary conditions. In z-direction 100 points are used for 5 mm. Approximately one million time steps are required for the solution to converge.

Overall, this basic diffusion model can describe the dominant effects of the region above the cavities. However, some aspects are neglected, so that the results can only provide a rough indication of the density distribution and must always be critically reviewed. In an extended model, the boundary conditions would have to be further specified. For example, the cavities and the metal grid are not only a source of atomic oxygen, but can also bind it to the surfaces of the dielectric or metal grid. This surface loss is neglected in the model. Furthermore, a constant (room) temperature is assumed, although there is a strong temperature gradient between the cavities and the volume above.

In addition to the boundary conditions, the chemical model is very simplified, as only one loss reaction is used. In reality, a large number of other reactions come into consideration, each of which can represent a source or a loss for O, O_2 or O_3. Overall,

the assumption of a constant gas composition in the volume above the cavities is more likely to be fulfilled than in the plasma volume. Nevertheless, the proportion of O_2 and thus the formation of O_3 can change locally and temporally (dissociation due to discharge, interaction with surface, etc.).

A further simplification of the model (and the measurements) is the reduction of the problem to two dimensions (y and z-direction). In reality, the cavities interact with each other in three dimensions. If further cavities (in y-direction) are added (or are not active) this further influences the density in the region above the cavities. However, the inclusion of these effects would make the model very complex and are beyond the scope of this work.

6.4.3 Temporal build-up and decay of atomic oxygen

In order to synchronize the laser system with the discharge, a pre-trigger signal from the laser is used to start the voltage waveform at the reactor. For this reason, no continuous waveform can be used for measurements in the volume above the cavities. Instead, a burst mode is used with a frequency of 15 kHz (as before) and a total of 60 repetitions. Since the discharge is completely switched off between the individual bursts, it must be ensured that an equilibrium has built up at the time of the measurement. To check this, TALIF measurements are taken as close as possible to the electrode without causing scattering effects or similar (center of laser beam at z = 350 µm). For each measuring point within a burst cycle (4.1 ms) the delay in respect to the applied voltage is shifted by 135 µs. The two-dimensional fluorescence signals captured by the ICCD camera are averaged in the area of the laser beam to obtain a single measurement point. On the one hand, this can improve the signal-to-noise ratio, but on the other hand, this procedure limits the local resolution in z-direction (approximately 150 µm FWHM).

The results are shown in Figure 6.15 (top) for three different admixtures as a function of time (dots). Figure 6.15 (bottom) shows the voltage waveform used for an overview. Since the density is measured outside the cavity and must first diffuse there over time, the diffusion model described above can be evaluated in one dimension (z-direction) as a function of time at the position z = 350 µm. The solution for the respective admixture
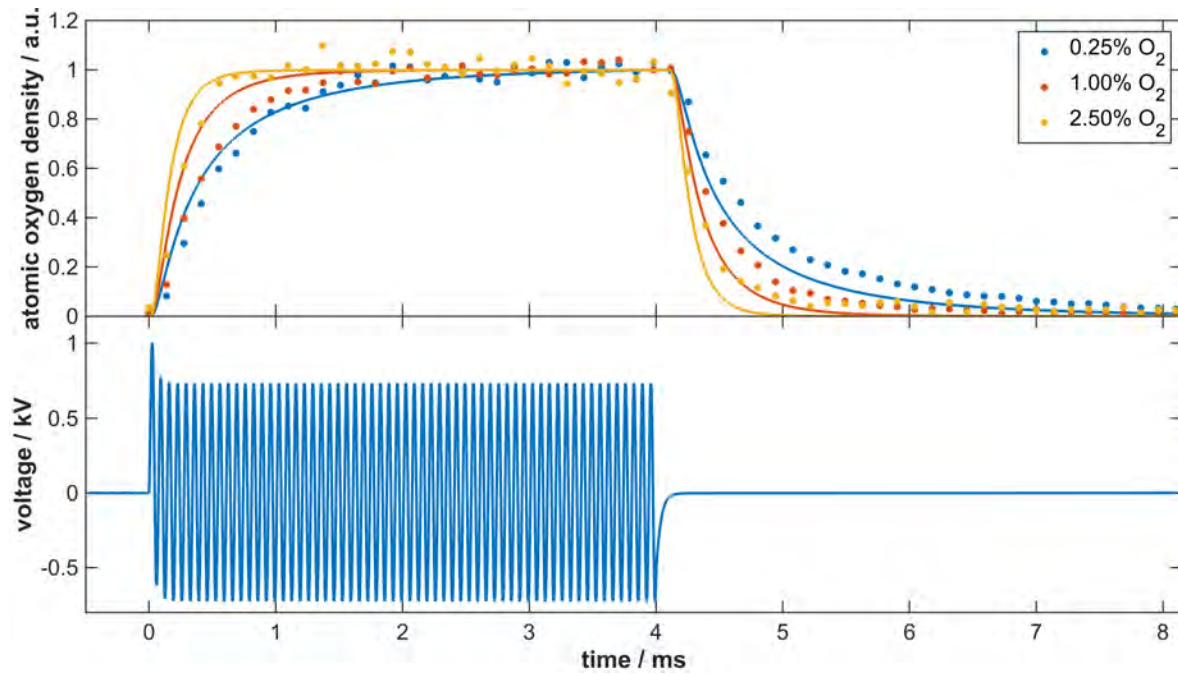
Figure 6.15: Measured (dots) and calculated (lines) atomic oxygen for different O_2 admixtures depending on time (top) and voltage waveform (bottom). Conditions: 1 slm total gas flow (He + O_2); 700 V; d = 200 µm; z = 350 µm; gate time = 30 ns; exposure time = 60 s. Adapted from [145].

is also shown in Figure 6.15 (top,lines). Both the measurement and the model were normalized for better comparability. However, the absolute densities are discussed in the following sections.

First of all, the model can reproduce the measurement very well in terms of the basic process. When the voltage is switched on, the density above the cavities initially rises steeply until saturation is reached. The higher the admixture, the faster saturation can be reached. Regardless of the admixture used, the density is always saturated after 3 ms at the latest. In the measurements shown later, a fixed delay of 3.8 ms is selected in order to ensure saturation. If the voltage is switched off, the density drops exponentially. This was to be expected, as atomic oxygen diffuses and reacts with molecular oxygen to form ozone. As before, the higher the admixture, the faster the drop.

In order to be able to compare the measurement with the model even better, the measurements can be fitted using an exponential function in order to determine the time

constant for temporal build up or decay of atomic oxygen. This can be compared with the results of the diffusion model (see Figure 6.16). The error bars describe again the uncertainty of the fit. As already known, the time constants for build up and decay decrease with the admixture. This can be explained with the help of the loss channel to ozone. The higher the proportion of molecular oxygen in the gas composition, the higher the losses to ozone and the faster an equilibrium between source and loss components is reached.

Overall, the model can reproduce the measurement very well. Both the curves and the absolute magnitude of the time constant (200-800 µs) agree. However, the measured time constants are slightly higher than predicted by the model. This may indicate a too large loss term (formation of ozone) in the model. As previously discussed, the assumed constant gas composition may deviate from reality, as the proportion of atomic oxygen and ozone in the total density are neglected. Furthermore, the simplification to a one-dimensional space can lead to errors, as neighboring cavities (both in x and y-direction) can influence the density at the selected location.
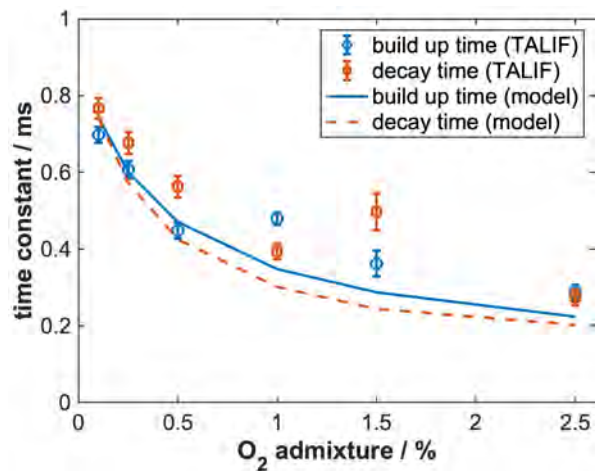
Figure 6.16: Measured (dots) and calculated (lines) time constants depending on O_2 admixture. Conditions: 1 slm total gas flow (He + O_2); 700 V; d = 200 µm; z = 350 µm; gate time = 30 ns; exposure time = 60 s. Adapted from [145].

Beyond the aspects already discussed, it is striking that neither the measurement nor the model show any dependence on the 15 kHz frequency used, which has a major influence within the cavities (actinometry measurements), which is reflected in their different characteristics in the two half-phases. However, TALIF measurements only show a constant value, independent of the time within the period. This phenomenon can again be explained by the model. If the starting density (boundary condition) is

Figure 6.17: Calculated atomic oxygen density for different z-positions depending on time.

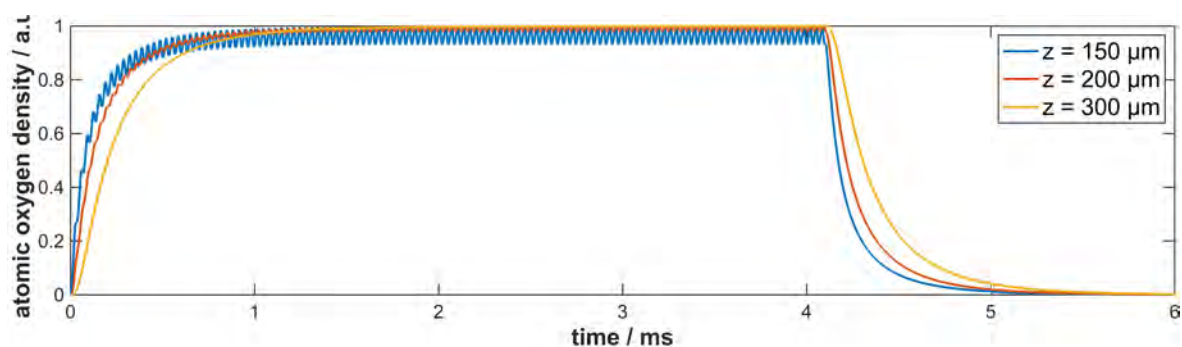periodically switched on and off (e.g. 20 µs on, 13 µs off), an effect can be observed very close to the surface (see Figure 6.17). A clear influence of the voltage period (IPP and DPP lead to two discharges per period, i.e. 30 kHz) can be seen at the position z = 150 µm. However, this influence decreases significantly with greater distance from the cavities. The effect disappears at distances greater than z = 300 µm. The influence is therefore not measurable at the measurement position z = 350 µm. This result shows that even measurements closer to the surface could hardly reproduce the periodic change in density, as the difference is of the order of magnitude of the noise level.

Even if the model does not perfectly reproduce the TALIF measurement, it can be shown that the volume above the cavities is dominated by diffusion and the reaction to ozone. It also shows why the periodic density changes known from the cavities are not measurable here.

6.4.4 2D resolved density distributions above the cavities

In addition to time-resolved measurements, the setup can be used to perform spatially resolved measurements. To do this, the reactor is moved in the z-direction using a translation stage. A position at which the laser is completely blocked by the reactor wall is selected as the starting point. With each step in the z-direction, a further part of the laser beam can pass through the reactor allowing measurements to be taken directly in front of the grid surface. The entire volume above the cavities can thus be scanned step by step. As the laser beam passes in y-direction, a two-dimensional

density profile can be obtained. In the previous measurements, the entire laser width was averaged in z-direction to improve the signal-to-noise ratio. In contrast, the local resolution is more decisive here. For this reason, only a 50 µm wide part of the laser is evaluated instead of 150 µm. This corresponds to the selected step size of the translation stage. To minimize scattering, reflections, and fluorescence effects when the laser is close to the surface, only the 50 µm section of the laser or fluorescence beam nearest the surface is analyzed. While this reduces intensity (which would be higher at the beam center), it significantly decreases disturbances since the laser's center remains further from the surface at each point.

In addition to the scattering effects, even the quartz cover can distort the measurement due to small defects or contamination. One way to eliminate both, the effects of the quartz cover and those of the surface, is to perform a calibration measurement with xenon. The same z-scan as for atomic oxygen can be carried out for this purpose. Xenon is added to the helium flow instead of oxygen and the laser is moved to 224.29 nm. The bandpass filter is wide enough and does not need to be changed for this measurement, unlike for density calibration. As the xenon density should be constant at all locations when the discharge is switched off, variations in the TALIF signal can be directly attributed to the influence of the surface or the quartz cover. The oxygen measurements can therefore be corrected directly with the normalized xenon measurement. With this method, densities can be measured down to a few µm from the surface.

The results are shown in Figure 6.18. The upper surface of the micro cavity plasma array is positioned at z = 0 mm. The cavity openings point downwards to allow the outflow of the cavities to propagate in the positive z-direction. The position of the ICCD camera is chosen in such a way that the entire 200 µm and also part of the 150 µm diameter cavity structure is visible. The measurements were carried out for three different oxygen admixtures and were absolutely calibrated in each case.

As expected, the atomic oxygen density is at its maximum around the cavities (z=0) and drops exponentially in the region above. The atomic oxygen density initially increases with the addition of oxygen, but decreases again with larger admixtures. As
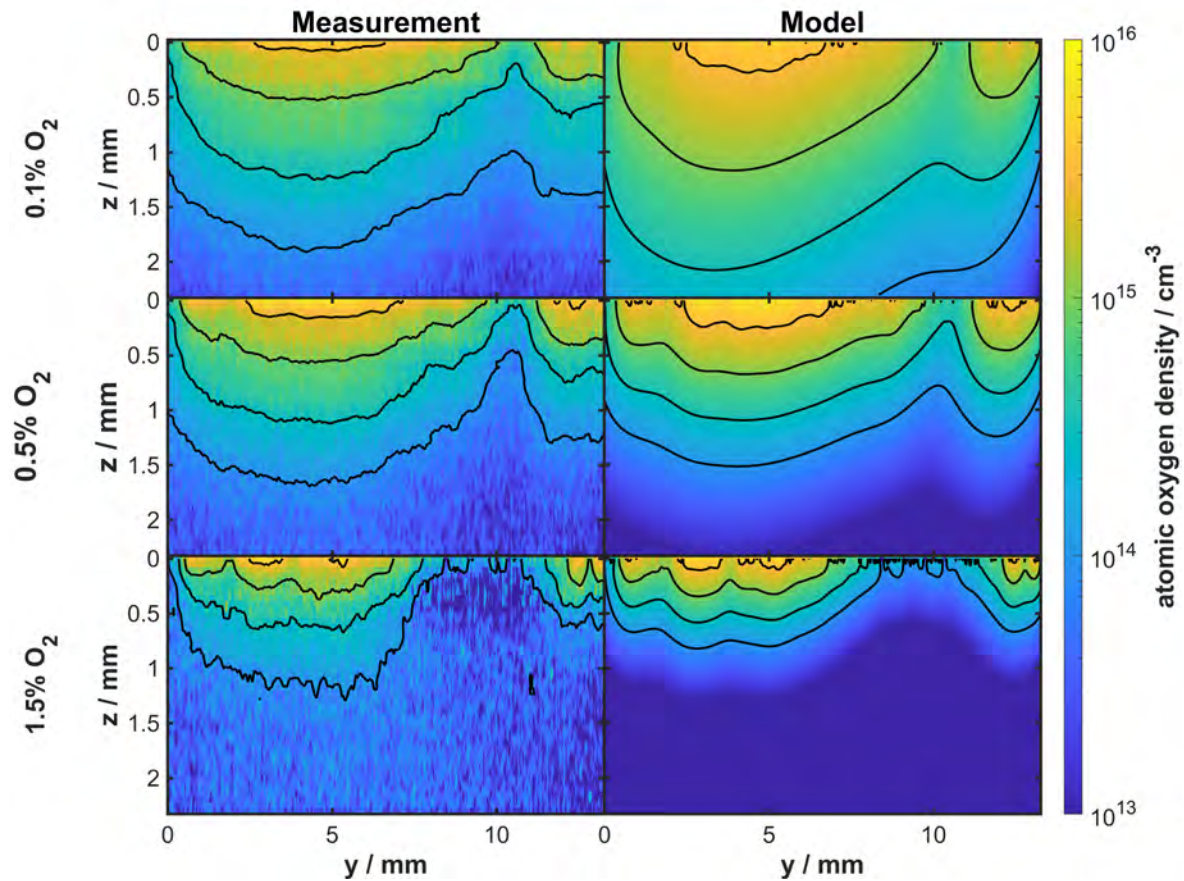
Figure 6.18: Measured (left) and calculated (right) 2d resolved atomic oxygen density for different admixtures. Conditions: $1\,\mathrm{slm}$ total gas flow (He + O_2); $700\,\mathrm{V}$; d = $200\,\mu\mathrm{m}/150\,\mu\mathrm{m}$; gate time = $30\,\mathrm{ns}$; exposure time = $60\,\mathrm{s}$. Adapted from [145].

previously observed, not all cavities can ignite at 1.5% admixture, resulting in individual density maxima or minima. However, the width of the laser is so broad that it could theoretically be spread over two rows of cavities in the x-direction (in depth). In addition, there is diffusion in the x and y-directions, which means that more distant cavities may have an influence on the measuring point. Structures therefore only arise when an entire cluster of cavities expires. The absolute densities are discussed in more detail in the following section 6.4.5. The results in the $150\,\mu\mathrm{m}$ area differ neither in terms of absolute density nor density distribution from the $200\,\mu\mathrm{m}$ structures. This matches the findings from the actinometry measurements, where the density also does not change with the cavity size.

In addition to the measurements, the results of the basic diffusion model are also shown in Figure 6.18 (right column). The first line of the measured values (z = 0) was used

as the starting density in each case. In reality, this point is approximately 20 µm away from the surface due to inaccuracies in the adjustment. Except from the smallest admixture (0.1%), the model can reproduce the measurements almost perfectly. The deviation at low admixture can have various reasons. Firstly, deviations in the MFCs or the premixed gas cylinder have a relatively greater influence on the actual admixture at lower admixtures. If the admixture were higher than assumed, this would strongly influence the model and reduce the deviation from the measurement. Furthermore, the model only uses the three body impact between O, O_2 and He as loss term. At higher admixtures, this term seems to dominate. At lower admixtures, however, the losses approach zero as the rate depends directly on the admixture. Further loss terms, which for example do not depend on the molecular oxygen density, but only on atomic oxygen or helium, or diffusion in x-direction could correct the model. However, this requires a complex (chemical) model that goes beyond the scope of this work.

The measurements and the model show that atomic oxygen can leave the cavities by a few mm, depending on the admixture. This is particularly important for plasma catalytic applications, as the reactive species can react in the gas volume or interact on a surface placed close to the cavities. Contour lines have been added to both the model and the measurement for better comparability. The model and measurement are very comparable, except for the 0.1% admixture already discussed. The exponential decay is almost identical up to densities of approximately 2×10^{14} cm^{-3}. At lower densities, the noise level (detection limit) is reached during the measurement, resulting in deviations.

The model can also be used to complement the measurements. For example, the influence of the gas flow (directed from right to left) is taken into account in the model, which is visible in the results. Nevertheless, it can be seen that the influence is very small. This means, for example, that no oxygen atoms from the 150 µm structures interact with the outflow of the 200 µm structures (1 mm away) and thus the density cannot accumulate. The calculations show that significantly higher flow velocities (one order of magnitude or more) would be necessary, which could be important for applications. On closer analysis, the effect of the gas flow is also visible in the measurements. However, the effect appears to be even smaller in the measurement, which may be due

to the limited signal-to-noise ratio. Moreover, despite the assumed laminar gas flow, it can be expected that the flow velocity directly in front of the surface is slower than in the rest of the volume, and thus has only a minor influence in reality.

In the previous section, it was discussed that the influence of the voltage period is only visible very close to the surface. However, the z-scans are measured exactly in this area. In order to minimize the error, all measurements are therefore carried out at the same time at the end of the DPP. This has two advantages: First, the oxygen production is expected to be at its maximum here (see section 6.3.2). Secondly, the measurement is not possible in the IPP, as the discharge also ignites outside the cavity and thus influences the measurement through plasma emission. Accordingly, the model can not take into account changes in density within the half-phase or between IPP and DPP.

6.4.5 Dependence on gas composition and comparison with SEA

The influence of the admixture in the volume above the cavities, for example due to the reaction to ozone, has already been discussed in the previous sections. In the following section, this influence is examined in more detail. As before, measurements are taken at a fixed position ($z = 350\,\mu\text{m}$) and the admixture is varied. The measurements are then absolutely calibrated. As more and more cavities expire with high admixture, the density above the cavities can be distorted by this effect. To correct this, the ignited cavities close to the laser beam are counted for each admixture and the measurement is corrected accordingly.

The results are shown in Figure 6.19. The error bars are derived from the standard deviation of ten individual measurements. Initially, the density increases with the admixture, reaching a maximum of $8.4\times10^{14}\,\text{cm}^{-3}$ at approximately 0.4% admixture. The density then falls with the admixture, resulting in a density of only $2.9\times10^{14}\,\text{cm}^{-3}$ at 2.5% admixture. The absolute density is therefore consistent with the z-scans shown above. Small deviations are due to the fact that in this case the density was averaged along the entire laser or fluorescence beam above a row of the array structure, whereas in the z-scans each y-value was evaluated individually.
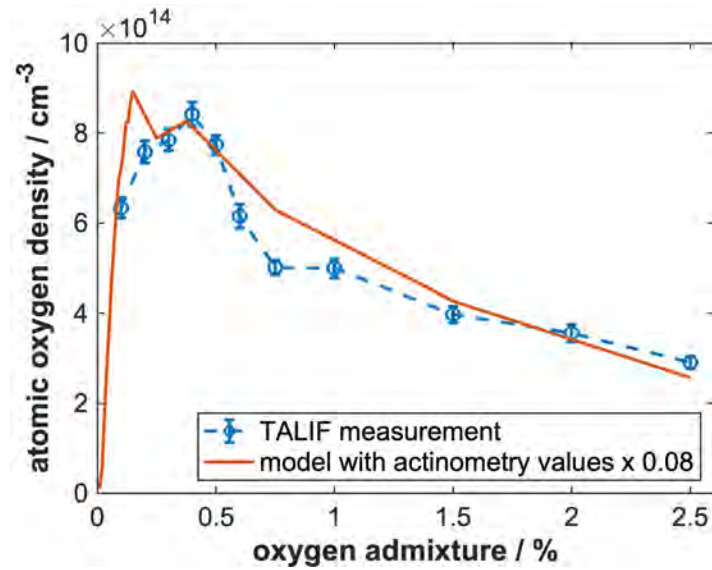
Figure 6.19: Comparing TALIF data with a basic diffusion model based on SEA data depending on the admixture. Conditions: 1 slm total gas flow (He + O_2); z = 350 µm; 700 V; d = 200 µm; gate time = 30 ns; exposure time = 60 s. Adapted from [145].

At first glance, the density curve clearly deviates from the already known curve within the cavities (see Figure 6.11). This deviation can be resolved using the diffusion model. If the actinometry measurements are used as the initial density value within the cavity and the model is evaluated in the region above, the density curve can be reproduced almost perfectly. The model can be refined even further by using the actual discharge times, i.e. switching the source on and off (see Figure 6.4).

In spite of the consistency of the curves, a correction factor of 0.08 is required to match the absolute densities. There are many reasons for this. For example, only the (ignited) cavities themselves are considered in the actinometry measurements. In the diffusion-determined volume above the cavities, however, the density is composed of the 3d interaction of several (possibly non-ignited) cavities. Even if all cavities were always ignited, the cavity area to electrode area ratio is only 20%, which leads to a considerable reduction in the actual density above the cavities.

In addition, the actinometry measurements do not provide any information about the z-position at which the density is generated, as integration is performed in this direction. The density is assumed for the model at the bottom of the cavity. However, as is

already known from the literature [77] or this work, the discharge volume and location changes drastically between IPP and DPP. As already discussed, the absolute densities of actinometry should generally be critically questioned.

Another source of error is the model itself. Surface losses are completely ignored here. However, these are at a maximum within the cavity surrounded by the electrode and dielectric, raising the question of how much of the oxygen generated in the cavity can leave it.

Despite the uncertainty discussed, this result can serve as a further benchmark for actinometry. The trends of the density curve is almost identical between TALIF and actinometry measurements. The deviations in absolute density can largely be explained by surface losses or the cavity to electrode area ratio. In conclusion, all phenomena above the cavities can be described with the already determined discharge dynamics within the cavities.

6.5 Outcome: optimizing the conversion of gases

In this chapter, oxygen was considered as a model system for plasma-catalytic applications. The following discussion addresses how the insights gained can be applied to more complex systems such as n-butane, methane, or carbon dioxide, and how the reactor can be optimized for these applications.

The results can be summarized into three key findings, which can answer the remaining research questions of this work. First, the discharge dynamics change drastically with the addition of reactive components. The discharge shifts from a homogeneous continuous glow mode to a pulsed and later unstable filamentary mode. Second, measurements show that very high dissociation rates of up to 100% are achieved within the cavities. The density does not accumulate over a long period but reaches its maximum after just half a phase. Third, the density distribution outside the cavities is determined exclusively by diffusion and chemical reactions. The influence of the discharge and the external gas flow can be neglected.

These findings highlight the interplay between discharge dynamics and conversion. Fundamentally, the cavities provide optimal conditions for the dissociation of molecules. Time-resolved measurements reveal the significant contribution of each individual discharge pulse. Therefore, for efficient reactor operation, the pulses should be explicitly controlled. The basic discharge mode can be set by adjusting the admixture. The optimal balance between the maximum admixture and the number and duration of pulses should be sought. The results also indicate that the maximum dissociation can be reached after only a few pulses. This means that the number of pulses or the period duration should be fine-tuned using applied voltage, frequency, or waveform to avoid operating the discharge longer than necessary.

Besides discharge dynamics, transport dynamics emerge as a crucial parameter. The discharge or gas flow has a negligible influence on the dynamics, which are mainly determined by diffusion. Due to the laminar, slow gas flow, it can be assumed that gas exchange in the cavities occurs rather slowly. For efficient conversion, the gas dynamics should be adjusted so that the gas in the cavities is exchanged for every half-phases. This could be achieved by adjusting the reactor design, for example, by changing the geometry to shift the gas flow from laminar to turbulent.

Overall, the measurements suggest that each individual cavity contributes to the conversion. However, the results show no evidence of synergy effects between the cavities. This means that plasma species are not transported from one cavity to another. The diffusion characteristics indicate that the species can escape a few millimeters from the cavities. Therefore, the reactor geometry should be adjusted to utilize the reactive species outside the discharge volume. For example, an additional catalytic surface or another array of cavities could be placed in this region. Additionally, the gas flow and the distance between two cavities could be improved to enhance transport.

Even though other gas systems may behave differently than oxygen, it can be expected that the effects discussed here still lead to optimization of the conversion.

7 Summary and Outlook

The aim of this work was to investigate the discharge characteristics of a micro cavity plasma array in helium-oxygen mixtures, using oxygen as a model system to gain insights into its potential applications in plasma catalytic processes. The work focused on describing the fundamental discharge dynamics, observing the influence of oxygen on the discharge and investigating the resulting plasma chemistry, for example by determining the degrees of dissociation.

The first research question to be answered in this thesis was related to the description of the discharge mode of the reactor within a pure helium system. To address this, power measurements were carried out using the equivalent circuit approach. In addition, the emission of the discharge was observed. This allowed parameters such as gap voltage, discharge current, transported charge, ignition times, discharge durations and surface covering to be determined as a function of the applied voltage or frequency. In particular, the ability to precisely determine the dissipated power can help to quantify the energy efficiency of gas conversion or plasma catalysis in the future. Based on these measurements, it could be concluded that the micro cavity plasma array is a combination of surface DBD and volume DBD. In the range of low voltages, not all cavities are ignited and the discharge can spread further with increasing voltage (surface DBD). As soon as a voltage is reached at which all cavities ignite, the discharge can only spread into the volume as the voltage increases (volume DBD). Furthermore, the reactor could be assigned to a discharge mode under pure helium. The behavior corresponds very well with the behavior of an atmospheric pressure glow discharge (APGD) known from the literature. The fact that metastable helium atoms also play a major role and strongly support the ignition means that the discharge takes the form of a continuous or quasi pulseless glow discharge. This characterization helps to compare the reactor

with similar plasma sources and to differentiate it from others (streamer-dominated, filamentated or Townsend discharges).

As the previously determined discharge dynamics are influenced by surface charges, particularly in the case of the dielectric barrier system, these were also investigated further in this work. For this purpose, the equivalent circuit approach was extended and applied in combination with a new method. The reactor is disconnected from the voltage at certain points in time to allow volume charges to decay, leaving only surface charges that can be measured in the next step. For the parameters typically used in this work, the surface charge density was determined to be $16\,\mathrm{nC/cm^2}$. The method can furthermore be used to precisely set the surface charge, for example to influence the next ignition. Another method, laser-assisted charge ablation, was additionally used. Here, the charge carrier density is actively manipulated with a laser. The advantage is that the charge can be determined and controlled in a similar way to the switching off method, but the discharge does not have to be stopped and continuous operation is possible as a result. However, the use of this diagnostic method is considerably more complex. In addition to the required laser set-up, the evaluation is complicated because, in addition to a modification of the surface charges on the dielectric, secondary effects induced by the laser also take place on the metal electrode. Overall, both methods open the door to deeper investigations into the interaction of surface charges and catalytic surfaces, which could lead to an understanding and optimization of plasma catalytic systems.

The surface charges are mainly influenced by the electric field. This directs the charged particles to the surface or accelerates them away from the surface. However, the surface charges also influence the electric field through shielding. For this reason, one of the research questions in this work addresses the spatial distribution and direction of the electric field. This could be investigated with the help of the Stark broadening or shifting of a helium line pair, taking into account the polarization properties. Fundamental differences between the two half-phases (increasing and decreasing potential phase) could be seen both in the two-dimensional distribution and in the direction of the electric field. While the field in the DPP is strongly influenced and shielded by

surface charges and is directed more parallel to the dielectric (leading to striations with oxygen), the field in the IPP is weaker and more diffuse. These results in combination with findings on surface charges and the general discharge dynamics make it possible to design more accurate models of the discharge in the future or could serve as input parameters or benchmarks for more complex simulations.

After the discharge of a pure helium system had been described in detail, the influence of oxygen on the discharge was investigated. Power, emission and spectroscopy measurements were carried out again and the oxygen admixture was varied. A drastic transition from a continuous glow discharge to a pulsed and filamentized discharge is particularly visible in the emission. However, this transition is also evident in the power characteristics or the electric field. What is particularly exciting is that all diagnostics indicate that there is a discrete point (approximately 0.3-0.5% oxygen admixture) at which a mode transition takes place. Up to this point, the discharge still behaves largely like a pure helium glow discharge despite the addition of oxygen, with the difference that individual pulses occur instead of a continuous discharge. After the transition, the influence of oxygen becomes more dominant, which results in the discharge being quenched more strongly, ignited only at higher voltages and lasting for a shorter time. For the oxygen system, the point of the mode transition therefore represents an optimum between maximum reactive admixture and discharge duration or stability. Since oxygen is important for many plasma catalytic applications, but can also serve as a model system for other gas compositions, the results can be used for future applications. They can help to adapt the reactor to the respective application in the future regarding geometry, voltage or heat resistance.

For plasma catalysis, the conversion or dissociation of molecules and thus the monitoring of their densities is indispensable. However, due to the small reactor dimensions and limited optical access, particularly spatially and time-resolved diagnostics can only be used to a certain extent. But this is particularly important for reactive species with short lifetimes, as they are supposed to react directly within the discharge volume or in the immediate vicinity. To investigate the influence on the plasma chemical mechanisms, integrating measurements such as mass spectrometry or absorption spec-

troscopy are therefore not sufficient. For this reason, a new diagnostic method, helium state enhanced actinometry (SEA), was developed in the course of this work. This method is based on optical emission spectroscopy and makes it possible to determine atomic oxygen densities and mean electron energies at the same time. The method was benchmarked against laser spectroscopic measurements at a reference source, the COST reference microplasma jet. In addition, two measurement setups were developed. On the one hand, an ICCD-camera based setup with an electronically tunable filter offers the possibility of 2D resolved measurements. On the other hand, a photomultiplier setup offers the possibility of high time resolution. This provides a real alternative to laser spectroscopic diagnostics if these are not available or cannot be used for geometric reasons, for example.

Using SEA diagnostics, it investigated which dissociation degrees can be achieved with the reactor and on which parameters the conversion depends. Both setups were used to obtain both spatially and time-resolved measurements. In each case, very high atomic oxygen densities were found, corresponding to a degree of dissociation of almost 100%. Time-resolved measurements show that this degree of dissociation is already achieved within the first periods and does not have to build up over a longer period of time. A clear asymmetry between IPP and DPP is again evident. Furthermore, it becomes clear that the density is less dependent on the cavity dimensions or the voltage, but is rather influenced by the admixture or the discharge mode.

Outside the cavities, the density distributions were determined using TALIF. This shows that the reactive species can leave the cavities up to several mm, which is promising for applications. In addition, a basic model shows that the transport is determined exclusively by diffusion. This allows the results outside the cavity to be compared with those inside, with a high degree of agreement.

The results found in this work offer numerous possibilities for the future. The new findings on fundamental properties such as electric fields, surface charge, and discharge mode can be used to develop more complex models and simulations. In particular, the discharge dynamics could be explored in greater depth, including the interaction be-

tween the cavities. Furthermore, various materials for the electrode, dielectric, and catalyst could be tested or simulated, allowing for further optimization of the reactor. The high degrees of dissociation achieved provide a solid foundation for plasma-catalytic applications. By tailoring discharge pulses and gas dynamics, the knowledge gained here can be used to design a highly efficient reactor. This fundamental understanding, combined with high conversion rates and a multitude of spatially and temporally resolved diagnostics, enables systematic and comprehensive investigations of plasma catalysis in the future. For example, conversion efficiency can be determined as a function of surface charges or electric field distributions to decouple various relevant mechanisms.

Publications in the course of this dissertation

The results of this work have been included in the following publications. These refer to the topics helium state enhanced actinometry [1-3], electric field measurement [4-5], surface charge measurements [6], atomic oxygen density measurements using two photon absorption laser induced fluorescence [7-13] and the characterization of discharge modes [14]:

Own publications

1. D. Steuer, H. van Impel, A. Gibson, V. Schulz-von der Gathen, M. Böke and J. Golda. "State enhanced actinometry in the COST microplasma jet". *Plasma Sources Science and Technology* **31** 10LT01 (2022)

2. T. Winzer, D. Steuer, S. Schüttler, N. Blosczyk, J. Benedikt and J. Golda. "RF-driven atmospheric-pressure capillary plasma jet in a He/O$_2$ gas mixture: Multi-diagnostic approach to energy transport". *Journal of Applied Physics* **132** 183301 (2022)

3. D. Steuer, H. van Impel, V. Schulz-von der Gathen, M. Böke and J. Golda. "Spatially and temporally resolved atomic oxygen densities in a micro cavity plasma array". *Plasma Sources Science and Technology* **32** 025013 (2023)

4. S. Dzikowski, D. Steuer, S. Iséni, J. Golda, M. Böke and V. Schulz-von der Gathen. "Electric field strengths within a micro cavity plasma array measured by Stark shift and splitting of a helium line pair". *Plasma Sources Science and Technology* **31** 065014 (2022)

5. H. van Impel, D. Steuer, R. Labenski, V. Schulz-von der Gathen, M. Böke and J. Golda. "Electric field components within a micro-scaled DBD measured by Stark shifting and splitting of helium lines". *Plasma Sources Science and Technology* **accepted** (2024)

6. R. Labenski, D. Steuer, H. van Impel, M. Böke, V. Schulz-von der Gathen and J. Golda. "Novel methods for determination and manipulation of surface charges performed on an atmospheric DBD microplasma". *Plasma Sources Science and Technology* **accepted** (2024)

7. D. Steuer, I. Korolov, S. Chur, J. Schulze, V. Schulz- von der Gahten, J. Golda and M. Böke. "2D spatially resolved O atom density profiles in an atmospheric pressure plasma jet: from the active plasma volume to the effluent". *Journal of Physics D: Applied Physics* **54** 355204 (2021)

8. I. Korolov, D. Steuer, L. Bischoff, G. Hübner, Y. Liu, V. Schulz-von der Gathen, M. Böke, T. Mussenbrock and J. Schulze. "Atomic oxygen generation in atmospheric pressure RF plasma jets driven by tailored voltage waveforms in mixtures of He and O_2". *Journal of Physics D: Applied Physics* **54** 125203 (2021)

9. Y. He, P. Preissing, D. Steuer, M. Klich, V. Schulz-von der Gathen, M. Böke, I. Korolov, J. Schulze, V. Guerra, R. Brinkmann and E. Kemaneci. "Zero-dimensional and pseudo-one-dimensional models of atmospheric-pressure plasma jets in binary and ternary mixtures of oxygen and nitrogen with helium background". *Plasma Sources Science and Technology* **30** 105017 (2021)

10. Y. Liu, I. Korolov, J. Trieschmann, D. Steuer, V. Schulz-von der Gathen, M. Böke, L. Bischoff, J. Schulze and T. Mussenbrock. "Micro atmospheric pressure plasma jets excited in He/O_2 by voltage waveform tailoring: a study based on a numerical hybrid model and experiments". *Plasma Sources Science and Technology* **30** 064001 (2021)

11. Y. Liu, M. Vass, G. Hübner, D. Schulenberg, T. Hemke, L. Bischoff, S. Chur, D. Steuer, J. Golda, M. Böke, J. Schulze, I. Korolov and T. Mussenbrock. "Micro atmospheric pressure plasma jets excited in He/O_2 by voltage waveform tailoring: a study based on a numerical hybrid model and experiments". *Plasma Sources Science and Technology* **32** 025012 (2023)

12. M. Vass, D. Schulenberg, Z. Donkó, P. Hartmann, D. Steuer, M. Böke, V. Schulz-von der Gathen, I. Korolov, T. Mussenbrock and J. Schulze. "Energy efficiency of reactive species generation in radio frequency atmospheric pressure plasma jets driven by tailored voltage waveforms in He/O_2 mixtures". *Plasma Sources Science and Technology* **under revision** (2024)

13. D. Steuer, B. Bentz, K. Youngman, H. van Impel, V. Schulz-von der Gathen, M. Böke and J. Golda. "Measurement of atomic oxygen densities using TALIF on a dielectric barrier discharge: Insights into the volume above a micro cavity plasma array". *Plasma Sources Science and Technology* **under review** (2024)

14. D. Steuer, H. van Impel, R. Labenski, V. Schulz-von der Gathen, M. Böke and J. Golda. "Mode transition in a helium barrier discharge with oxygen admixtures: Insights into a micro cavity plasma array reactor". *Journal of Physics D: Applied Physics* **under review** (2024)

Acknowledgments

- Alicia Gonzalez Fontela, die mich im Kampf mit der Bürokratie und bei allen anderen organisatorischen Fragen (inklusive Urlaubstipps) immer tatkräftig unterstützt hat.

- Die Techniker Kevin Youngman, Björn Redeker, Kai Fiegler, Michael Konkowski und Axel Lang für die Unterstützung in allen technischen Fragen.

- Steffen Schüttler und Sascha Chur, die mich seit Beginn des Studiums begleiten. Danke für Eure Freundschaft, ereignisreiche Reisen zu Konferenzen, lustige Abende und nervenaufreibende Stadionbesuche.

- Den gesamten Lehrstuhl EP2, insbesondere der Gruppe *Plasma Interface Physics*, für die hervorragende Arbeitsatmosphäre und Hilfsbereitschaft.

- Meine Freunde und meine Familie, die mich das ganze Studium und während der Entstehung dieser Arbeit stets unterstützt haben. Danke für viele schöne gemeinsame Erlebnisse, die Entspannung und Ablenkung in den immer wieder anstrengenden Doktorandenalltag gebracht haben.

- Leonie Eiselt für Ihre Liebe, bedingungslose Unterstützung, unendliche Geduld und Ihren emotionalen Rückhalt. Ich liebe Dich!

Bibliography

[1] *Max-Planck-Gesellschaft: Jahrbuch 1991.* Vanderhoeck & Ruprecht, 1991.

[2] L. Martinu, O. Zabeida, and J. Klemberg-Sapieha. "Plasma-Enhanced Chemical Vapor Deposition of Functional Coatings". *Handbook of Deposition Technologies for Films and Coatings.* Elsevier, 2010.

[3] E. Liston, L. Martinu, and M. Wertheimer. "Plasma surface modification of polymers for improved adhesion: a critical review". *Journal of Adhesion Science and Technology* **7** (1993), 1091–1127.

[4] V. M. Donnelly and A. Kornblit. "Plasma etching: Yesterday, today, and tomorrow". *Journal of Vacuum Science & Technology A: Vacuum, Surfaces, and Films* **31** (2013), 050825.

[5] V. Banine and R. Moors. "Plasma sources for EUV lithography exposure tools". *Journal of Physics D: Applied Physics* **37** (2004), 3207.

[6] G. Fridman et al. "Applied Plasma Medicine". *Plasma Processes and Polymers* **5** (2008), 503–533.

[7] K.-D. Weltmann and T. Von Woedtke. "Plasma medicine-current state of research and medical application". *Plasma Physics and Controlled Fusion* **59** (2017), 014031.

[8] J. Linke et al. "Challenges for plasma-facing components in nuclear fusion". *Matter and Radiation at Extremes* **4** (2019), 056201.

[9] A. Bogaerts et al. "The 2020 plasma catalysis roadmap". *Journal of Physics D: Applied Physics* **53** (2020), 443001.

[10] P. Hinde et al. "Plasma Catalysis: A Review of the Interdisciplinary Challenges Faced : Realising the potential of plasma catalysis on a commercial scale". *Johnson Matthey Technology Review* **64** (2020), 138–147.

[11]   J. Van Durme et al. "Combining non-thermal plasma with heterogeneous catalysis in waste gas treatment: A review". *Applied Catalysis B: Environmental* **78** (2008), 324–333.

[12]   J. C. Whitehead. "Plasma–catalysis: the known knowns, the known unknowns and the unknown unknowns". *Journal of Physics D: Applied Physics* **49** (2016), 243001.

[13]   R. Schlögl. "Heterogeneous Catalysis". *Angewandte Chemie International Edition* **54** (2015), 3465–3520.

[14]   I. Adamovich et al. "The 2022 Plasma Roadmap: low temperature plasma science and technology". *Journal of Physics D: Applied Physics* **55** (2022), 373001.

[15]   H. Chen et al. "Review of plasma catalysis on hydrocarbon reforming for hydrogen production-Interaction, integration, and prospects". *Applied Catalysis B: Environmental* **85** (2008), 1–9.

[16]   J. Jiang and P. J. Bruggeman. "Tuning plasma parameters to control reactive species fluxes to substrates in the context of plasma catalysis". *Journal of Physics D: Applied Physics* **54** (2021), 214005.

[17]   C. Tendero et al. "Atmospheric pressure plasmas: A review". *Spectrochimica Acta Part B: Atomic Spectroscopy* **61** (2006), 2–30.

[18]   K. H. Becker, K. H. Schoenbach, and J. G. Eden. "Microplasmas and applications". *Journal of Physics D: Applied Physics* **39** (2006), R55.

[19]   U. Kogelschatz. "Dielectric-Barrier Discharges: Their History, Discharge Physics, and Industrial Applications". *Plasma Chemistry and Plasma Processing* **23** (2003), 1–46.

[20]   K. Ollegott et al. "Fundamental Properties and Applications of Dielectric Barrier Discharges in Plasma-Catalytic Processes at Atmospheric Pressure". *Chemie Ingenieur Technik* **92** (2020), 1542–1558.

[21]   N. Peters et al. "Catalyst-enhanced plasma oxidation of n-butane over MnO_2 in a temperature-controlled twin surface dielectric barrier discharge reactor". *Plasma Processes and Polymers* **18** (2021), 2000127.

[22] S. Dzikowski et al. "Modular constructed metal-grid arrays-an alternative to silicon-based microplasma devices for catalytic applications". *Plasma Sources Science and Technology* **29** (2020), 035028.

[23] S.-J. Park et al. "Silicon microdischarge devices having inverted pyramidal cathodes: Fabrication and performance of arrays". *Applied Physics Letters* **78** (2001), 419–421.

[24] J. G. Eden et al. "Microplasma devices fabricated in silicon, ceramic, and metal/polymer structures: arrays, emitters and photodetectors". *Journal of Physics D: Applied Physics* **36** (2003), 2869.

[25] J. G. Eden and S.-J. Park. "Microcavity plasma devices and arrays: a new realm of plasma physics and photonic applications". *Plasma Physics and Controlled Fusion* **47** (2005), B83.

[26] J. G. Eden et al. "Plasma Science and Technology in the Limit of the Small: Microcavity Plasmas and Emerging Applications". *IEEE Transactions on Plasma Science* **41** (2013), 661–675.

[27] J. Kim et al. "Commercialization of microcavity plasma devices and arrays: Systems for VUV photolithography and nanopatterning, disinfection of drinking water and air, and biofilm deactivation for medical therapeutics". *Plasma Processes and Polymers* **19** (2022), 2200075.

[28] S. Dzikowski et al. "Electric field strengths within a micro cavity plasma array measured by Stark shift and splitting of a helium line pair". *Plasma Sources Science and Technology* **31** (2022), 065014.

[29] S. Veerapandian et al. "Abatement of VOCs Using Packed Bed Non-Thermal Plasma Reactors: A Review". *Catalysts* **7** (2017), 113.

[30] K. M. Bal et al. "Effect of plasma-induced surface charging on catalytic processes: application to CO_2 activation". *Plasma Sources Science and Technology* **27** (2018), 024001.

[31] A. M. Vandenbroucke et al. "Non-thermal plasmas for non-catalytic and catalytic VOC abatement". *Journal of Hazardous Materials* **195** (2011), 30–54.

[32]   K. H. R. Rouwenhorst et al. "Plasma-driven catalysis: green ammonia synthesis with intermittent electricity". *Green Chemistry* **22** (2020), 6258–6287.

[33]   S. Liu, L. R. Winter, and J. G. Chen. "Review of Plasma-Assisted Catalysis for Selective Generation of Oxygenates from CO_2 and CH_4". *ACS Catalysis* **10** (2020), 2855–2871.

[34]   C. Stewig, L. Chauvet, and A. v. Keudell. "Impact of catalysis on n-butane oxidation in an RF atmospheric pressure plasma". *Plasma Sources Science and Technology* **32** (2023), 105006.

[35]   S. Yu, S. Vervloedt, and A. v. Keudell. "Controlled synthesis of NO in an atmospheric pressure plasma by suppressing NO destruction channels by plasma catalysis". *Journal of Physics D: Applied Physics* **57** (2024), 245203.

[36]   E. C. Neyts and A. Bogaerts. "Understanding plasma catalysis through modelling and simulation-a review". *Journal of Physics D: Applied Physics* **47** (2014), 224010.

[37]   I. Radu, R. Bartnikas, and M. Wertheimer. "Frequency and voltage dependence of glow and pseudoglow discharges in helium under atmospheric pressure". *IEEE Transactions on Plasma Science* **31** (2003), 1363 –1378.

[38]   L. Dosoudilová et al. "Investigation of helium barrier discharges with small admixtures of oxygen". *Journal of Physics D: Applied Physics* **48** (2015), 355204.

[39]   W. Siemens. "Über die elektrostatische Induction und die Verzögerung des Stroms in Flaschendrähten". *Annalen der Physik und Chemie* **178** (1857), 66–122.

[40]   F. Massines et al. "The Role of Dielectric Barrier Discharge Atmosphere and Physics on Polypropylene Surface Treatment". *Plasmas and Polymers* **6** (2001), 35–49.

[41]   U. Kogelschatz et al. "High-intensity sources of incoherent UV and VUV excimer radiation for low-temperature materials processing". *Applied Surface Science* **168** (2000), 29–36.

[42]   J. P. Boeuf. "Plasma display panels: physics, recent developments and key issues". *Journal of Physics D: Applied Physics* **36** (2003), R53.

[43] T. C. Corke, M. L. Post, and D. M. Orlov. "Single dielectric barrier discharge plasma enhanced aerodynamics: physics, modeling and applications". *Experiments in Fluids* **46** (2009), 1–26.

[44] S. Nijdam, J. Teunissen, and U. Ebert. "The physics of streamer discharge phenomena". *Plasma Sources Science and Technology* **29** (2020), 103001.

[45] E. Marode. "The mechanism of spark breakdown in air at atmospheric pressure between a positive point and a plane. I. Experimental: Nature of the streamer track". *Journal of Applied Physics* **46** (1975), 2005–2015.

[46] A. Fridman, A. Chirokov, and A. Gutsol. "Non-thermal atmospheric pressure discharges". *Journal of Physics D: Applied Physics* **38** (2005), R1.

[47] R. Brandenburg. "Dielectric barrier discharges: progress on plasma sources and on the understanding of regimes and single filaments". *Plasma Sources Science and Technology* **26** (2017), 053001.

[48] P. Viegas et al. "Quantification of surface charging memory effect in ionization wave dynamics". *Scientific Reports* **12** (2022), 1181.

[49] F. Massines et al. "Recent advances in the understanding of homogeneous dielectric barrier discharges". *The European Physical Journal Applied Physics* **47** (2009), 22805.

[50] F. T. Fumiyoshi Tochikubo, T. C. Takuma Chiba, and T. W. Tsuneo Watanabe. "Structure of Low-Frequency Helium Glow Discharge at Atmospheric Pressure between Parallel Plate Dielectric Electrodes". *Japanese Journal of Applied Physics* **38** (1999), 5244.

[51] M. Bogaczyk et al. "Surface charge accumulation and discharge development in diffuse and filamentary barrier discharges operating in He, N_2 and mixtures". *Journal of Physics D: Applied Physics* **45** (2012), 465202.

[52] Kai Wu and L. Dissado. "Model for electrical tree initiation in epoxy resin". *IEEE Transactions on Dielectrics and Electrical Insulation* **12** (2005), 655 – 668.

[53] F. Bronold et al. "Wall Charge and Potential from a Microscopic Point of View: Wall Charge and Potential from a Microscopic Point of View". *Contributions to Plasma Physics* **52** (2012), 856–863.

[54] R. L. Heinisch, F. X. Bronold, and H. Fehske. "Electron surface layer at the interface of a plasma and a dielectric wall". *Physical Review B* **85** (2012), 075323.

[55] U. Kogelschatz. "Filamentary, patterned, and diffuse barrier discharges". *IEEE Transactions on Plasma Science* **30** (2002), 1400 –1408.

[56] R. Bartnikas. "Note on discharges in helium under a.c. conditions". *Journal of Physics D: Applied Physics* **1** (1968), 659.

[57] N. Naudé et al. "Electrical model and analysis of the transition from an atmospheric pressure Townsend discharge to a filamentary discharge". *Journal of Physics D: Applied Physics* **38** (2005), 530.

[58] Y. B. Golubovskii et al. "Modelling of the homogeneous barrier discharge in helium at atmospheric pressure". *Journal of Physics D: Applied Physics* **36** (2003), 39.

[59] F. Massines et al. "Experimental and theoretical study of a glow discharge at atmospheric pressure controlled by dielectric barrier". *Journal of Applied Physics* **83** (1998), 2950–2957.

[60] R. Brandenburg et al. "Diffuse barrier discharges in nitrogen with small admixtures of oxygen: discharge mechanism and transition to the filamentary regime". *Journal of Physics D: Applied Physics* **38** (2005), 2187.

[61] K. V. Kozlov and H. Wagner. "Progress in Spectroscopic Diagnostics of Barrier Discharges". *Contributions to Plasma Physics* **47** (2007), 26–33.

[62] V. Léveillé and S. Coulombe. "Atomic Oxygen Production and Exploration of Reaction Mechanisms in a He-O_2 Atmospheric Pressure Glow Discharge Torch". *Plasma Processes and Polymers* **3** (2006), 587–596.

[63] A. Descoeudres, L. Sansonnens, and C. Hollenstein. "Attachment-induced ionization instability in electronegative capacitive RF discharges". *Plasma Sources Science and Technology* **12** (2003), 152.

[64]   D. Lee et al. "Numerical simulation on mode transition of atmospheric dielectric barrier discharge in helium-oxygen mixture". *IEEE Transactions on Plasma Science* **33** (2005), 949 –957.

[65]   G. Myers and A. J. Cunningham. "Quenching reactions of Helium metastables in the presence of N2 and O2". *The Journal of Chemical Physics* **67** (1977), 3352–3359.

[66]   R. Dussart et al. "Integrated micro-plasmas in silicon operating in helium". *The European Physical Journal D* **60** (2010), 601–608.

[67]   J. G. Eden et al. "Microplasma light tiles: thin sheet lamps for general illumination". *Journal of Physics D: Applied Physics* **44** (2011), 224011.

[68]   M. K. Kulsreshath et al. "Width-dependent interaction of trench-like microdischarges arranged in sub-arrays on a single silicon-based chip". *Plasma Sources Science and Technology* **23** (2014), 045012.

[69]   P. von Allmen et al. "Linear, segmented microdischarge array with an active length of 1 cm: cw and pulsed operation in the rare gases and evidence of gain on the 460.30 nm transition of Xe+". *Applied Physics Letters* **82** (2003), 4447–4449.

[70]   Sung-O Kim and J. Eden. "Arrays of microplasma devices fabricated in photodefinable glass and excited AC or DC by interdigitated electrodes". *IEEE Photonics Technology Letters* **17** (2005), 1543 –1545.

[71]   S.-J. Park, K. S. Kim, and J. G. Eden. "Nanoporous alumina as a dielectric for microcavity plasma devices: Multilayer Al/Al2O3 structures". *Applied Physics Letters* **86** (2005), 221501.

[72]   H. Boettner et al. "Excitation dynamics of micro-structured atmospheric pressure plasma arrays". *Journal of Physics D: Applied Physics* **43** (2010), 124010.

[73]   J. Waskoenig et al. "Spatial dynamics of the light emission from a microplasma array". *Applied Physics Letters* **92** (2008), 101503.

[74]   P. M. Bryant et al. "Time-Resolved Imaging of a Silicon Micro-Cavity Discharge Array". *IEEE Transactions on Plasma Science* **36** (2008), 1248 –1249.

[75]   M. J. Kushner. "Modeling of microdischarge devices: Pyramidal structures".
       Journal of Applied Physics **95** (2004), 846–859.

[76]   A. Wollny et al. "Ionization wave propagation on a micro cavity plasma array".
       Applied Physics Letters **99** (2011), 141504.

[77]   S. Kreuznacht, M. Böke, and V. Schulz-von der Gathen. "Intra-cavity dynamics
       in a microplasma channel by side-on imaging". *Plasma Sources Science and
       Technology* **30** (2021), 015014.

[78]   H. van Impel. "Analyse des elektrischen Feldes in einer mikroskalierten dielek-
       trisch behinderten Entladung". Master thesis, Ruhr-University Bochum, 2023.

[79]   M. K. Kulsreshath et al. "Ignition dynamics of dry-etched vertical cavity single-
       hole microdischarge reactors in ac regime operating in noble gases". *Journal of
       Physics D: Applied Physics* **47** (2014), 335202.

[80]   Q.-Z. Zhang and A. Bogaerts. "Propagation of a plasma streamer in catalyst
       pores". *Plasma Sources Science and Technology* **27** (2018), 035009.

[81]   A. Pipa et al. "The simplest equivalent circuit of a pulsed dielectric barrier
       discharge and the determination of the gas gap charge transfer". *Review of
       Scientific Instruments* **83** (2012), 115112.

[82]   A. Pipa and R. Brandenburg. "The Equivalent Circuit Approach for the Elec-
       trical Diagnostics of Dielectric Barrier Discharges: The Classical Theory and
       Recent Developments". *Atoms* **7** (2019), 14.

[83]   F. Peeters and T. Butterworth. "Electrical Diagnostics of Dielectric Barrier
       Discharges". *Atmospheric Pressure Plasma - from Diagnostics to Applications.*
       Ed. by A. Nikiforov and Z. Chen. IntechOpen, 2019.

[84]   T. C. Manley. "The Electric Characteristics of the Ozonator Discharge". *Trans-
       actions of The Electrochemical Society* **84** (1943).

[85]   F. J. J. Peeters and M. C. M. van de Sanden. "The influence of partial surface
       discharging on the electrical characterization of DBDs". *Plasma Sources Science
       and Technology* **24** (2014), 015016.

[86] S. Liu and M. Neiger. "Electrical modelling of homogeneous dielectric barrier discharges under an arbitrary excitation voltage". *Journal of Physics D: Applied Physics* **36** (2003), 3144.

[87] S. Nemschokmichal and J. Meichsner. "Spatio-temporal characterization of nitrogen metastables in diffuse nitrogen barrier discharges". *Journal of Physics D: Applied Physics* **48** (2015), 405203.

[88] T. Butterworth and R. W. K. Allen. "Plasma-catalyst interaction studied in a single pellet DBD reactor: dielectric constant effect on plasma dynamics". *Plasma Sources Science and Technology* **26** (2017), 065008.

[89] C. Meyer, J. Franzke, and E. L. Gurevich. "Experimental estimation of the surface charge density in micro dielectric barrier discharges". *Journal of Physics D: Applied Physics* **45** (2012), 355205.

[90] D. F. Opaits et al. "Surface charge in dielectric barrier discharge plasma actuators". *Physics of Plasmas* **15** (2008), 073505.

[91] R. Wild and L. Stollenwerk. "Phase-resolved measurement of the spatial surface charge distribution in a laterally patterned barrier discharge". *New Journal of Physics* **16** (2014), 113040.

[92] R. Tschiersch, S. Nemschokmichal, and J. Meichsner. "Influence of released surface electrons on the pre-ionization of helium barrier discharges: laser photodesorption experiment and 1D fluid simulation". *Plasma Sources Science and Technology* **26** (2017), 075006.

[93] P. F. Ambrico et al. "Thermoluminescence study of the trapped charge at an alumina surface electrode in different dielectric barrier discharge regimes". *Journal of Physics D: Applied Physics* **43** (2010), 325201.

[94] M. Li et al. "Effect of surface charge trapping on dielectric barrier discharge". *Applied Physics Letters* **92** (2008), 031503.

[95] R. Tschiersch, S. Nemschokmichal, and J. Meichsner. "The influence of negative ions in helium–oxygen barrier discharges: I. Laser photodetachment experiment". *Plasma Sources Science and Technology* **25** (2016), 025004.

[96]   H. R. Griem. *Principles of plasma spectroscopy.* Cambridge monographs on plasma physics. Cambridge University Press, 2005.

[97]   U. Fantz. "Basics of plasma spectroscopy". *Plasma Sources Science and Technology* **15** (2006), S137.

[98]   S. Iseni et al. "On the validity of neutral gas temperature by emission spectroscopy in micro-discharges close to atmospheric pressure". *Plasma Sources Science and Technology* **28** (2019), 065003.

[99]   A. Y. Nikiforov et al. "Electron density measurement in atmospheric pressure plasma jets: Stark broadening of hydrogenated and non-hydrogenated lines". *Plasma Sources Science and Technology* **24** (2015), 034001.

[100]   H. M. Katsch et al. "Detection of atomic oxygen: Improvement of actinometry and comparison with laser spectroscopy". *Journal of Applied Physics* **88** (2000), 6232–6238.

[101]   P. Paris et al. "Intensity ratio of spectral bands of nitrogen as a measure of electric field strength in plasmas". *Journal of Physics D: Applied Physics* **38** (2005), 3894.

[102]   K. Orr et al. "Measurements of electric field in an atmospheric pressure helium plasma jet by the E-FISH method". *Plasma Sources Science and Technology* **29** (2020), 035019.

[103]   M. Hofmans and A. Sobota. "Influence of a target on the electric field profile in a kHz atmospheric pressure plasma jet with the full calculation of the Stark shifts". *Journal of Applied Physics* **125** (2019), 043303.

[104]   N. Cvetanović et al. "Electric field measurement in gas discharges using stark shifts of He I lines and their forbidden counterparts". *Journal of Physics D: Applied Physics* **48** (2015), 205201.

[105]   B. M. Obradović, S. S. Ivković, and M. M. Kuraica. "Spectroscopic measurement of electric field in dielectric barrier discharge in helium". *Applied Physics Letters* **92** (2008), 191501.

[106]   J. S. Foster. "Application of quantum mechanics to the stark effect in helium". *Proceedings of the Royal Society of London. Series A, Containing Papers of a Mathematical and Physical Character* **117** (1927), 137–163.

[107]   H. Van Impel et al. "Electric field components within a micro-scaled DBD measured by Stark shifting and splitting of helium lines". *Plasma Sources Science and Technology* **accepted** (2024).

[108]   D. Steuer et al. "State enhanced actinometry in the COST microplasma jet". *Plasma Sources Science and Technology* **31** (2022), 10LT01.

[109]   T. Winzer et al. "RF-driven atmospheric-pressure capillary plasma jet in a He/O2 gas mixture: Multi-diagnostic approach to energy transport". *Journal of Applied Physics* **132** (2022), 183301.

[110]   D. Steuer et al. "Spatially and temporally resolved atomic oxygen densities in a micro cavity plasma array". *Plasma Sources Science and Technology* **32** (2023), 025013.

[111]   J. W. Coburn and M. Chen. "Optical emission spectroscopy of reactive plasmas: A method for correlating emission intensities to reactive particle density". *Journal of Applied Physics* **51** (1980), 3134–3136.

[112]   R. E. Walkup, K. L. Saenger, and G. S. Selwyn. "Studies of atomic oxygen in O_2 +CF_4 rf discharges by two-photon laser-induced fluorescence and optical emission spectroscopy". *The Journal of Chemical Physics* **84** (1986), 2668–2674.

[113]   K. Niemi et al. "Diagnostic based modelling of radio-frequency driven atmospheric pressure plasmas". *Journal of Physics D: Applied Physics* **43** (2010), 124006.

[114]   A. Greb et al. "Energy resolved actinometry for simultaneous measurement of atomic oxygen densities and local mean electron energies in radio-frequency driven plasmas". *Applied Physics Letters* **105** (2014), 234105.

[115]   T. Tsutsumi et al. "Investigation of the radially resolved oxygen dissociation degree and local mean electron energy in oxygen plasmas in contact with different surface materials". *Journal of Applied Physics* **121** (2017), 143301.

[116] G. J. M. Hagelaar and L. C. Pitchford. "Solving the Boltzmann equation to obtain electron transport coefficients and rate coefficients for fluid models". *Plasma Sources Science and Technology* **14** (2005), 722.

[117] J. E. Caplinger, G. P. Perram, and S. F. Adams. "A combined actinometry approach for medium pressure N_2 –O_2 plasmas". *Plasma Sources Science and Technology* **30** (2021), 015008.

[118] J. Golda et al. "Concepts and characteristics of the 'COST Reference Microplasma Jet'". *Journal of Physics D: Applied Physics* **49** (2016), 084003.

[119] F. Riedel et al. "Reproducibility of 'COST reference microplasma jets'". *Plasma Sources Science and Technology* **29** (2020), 095018.

[120] J. Schulze et al. "Excitation dynamics in electrically asymmetric capacitively coupled radio frequency discharges: experiment, simulation, and model". *Plasma Sources Science and Technology* **19** (2010), 045028.

[121] S. Brandt et al. "Electron power absorption dynamics in capacitive radio frequency discharges driven by tailored voltage waveforms in CF_4". *Plasma Sources Science and Technology* **25** (2016), 045015.

[122] P. J. Dagdigian, B. E. Forch, and A. W. Miziolek. "Collisional transfer between and quenching of the 3p 3p and sp states of the oxygen atom". *Chemical Physics Letters* **148** (1988), 299–308.

[123] K. Niemi, V. Schulz-von Der Gathen, and H. F. Döbele. "Absolute atomic oxygen density measurements by two-photon absorption laser-induced fluorescence spectroscopy in an RF-excited atmospheric pressure plasma jet". *Plasma Sources Science and Technology* **14** (2005), 375.

[124] P. S. Barklem. "Electron-impact excitation of neutral oxygen". *Astronomy & Astrophysics* **462** (2007), 781 –788.

[125] T. Mori et al. "Reactions of highly excited oxygen atoms O with simple gas molecules". *The Journal of Chemical Physics* **97** (1992), 9094–9098.

[126] N. Sadeghi et al. "Quenching rate constants for reactions of Ar atoms with 22 reagent gases". *The Journal of Chemical Physics* **115** (2001), 3144–3154.

[127] T. Gans et al. "Phase-resolved emission spectroscopy of a hydrogen rf discharge for the determination of quenching coefficients". *Physical Review A* **67** (2003), 012707.

[128] *LXCAT*. URL: `www.lxcat.net/Biagi` (visited on 05/06/2022).

[129] J. E. Chilton et al. "Measurement of electron-impact excitation into the 3p5 4p levels of argon using Fourier-transform spectroscopy". *Physical Review A* **57** (1998), 267.

[130] R. R. Laher and F. R. Gilmore. "Updated Excitation and Ionization Cross Sections for Electron Impact on Atomic Oxygen". *Journal of Physical and Chemical Reference Data* **19** (1990), 277–305.

[131] M. B. Schulman et al. "Emission from oxygen atoms produced by electron-impact dissociative excitation of oxygen molecules". *Physical Review A* **32** (1985), 2100.

[132] M. Mo et al. "Atomic oxygen densities in pulsed inductively-coupled plasmas: Laser spectroscopy & energy resolved actinometry". *Bulletin of the American Physical Society*. 74th Annual Gaseous Electronics Conference. Vol. 66.7. American Physical Society, 2021.

[133] I. Korolov et al. "Atomic oxygen generation in atmospheric pressure RF plasma jets driven by tailored voltage waveforms in mixtures of He and O_2". *Journal of Physics D: Applied Physics* **54** (2021), 125203.

[134] D. Steuer et al. "2D spatially resolved O atom density profiles in an atmospheric pressure plasma jet: from the active plasma volume to the effluent". *Journal of Physics D: Applied Physics* **54** (2021), 355204.

[135] C. Drag, F Marmuse, and C Blondel. "Measurement of the two-photon excitation cross-section of the 6p'$[3/2]_2$ and 6p'$[1/2]_0$ levels of Xe I at the wavelengths 224.3 and 222.6 nm". *Plasma Sources Science and Technology* **30** (2021), 075026.

[136] J. Waskoenig et al. "Atomic oxygen formation in a radio-frequency driven micro-atmospheric pressure plasma jet". *Plasma Sources Science and Technology* **19** (2010), 045018.

[137]   T. Hemke et al. "Spatially resolved simulation of a radio-frequency driven micro-atmospheric pressure plasma jet and its effluent". *Journal of Physics D: Applied Physics* **44** (2011), 285206.

[138]   J. Golda, J Held, and V. Schulz-von der Gathen. "Comparison of electron heating and energy loss mechanisms in an RF plasma jet operated in argon and helium". *Plasma Sources Science and Technology* **29** (2020), 025014.

[139]   P. J. Bruggeman et al. "Gas temperature determination from rotational lines in non-equilibrium plasmas: a review". *Plasma Sources Science and Technology* **23** (2014), 023001.

[140]   S. Reuter et al. "Atomic oxygen in a cold argon plasma jet: TALIF spectroscopy in ambient air with modelling and measurements of ambient species diffusion". *Plasma Sources Science and Technology* **21** (2012).

[141]   A. F. H. Van Gessel, S. C. Van Grootel, and P. J. Bruggeman. "Atomic oxygen TALIF measurements in an atmospheric-pressure microwave plasma jet with *in situ* xenon calibration". *Plasma Sources Science and Technology* **22** (2013), 055010.

[142]   K. Niemi. *Nachweis leichter Atome in reaktiven Plasmen mittels Zweiphotonen laserinduzierter Fluoreszenzspektroskopie unter besonderer Berücksichtigung der Absolutkalibrierung.* Cuvillier Verlag, 2003.

[143]   K. Niemi, V. Schulz-von der Gathen, and H. F. Döbele. "Absolute calibration of atomic density measurements by laser-induced fluorescence spectroscopy with two-photon excitation". *Journal of Physics D: Applied Physics* **34** (2001), 2330.

[144]   R. Labenski et al. "Novel methods for determination and manipulation of surface charges performed on an atmospheric DBD microplasma". *Plasma Sources Science and Technology* **accepted** (2024).

[145]   D. Steuer et al. "Measurement of atomic oxygen densities using TALIF on a dielectric barrier discharge: Insights into the volume above a micro cavity plasma array". *Plasma Sources Science and Technology* **under Review** (2024).

[146]   Z. Shu, N. A. Popov, and S. M. Starikovskaia. "Absolute calibration of the ratio of Xe/O two-photon absorption cross-sections for O-TALIF applications". *Plasma Sources Science and Technology* **33** (2024), 025019.

[147] H. Böttner. "Dynamics in micro-scaled atmospheric pressure plasma arrays". PhD thesis. Ruhr-University Bochum, 2011.

[148] C. R. Paul. *Analysis of Multiconductor Transmission Lines*. John Wiley & Sons, 2007.

[149] H. Mahdikia et al. "CO2 Dissociation in Barrier Corona Discharges: Effect of Elevated Pressures in CO2/Ar Mixtures". *Plasma Chemistry and Plasma Processing* (2023), 2035–2063.

[150] N. Benard and E. Moreau. "Electrical and mechanical characteristics of surface AC dielectric barrier discharge plasma actuators applied to airflow control". *Experiments in Fluids* **55** (2014), 1846.

[151] A. V. Pipa et al. "Dependence of dissipated power on applied voltage for surface barrier discharge from simplest equivalent circuit". *Plasma Sources Science and Technology* **29** (2020), 12LT01.

[152] M. Bogaczyk, G. B. Sretenović, and H.-E. Wagner. "Influence of the applied voltage shape on the barrier discharge operation modes in helium". *The European Physical Journal D* **67** (2013), 212.

[153] L. Mangolini et al. "Radial structure of a low-frequency atmospheric-pressure glow discharge in helium". *Applied Physics Letters* **80** (2002), 1722–1724.

[154] I. Radu, R Bartnikas, and M. R. Wertheimer. "Dielectric barrier discharges in atmospheric pressure helium in cylinder-plane geometry: experiments and model". *Journal of Physics D: Applied Physics* **37** (2004), 449.

[155] R. Bartnikas and J. Novak. "On the spark to pseudoglow and glow transition mechanism and discharge detectability". *IEEE Transactions on Electrical Insulation* **27** (1992), 3 –14.

[156] R. Labenski. "Laser-induced influence on the charges in a surface dielectric barrier discharge at atmospheric pressure". Master thesis, Ruhr-University Bochum, 2023.

[157] R. Brandenburg et al. "Novel insights into the development of barrier discharges by advanced volume and surface diagnostics". *Journal of Physics D: Applied Physics* **46** (2013), 464015.

[158] R. Tschiersch, M. Bogaczyk, and H.-E. Wagner. "Systematic investigation of the barrier discharge operation in helium, nitrogen, and mixtures: discharge development, formation and decay of surface charges". *Journal of Physics D: Applied Physics* **47** (2014), 365204.

[159] D. Steuer et al. "Mode transition in a helium barrier discharge with oxygen admixtures: Insights into a micro cavity plasma array reactor". *Journal of Physics D: Applied Physics* **submitted** (2024).

[160] I. P. Raĭzer. *Gas discharge physics.* Springer, 1997.

[161] Q. Wang et al. "Experimental and theoretical study of the effect of gas flow on gas temperature in an atmospheric pressure microplasma". *Journal of Physics D: Applied Physics* **40** (2007), 4202.

[162] N. K. Bibinov, A. A. Fateev, and K Wiesemann. "On the influence of metastable reactions on rotational temperatures in dielectric barrier discharges in He-N$_2$ mixtures". *Journal of Physics D: Applied Physics* **34** (2001), 1819.

[163] Y.-R. Zhang et al. "Can plasma be formed in catalyst pores? A modeling investigation". *Applied Catalysis B: Environmental* **185** (2016), 56–67.

[164] D. S. Stafford and M. J. Kushner. "O2 production in He/O2 mixtures in flowing low pressure plasmas". *Journal of Applied Physics* **96** (2004), 2451–2465.

[165] M. M. Turner. "Uncertainty and sensitivity analysis in complex plasma chemistry models". *Plasma Sources Science and Technology* **25** (2016), 015003.

David Frithjof Steuer

PHD Candidate – Ruhr University Bochum

Curriculum Vitae

Name	**David Frithjof Steuer**
Date of Birth	**21.08.1995**
Place of Birth	**Herne**, Germany

Education

since 2020	**PhD. Student**, *Physics*, Ruhr-University Bochum
2018-2020	**Master of Science**, *Physics*, Ruhr-University Bochum
2014-2018	**Bachelor of Science**, *Physics*, Ruhr-University Bochum
2014	**Abitur**, Märkisches Gymnasium Wattenscheid
2006-2014	**Secondary School**, Märkisches Gymnasium Wattenscheid
2002-2006	**Primary School**, Swidbertschule Wattenscheid

Employment

since 2020	**Research Assistant**, Group Plasma Interface Physics, Ruhr-University Bochum
2018-2019	**Student Assistant**, Chair for Experimental Physics II, Ruhr-University Bochum
2015-2018	**Working Student**, Technology Development, KOSTAL Automotive Electrics

Research Stays and International Presentations

2024	**Gordon Research Conference**, Andover, USA, Poster Presentation
2024	**Sandia Plasma Research Facility**, Albuquerque, USA Ten week research stay as part of a cooperation project with Dr. Brian Z. Bentz
2023	**International Symposium on Plasma Chemistry**, Kyoto, Japan, Oral Presentation
2023	**International Online Plasma Seminar**, Online, Invited Oral Presentation
2022	**International Conference on Plasma Science**, Seatlle, USA, Oral Presentation
2021	**Annual Gaseous Electronics Conference**, Online, Oral Presentation

Awards and Achievements

2023	**Scholarship (PR.INT)**, awarded by the Research School of the Ruhr-University Bochum
2021	**Award for students with outstanding final theses**, Ruhr-University Bochum